Proceedings

Maurizio Ferrari

Marian Marciniak

Giancarlo C. Righini

Tomasz Szoplik

Stefano Varas

Editors

IFN CNR

Micro- and nano-photonic materials and devices

Proceedings of MINAP 2012 – Final Conference of the MP0702 COST Action (Trento, Italy, 16-18 January 2012)

Editors:

Maurizio Ferrari, Marian Marciniak, Giancarlo C. Righini, Tomasz Szoplik, Stefano Varas

CNR

National Research Council, Italy

Editors

Maurizio Ferrari, *Institute of Photonics and Nanotechnology (IFN – CNR, Trento, Italy)*

Marian Marciniak, *National Institute of Telecommunications (Warsaw, Poland)*

Giancarlo C. Righini, *Nello Carrara Institute of Applied Physics (IFAC – CNR, Firenze, Italy)*

Tomasz Szoplik, *Warsaw University (Warsaw, Poland)*

Stefano Varas, *Institute of Photonics and Nanotechnology (IFN – CNR, Trento, Italy)*

Organizers

The Conference MINAP 2012 was promoted by the COST Action MP0702 and organized by IFN – CNR in close collaboration with Fondazione Bruno Kessler (FBK, Trento) and IFAC – CNR.

Web site of Conference: http://minap2012.fbk.eu

Conference Sponsors:

Printed by Bel Studio (Warsaw, Poland) on behalf of the Institute of Photonics and Nanotechnology (IFN – CNR, Trento, Italy) - January 2012.

ISBN: 978-83-7798-020-0

MINAP 2012 Programme Committee:

Conference Co-chairs:

Maurizio Ferrari (CNR-IFN, Trento)

Giancarlo C. Righini (CNR-IFAC, Firenze)

Scientific Committee:

Paulo André (Portugal)

Trevor Benson (U.K.)

Pavel Cheben (Canada)

Jiri Ctyroky (Czech Republic)

Martina Gerken (Germany)

Bozena Jaskorzynska (Sweden)

Nigel Johnson (U.K.)

John McInerney (Ireland)

Bjorn Maes (Belgium)

Marian Marciniak (Poland)

Tanya Monro (Australia)

Ekmel Ozbay (Turkey)

Krasimir Panayotov (Bulgaria)

Bouchta Sahraoui (France)

Marc Sciamanna (France)

Concita Sibilia (Italy)

Clivia Sotomayor Torres (Spain)

Misha Sumetsky (USA)

Local Organizing Committee:

Cristina Armellini (CNR-IFN, FBK)

Marina Bertoldi (CNR-IFN)

Olga Bolszo (NIT, Warsaw)

Alessandro Carpentiero (CNR-IFN)

Andrea Chiappini (CNR-IFN)

Elena Gerola (CNR-IBF)

Silvia Malesardi (FBK)

Tiziana Martinelli (CNR-IFN, FBK)

Anna Piotrowska (NIT, Warsaw)

Stefano Varas (CNR-IFN)

Introduction

COST Action MP0702 - Towards Functional Sub-Wavelength Photonic Structures 2008-2012

> *The main objective of the Action is to establish active links between European laboratories working in the field of artificial materials for photonics applications, where the structural dimensions are at or below the wavelength of light.*

This Final Conference of the Action reports on the main results as well as on the problems opened to future study, and it is an important milestone in the four-year activities of the Action. I appreciate all Colleagues who have agreed to contribute to this event and to report their latest COST-related results, and I wish all of you fruitful interactions with other Members, as well as an enjoyable stay in this charming part of North Italy.

Let me recall a number of precedent important Action open events organised so far: Kick-off Workshop in Warsaw (2008), workshops in Bratislava (2008), in Angers (2009&2011), and Annual Conferences in Azores (2009), in Munich (2010), and in Stockholm (2011). Those have been completed with a series of Training Schools in Metz (2009), in Porquerolles (2009), in Erice (2010), in Naples (2010), and recently in Tampere (August 2011).

This is the right time to express my thanks for excellent coordination of Working Group and Project activities by WG Leaders and Project Coordinators. Especially active Short-Term Scientific Mission, STSM exchange has to be emphasized. An excellent coordination of STSM exchange by Trevor merits to be specially applauded. The Management Committee of the Action has decisively contributed to Action's progress with wise and timely decisions. I am thanking all MC Members for their valuable support. Needless to say the continuing support I have been receiving from Concita – both as from the Vice-Chair, and as from the Chair of the precedent Action P11, has to be specially acknowledged.

The involvement of non-COST laboratories provides us with a valuable insight to the frontier research in sub-wavelength photonics carried out there. This assures to the Action a truly global dimension. I warmly invite the non-COST Colleagues to maintain the professional and personal links established within this Action in the coming years.

I appreciate the valuable synergy with sister COST Actions: MP0803 Plasmonic components and devices, and MP0805 Novel Gain Materials and Devices Based on III-V-N Compounds. I wish those Colleagues a smooth progress towards their ambitious goals.

After serving the Action as the chair for past four years I am pleased to state with have formed an efficient and friendly community, and we have combined frontier research, exciting results, and durable scientific interactions with friendly social contacts as proclaimed in the Memorandum of Understanding, 'The Main Objective' section.

I am thanking for COST Office staff support: Science Officers Piotr and Caroline, and Administrative Officers Stéphanie, Marie-Eve, and Milena. I thank my young colleague Olga for her priceless services as of the Voluntary Secretary for the Action.

I am pleased to emphasize the presence and contributions of External Experts including the two eminent scientists who act as the Evaluators,and the Rapporteur for this Final Conference.

I appreciate the kind hospitality of the hosting institutions, in particular of FBK, and local authorities. I am pleased to acknowledge the devotion and organisational efforts of all the members of the Local Organising Committee, and of the co-chairs Giancarlo and Maurizio.

I wish all of you to continue fruitful and friendly interactions in this Final Conference, and beyond.

Marian

Marian Marciniak
Chair MP0702 (2008-2012)

Table of Contents

NOTE: In the present volume all the figures are in black and white, due to economic reasons. Color figures are maintained in the on-line version of these Proceedings, available to participants on the web site http://minap2012.fbk.eu

Optical Buffer Memories Based on Photonic Crystals

Andrea Blanco[1], Imanol Andonegui[1], Joseba Zubía[2]
[1] TECNALIA, TELECOM Unit, Parque Tecnológico de Bizkaia,Edificio 202, 48170 Zamudio (Bizkaia),Spain.
Tel: +34664114936; e-mail: andrea.blanco@tecnalia.com
[2] UPV/EHU, ETSI de Bilbao, Alameda de Urkijo,s/n, 48013, Bilbao, Spain.

ABSTRACT

In this paper, the need of optical buffers for enabling other optical processing functions is reasoned. Photonic crystal slow-light waveguides and coupled cavities are presented as a promising approach to make continuously tunable optical delay lines. Results on the optimization of the quality factor and modal volume of photonic crystal cavities using a Finite Element Method approach combined with a multi-objective genetic algorithm are given. Finally, the possibility of fast and efficient electro-optic reconfiguration of photonic crystals is proved by a series of simulation results showing the Pockels-induced shift of the resonant wavelength in a lithium niobate photonic crystal cavity.

Keywords: Optical buffer, tunable optical delay line, photonic crystal cavities, delay-bandwidth product, reconfigurability, electro-optic effect

1. INTRODUCTION

Signal processing is the basis of many telecommunication functions as it enhances system performance and efficiency. Nowadays, telecommunication equipment carries out all internal signal processing functions in the electronic domain, even in the core routers of optical networks. By performing optical signal processing the inefficiencies associated to optical-to-electronic (O/E) and electronic-to-optical (E/O) conversions could be avoided and the unmatched high-bandwidth ofoptics could be better utilized. In order to perform any kind of optical signal processing we must first achieve temporal control over light signals and thuscontinuously tunable optical delay lines serving as optical buffers are needed[1].

Unluckily, continuously tunable optical delay lines have been historically difficult to realize. So far, the unique practical implementations of delay lines have been based in lengthening the physical path to be covered by light signals. Some kind of coarse tunabilityis achieved in this approach by switching between a set of predefined paths. However, this technique is not satisfactory since its delay resolution is limited to sub-nanoseconds (the shortest path length) and besides, losses and bulkiness impede its scalability[2].

Using photonic crystal slow-light waveguides and cavities appears as a strong alternative to build continuously tunable optical delay lines. These set of techniques aims at reducing and controlling the propagation speed of light pulses and they are normally based on creating and exploitingenhanced group index resonances. Unfortunately, this principle entails dispersion, attenuation and filtering effects over the delayed signals. Therefore, to provide continuously tunable large delays over wide-bandwidth signals, the deleterious effects affecting data fidelity need to be compensated first [3].

Some of the key features to be fulfilled by tunable optical delay lines and, most particularly by its application to optical buffering, are: large delay range, continuous and fast tunability, wide bandwidth, low power dissipation, transparency to modulation formats and bit rate, and low amplitude and phase degradation. By now, it is clear that the capacities of current electronic memories (RAMs) will not be achievable by photonic buffer memories, at least in a medium term. Nevertheless, it has also been made patent that an optical buffering capacity of a few packets (10-20) may be enough in future optical networks [4]. Therefore, all efforts are currently set in achieving photonic buffers providing small but acceptable storage capabilities while maintaining the premises of wide-bandwidth, fast access to data and low signal distortion among others.

Along the rest of this paper, photonic crystal (PhC) based approaches to optical buffering will be presented. In section 2 a special emphasis on the maximization of the delay range of photonic crystal cavities is made, based on a figure of merit considering the quality factor and the modal volume. Section 3 focuses in the issue of fast reconfigurability in photonic crystal structures, exploring the fast electro-optic effect in nonlinear media.

2. PHOTONIC CRYSTAL APPROACH TO OPTICAL BUFFERING

Photonic crystals are periodic, dielectric, artificial materials which present singular properties for electromagnetic waves propagation[5]. The most remarkable of these properties is the appearance of the so called photonic band gap, a range of frequencies unable to propagate through the material (see Fig.1). Many profitable effects stem from the existence of photonic band gaps: from the possibility of tight sub-wavelength light confinement to the opportunity of achieving extremely low group velocities. The most obvious application of the dramatic reduction of the speed of light is the creation of optical delay lines or photonic buffers, where light pulses are temporary stored.

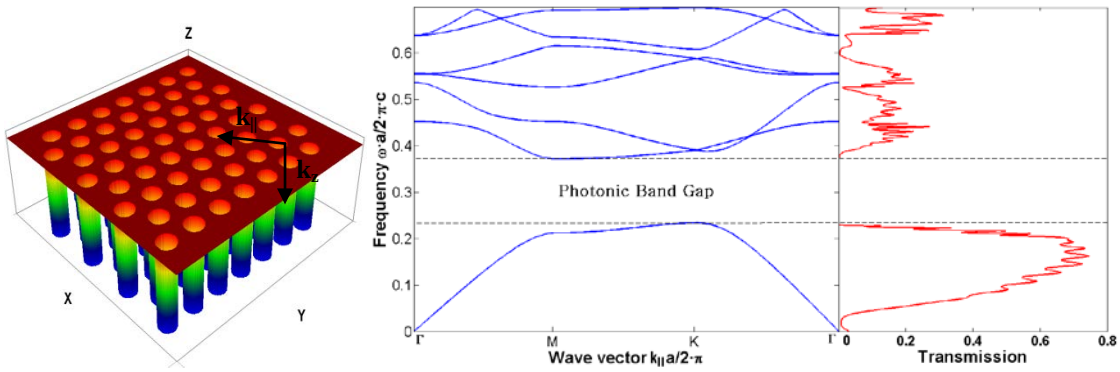

Figure 1. (Left) 2D hexagonal lattice of holes in silicon; (right) its corresponding in-plane band &transmission diagrams for TE modes. The lattice period is a, the dielectric constant is ε=11,9716 and the hole radii r=0.36·a

2.1 Slow light in photonic crystal waveguides

To exploit photonic crystal capacities for storing light pulses, one has to resort to the creation of defects within the otherwise perfectly periodic structure. Punctual and linear defects within the photonic crystal allow for tight confinement of light, at band gap frequencies, inside cavities and waveguides.

One can create a photonic crystal waveguide by creating a linear defect, e.g. by simply removing a single row of holes in the PhC of Fig.1. Such a waveguide, normally referred as W1, results in the appearance of a number of defect modes within the photonic band gap. As monomode behaviour is desirable, narrowing the waveguide is normally required.

These waveguides present extremely low group velocities within a very narrow frequency range at the band edges. Unfortunately, these working regions are not desirable in practice. At the band edges, any fluctuation in the structure, due to fabrication imperfections, causes oscillations between guided and not guided states. Moreover, the bandwidth for this ultra-low velocity is very small. Several waveguide designs have been proposed to minimize dispersion and enable higher bandwidths[3][6][7]. To this purpose our group has recently proposed a W0.64 PhC waveguide created by diminishing the radii of a row of holes and filling it with a lower-index material[8]. Group velocities of c/100 are achieved for a 33% of the k-vector space, achieving a good balance between low information velocity and bandwidth but still unsatisfactory to develop a real optical buffer and thus requiring the introduction of cavities in the design.

2.2 Photonic crystal cavities as a basic building block for optical buffer memories

The dispersion problem of photonic crystal waveguides can also be tackled by coupling a series of punctual defects (cavities) within the photonic band gap material. By enhancing the amount of confined energy and the coupling between cavities and waveguides photons can be stored for a relative long time in an extremely small volume. Since the structural design of new cavities should accomplish both conditions, we have proposed a finite element method approach combined with a multi-objective genetic algorithm optimization. In this process each individual's transmittance response and defect mode's spatial distribution is calculated and a figure of merit of its characteristics is obtained. The initial population for the genetic algorithm (GA) is randomly initialised but its configuration is bounded to a drilled triangular lattice of silica. Then, the genetic algorithm induces disorder into the first two periods surrounding an initial punctual defect and at the same time it tunes each of these holes radii. For each individual (see Fig.2), a discrete set of transmittance response data is calculated and an exponentially modified Gaussian (EMG) fitting is applied to the resonant spectra. Consequently, the Q factor is determined by the relation of the peak centre to the full-width half maximum (FWHM). Finally, the individuals obtained through the GA´s iterative process will be replicated, since the nearby evanescent fields of cavities, i.e the radiated energy, can be coupled to a second resonator. This process can be expanded in the so-called coupled-resonator optical waveguide (CROW). Remarkable achievements have been done in this field, as in [9] where more than 100 high-Q cavities were coupled, achieving vg of c/170 in pulse propagation experiments and notable storage capacity. The resulting configurations are still subject to weak coupling factors from PhCW (Photonic Crystal Waveguides) which need to be redesigned for each nanocavity configuration.

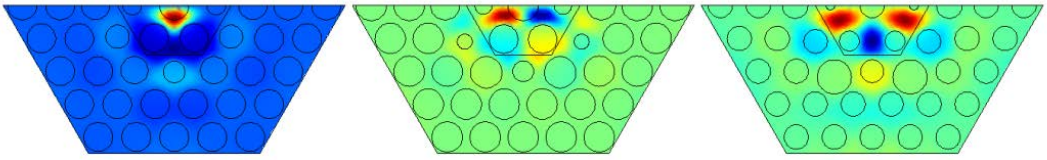

Figure 2.Hz modal field distributions for different individuals showing the used computational domain

3. FAST RECONFIGURABILITY OF PHOTONIC CRYSTAL STRUCTURES USING THE ELECTRO-OPTIC EFFECT

Most of the work done in photonic crystals has been realized in silicon and other high-index semiconductor materials[10][11].However, changing the refractive index of silicon, in order to obtain reconfigurability [12], is a challenge, since the internal symmetry of the atomic crystal of silicon forbids any linear electro-optic effect, and hence other effects must be exploited, as thermo-optical effect [13] and/or injection of free-carriers [14].

Electro-optics crystals, such as lithium niobate ($LiNbO_3$), have only recently been proposed as a suitable material for photonic crystal based devices. These are commonly used in optics and telecom due to its transparency in a wide wavelength range and due to its due to its excellent nonlinear- and electro-optical properties. The reason for this is that its high resistivity towards different etching techniques makes its nanostructuring more difficult than that of silicon. Nevertheless these technical fabrication challenges are being overcome [15][16]and thence it is worth to explore $LiNbO_3$ photonic crystals and their possibilities of fast and efficient electro-optic reconfiguration.

3.1 Photonic crystal cavity on lithium niobate

We have designed and simulated the photonic crystal structure on lithium niobate,shown in Fig. 3.a., consisting on a slow-light coupling waveguide and a cavity created by removing a single hole and modifying the radii of its neighbours. The lattice period is a=510nm, the radius of the lattice holes is r=0.3a and the waveguide is a simple W1. The radius of the two lateral neighbours to the missing hole is r_1=0.33a and the radius of the two holes above and the two holes under the missing one is r_2=0.29a. This is a monomode resonant cavity with a resonance around 1.5μm, precisely at 1499.1nm, that causes a drop peak in the transmission spectrum of the waveguide shown in Fig.3.c and Fig.3.d.

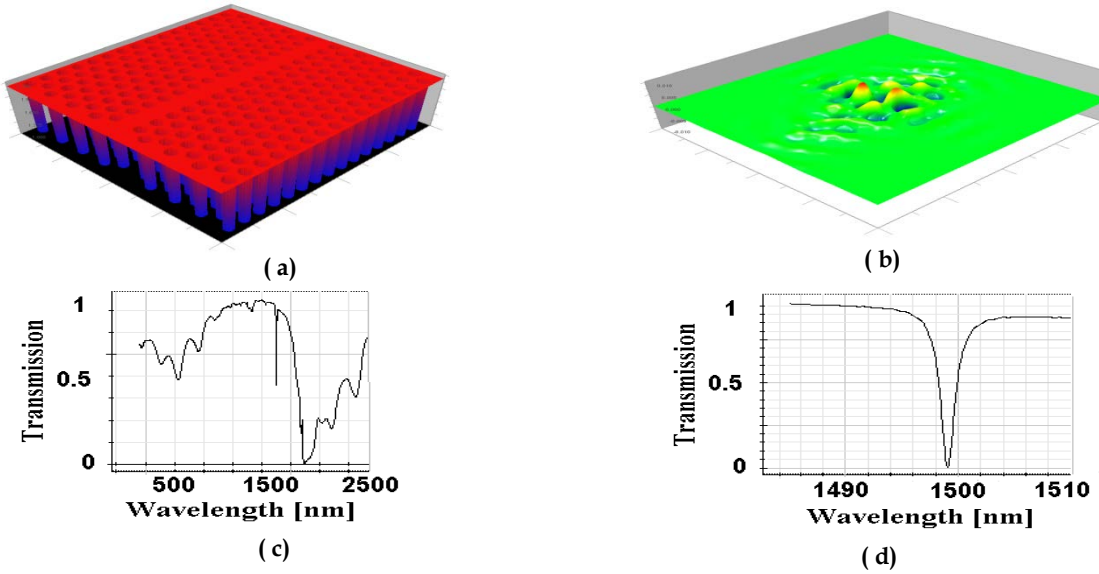

Figure. 3. (a) Photonic crystal cavity with coupling slow-light waveguide on lithium niobate; (b) Perpendicular component of the magnetic field of the resonant optical wave; (c) Transmission spectrum measured at the output of the waveguide over a wide spectrum; and(d)transmission spectrum zoomed in the drop resonance.

3.2 Fast reconfigurability based on the electro-optic effect

Lithium niobate is a uniaxial crystal of 3m symmetry. Since r_{33} is the largest Pockels coefficient of $LiNbO_3$, the largest index change is obtained in n_z when the electric field is applied along the *z* axis. The change of the extraordinary index in response to such a field is given by equation (1), as obtained in [17].

$$\Delta n_e = -\left(\frac{n_e^3}{2}\right) r_{33}\left(\frac{V}{d}\right) \tag{1}$$

In normal applications the applied electric field takes values from 0.1 to 10MV·m^{-1}. This range of field values gives rise to index changes from $\Delta n_e = 1.55\cdot10^{-5}$ to $\Delta n_e = 1.55\cdot10^{-3}$ at around λ=1.5μm. We have computed the resonances of the photonic crystal structure in Fig.3.a using a 2D FDTD method, in order to measure the resonant wavelength shift originating from thoseelectro-optically induced index changes. The results, presented in Fig. 4, show a quasi-linear red-shift (resp. blue-shift) of the resonance for positive increments (resp. negative increments) of the refractive index.

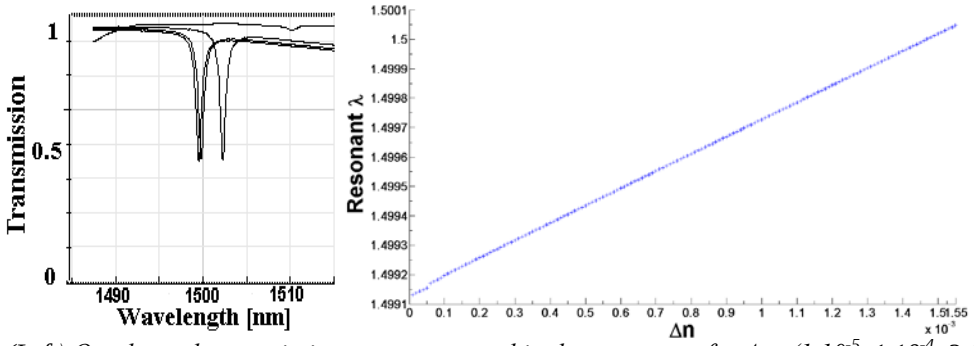

Figure 4.(Left) Overlapped transmission spectra zoomed in the resonance for $\Delta n=(1\cdot10^{-5}, 1\cdot10^{-4}, 3\cdot10^{-3})$ and (right) resonant wavelength as a function of the electro-optically induced index changes

A maximum wavelength shift of ± 915pm is obtained for the considered range, and a wavelength shift of 6pm is observed in response to every $1\cdot10^{-5}$index change. These results prove the capabilities of fast and efficient reconfiguration and/or tunability of a lithium niobate photonic crystal optical buffer and can be further improved by using higher-Q cavities, as the ones introduced in section 2.2.

4. CONCLUSIONS

Optical buffers are needed as an enabling technology for optical packet switching and other signal processing functions. Slow light and cavities in photonic crystals appear as strong candidates to realize integrated photonic buffers. Research efforts are set in solving their limitations in delay-bandwidth product and reconfigurability. Along the paper we have shown part of our progress in improving a cavity's' figure of merit based on a combination of Q and modal volume. Finally, we have presented some results on the capabilities of reconfiguration of photonic crystals by using Pockels effect.

REFERENCES

[1] R.S. Tucker: Slow light buffers for packet switching, in *Slow light - science and applications*, J. Khurgin, R. Tucker, CRC Press-Taylor and Francis Group, Boca Raton, USA

[2] A. Willner, S.R. Nuccio: Recent advances in tunable optical delays and their applications, in *Proc. SPIE Photonics West 2011*, San Francisco, CA, USA, January 2011

[3] T. Baba: Slow light in photonic crystals, *Nature Photonics*, vol.2, pp. 465-473, Aug. 2008.

[4] N. Behetsi, *et al.*: Buffer sizing in all-optical packet switches, in *Proc. Optical Fiber Communications Conference OFC/NFOEC 2006*, Anaheim, CA, USA, 2006

[5] J. Joannopoulos, *et al.*:*Photonic Crystals: Molding the Flow of Light*, Princeton University Press, USA

[6] L. O'Faolain, *et al.*: Low loss dispersion engineered photonic crystal waveguides for optical delay lines, in *Proc. of 6th IEEE International Conf. on Group IV Photonics*, pp. 40–42, San Francisco, USA, Sept. 2009

[7] B. Corcoran, C. Monat, D. Pudo, B.J. Eggleton, T.F. Krauss, D.J. Moss, L. O'Faolain, L., M. Pelusi, T. P. White: Nonlinear loss dynamics in a silicon slow-light photonic crystal waveguide, *Optics Letters*, Vol. 35, Issue 7, pp. 1073-1075

[8] I. Andonegi, A. Blanco, A. Garcia-Adeva, A.: Characterization of slow light regime in 2D ohotonic crystal waveguides, in *Proc. Photonics, Plasmonics and Magnetooptics*2011, Bilbao, Spain, April 2011

[9] M. Notomi, *et al.*: Large-scale arrays of ultrahigh-Q coupled nanocavities, *Nature Photonics*, vol. 2, pp. 741-747, Dec. 2008

[10] Y. Akahane, T. Asano, B. S. Song, S. Noda: High-Q photonic nanocavity in a two-dimensional photonic crystal, *Nature* , vol. 425, pp. 944-947, Oct. 2003.

[11] V. R. Almeida, C. A. Barrios, R. R. Panepucci, M. Lipson: All-optical control of light on a silicon chip, *Nature*, vol. 431, pp. 1081-1084, Oct. 2004.

[12] A. Blanco, E. Areizaga, J. Zubía: Slow light for microwave photonics applications, in *Proc. IEEE Mediterranean Microwave Symposium (MMS) 2009*, Tangiers, Morocco, Nov. 2009

[13] C. A. Barrios,*et al.*: Compact silicon tunable Fabry-Pérot resonator with low power consumption, *IEEE Photonics Technology Lett.*, vol. 16, n 2, pp. 506-508 Feb. 2004.

[14] R. Soref, B. Bennet: Electrooptical effects in Silicon, *IEEE Journal of Quantum Electronics*, vol.23, issue 1, pp.123-129, Jan. 1987

[15] F. Sulser, et al.: Photonic crystal structures in ion-sliced lithium niobate thin Films, *Optics Express*, vol. 17, no. 22, pp. 20291-20301, Oct. 2009

[16] H. Hui, R. Ricken and W. Sohler: Etching of lithium niobate: from ridge waveguides to photonic crystal structures, *Proc. ECIO'08*, Eindhoven, The Netherlands, June 2008, paper WeD3.

[17] J. Liu, *Photonic Devices*, Cambridge University Press, Cambridge, UK

Analysis of metallic photonic structures

Reinhold Pregla, *Life Fellow, IEEE*
University of Hagen, Germany

At optical frequencies metals behave like dielectric materials with complex permittivity. E.g. the permittivity of silver at the wavelength λ=0.6μm is equal to ε_r= –14.7897 –j0.4088. Because of this fact the surface impedance is inductive with a positive imaginary part. Therefore, the surface can guide a TM-polarized wave. The guiding parameters are easily obtained from the lateral surface impedances. They must be equal with a negative sign. Because of the complex ε_r the propagation loss is not negligible.

The aim of this contribution is to analyze structures like that in Figure 1 for which the confinement of the field increases because of the higher value for the imaginary part of the surface impedance.

The wave is propagating in the upper part. The depth of the teeth (L_W in Figure 2.) must be chosen in a suitable way to obtain a surface impedance with a positive imaginary part on the surface above the periodic structure.

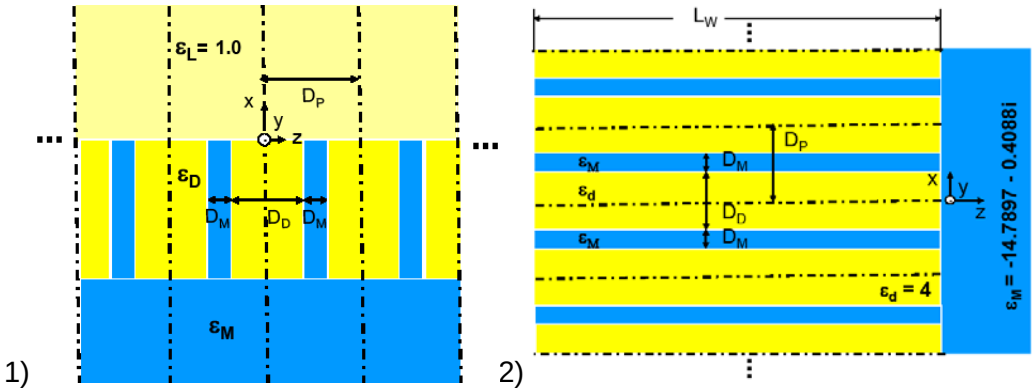

Figure 1: 2-D periodic structure of silver dielectric material: propagation in z-direction.

Figure 2: 2-D periodic multilayered structure for the analysis of the field between the teeth

NOTES

Nanophotonic Sensors

Nigel P Johnson[1], Basudev Lahiri[2], Graham Sharp[1], Ali Khokhar[1], Ghazali A Rahman[1], Philippe Velha[1], Richard M De La Rue, Scott McMeekin[4]

[1]*School of Engineering, Optoelectronics Research Group, University of Glasgow, Rankine Building, Oakfield Avenue, Glasgow G12 8LT, UK*
Tel: +441413304110; e-mail: nigel.johnson@glasgow.ac.uk

[2]*Center for Nanoscale Science and Technology, National Institute of Standards and Technology, 100 Bureau Drive, Mail Stop 6204 Gaithersburg, MD 20899-6204, USA*

[3] *Photonics Research Centre, Physics Department, Science Faculty, University of Malaya, 50603 Kuala Lumpur, Malaysia.*

[4]*School of Engineering and Built Environment, Glasgow Caledonian University, Glasgow, G4 0BA, UK*

ABSTRACT
Device structures such as photonic crystals, photonic wires and optical metamaterials - all with submicron features can be described as 'nanophotonic'. Many of these devices and structures can be used as sensors – relying on the change in refractive index of a surrounding medium. In this paper, we discuss several nanophotonic sensing systems, including asymmetric split ring resonators, photonic wire cavities and polymer Bragg gratings.
Keywords: Nanophotonic, sensors, asymmetric split ring resonators, polymer Bragg gratings.

1. INTRODUCTION

The ability to detect small refractive index changes in analytes is importantbecause changes of refractive index can be directly correlated to the presence of small amounts of chemicals or biological material within analytes. We present several optical methods ranging from nanobeams with a high Q cavity, an intermediate Q system formed in polymer waveguides, and a low Q system but with a large wavelength shift that gives high sensitivity.

2. NANOBEAM CAVITIES

1-D photonic wire microcavities are also known as nanobeam cavities are one of the emerging configurations for refractive index based optical sensors. Here, we present the design, modelling and fabrication of Silicon-On-Insulator (SOI) nanobeam cavities. The sensitivity of such optical sensor depends on width of the resonance wavelength (Q-factor) [1], and the achievable resonance wavelength shift. As the light bounces between the two mirrors forming the cavity, the mode overlaps with the analytes which results in a potentially large wavelength shifts. To optimize and fine-tune the nanobeams, we have used a well demonstrated rule based on gradually increasing holes sizes holes inside the cavity, this is known as tapering [2]. When the light is strongly confined in the cavity mode, the sensitivity, $S = \Delta\lambda/\Delta n$ has a value greater than 200 nm/RIU (refractive index unit, RIU). We have modelled and optimized a suspended nanobeam cavity working in a water-based (n = 1.333) environment and achieved a Q-factor of more than 20 000. The simulation in figure 2 (a) showsthe shift in peak position for a change in refractive index of the surrounding medium from 1.333 to 1.350 while figure 2 (b) shows the fabricated structure.

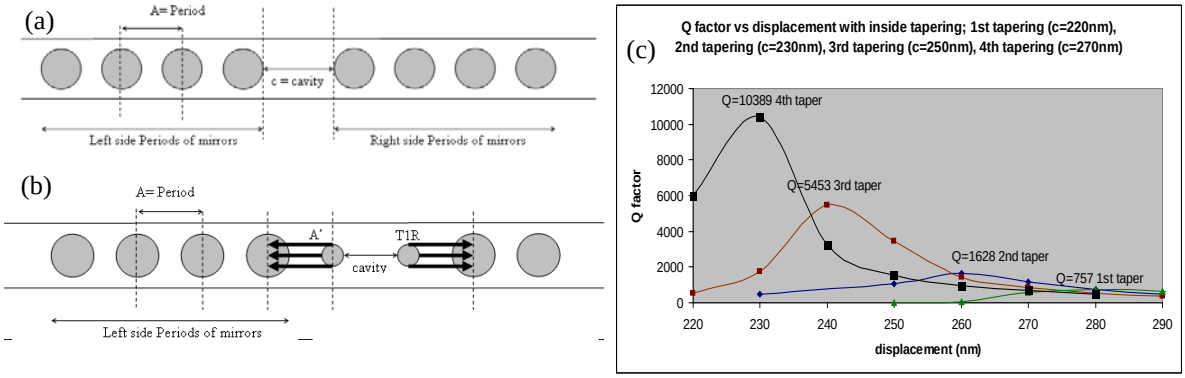

Figure 1(a) basic cavity with mirrors. (b) Showing one tapered hole with displaced position (c) Optimisation of the displacement for 1st to 4th tapered holes.

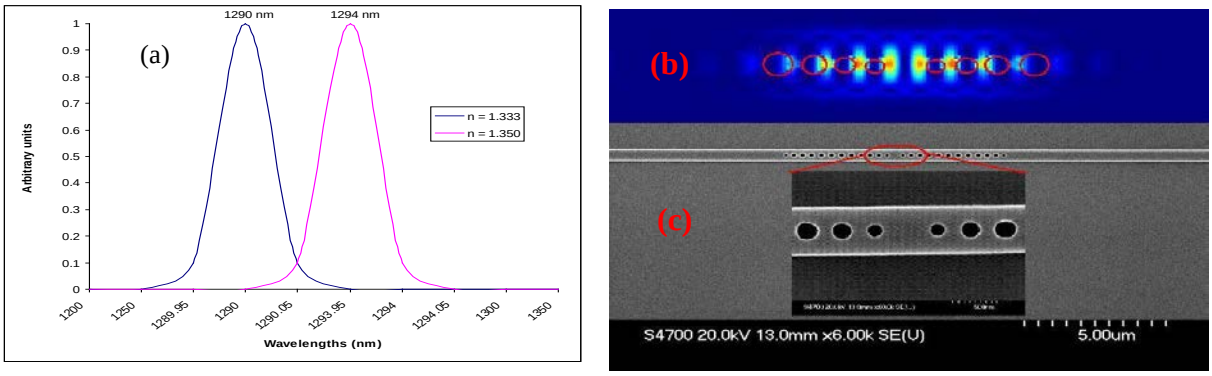

Figure 2 (a) simulation of peak shift for a surrounding medium change of refractive index from1.333 to 1.350. (b) E-field distribution profile along the centre of the cavity (c) SEM micrograph of fabricated tapered structure.

3. BIO-SENSING AND POINT-OF-CARE DIAGNOSIS

Each year, 1.1 Million new stroke events occur within the EU, Switzerland, Iceland and Norway – taken together it is predicted that the number of new stroke events will increase to 1.5 Million, by year 2025. The estimated total annual cost, within the EU, of treating people affected by stroke – and dealing with the consequences of people having strokes - is estimated to be 21 billion Euro. So there is a need for a quick, easy and reliable blood test based on a *panel* of biomarkers. By incorporating the bio-sensing surface into an optical waveguide micro-cavity resonator, the small refractive index change can translate into a sensitive, but label-free, means for detecting that a binding immuno-reaction has taken place [3].

3.1 Polymer Bragg gratings

Polymer offers a potential low cost solution for bio-sensor fabrication with the possibility of roll-to-roll nanoimprinting of the sensors. However, because of the relatively low refractive index contrast between high and low index polymers 2-D photonic crystals offer too little confinement and a more conventional Bragg grating bus-bar design was chosen. Polyimide was chosen as the high index polymer initially on a low index material such as Cytop. However, due to the relative softness of the low index material is was necessary as an interim solution to use thermally grown silica as the lower index cladding layer.

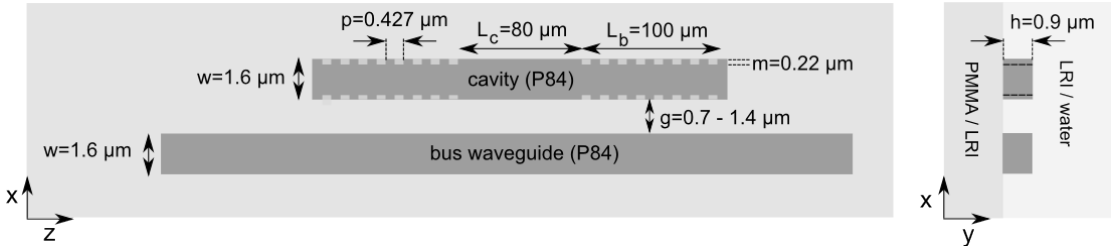

Figure 3 Example geometry of the side coupled cavity transducer; width = 1.6 µm; height = 0.9 µm; period = 0.427 µm; duty cycle = 0.5; cavity length = 80 µm; Bragg grating length = 100 µm; Bragg modulation 0.22 µm; coupling gap: 0.7-1.4 µm.

3.2 Nanoimprint Lithography

Nanoimprint Lithography (NIL) provides a cost effective method of transferring 3-D structures into deformable materials such as polyimide. The heat and pressure method was employed with all the alignment between the three level stamp accomplished by electron beam lithography and subsequent dry etching. The silicon stamp and resulting Bragg grating bus-bar structure are shown in figure 4.

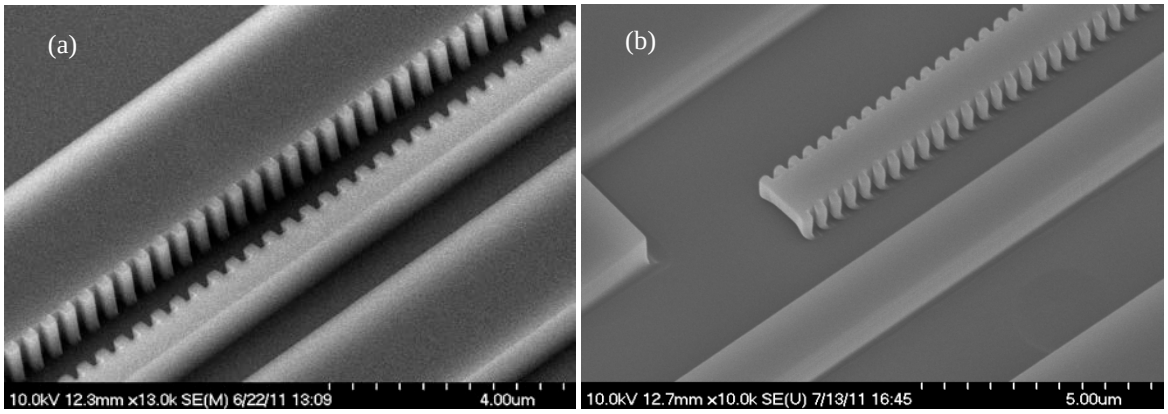

Figure 4 (a) Etched silicon stamp showing the teeth of Bragg grating. (b) Nano imprinted polyimide grating and bus-bar waveguide on silica.

4. ASYMMETRIC SPLIT RING RESONATORS AS SENSORS

4.1 Two separate metallic arcs of asymmetric lengths that share the same centre-of-curvature are known as asymmetric split ring resonators (A-SRRs). When the resonances from the two arcs interact they produce a steep slope in the reflection spectrum and a so called trapped mode. It is well known that the spectral position of the resonances can be tuned with size, however we also show that when PMMA is used as an organic probe on top of the A-SRR array a shift in resonance proportional the thickness is observed up to a thickness of around 150-200 nm. In addition, it is possible to tune the resonance of the structure to match the molecular resonance of the probe material.

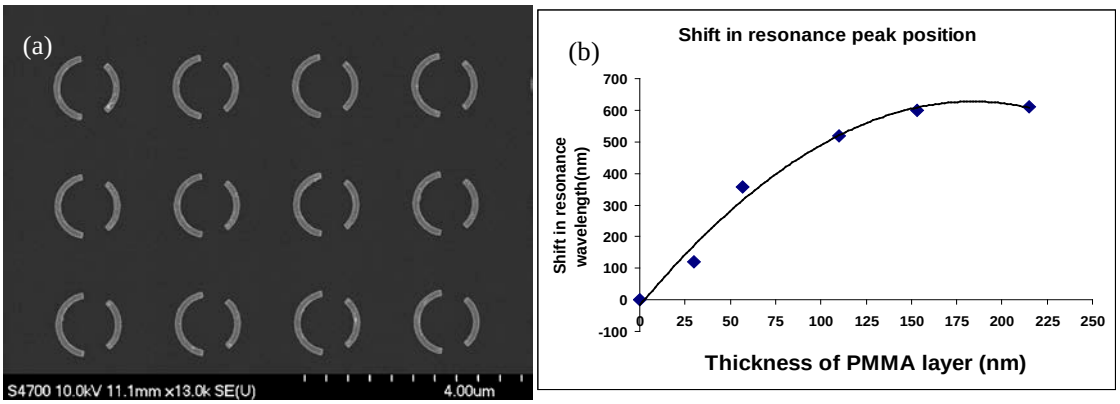

Figure 5 (a) An array of A-SRRs (b) shift in resonance peak position as a function of probe material thickness corresponding to a sensitivity of 1235 nm/ RIU (refractive index unit).

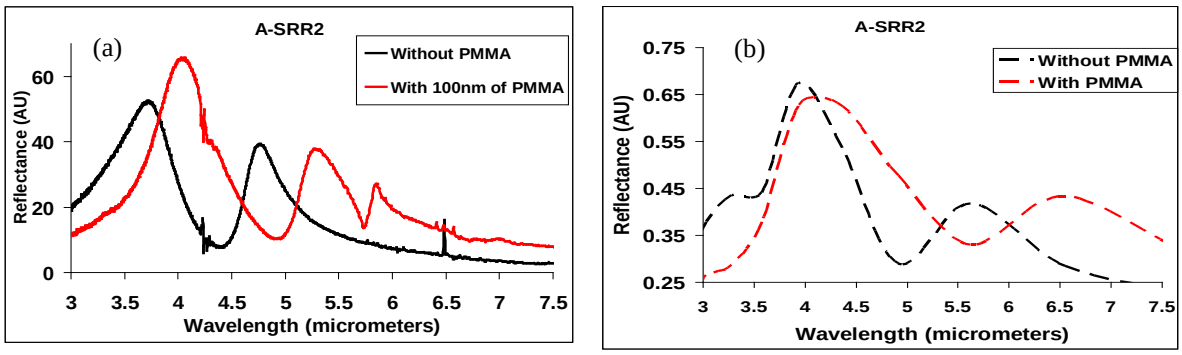

Figure 6 (a) measurements and (b) simulations of the shift from a 100 nm thick layer of PMMA on the surface of an array of ASSRS.

5. CONCLUSIONS

Nanophotonic devices fashioned from various techniques such as electron beam lithography and nano imprint lithography are able to produce devices that either with high Q and moderate shift in wavelength, or moderate Q and large shift in wavelength, can produce sensitive devices for molecular detection.

ACKNOWLEDGEMENTS

We acknowledge the use of the facilities at the James Watt Nanofabrication Centre and support from COST MP0702 and the EU FP7 project P3SENS.

REFERENCES

[1] Velha P. et al. Optics Express, Vol. 15, 24 (2007).

[2] Ahmad Rifqi Md Zain, Nigel P. Johnson, Marc Sorel and Richard M. De La Rue, 'Design and Fabrication of High Quality-Factor 1-D Photonic Crystal/Photonic Wire Extended Microcavities', , , *IEEE Photonics Technology Letters*, **22**(9), pp. 610 - 612, 1st May (2010).

[3] F. Dortu, H. Egger, K. Kolari, T. Haatainen, P. Furjes, Z. Fekete, D. Bernier, G.Sharp,B. Lahiri, S. Kurunczi, J.-C. Sanchez, N. Turck, P. Petrik, D. Patko, R. Horvath, S. Eiden, T. Aalto, S. Watts, N.P. Johnson, R.M. De La Rue, D. Giannone,'Design and process development of a photonic crystal polymer biosensor for point of care diagnostics', *Proc. SPIE*, **8087**, 80870D (2011); doi:10.1117/12.889420.

[4] B. Lahiri, A.Z. Khokhar, R.M. De La Rue, S.G. McMeekin and N.P. Johnson, 'Asymmetric split ring resonators for optical sensing of organic materials', Optics Express, 17(2), 1107-1115, 19th January (2009).

Microstructured and Standard Optical Fibers for the Detection of Relevant Components in Biological Fluids

Stefano Selleri
Information Engineering Department, University of Parma, I-43124, Italy.
Tel: +390521 905763; e-mail: stefano.selleri@unipr.it

ABSTRACT
Fiber optic biosensors are very promising optical-based sensing systems and offer all the main advantages related to the usage of standard as well as microstructured optical fibers. This work will describe the activity performed for the detection of relevant components in food biological fluids, providing performances of labelled and label-free schemes. DNA detection procedures will be shown.

Keywords: Biosensor, DNA detection, Optical Fibers, Microstructured Fibers, PNA Probe, Fuctionalization.

1. INTRODUCTION

New technological approaches aimed to the development of biosensorshave attracted considerable academic and industrial interest during the last three decades, as biosensors can play a significant role in different applications. The market trend shows how the biosensor industry is expanding particularly in certain areas like, for example, medical, environmental, food, safety and security as well as defence [1].
Standard and microstructured fibers can provide a very efficient platform for such a development and fiber based optical sensors have been widely developed for years [2-4]. In particular, microstructured optical fibers and Photonic Crystal Fibers (PCFs), have been deeply studied because of a number of unique features [5]. The cross-section of such fibers is defined by an array of air-holes, running all along the whole length, in a matrix of dielectric material, and it can be infiltrated with liquids or gasses under test. The light-guiding and the sample microfluidics properties can thus be tailored with unprecedented degrees of freedom, thus opening up a new fascinating branch in the fiber-based sensor field [6-7]. For example, a very long interaction length, even in presence of very limited quantity of sample can be easily obtained thanks to the micro- or even nano-metric dimensions of the holes. In addition, the probing light can be confined to a small area, which means that high intensities can be achieved, facilitating optical nonlinearity-based sensing techniques [8]. In this perspective, optical biosensors based on the use of PCFs can be classified as true intrinsic sensors, where interaction with the sample occurs within the fiber itself, differently from extrinsic sensors, in which the optical fiber is used as signal transmission medium to couple light, usually to and from the region where the light beam is influenced by the liquid solution under test.
However it's worth remember that standard fiber technology has achieved such a high fabrication level to allow very efficient applications. Fiber Bragg Gratings (FBGs) and long period gratings [9], in different configurations, can be successfully integrated in sensor devices, while tapered structures and nanowires can be used to strongly enhance sensitivity due to the evanescent field.
The following sections will provide a brief discussion about the main issues related to the use of standard and microstructured fibers in sensing applications. Being aware of the immense number of different configurations and working principles of biological sensors, which can be based for example on absorbance, reflectance, fluorescence, luminescence, refractive index variation and other measurement techniques, a brief overview and some examples of optical sensing mechanisms will be given, focusing on selected structures and applications, in particular for the detection of DNA.

2. LIGHT GUIDING AND MICROFLUIDICS

One of the main crucial point for the fiber-based sensor realisation is getting light and fluids into the fiber at the same time. Different approaches have been already suggested to this aim. When using PCFs, the usual procedure is to fill the holes through one of the fiber ends. This increases the complexity of using such structures when compared with conventional fibers, as light in- and out-coupling requires to manage the fiber ends. For example, selective infiltration of analytes or reagents within a definite number of channels can also be obtained by obtruding the terminal holes of a selected number of channels. Another potential and intriguing solution to this issue is to generate a lateral access to the PCF holes, through which the sample can be inserted. This approach cannot be applied to triangular lattice PCFs where too many holes should be taken into account, while can be effective, for example, in air-suspended core fibers, where few and relative large holes are easily accessible [10]. This approach, which doesn't interfere with light guidance, has the great advantage to separately manage light coupling into the core and sample insertion in to the fiber holes. However, the simplest way to infiltrate liquid solutions into the fiber holes is using the capillary effect which, however, cannot allow a fine control of the

considered volumes. Tapered tips can also be considered as alternative approach to access liquids, still through capillary effect, once properly designed and realized. As an alternative to the capillary effect, proper microfluidic pumps can be used which allow a very precise control of the infiltrated solution. Fig. 1 shows a set-up example used in the laboratory at Parma University based on a microfluidic pump.

Figure 1. A possible experimental set-up showing the microfluidic pump, the withe device in the back on the left, which can be used to flow small volumes of liquid around a fiber inserted in a sailed tube or to infiltrate reagents and samples into the holes of a microstructured fiber which is hung between the two vertical holders in the front of the set-up. On the right is clearly visible the light coupled into the fiber.

3. FLUORESCENCE BASED AND GRATING-BASED DETECTION

The detection configurations can be generally classified into two main categories: fluorescence-based detection and label-free detection. In fluorescence-based detection, molecules under test are labelled with fluorescent markers. The intensity of the fluorescence indicates the presence of the target molecules. Fluorescence-based detection is extremely sensitive, with the detection limit down to a single molecule, but it suffers from laborious labelling processes. In contrast, in label-free detection, target molecules are detected in their natural form thereby greatly simplifying the sample treatment. Typical optical fiber label-free biosensors exploit the presence of different kinds of gratings and Fabry-Perot etalons and measure the change of a resonance wavelength introduced by the presence of a biological agent. The main disadvantage of grating based sensor, even though the grating scribing in standard optical fibers constitutes a mature technology, is that the progress achieved in photonic crystal and microstructured fibers is still limited and challenging due to the presence of effects such as the side-illumination scattering induced by the capillary structure, the complex geometry core and the absence of significant photosensitivity for the case of all-silica fibers.Two examples will be reported in the following about fluorescence based and label-free detection using respectively microstructured fibers and standard ones with gratings.

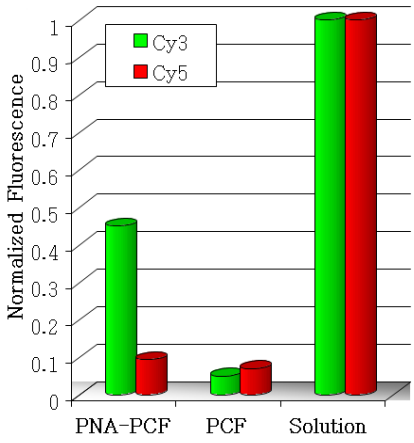

Figure 2. Fluorescence intensities observed after hybridization for PNA-modified suspended core PCF and unmodified fiber, compared to those obtained for the initial solution deposited on an unmodified fiber. Data are normalized for each channel to the intensity of the initial solution, in order to take into account the different sensitivity of each channel.

3.1Fluorescence based detection

To realized the fluorescence-based biosensor, the so called suspended core fiber has been considered and functionalized. Peptide Nucleic Acids (PNAs) which are nucleic acid analogs, known to bind very effectively to complementary DNA, have been chosen as probes. In order to obtain a PNA-modified surface, the functionalization of the internal channels of the suspended core fiber has been performed [11]. To test the sensor effectiveness, unmodified fibers and a functionalized fiber have been considered, as well as different DNA chain, matching and not matching with the specific PNA probe. If the PNA is present on the surfaceof the modified fiber, a sequence-specific DNA binding shouldbe revealed by the uptake offluorescently labeled DNA by the functionalized fiber, marked with Cy3 label, higher than that of the mismatched DNA, marked with Cy5 label, of afunctionalized fiber, and of course lower as compared to reference solution. The results are reported in Fig. 2 for an olive oil DNA and clearly report the occurred hybridization process of the first case, as expected. Consider that the sensor is able to discriminate the DNA with onlya single-base difference in a 100 nM DNA solution using less than 20 nano litre volume.

3.2 Label-free detection using gratings

The proposed DNA label-free biosensor is based on an optical fiber ring cavity, which has been realized utilizing a Double Tilted Fiber Bragg Grating (DTFBG) as a detector element. A specific functionalization of the external surface of the fiber has been performed and a liquid handling system, composed of a teflon tubing, has been implemented for the packaging and the functionalization of the fiber sensor. The DTFBG sensor [12] consists of two identical blazed fiber gratings separated by a proper distance, as shown in Fig. 3, forming a Fabry-Perot structure that creates two interferences. At the Bragg wavelength the light incident on the grating is back reflected into the core, creating a Fabry-Perot interference. At lower wavelengths there is a ring resonance generated by the reflections from the core mode into the cladding modes and then back into the original core mode. This resonance is monitored to detect variations of the environment around the fiber. In particular the measurement of the refractive index of the medium surrounding the fiber affects the level of the interference between the two blazed gratings and changesthe lower wavelength spectrum according to how much light is lost from the counter-propagating cladding modes. By checking the variation of the visibility of the spectrum [12] it is possible to get information about the hybridization occurred on the outer surface of the fiber.

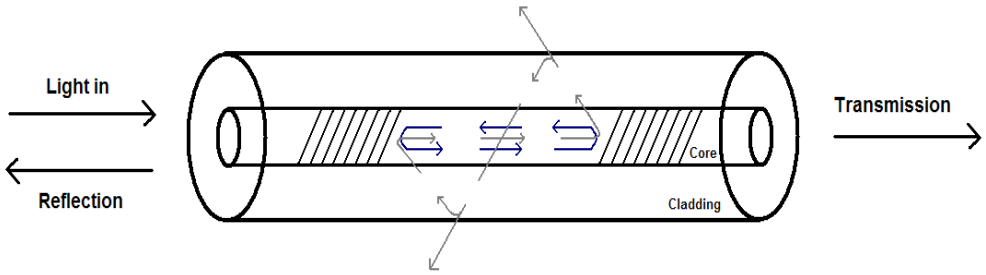

Figure 3. The etalon generated by the two double tilted fiber Bragg gratings.

As an example, after the functionalization process, a 10 nM DNA solution was passed through in the system and the spectrum visibility monitored. Tomato DNA has been used. The DNA hybridization causes aclear decrease of the visibility of fringes with respect to the case of a fiber which has not been functionalized. The visibility change is clearly reported in Fig.4 and it provides a measure of the hybridization process which allow the DNA to be identify.

4. CONCLUSIONS

Fiber optics technology is a very promising platform for biosensing. Standard as well as microstructured fiberscan play a significant role in the development of physical, chemical and biological sensors because of their mature technology and unique features of direct and strong interaction with the analytes under test. These sensor types have been the objective of a large number of investigations in the last years and they provide numerous ways of performing a rapid, remote, in-line and in-situ determination of many types of analytes in a wide range of application fields. Two examples have been reported for standard and microstructured fiber based DNA biosensors in label-free and labelled configuration.Experimental results confirm the unique selectivityof the sensors that are able to discriminate the DNA with onlya single-base difference and very low concentrations. If,in the next future, standard and photonic crystal fiber based biosensors will be able to demonstratedevices flexible and simple in use, miniaturized, with enhanced optical read-out and able to be in line with the increasing

need of fast-response instrumentation, they will provide crucial beneficial effects on healthcare system and on the society.

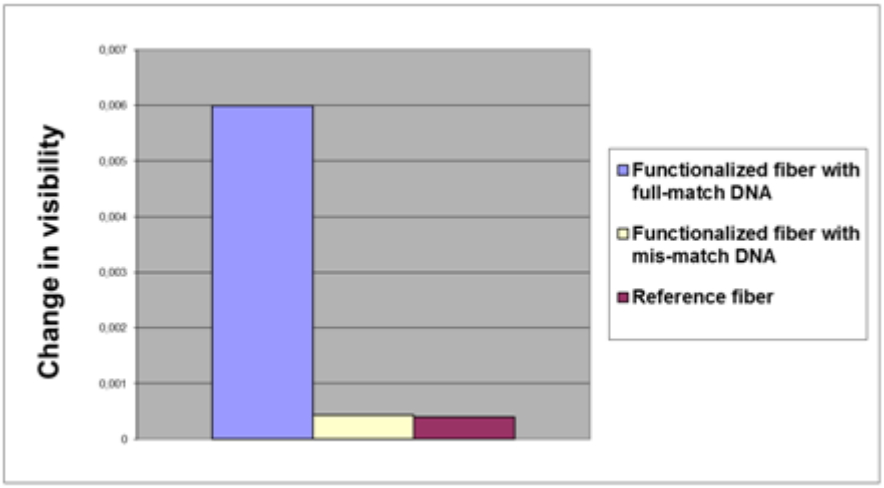

Figure 4. The graph shows the average change in visibility for the functionalized fiber with full-matched DNA, for a functionalized fiber with mis-matched DNA, and for the reference fiber which has not been treated.

ACKNOWLEDGEMENTS

The author would like to acknowledge all collaborators in Parma University, in particular Roberto Corradini, Annamaria Cucinotta, Michele Sozzi and Alessandro Candiani.

REFERENCES

[1] J. H.T. Loung, K. B. Male, and J. Glennon: Biosensor technology: Technology push versus market pull, Biotechnology Advances, Vol. 26, pp. 492-500, 2008.

[2] L. Rindorf , P.E. Høiby, J.B. Jensen, L.H. Pedersen, O. Bang, O. Geschke:Towards biochips using microstructured optical fiber sensors, Anal Bioanal Chem vol. 385 n.8, pp. 1370–1375, 2006.

[3] D. Passaro, M. Foroni, F. Poli, A. Cucinotta, S. Selleri, J. Lægsgaard, A. Bjarklev: All-Silica Hollow-Core Microstructured Bragg Fibers for Biosensor Application,IEEE Sensors J, vol. 8, n.7, pp 1280-1286, 2008.

[4] R. Narayanaswamy, O.S. Wolfbeis: Optical Sensors, Springer, New York, 2004.

[5] F. Poli, A. Cucinotta, S. Selleri, Photonic Crystal Fibers, Properties and Applications, Material Science Springer-Verlag, Dordrecht, The Netherlands, 2007.

[6] J, Fini: Microstructure fibres for optical sensing in gases and liquids, Meas. Sci. Technology, vol. 15, pp. 1120–1128, 2004.

[7] J.B. Jensen, L.H. Pedersen, P.E. Hoiby, L.B. Nielsen, T.P. Hansen, J.R. Folkenberg, J. Riishede, D. Noordegraaf, K. Nielsen, A. Carlsen, A. Bjarklev: Photonic crystal fiber based evanescent-wave sensor for detection of biomolecules in aqueous solutions, Optics Letters, vol. 29, n.17,pp. 1974–1976, 2004.

[8] M.H. Frosz , A. Stefani, O. Bang: Highly sensitive and simple method for refractive index sensing of liquids in microstructured optical fibers using four-wave mixing, Optics Express, vol. 19, n. 11, pp. 1471-10484, 2011.

[9] M. Sozzi, A. Cucinotta, R. Corradini, R. Marchelli, M. Konstantaki, S. Pissadakis, S. Selleri: Modification of a long period grating-based fiber optic for DNA biosensing, in Proc. Optical Fibers, Sensors, and Devices for Biomedical Diagnostics and Treatment XI, Gannot, Israel, paper 78940J.

[10] C.M.B. Cordeiro, E.M.dos Santos, C.H. Brito Cruz: Lateral access to the holes of photonic crystal fibers – selective filling and sensing applications, Optics Express, vol. 14, n. 18, pp. 8403-8412, 2006.

[11] E. Coscelli, M. Sozzi, F. Poli, D. Passaro, A. Cucinotta, S. Selleri, R. Corradini, R. Marchelli: Toward A Highly Specific DNA Biosensor: PNA-Modified Suspended-Core Photonic Crystal Fibers, IEEE J. Selected Topics Quantum Electronics, vol. 16, n.4, pp. 967-972, 2010.

[12] A. Candiani, M. Sozzi, A. Cucinotta, S. Selleri, R. Veneziano, R. Corradini, R. Marchelli, P. Childs, S. Pissadakis: Optical fiber ring cavity sensor for label-free DNA detection, IEEE J. Selected Topics Quantum Electronics, to be published, 2011.

Femtosecond laser micromachining for the fabrication of optofluidic devices

Roberto Osellame, Rebeca Martinez Vazquez, Andrea Crespi, Giulio Cerullo, Roberta Ramponi
IFN – CNR and Department of Physics – Politecnico di Milano, Piazza Leonardo da Vinci 32, 20133 Milano, Italy.
Tel: +3902 23996150; e-mail: roberta.ramponi@fisi.polimi.it

ABSTRACT
Femtosecond laser micromachining is a powerful tool for the fabrication of both optical waveguides and, when followed by chemical etching, of microchannels, with unprecedented intrinsic 3D capabilities. Basics of the technique and examples of fully integrated optofluidic devices are presented.Applications to the biomedical field are shown: in particular we describe integration of optical functionalities in a lab-on-chip for capillary electrophoresis and a monolithic device, completely fabricated by femtosecond laser technology, for label-free and spatially-resolved sensing in a microfluidic channel based on an integrated Mach-Zehnder interferometer.

Keywords: optofluidics, lab-on-a-chip, femtosecond laser micromachining.

1. INTRODUCTION

Optofluidics is a rather new technology that, by combining microfluidics and optics, allows the realization of integrated devices that synthesize novel functionalities [1]. In biomedical applications, a major role is played by lab-on-chips. A lab-on-chip (LOC) is a device that squeezes onto a single glass substrate the functionalities of a biological laboratory, by incorporating a network of microfluidic channels, reservoirs, valves, pumps and micro-sensors [2]. It offers the capabilities of preparation, transport, reaction and analysis of very small volumes (nano- to picoliters) of biological samples. Its main advantages are high sensitivity, speed of analysis, low sample and reagent consumption and the possibility of measurement automation and standardization. The LOC concept has a huge application potential in many fields, ranging from basic science (genomics and proteomics), to chemical synthesis and drug development, point-of-care medical analysis and environmental monitoring. The next technological challenge of LOCs is direct on-chip integration of photonic functionalities, by manufacturing optical waveguides for sensing of biomolecules flowing in the microchannels. Such integrated approach has many advantages over traditional free space optical sensing, including compactness, sensitivity, enhanced device portability and the possibility of multipoint excitation. However, standard waveguide fabrication methods are planar multistep processes, which considerably complicate the LOC device production.

Femtosecond-laser induced refractive index modification is a powerful technique enabling direct, maskless three-dimensional fabrication of optical waveguides in glass [3], and appears to be particularly suited for their integration into LOCs. It can be performed as a post-processing technique allowing to position optical waveguides (or more complex photonic devices such as splitters, couplers and interferometers) inside a pre-existing LOC without affecting the manufacturing procedure of the microfluidic part of the device, thus greatly simplifying the production process. In addition, femtosecond-laser irradiation of fused silica followed by chemical etching in HF solution allows the manufacturing of directly buried microfluidic channels [4], due to the enhanced (by up to two orders of magnitude) etching rate of the irradiated material with respect to the pristine one. This opens the possibility of using a single femtosecond laser system for the production and the integration of microfluidic channels and optical waveguides [see Fig. 1(a)].

In this work we demonstrate the fabrication, by femtosecond laser irradiation, of both high-quality optical waveguides and microfluidic channels on the same fused silica substrate. We also use the femtosecond laser to inscribe optical waveguides on a commercial LOC for capillary electrophoresis (CE), for the realization of compact high sensitivity integrated optical sensors.

2. FABRICATION TECHNIQUE

The femtosecond laser fabrication process can be achieved with different types of lasers, with pulse durations ranging from 50 fs to about 200 fs, repetition rates from 1 kHz to 25 MHz, energies per pulse from tens of nanojoules to hundreds of microjoules, wavelengths in the NIR (800-1040 nm). The choice of the laser determines the fabrication regime and, in particular, the importance of pulse-to-pulse cumulative effects and thermal diffusion. In most experiments reported in this work, a regeneratively amplified Ti:sapphire laser generating 150-fs, 500-μJ, 800-nm pulses at 1 kHz has been used. A fraction of the beam is focused, by either a 20× (NA = 0.3) or a 50× (NA = 0.6) objective, at a depth ranging from 100 μm to 500 μm below the surface of the fused silica sample, which is moved perpendicularly to the beam propagation direction by a precision translation stage at a speed of ≈20 μm/s. In order to produce modifications with a circular cross-section, the

beam is astigmatically shaped by passing it through a cylindrical telescope [5]. The optical waveguides, fabricated using the 20× objective and 4 μJ pulse energy, are very uniform, have a nearly circular cross section with 10 μm diameter and are single mode in the visible [see Figs. 1(b)-(d)]. The peak refractive index change is 1×10^{-3}. Propagation losses in the visible are 0.5dB/cm, which is a lower value than those obtained for waveguides integrated on LOCs by standard photolithographic techniques. The microfluidic channels are manufactured by higher intensity laser irradiation (pulse energy of 4 μJ through a 50× objective) and subsequent etching for 3 hours in an ultrasonic bath with a 20% HF solution in water. With double side etching, channel lengths up to 3 mm with 100 μm cross section are obtained [6]. The channels are directly buried and can be positioned at any depth with respect to the sample surface, in a three-dimensional geometry. Increased channel lengths, as would be required for the LOC applications, can be obtained by a combination of iterative etching, concentration gradient and non-uniform sample irradiation. The quality of the microchannels is high, as shown in the SEM image of one of Fig.1e.

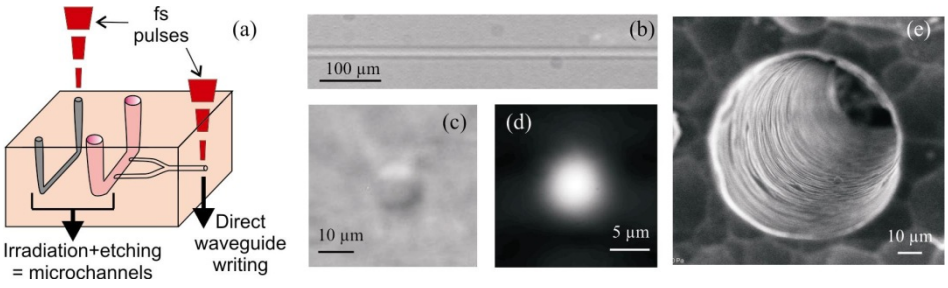

Fig. 1. (a) Conceptual scheme of the use of the femtosecond laser for the fabrication of optical waveguides and microfluidic channels; (b,c) top and end view of a femtosecond written waveguide; (d) waveguide mode at 532 nm;(e) SEM image of a microfluidic channel obtained by femtosecond laser irradiation followed by chemical etching.

For the realization of an integrated waveguide Mach-Zehnder interferometer (MZI), a different laser system was used, i.e. a mode-locked Yb:KYW laser producing 350-fs pulses at 1030 nm, with energy up to 1 μJ. The repetition rate was set to 1 MHz and the second harmonic, produced by a lithium triborate crystal, was used since this fabrication wavelength yields smoother waveguides. In this case, this laser is preferable to the amplified Ti:Sapphire laser reported above, since it provides waveguides with a higher refractive index contrast ($\Delta\sim5\times10^{-3}$), thus allowing smaller curvature radii, essential for the layout of the MZI.

3. MICRO-OPTOFLUIDIC DEVICES

We report two different devices. As a first example of applicability of our fabrication technique to real-world devices, we inscribed optical waveguides in a commercial LOC for capillary electrophoresis (LioniX bv, the Netherlands), a schematic layout of which is shown in Fig.2(a). This chip has two crossing microchannels, that are responsible for the sample injection (channel going from reservoir 1 to 3) and for the electrophoretic separation (channel going from reservoir 2 to 4). Several optical waveguides have been inscribed perpendicular to the separation channel towards its end, to provide highly localized excitation for laser-induced fluorescence (LIF). A precise alignment procedure has been developed in order to have the 10 μm-diameter waveguides exactly crossing the 12-μm-high microfluidic channel. A low power green laser was coupled to a waveguide by a single mode optical fiber and the separation channel was filled with a solution of Rhodamine 6G. Figure 2(b) shows the yellow fluorescence excited by the green light coupled into the waveguide. The excitation is very selective in space (10 μm, as the waveguide diameter), indicating very low light leakage out of the waveguide. In addition, the excited fluorescence covers the whole width (50μm) of the channel due to the low divergence of light coming from a waveguide with a numerical aperture below 0.1. As shown in Fig.2(a), the LIF signal is collected by an ultrahigh numerical aperture optical fiber (NA = 0.5) glued to the chip in correspondence to the excited portion of the microchannel in a 90° geometry with respect to the exciting waveguide, thus strongly suppressing the excitation light background. The signal is detected by a photon counting photomultiplier after notch and interference filters, used to further reject the excitation light and chip autofluorescence. Preliminary measurements indicate a limit of detection of 1 nM, comparable to what obtained with standard free-space optics, with the clear advance of enhanced compactness and portability.

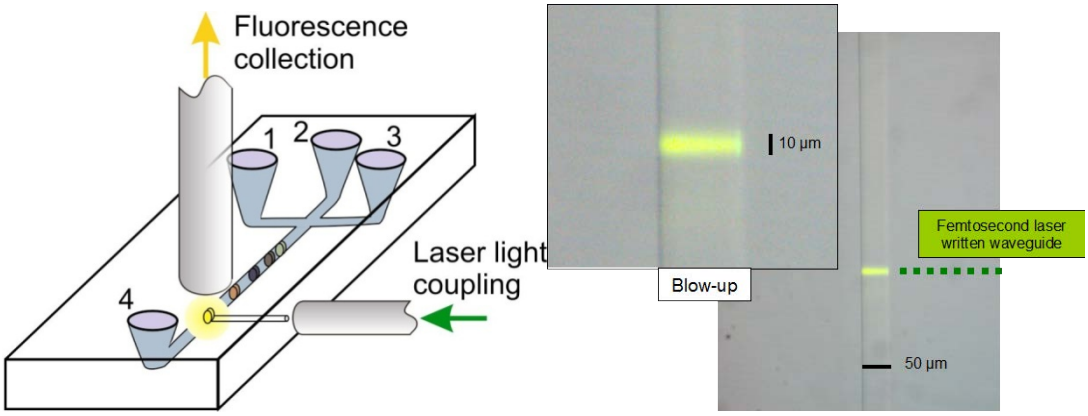

(a) (b)

Fig. 2. (a) Schematic diagram of the commercial microfluidic chip with femtosecond laser inscribed optical waveguides; (b) fluorescence induced in the microchannel by the optical waveguide.

As a second application we present a monolithic device, completely fabricated by femtosecond laser technology, for label-free and spatially-resolved sensing in a microfluidic channel. The layout of the optofluidic device is shown in Fig. 3. It consists of a MZI fabricated in a fused silica sample, with the sensing arm orthogonally crossing the channel and the reference arm passing over it. The device is capable of refractive index sensing with a spatial resolution of the order of the waveguide mode diameter (~15 µm). The innovative 3D layout of the MZI, which is required for spatially-resolved sensing, is only made possible by the unique capabilities of femtosecond laser microstructuring. Since this geometry implies a very small interaction length with the analyte, evanescent field sensing would provide a limited sensitivity; therefore, in our configuration, the sensing arm directly intersects the microchannel. The device is statically and dynamically tested by filling the channel with glucose solutions and displays sensitivity down to 10^{-4} Refractive Index Units (RIU).

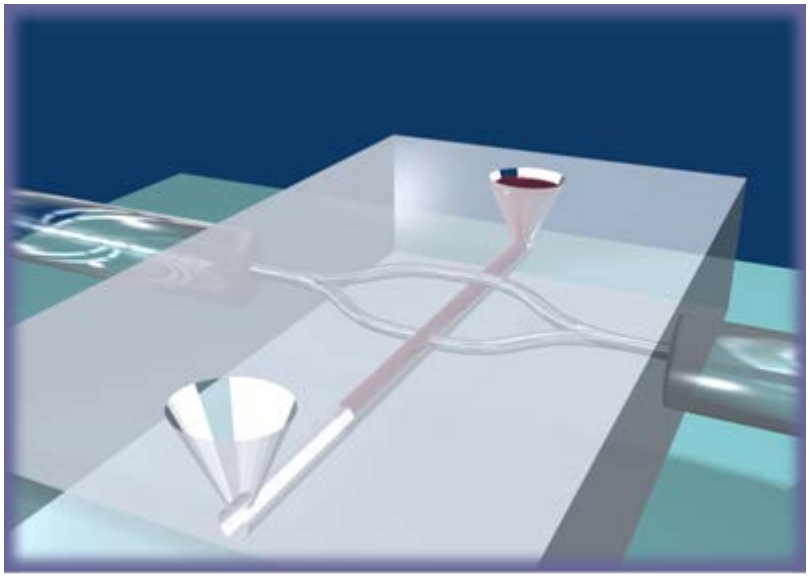

Fig. 3. Schematic of the femtosecond-laser-fabricated microfluidic channel and integrated MZI. The sensing arm crosses orthogonally the channel, while the reference one passes over it. The microchannel is filled through top access holes; the MZI is coupled to optical fibres.

In particular, to characterize the sensitivity and the linearity of the interferometer response, the microchannel is filled with different concentrations of aqueous glucose-D solutions, and for each of them the spectral response of the optofluidic device is measured statically (see inset in Fig. 4). Figure 4 shows the phase of the Fourier

transform calculated from the experimental data, as a function of glucose concentration. X-axis top scale represents the corresponding refractive index variation of the solutions with respect to pure water.

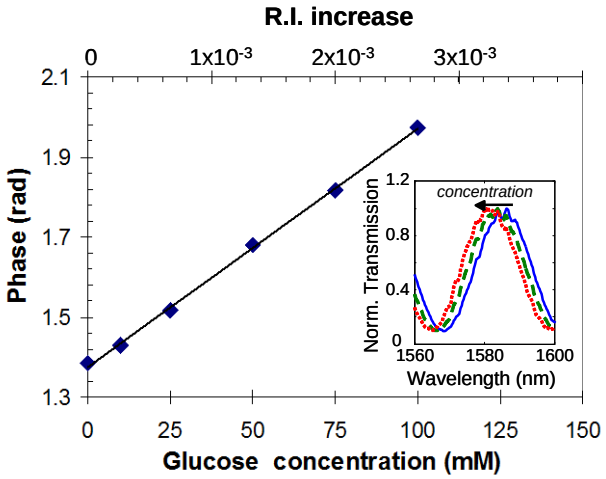

Fig. 4. Measured phase from spectral data for different concentrations of glucose-D in water (inset: 0 mM solid blue; 50 mM dashed green; 100 mM dotted red); the correspondent refractive index increase is also shown.

4. CONCLUSIONS

In conclusion, the femtosecond laser is a powerful tool for the fabrication of optical waveguides and microfluidic channels and their combination in optofluidic devices. It can be used to integrate optical excitation/detection in commercial LOCs without affecting their manufacturing process, strongly increasing device compactness and portability. It can also be used to fabricate all the components of integrated micro-optofluidic devices, allowing 3D geometry, thus resulting in unprecedented design flexibility.

ACKNOWLEDGEMENTS

We acknowledge financial support by EU FP6 STREP Project HIBISCUS and EU FP7 STREP Project MicroFLUID.

REFERENCES

[1] D. Psaltis, S.R. Quake, and C. Yang, “Developing optofluidic technology through the fusion of microfluidics and optics,” Nature, vol. 442, pp. 381-386, 2006.

[2] G.M.Whitesides, “The origins and the future of microfluidics,” Nature vol. 442, pp. 368-373, 2006.

[3] K. M. Davis, K. Miura, N. Sugimoto and K. Hirao, “Writing waveguides in glass with a femtosecond laser,” Opt. Lett., vol. 21, pp. 1729-1731, 1996.

[4] A. Marcinkevicius, S. Juodkazis, M. Watanabe, M. Miwa, S. Matsuo, and H. Misawa “Femtosecond laser-assisted three-dimensional microfabrication in silica”, Opt. Lett., vol. 26, pp. 277-279, 2001.

[5] R. Osellame, S. Taccheo, M. Marangoni, R. Ramponi, P. Laporta, D. Polli, S. De Silvestri, G. Cerullo, “Femtosecond writing of active optical waveguides with astigmatically shaped beams”, J. Opt. Soc. Am. B, vol. 20, pp. 1559-1567, 2003.

[6] R. Osellame, V. Maselli, R. Martinez Vazquez, R. Ramponi, and G. Cerullo, “Integration of optical waveguides and microfluidic channels both fabricated by femtosecond laser irradiation,” Appl. Phys. Lett., vol. 90, 231118, 2007.

Magnetic resonance force microscopy at millikelvin temperature

Andrea Vinante, Geert Wijts, Oleksandr Usenko and Tjerk H. Oosterkamp
Leiden Institute of Physics, Leiden University, Niels Bohrweg 2, 2333CA Leiden, The Netherlands.
Tel: +310715275661; e-mail: vinante@physics.leidenuniv.nl

ABSTRACT
Magnetic resonance force microscopy (MRFM) is a scanning probe technique which combines the three-dimensional capabilities of conventional magnetic resonance imaging with the high spatial resolution of atomic force microscopy. MRFM exploits the strong gradient-dipole interaction between a nanoscale magnetic tip affixed on a cantilever and the spins in a sample. The strong magnetic field gradient generated by the tip allows to selectively address spins in different locations, similarly to external gradients in conventional magnetic resonance imaging (MRI). MRFM has an outstanding potential for application to molecular imaging, in particular for the reconstruction of the spatial structure of proteins and complex biomolecules. It has also been suggested as a mean for imaging and control of defects and single dopants in semiconductors. Here, I will describe a new approach to MRFM, based on a superconducting readout, which enables the operation at ultralow temperature. Using this new setup we have performed MRFM detection of paramagnetic defects in Si-SiO_2 interface at temperatures below 100 mK. We have found evidence of spin diffusion which may be related with magnetic noise and decoherence in several types of qubit.

Keywords: Magnetic Resonance Force Microscopy, molecular imaging, paramagnetic centers

1. INTRODUCTION

Magnetic Resonance Force Microscopy (MRFM) is a scanning probe technique based on detecting the tiny force between an ultrasoft magnetically tipped cantilever and the spins in a sample, when these are manipulated by means of magnetic resonance techniques. MRFM combines the three-dimensional imaging capabilities, hence subsurface, offered by magnetic resonance, with the excellent force sensitivity provided by micromachined mechanical resonators, as in conventional AFM. The spatial selectivity in MRFM is provided by the strong field gradient generated by the magnetic tip, similarly to external field gradients used in conventional Magnetic Resonance Imaging (MRI). MRFM is nowadays considered one of the most viable routes towards three-dimensional imaging of biomolecules or nanostructures with atomic resolution [1]. It has been further proposed as a mean to image and control single dopants in semiconductors [2]. While these ambitious goals have not been reached yet, several milestones have already been demonstrated, including mechanical detection of a single electron spin [3] and 3D nuclear spin imaging of a virus with a few nanometers resolution [4], roughly 8 orders of magnitude better, in volume, with respect to conventional MRI.

One of the main limiting factors on MRFM resolution is the thermal force noise of the cantilever, $S_f=4k_BT\gamma$, where T is the temperature and γ is the damping factor. For this reason, MRFM is normally operated at liquid helium temperature, with the cantilever being measured by a low-power fiber interferometer. State of art force sensors are based on ultrasoft micromachined silicon cantilevers and reach a typical force noise of the order of 1 aN/√Hz, while interferometric detection provides displacement noise of the order of 0.1 pm/√Hz. Further improvements require softer and less dissipative mechanical sensors and possibly a further reduction of operating temperature$T$.

We have recently developed a novel approach to MRFM, which enables operation down to millikelvin temperature [5]. A key ingredient is a new cantilever detection scheme based on a Superconducting Quantum Interference Device (SQUID), which provides much lower cantilever overheating compared to optical detection. In this scheme, the motion of the magnetic tip on the cantilever modulates the magnetic flux threaded in a superconducting pick-up coil, and the flux change is detected by the SQUID.

In this paper, I will describe the first MRFM experiment performed with this new setup. In this experiment, we were able to mechanically detect and manipulate paramagnetic centers located close to the surface of the chip supporting the superconducting pick-up coil. Paramagnetic centers in thin film surfaces and interfaces have been recently subject of various studies [6-8], because they are possibly related to the 1/f magnetic observed in SQUIDs and to some dephasing mechanisms in superconducting qubits [7] and in single dopant qubits [8].

2. EXPERIMENTAL RESULTS

A general scheme of our experimental is shown in Fig. 1a. The force sensor is an ultrasoft microfabricated silicon cantilever [9], with length 90 μm, thickness 100 nm, width 5 μm, and stiffness $k=2\times10^{-4}$ N/m. A micron-sized spherical ferromagnetic particle made of a neodymium-iron-boron alloy is attached to the end of the cantilever by Pt electron beam deposition. The particle (from now on the magnet) has a diameter of 5.2 μm and a

saturation magnetic moment μ=8×10^{-11} A/m. An electron microscope micrograph of a cantilever with a magnet attached to it is shown in Fig. 1b. The loaded cantilever has a resonant frequency f_0=3093 Hz and quality factor Q=50000 at cryogenic temperature. The cantilever is approached vertically to the surface of a silicon chip, supporting a thin film superconducting Nb pick-up coil. Assuming the z-axis perpendicular to the chip surface, both the magnetic moment of the magnet and the cantilever fundamental mode deflection are oriented along the x-axis. The motion of the magnet is detected by measuring themagnetic flux ϕ induced in the superconducting pick-up coil, which is connected to a SQUID amplifier. A Nb microwire integrated on chip allows to generate a rf/microwave field B_1, which can be used for magnetic resonance manipulation of spins.

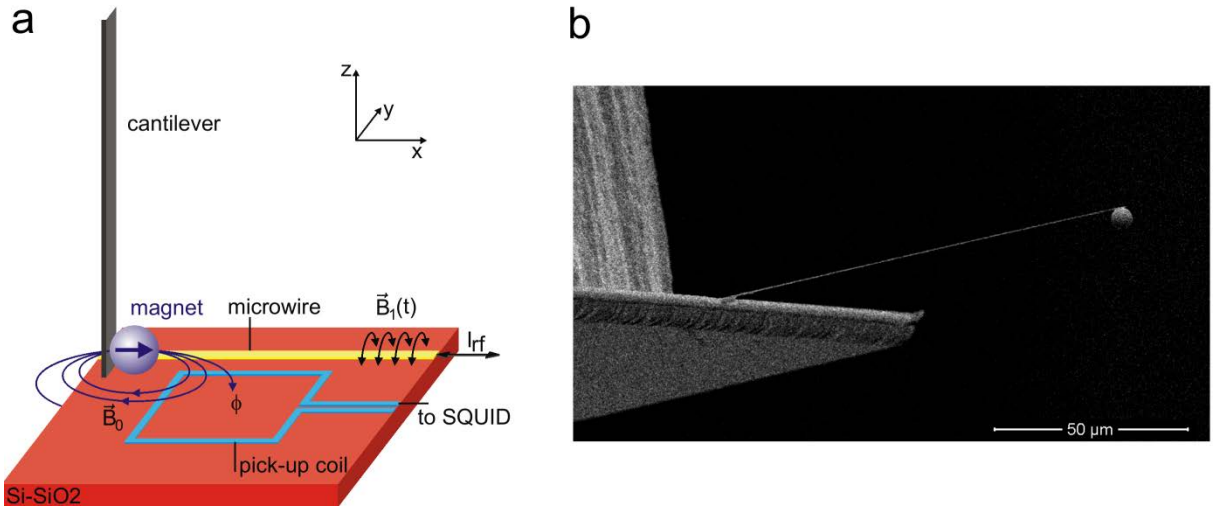

Figure 1: (a) experimental scheme and (b) SEM micrograph of the cantilever.

The SQUID detection scheme to measure the motion of the cantilever has been specifically developed to be compatible with ultralow temperature. In fact, conventional cantilever detection based on optical interferometry appears not suitable for operation below ~1 K, because photon absorption limits the effective cooling of the cantilever. In practice the effective temperature of the cantilever achievable, hence the thermomechanical force noise, is limited to about 1 K. Conversely, SQUID detection does not involve a direct absorption of power by the cantilever. Using SQUID detection we have been able to detect the motion of an ultrasoft silicon cantilever down to an effective temperature of 25 mK [5], corresponding a record force noise of 0.3 aN/√Hz.

When the cantilever with the magnet is approached to the surface, it interacts with nuclear or electron spins in a sample placed on the surface via gradient-dipole interaction. The field gradient provided by the micron-size particle close to its surface is 2×10^5 T/m. In the experiment described here, the sample is simply constituted by paramagnetic electron spins on to the chip surface. Paramagnetic defects are found to be almost ubiquitous on the surface of thin film devices [6], with typical density of 0.1-1 nm^{-2}. In particular, Si/SiO$_2$ interfaces are relatively rich of dangling bonds paramagnetic centers, also known as P_b centers. Some interesting effects emerge at temperatures below 1 K due to paramagnetic ordering. For instance, 1/f magnetic noise and dephasing in SQUIDs and superconducting qubits at millikelvin temperature are nowadays attributed to surface paramagnetism [7]. High densities of paramagnetic defects can also be a significant source of dephasing in single dopant qubits, like phosphor donors in silicon [8].

In our experiment, gradient-dipole interaction between the magnet on the cantilever and the surface spins shows up as a static cantilever frequency shift [10]. Spins located immediately underneath the magnet, at the experimental distance d=3.6 µm between surface and magnet center, feel a magnetic field of about 0.2 T. At the operating temperature T=30 mK, this corresponds to almost full spin polarization. A fully polarized spin in the field B_0 of the magnet produce a change Δk of the effective spring constant of the cantilever, which cause a frequency shift Δf related to Δk by $\Delta k/k=2\Delta f/f$. Fig. 2a shows the calculated Δk (black line) due to a fully polarized single electron spin, as a function of the coordinate x, (y,z=0). It is apparent that spins can produce both a positive or negative frequency shift, depending on the position with respect to the magnet. The total shift can be estimated by integrating over the surface. In our case, the total frequency shift due to the interaction between magnet and surface spins is 4.5 Hz. Assuming that the effect is produced by an uniform layer of spins with density σ, from the measured frequency shift we infer $\sigma\approx$0.2 nm^{-2}, a value reasonably close to estimations from other authors [6].

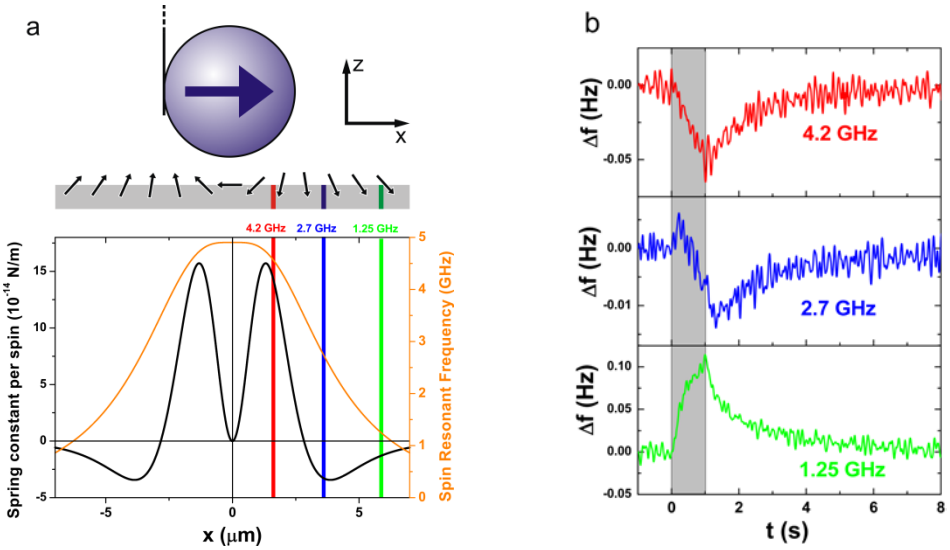

Figure 2: (a) Magnet-spins interaction and (b) microwave induced frequency shift.

To demonstrate that the measured static frequency shift is indeed due to a magnetic interaction with polarized surface electron spins, we have performed a simple saturation-recovery MRFM measurement. For spin manipulation, we generate a microwave field $B_1 \approx 1$ μT at a frequency in the range 1-5 GHz by sending a current through the microwire deposited on chip (see Fig. 1a). Because of the strong magnetic field gradient, the static field B_0 produced by the magnet, and hence the electron spin magnetic resonance frequency $f = g\mu_B B_0/h$ (with gLandè factor, μ_B Bohr magneton, h Planck constant) represented by orange line in Fig. 2a, are strongly varying with position. In particular for a given microwave frequency, only the spins in a thin slice, the so called *resonant slice*, will satisfy the magnetic resonance condition. In Fig. 2a the resonant slices for three representative frequencies (1.25 GHz, 2.7 GHz and 4.2 GHz) are indicated by coloured vertical stripes.

In our measurement protocol, we turn on the microwave field for a fixed time t=1 s (shaded grey region in Fig. 2b), thereby saturating spins in the resonant slice, and then we turn the field off. During the saturation process, the microwave field destroys the spin polarization by equalizing the population of the two Zeeman levels and therefore suppresses the contribution of the resonant spins to the cantilever frequency shift (black line in Fig. 2a). After the microwave field is turned off, the spins relax back to thermal equilibrium and repolarize. We can track the frequency shift in real time by self-oscillating the cantilever in a phase-locked loop. Figure 2b shows the cantilever resonant frequency as a function of time when saturating different resonant slices. Microwave field at 1.25 GHz (green resonant slice in Fig. 2a) saturates spins with a negative frequency shift contribution, leading to a net positive frequency shift. Microwave field at 4.2 GHz (red resonant slice in Fig. 2a) saturates spins close to the magnet with positive frequency shift contribution, leading to a net negative frequency shift. Finally, at an intermediate frequency of 2.7 GHz (blue resonant slice), we observe a mixed behaviour with an unexpected negative frequency shift following the expected initial positive transient. We attribute this complex behaviour to spin diffusion. In this picture, we have two transients: after spins in the resonant slice are saturated leading to an initial positive frequency shift, the spin polarization can spatially diffuse across the sample via flip-flop mechanisms. Since the blue resonant slice is close to the frequency shift inversion point in Fig. 2a, polarization eventually flows to the opposite sign region, leading to a sign inversion of the measured frequency shift. This picture has been validated by numerical simulations [10].

Spin diffusion of paramagnetic spins at millikelvin temperature has been recently proposed as a possible mechanism to explain the universal appearance of 1/f magnetic noise and decoherence in SQUIDs and superconducting qubits [7]. While the precise mechanism for 1/f generation has not been clarified yet, experimental evidence points to paramagnetic defects at the surface, or in buried film interfaces, as the noise source. Our experimental results support the spin diffusion model [7], by revealing for the first time spin diffusion phenomena in paramagnetic layers at millikelvin temperature.

3. CONCLUSIONS AND PROSPECTS

We have developed a new experimental setup for MRFM that for the first time can be operated down to millikelvin temperature. This achievement provides a mean to push this technique towards single spin resolution, possibly opening new horizons for three-dimensional imaging of biomolecules or imaging and control of single dopants in semiconductors. We applied for the first time MRFM to detect layers of paramagnetic defects in Si-SiO_2 interface, revealing spin diffusion phenomena. We have also demonstrated the basic features of this technique, in particular the field-gradient-induced spin selectivity.

Future developments rely on the implementation of a full three-dimensional scanner, and an increase of the B_1 field to enable advanced magnetic resonance manipulation techniques, like adiabatic rapid passage. A further optimization of the different parts of the apparatus will be needed to achieve single spin resolution, including more sensitive cantilevers and submicron magnetic tips.

ACKNOWLEDGEMENTS

This work has been partially supported by an ERC starting grant and by the FP7 project Microkelvin.

REFERENCES

[1] S. Kuehn, S.A. Hickman and J.A. Marohn: Advances in mechanical detection of magnetic resonance. *Journ. Chem. Phys.*, vol. 128 pp. 052208, 2008.

[2] D. Rugar, R. Budakian, H.J. Mamin and B.W. Chui: Single spin detection by magnetic resonance force microscopy. *Nature*, vol. 430 pp. 329-332, 2004.

[3] C.L. Degen, M. Poggio, H.J. Mamin, C.T. Rettner and D. Rugar: Nanoscale magnetic resonance imaging. *Proc. Natl. Acad. Sci.* vol. 106 pp. 1313-1317, 2009.

[4] G.P. Berman *et al.*: Solid-state nuclear-spin quantum computer based on magnetic resonance force microscopy, *Phys. Rev. B*,vol. 61pp. 14694, 2000.

[5] O. Usenko, A. Vinante, G. Wijts and T.H. Oosterkamp: A superconducting quantum interference device based read-out of a subattonewton force sensor operating at millikelvin temperatures, *Appl. Phys. Lett.*, vol. 98 pp. 133105, 2011.

[6] H. Bluhm *et al.*: Susceptibility of Metallic and Insulating Thin Films at Low Temperature, *Phys. Rev. Lett.*, vol. 103 pp. 026805, 2009.

[7] L. Faoro and L.B. Ioffe: Microscopic Origin of Low-Frequency Flux Noise in Josephson Circuits, *Phys. Rev. Lett.*, vol. 100 pp. 227005, 2008.

[8] R. de Sousa: Dangling-bond spin relaxation and magnetic 1/f noise from the amorphous-semiconductor/oxide interface: Theory,*Phys. Rev. B*,vol. 76 pp. 245306, 2007.

[9] B.W. Chui *et al*: Mass-loaded cantilevers with suppressed higher-order modes for magnetic resonance force microscopy, in *Technical Digest 12th Int. Conf. on Solid-State Sensors and Actuators (Transducers '03)*, pp. 1120–1123: IEEE, Piscataway, 2003.

[10] A. Vinante, G. Wijts, O. Usenko, L. Schinkelshoek and T.H. Oosterkamp: Magnetic resonance force microscopy of paramagnetic electron spins at millikelvin temperature, *Nat. Commun.*, vol. 2 pp. 572, 2011.

Synthesis of plasmonic gold/carbon nanotubes hybrid structures for cell imaging and drug delivery

L. Minati[1], S. Torrengo[1], V. Antonini[2], M. Dalla Serra[2],G. Speranza[1]

[1] *Fondazione Bruno Kessler, Via Sommarive 18, 38123 Trento, Italy*
Tel: +39 0461314656; e-mail: luminati@fbk.eu
[2]*Istituto di Biofisica, Consiglio Nazionale delle Ricerche, Viaalla Cascata 56/C Trento 38123, Italy*

ABSTRACT
The application of inorganic materials as carbon nanotubes for large-scale biological application is hampered by their not well defined toxicity towards biological matter. In this work, multi-wall carbon nanotubes/gold core-shell nanostructures were synthetized by controlled reduction of gold precursor. The gold hybrid materials as well as the intermediate products were characterized by means of X-ray photoelectron spectroscopy that allows controlling the efficiencies of the reactions step-by-step. UV-visible absorption spectroscopy and electron microscopy were used to follow the gold precursor reduction on the inorganic substrates. These composites could be very attractive for biological applications like imaging exploiting the high scattering of gold nanoparticles. In addition, thank to the particular geometry the nanotubes/gold core shell can be useful for drug delivery porpoises.

Keywords: branched gold, oxidized carbon nanotubes, surface plasmon resonance, cell imaging.

1. INTRODUCTION

The development of functional carbon nanotubes is of considerably interest for applications in biological field. The key element is the possibility to exploit their geometry to increase drug carrier into cell or living tissues [1].Furthermore, it was reported that the endocytosis rate of functionalized carbon nanotubes is much faster respect to that of the conventional nanoparticles, although their dimensions are much higher [2]. The possibility of use carbon nanotubes as drug carriers open the way to the production of geometry-designed nanostructures for specific delivery applications. Recently, a great work was developed for the production of metal shell with both inorganic and organic core for bioimaging and therapy purposes [3]. For example, Kim et al. have produced gold-plated carbon nanotubes that show a big enhancement (two orders of magnitude) in photoacoustic (PA) and photothermal (PT) contrast respect to the pristine carbon nanotubes for *in vivo* applications [4]. By a simple chemical reaction they reduced a gold precursor onto short single wall carbon nanotubes forming gold nanostructures with strong near infrared absorption. By further functionalization with rabbit anti-mouse antibodies the golden carbon nanotubes were used to map the endothelial receptor by a combination of PA/PT techniques. One of the greater hindrances in the use of carbon nanotubes as clinical vectors for imaging or drug delivery is their not well-defined toxicity. This occurs because of some contradictory results obtained among several studies reported in the literature. For this reason carbon nanotubes coated by stable gold layer are of particular interest for possible application of these nanostructures in clinical studies. Among them, gold is non-toxic material and allows the easy functionalization of the carbon nanotubes with a plenty of molecules including antibody and polymers. Multi-walled carbon nanotubes with an inner diameter of around 10-20 nm can be filled with a high amount of drugs or biomolecules for applications in disease cure or cancer therapy [5]. In addition, anisotropic gold shell system possesses interesting optical and electronic properties that could render them desirable for applications like plasmonic and surface enhancement Raman scattering substrates. In this work, oxidized carbon nanotubes are investigated as substrate for the growth of gold nanostructures.
The gold precursor spontaneously adsorbs on the CNTs and then is reduced to metallic gold by bland reducing agent. The gold coated carbon nanotubes as well as the intermediate products were characterized by means of X-ray photoelectron spectroscopy that allows controlling the efficiencies of the reactions step-by-step. Transmission electron microscopy indicates the formation of anisotropic gold nanostructure on carbon nanotubes. Visible absorption spectroscopy shows a strong NIR absorption attributed to the localized surface plasmon resonance of the gold on the carbon nanotubes.
Commercial multiwall carbon nanotubes were treated in acid mixture in order to functionalize them with carboxylic groups. $HAuCl_4$ water solution was added to the suspension of the ox-CNT sample and incubated under stirring at ambient temperature. After some minutes the suspension containing the ox-CNT sample was collected from the master solution, diluted in water and then analyzed by Uv-vis absorption spectroscopy. The

reducing agent hydroxylamine hydrochloride $NH_2OH*HCl$ was then added to the suspension to start the gold reduction.
After some seconds the solution changes in colour from pale brown to dark violet indicating the reduction of the gold precursor. The suspension finally turns the colour into green-blue in around one minutes, indication of the total gold reduction (CNT@Au). The CNT@Au sample slowly precipitates forming a brown supernatant that contains unreacted carbon nanotubes without gold and a dark blue precipitate. After re-dispersion in water the final suspension was purified by centrifugation at 10000 rpm for 10 minutes and washed three times with distilled water to remove the unreacted carbon nanotubes (see Figure 1).

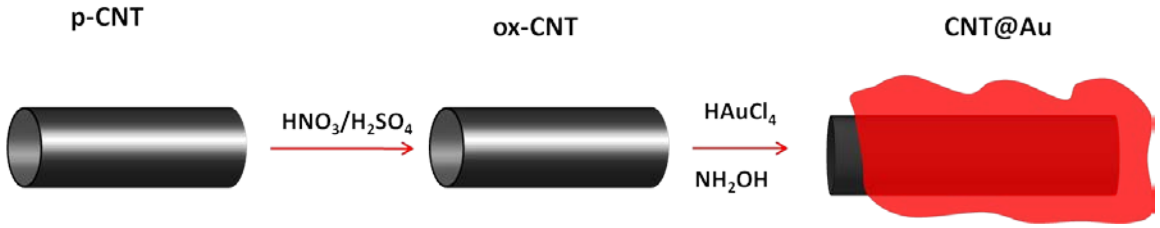

Figure 1. Synthesis of CNT/Au sample.

The oxidized carbon nanotubes show excellent stability in water and polar solvent even after months of storage. In Figure 2 XPS C1s core line of the pristine and oxidized carbon nanotubes are reported. No evidence of other elements besides carbon and oxygen are revealed by the XPS analysis. The region between 290 - 285 eV in the C1s core line exhibits the presence of carbon-oxygen bonds, like carboxyl (288.87 eV) as well as hydroxyl and ether-like bonds (286.36 eV).

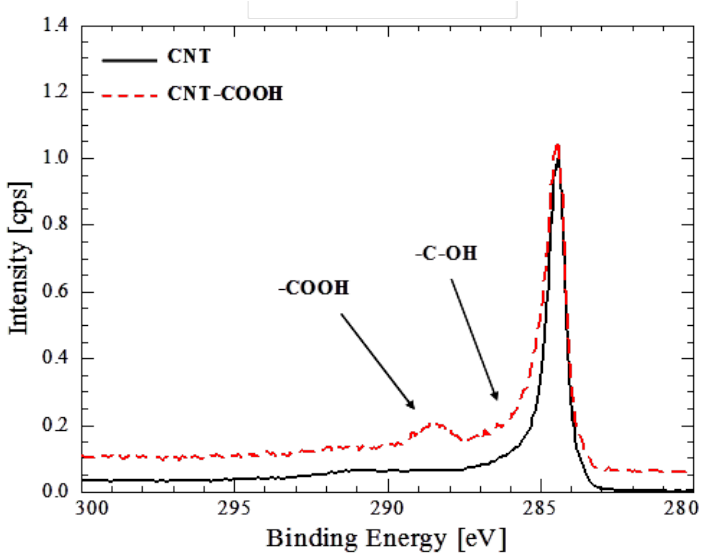

Figure 2. XPS of pristine (black continuous) and oxidized (red dashed) carbon nanotubes.

The XPS quantitative analysis of the sample indicates the presence of a high amount of carboxyl on the surface. The presence of these functional groups on the CNT surface is the main responsible of the great stability of the CNT suspension in water. The COOH group deprotonation form negative charges near the carbon nanotubes and stabilize them through electrostatic repulsion.
In figure 3 TEM image of CNT@Au sample is reported showing the presence of big particles with rod and star shape. This particular morphology is probably a consequence of the inglobation of a bundle of carbon nanotubes during the gold reduction that leads to the formation of anisotropic gold nanostructure with some similarities to star shaped and branched gold nanoparticles. The dimensions of these structures are around 100-200 nm. The EDXS analysis indicates the presence of gold, carbon and oxygen.

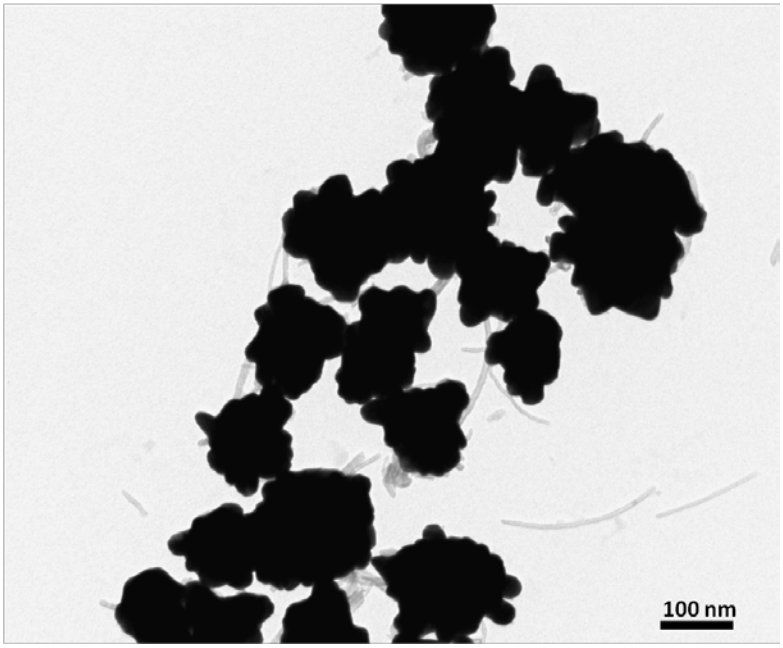

*Figure 3. TEM image of*CNT@Au*nanoparticles.*

The visible absorption spectroscopy of the CNT@Au samples shows an absorption feature located at around 530 nm and an intense broad absorption band in the 600–900 nm region. The peak at 530 nm is assigned to the transverse mode which is dependent on the shell thickness, while the broad absorption band at 840 nm is attributed to the longitudinal plasmon mode. The reason for the large band width is attributed to the non-uniform carbon nanotubes length of the starting material (100 - 400 nm) and the formation of multiple carbon nanotubes-gold structure that influence the final dimension of the composite. Despite the difference in the dimension, the shape of the CNT@Au particles presents a lot of similarities to that of gold nanostars. CNT@Au nanoparticles were further loaded with doxorubicin drug that can be adsorbed on carbon nanotubes and subsequently functionalized with thiolated PEG to increase the colloidal stability in water and biological media. A549 cancer cell lines were incubated with 0.1mg/ml of CNT@Au-dox nanoparticles for 15 hrs and then analyzed by laser scanning confocal microscopy.
The results show that the localization of the gold nanoparticles is in close vicinity to the cell membrane, while the doxorubicin penetrates in the cytosol compartment inside the cell.

2. CONCLUSIONS

In conclusion carbon nanotubes decorated by thick gold film were produced by simple and low-cost chemical routes. The visible absorption spectroscopy put in evidences the presence of a broad absorption band attributed to the plasmon resonance of the gold coated nanotubes. The scanning and transmission electron microscopy analysis confirms the formation of branched gold layer around the carbon nanotubes. Thanks to the particular shape, chemistry and optical properties, the gold coated carbon nanotubes could find application for drug delivery applications.

ACKNOWLEDGEMENTS

This research was performed in the framework of the COST Action MP0702, and Nanosmart project from Provincia Autonoma di Trento.

REFERENCES

[1]W. S. Kam, M O'Connell, J. A. Wisdom, H. Dai, *Proc. Natl. Acad. Sci*., vol. 102, pp. 11600, 2005.
[2]H. Jin, D. A. Heller, R. Sharma, M. S. Strano *ACSNano*, vol. 3,pp. 149, 2009.
[3]Y. Jin, C. Jia, S.W. Huang, M. O' Donnell, X.Gao *Nat. Comm.*, vol. 1, pp. 1, 2010.
[4] J.W. Kim, E. I. Galanzha, E. V. Shashkov, H. M. Moon, V. P Zharov, *Nat. Nanotech*., vol. 1, pp.688, 2009.
[5] Y.Liu, D. C. Wu, W. D.Zhang, X.Jiang, C. B.He, T. S.Chung, S. H.Goh, K. W. Leong, *Angew. Chem. Int. Ed.*, vol. 44, pp. 4782, 2005.

NOTES

Silicon photonics: recent results on high speed optoelectronic devices

Laurent Vivien, Delphine Marris-Morini, Gilles Rasigade, Melissa Ziebell, Papichaya Chaisakul, Mohamed-Saïd Rouifed, Eric Cassan, Jean-Marc Fédéli *

Institut d'Electronique Fondamentale – CNRS UMR 8622 - Univ. Paris Sud – 91430 Orsay Cedex France

** CEA-LETI, Minatec 17 rue des Martyrs, 38054 GRENOBLE cedex 9, France*

Silicon-based photonics have generated a growing interest with impressive results on passive and active devices in the last years. The main applications are optical telecommunications; optical interconnects in microelectronic circuits and biophotonics.

One of the rationales of the used of silicon photonics is the reduction of photonic system cost thanks to the high density integration of silicon devices and the used mature technology. Furthermore, the integration of photonic components with electronic integrated circuit on a common chip could also enhance the integrated chip performances.

An overview of our recent activities on silicon photonics for the definition of high speed optical link will be given focusing on the integration of high speed silicon-based optical modulators and germanium photodetectors.

NOTES

Subwavelength silicon nanophotonics

P. Cheben[a], P. J. Bock[a], J.H. Schmid[a], J. Lapointe[a], S. Janz[a], D.-X. Xu[a], R. Ma[a], A. Densmore[a], A. Delâge[a], B. Lamontagne[a], R. Halir[b], I. Molina-Fernández[b], A. Ortega-Moñux[b], C. Alonso-Ramos[b], A. Villafranca Velasco[c], M.L. Calvo[c], I. Glesk[d], J.-M. Fédélie[e], L. Vivien[f], M. Ibrahim[g], W.N. Ye[g]

[a]*Institute for Microstructural Sciences, National Research Council, Ottawa, Canada*
[b]*ETSI Telecomunicación, Universidad de Málaga, Málaga, Spain*
[c]*Facultad de CC. Fisicas, Universidad Complutense, Madrid, Spain*
[d] *University of Strathclyde, Glasgow, United Kingdom*
[e] *CEA, LETI, Minatec, Grenoble, France*
[f]*Institut d'Electronique Fondamentale,University of Paris Sud, Orsay, France*
[g]*Department of Electronics, Carleton University, Ottawa, Canada*
pavel.cheben@nrc.ca

We review recent advances in subwavelength nanophotonic structures in planar waveguides. We present a new type of microphotonic waveguide, exploiting the subwavelength grating (SWG) effect. The SWG technique [1] allows for engineering of the refractive index of a waveguide core over a range as broad as 1.5–3.5 simply by lithographic patterning using only two materials, for example Si and SiO_2.
We demonstrate several examples of subwavelength grating waveguides and components made of silicon and operating at telecom wavelengths. These include waveguide crossings with minimal loss (<0.03 dB) and negligible crosstalk, a subwavelength grating fibre-chip coupler with a loss as low as 0.9 dB, an apodized subwavelength surface grating coupler (Fig. 1), high-performance MMI couplers, a polarization rotator, athermal waveguides and several other emerging silicon subwavelength nanophotonic devices.

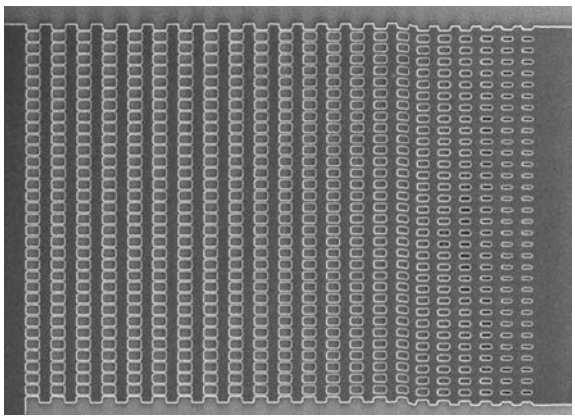

Fig. 1. Apodized surface grating coupler with subwavelength nanostructures.

REFERENCES

[1] Cheben, P., et al., Opt. Lett., 35, 2526 (2010)

NOTES

Optical coupling of double L7 photonic crystal microcavities on InP suspended slab with embedded quantum wells

L.E.Munioz-Camuniez[1*], I.Prieto[1], J.M.Llorens[1], P.A.Postigo[1]
[2]Instituto de Microelectrónica de Madrid (IMM-CNM- CSIC), Isaac Newton 8, E-28760, Tres Cantos Madrid, Spain

e-mail: luis.munioz@imm.cnm.csic.es

ABSTRACT
We present the fabrication and optical characterization of double L7 photonic crystal microcavities consisting of two L7 photonic crystal microcavities. The microcavities were fabricated on an indium phosphide (InP) slab with embedded InAsP quantum wells with emission around 1.5 microns. The optical characterization and theoretical calculations confirm the optical coupling between both L7.

Keywords: photonic crystal, microcavities, optical coupling, semiconductor slab

1. INTRODUCTION

Optical coupling in microcavities has been demonstrated in different systems, from Bragg reflector micropillars **[1]** to photonic crystal microcavities on thin slabs (PCMs) **[2,3]**. That kind of systems could be used for optical buffers **[4]**, enhancement of nonlinear optical processes **[5]** and high efficient entangled photon sources **[6]**. In particular, the coupling of two PC cavities could be a key element for a more complex photonic integrated circuit.

2. EXPERIMENTALRESULTS

We have fabricated PCMs comprising two parallel L7 microcavities separated by one, three and five rows of holes in the direction perpendicular to the L7 microcavities, Figure 1. The active medium consists of four InAsP QWs emitting around 1.5 microns, fig 1(a). Double-cavities separated in the parallel direction were also fabricated but did not show a clear coupling between them for all the separations, like the formers did. Other configurations could provide an enhanced coupling **[3].**.

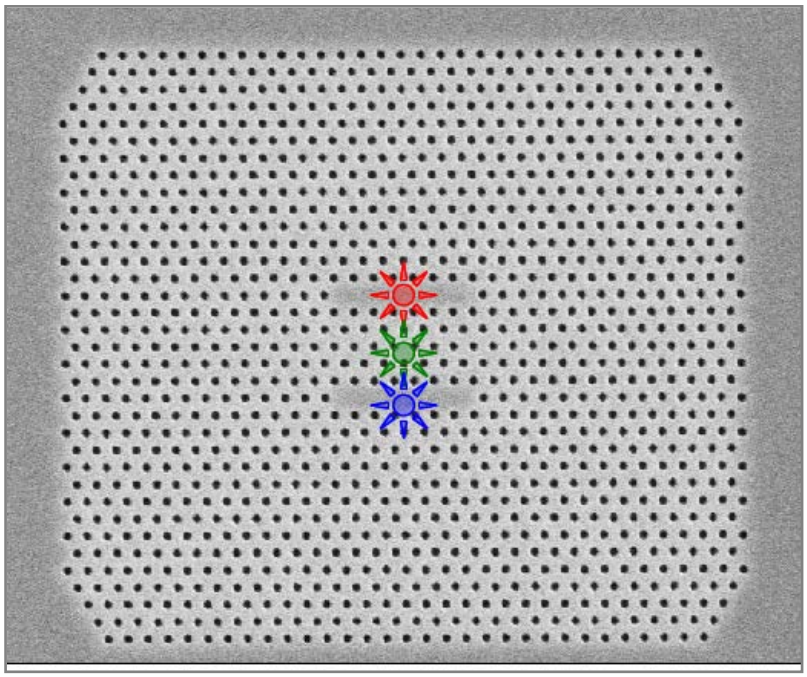

Figure 1. *Scanning Electron Microscopy image of a double L7 microcavity showing the different positions of the excitation spot.*

2.1 Fabrication

The fabrication process involves Electron Beam Lithography (EBL) on a thin layer of ZEP 520A resist. A transfer of the pattern to a SiO_x hard mask was done by a Reactive Ion Beam Etching (RIBE). A subsequent transfer of the pattern to the active slab layer was performed by a Reactive Ion Etching (RIE). Finally, a wet etching of the sacrificial layer (InGaAs) is carried out through the holes with a mixture of HF:H2O2:DI. Further details can be found in **[7]**.

The L7-type cavity consists of seven missing holes in a triangular photonic crystal array. We have designed the structures (single L7 PCMs) by Finite Difference Time Domain (FDTD) simulations**[8,9]**. We have selected a lattice constant *a*= 440 nm; different structures with a radius evolution from 0.20a to 0.29a have been fabricated to match the spectral region of interest. The thickness of the suspended membrane and the InGaAs sacrificial layer underneath is 237 nm and 1156 nm, respectively.

2.2 Optical Characterization

Optical characterization was performed by microphotoluminescence (μPL) spectroscopy at room temperature. The excitation laser has a wavelength of 785nm and is operated in CW mode. For a double PCM we carried out several measurements using different positions for the excitation spot (Figure 1). The diameter of the excitation spot is ~1.5μm. This method allows to identify whether the optical modes are "shared" between the microcavities (optically coupled system) or not (optically decoupled system). Figure 2(a) shows several μPL spectra from a double PCM changing the position of the spot of excitation as can be seen in Fig.1. The energies of the observed peaks are independent of the position of the spot used for excitation although their intensities do depend. That behavior shows that the PCMs are optically coupled for both the first and second modes.

On the other hand, Figure 2(b) shows the spectra of another double microcavity. In this case, the spectral position of the peaks depend on which microcavity is directly excited (i.e., the physical position of the spot for excitation) so we can conclude that the first and second modes are optically decoupled. Other double microcavities show that only the first or the second modes are optically coupled while the other ones are decoupled.

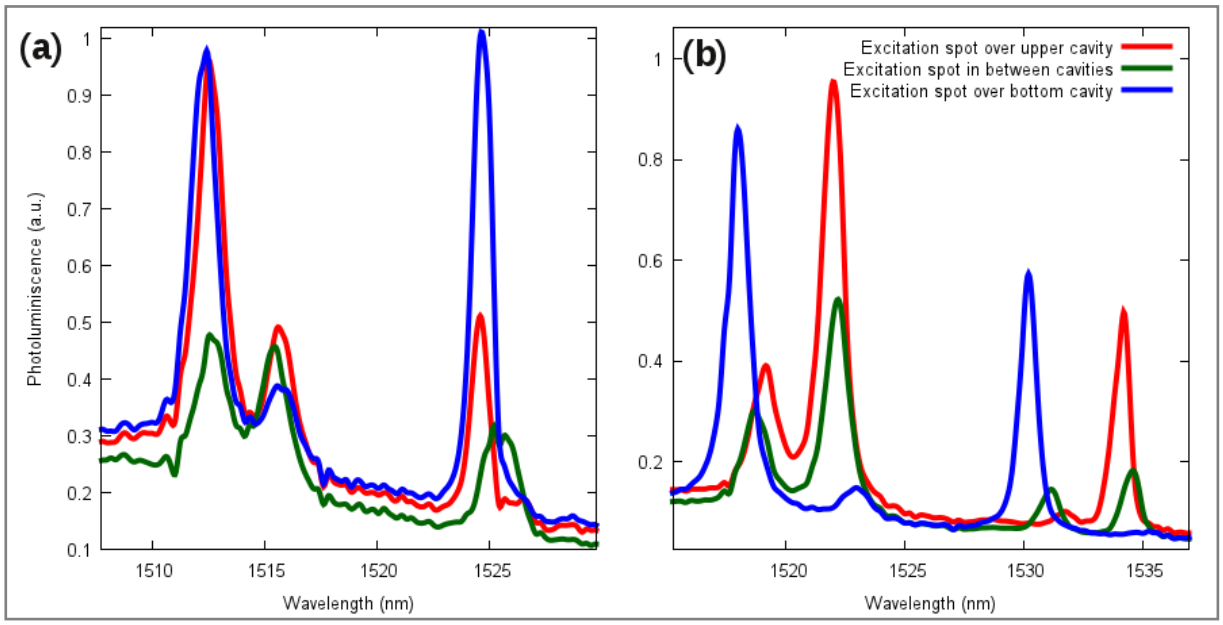

Figure 2. *μ-PL spectra of two double microcavities showing coupled modes (a) and decoupled (b). Red (blue) spectra were taken with the excitation spot over the upper (bottom) microcavity. Green spectra were taken in between the microcavities.*

In order to explain the observed coupling of double L7 microcavities, we have carried out calculations using the guided-mode expansion method (GME) **[10]**. The calculated energies for the optical modes of the microcavities and the experimental measurements do not agree well unless we include a shift in the calculated energies with an *ad-hoc* ratio. Once the *ad-hoc* ratio is included, there is a good correlation between measured and calculated values for the energies of the coupled modes. This discrepancy in energy can be attributed to a difference between the real refractive index and the one used the calculation, a thinner slab of InP than expected or differences in the *r/a* value. The resonance splitting of the 5-rows PMCs is well described by the theoretical model. In contrast, the 3-row PMCs are not so well described. We presume that the 3-row PMCs are more

sensible to fabrication defects than the 5-row PMCs. Hence, our ideal model performs better in describing the optical features of the latter than the former. The results above described provide a quite convincing basis to support that the microcavities are truly optically coupled. We notice that far-field measurements could improve the understanding of coupled modes as described in [11].

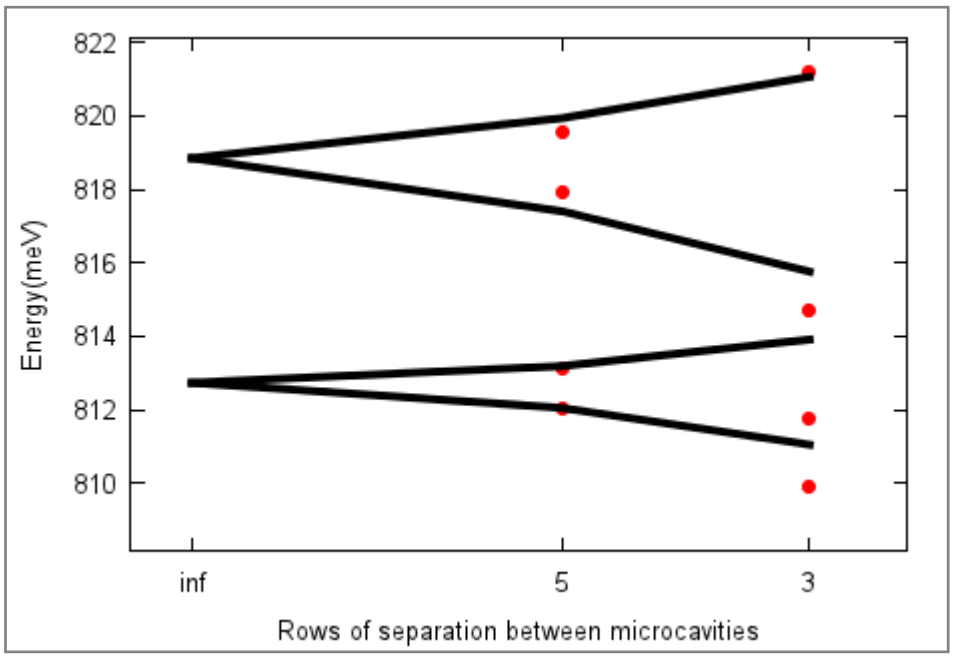

Figure 3. *Comparison between the measurements (red symbols) of two double L7 microcavities and GME calculations for these structures (black lines).*

3. CONCLUSIONS

In summary, we have fabricated and characterized double L7 photonic crystal microcavities on InP slab emitting around ~1.5 microns. The optical characterization show that some of the double PCMs present optical coupling between their modes. Theoretical calculations support the measurements. The results could contribute to the design and fabrication of future photonic integrated circuits.

ACKNOWLEDGEMENTS

LEMC and IP acknowledge financial support from both FPI fellowship. Support from Spanish MICINN and CAM through grants NANINPHO-QD (TEC2008- 06756-C03-01/03) and CAM2010 Q&C Light (S2009ESP-1503) is also acknowledged.

REFERENCES

[1] M. Bayer et al., Phys. Rev. Lett. **81** (1998) 2582.
[2] K. Atlasov et al., Opt. Express **16** (2008) 16255.
[3] A. Chalcraft et al., Opt. Express **19** (2011) 5670.
[4] E. Ozbay et al., IEEE J. Quantum Electron. **38** (2002) 837.
[5] S. Mookherjea et al., J.Sel. Top. Quantum. Electron. **8** (2002) 448.
[6] A. Dousse et al., Nature **466** (2010) 217.
[7] L. J. Martínez et al., J. Vac. Sci. Technol. B **27** (2009) 1801.
[8] Lumerical Solutions, Inc., Vancouver, BC, Canada.
[9] Oskooi et al., Comp.Phys.Comm. **181** (2010) 687.
[10] L .C. Andreani et al., Phys. Rev. B **73** (2006) 235114.
[11] M. Brunstein et al., Appl. Phys. Lett. **99** (2011) 111101.

NOTES

Real-time Mapping of Temporal Soliton formation and Pulse acceleration in III-V Semiconductor Photonic Crystal Waveguides

F. Raineri[1], Karle[1], P. Monnier[1], S. Combrié[2], A. De Rossi[2] , and R. Raj[1]

[1]Laboratoire de Photonique et de Nanostructures, Route de Nozay, Marcoussis 91460 France
[2]Thales Research and Technology, Route Départementale 128, 91767 Palaiseau, France
Tel :+33169636195 e-mail : rama.raj@lpn.cnrs.fr

ABSTRACT

Temporal mapping of 20pJ pulse propagation in a 2DPhC waveguide show of soliton formation. For high signal powers the photonic band is modified influencing the group velocity leading to an acceleration of the pulse propagation.

Keywords: Temporal Solitons, Photonic Crystal waveguide.

INTRODUCTION

In this work we report on the various manifestations of the effect of the low group velocity v_g and its management using the intertwining of the group velocity dispersion in a PhC waveguide in the low v_g regime and the self phase modulation in the material (GaInP). The exploration of the influence of these two processes in a line-defect PhC waveguides are carried out by measuring their effect, on the propagation of pico-second pulses through the sample, by means of accurate time domain measurements.

2DPhC line defect waveguides have been a topic of extensive studies since a few years in a lot of different contexts. PhC-based all-optical switching [1], lasing [2] and temporal solitons [3] have been demonstrated. The low group velocity $v_g$near the photonic band edge in PhC waveguides is an extremely interesting aspect of the photonic crystal which provides enhanced light matter interaction leading to exalted manifestations of nonlinearities. In order to exploit the advantages provided by the low v_g, precise characterisation and management of low group velocity is important. We report on a direct measurement of the delay between the linear propagation and soliton formation through a parametric amplification optical gating method.

The PhC waveguide used for our exploration corresponds to one line of holes removed in a hexagonal lattice of air holes drilled in a GaInP slab membrane [3]. The 1.3mm PhC waveguide is equipped with an inverse taper to reduce insertion loss. The waveguide dispersion was analysed using the parametric amplifier gating method for different wavelengths propagating through the waveguides giving a direct measurement of the time delay ΔT, yielding directly the group index $n_g = c\Delta T/L$.

The intense 810nm pump pulses are combined with the output signal pulse from the PhC waveguide in a BBO crystal. The interaction with the pump pulses parametrically amplifies the pulses coming out of the waveguide from 1490 to 1565nm. Indeed, for each measurement, the angle of the BBO crystal is set in such a way that these wavelengths correspond to the idler wavelength of the crystal. The amplification of the near infrared wavelengths is accompanied by the generation of amplified pulses at the BBO's signal wavelengths

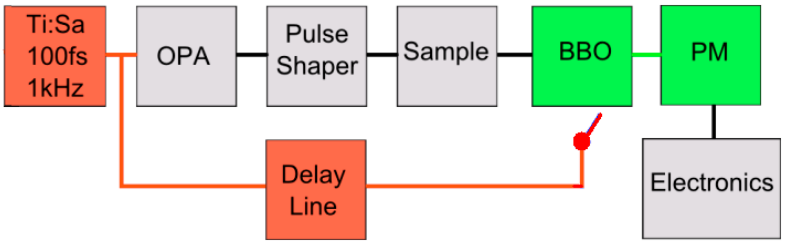

Figure 1 : Ultrafast measurement set-up

around 540nm. We eliminate the background noise in several steps: firstly we detect the signal at the nearly background free wavelength of 540nm which also has the advantage in that it's where the detector performance is optimum. Then in order to eliminate the noise due to the diffusion of the intense blue light arising from the SHG of the pump (at around 400nm), we use a high-pass filter. We also introduce an angle close to 10 degrees (in order to eliminate the blue light which is in the direction of the pump) to superimpose the pump and idler

beams and then we detect only the signal pulses using a Si photomultiplier. To further eliminate background noise, we electronically gate signal detected by the Si detector with a boxcar averager and use a lock-in amplifier to filter out the chopped pump (hence 400nm SHG as well). Then by optically delaying the 810nm gating pulse it is possible to "map" the temporal response of the pulses coming out of the waveguide with a resolution of 150fs. In Figure 1 we show a block-diagram of the optical elements traversed by the idler and pump wavelengths. The sample was monitored using an infrared camera.

Femto second light pulses at 810nm from a Ti-Sapph regenerative amplifier is used, on the one hand, to pump an optical parametric amplifier (OPA)at a repetition rate of 1kHz, which then delivers 150 femto second pulses with tunable wavelengths. The other part of the 810nm pulses is used as a pump in the parametric amplifier gated detection set-up. The pulses from the OPA are sent into a Dazzler that shapes the pulses to give Fourier transform limited Gaussian pulses whose temporal pulse widths may be varied from 1 to 4 picoseconds. The wavelength may be varied from 1495 to 1565. After propagation through the PhC waveguide, one part of the signal is sent into a spectrometer and the other into the time "mapping" set-up where the femto-second pump pulses are time delayed with respect to the signal and thus maps accurately the temporal shape of the signal.

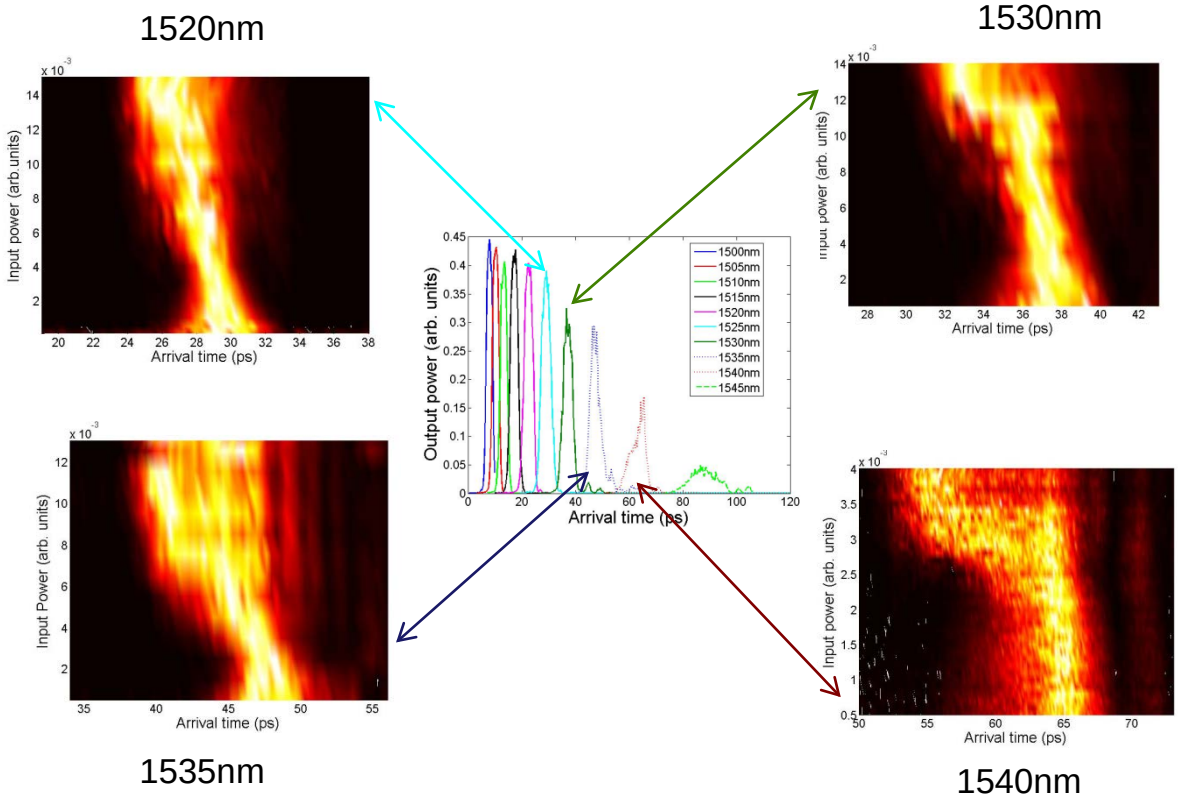

Figure 2 : Linear dispersion versus wavelength ; the peripheral plots are the pulse widths and the arrival time of the pulses at the output of the waveguide for increasing input pulse powers.

Figure 2 depicts the linear delay that the 2.2ps pulses undergo in propagating via the PhC waveguides. This delay is directly linked to the group indexgiving values for n_g= 6.05, 6.08, 11.07 and 13.8 respectively for 1525nm, 1530nm, 1535nm and 1540nm signal pulses. We then measured the temporal evolution of 2.2ps pulses as a function of the incident power for three wavelengths: 1525nm, 1530nm 1535nm and 1540nm. The four figures in the periphery of fig 2 depict the evolution of the pulse FWHM's as a function of the incident power. Here it is seen that for 1525nm, 1530nm, 1535nm and 1540nm the formation of solitons is clearly takes place when the FWHM narrows down in width. For these parameters, when a 2.2ps pulses is launched onto the PHC waveguide the 'soliton' propagates without any distortion as is clearly shown by the direct measurement. Interestingly, for increasing power, the evolution of the FWHM shows the signal moving towards shorter delays showing a change in the v_g as a function of the power. The pulses begin to accelerate. This corresponds to the bending of the band, which shifts the band to the region where the group velocity is higher.

CONCLUSION

We experimentally explored the effects of dispersion on picosecond pulse propagation in a 2DPhC line-defect waveguide by time domain measurements. The signal mapped by the parametric amplification showed the

formation of solitons for a specific wavelength corresponding to the exact cancellation of the GVD by self phase modulation for an input energy of the order of 20pJ. For high signal powers the photonic band is modified influencing the group velocity leading to an acceleration of the pulse propagation. This type of dispersion analysis is crucial because PhC waveguides exhibit large GVD effects due to the high confinement of the optical modes for short waveguide lengths as compared with conventional waveguides. The harnessing of this characteristic should, through controlled tailoring of the structure permit dispersion control, which could be applied to group delay lines, pulse shaping and dispersion compensation.

ACKNOWLEDGEMENTS

This work was done within the context of the FP7 European project COPERNICUS.

REFERENCES

[1] F. Raineri, Crina Cojocaru, P. Monnier, A. Levenson, and R. Raj: Ultrafast dynamics of the third-order nonlinear response in a two-dimensional InP-based photonic crystal, *Appl. Phys. Lett*. **85**, 1880-1882 (2004)

[2] Y. Halioua, T. J. Karle, F. Raineri, P. Monnier, I. Sagnes, G. Roelkens, D. Van Thourhout and R. Raj Hybrid InP-based photonic crystal lasers on silicon on insulator wires". Appl. Phys. Lett. **95**, 201119-(2009)

[3] Temporal solitons and pulse compression in photonic crystal waveguides" P. Colman, C. Husko, S. Combrié, I. Sagnes, C. W. Wong, A. De Rossi, Nature Photonics , 862-868 (2010)

NOTES

Zero Bias GaAs Schottky Junctions for Terahertz Array Camera

R. Casini, A. Di Gaspare, E. Giovine, A. Notargiacomo, M. Ortolani and V. Foglietti
IFN – CNR, Via Cineto Romano 42, 00156 Roma, Italy.
Tel: +3906 41522 227; e-mail: roberto.casini@ifn.cnr.it

ABSTRACT
We report the development of Zero Bias Schottky diode detectors based on quantum tunnelling through the narrow barrier of a sub-micrometric Au/Ti/n-GaAs junction. General device structure, physics and fabrication are discussed with particular attention to three-dimensional shaping of the junction geometry that provides an enhanced zero-bias tunnelling current, resulting in cut-off frequencies up to 0.55 THz, responsivity up to 200 V/W and noise equivalent power better than 10^{-9} W/Hz$^{0.5}$ without applied dc bias. An outlook on monolithic array and an alternative to the Silicon solid immersion lens approach.

Keywords: Schottky diode, Terahertz, quasi-optical, Zero Bias detector, tunnelling probability, GaAs micromachining

1. INTRODUCTION

The Schottky diode is probably the most important microelectronic device for operation in the sub-millimeter waves and terahertz (THz) range because of is a fast and high responsivity detector, and both cryogenic and room temperature operations are allowed [1]. Microelectronic rectifiers based on Schottky diodes fabricated on epitaxial layers of III-V semiconductors like GaAs are commonly employed as square-law power detectors in millimeter wave integrated circuits working up to 100 GHz . The working principle is based on the assumption that the non-linearity of current-voltage (*I-V*) characteristics exploited for diode operation at dc-to-gigahertz frequencies is somehow preserved in the sub-millimeter waves, where the concepts of power coupling and transit time delay are more properly used instead of simple *I-V* curves. In classical models the square-law responsivity is inversely proportional to the dynamic resistance of the device. For these reasons, a good rectifier should display both highly nonlinear characteristics and low resistance at the bias point.

In this paper, we introduce quasi-optical Schottky diodes without a dc bias, based on quantum tunneling through a curved sub-micrometric Au/Ti/n-GaAs junction, fabricated with integrated antennas and we show that the three-dimensional shaping of deeply sub-micron junctions on very highly doped n-GaAs can result not only in a low R_s and C_j, but also in an enhanced zero-bias tunneling probability: the result is a low values of R_d and nonlinear *I-V*characteristics at i = 0.

Over the measured range of 0.15 to 0.7 THz using a quasi-optical setup, noise equivalent power values between 1-5·10-10 W/Hz$^{0.5}$ are achieved.

The final application of these devices requires the construction of an array (linear array, focal plane array,...) with the aim of eliminate the high resistivity Silicon lens and illuminate the array from the free-space side, so we started to investigate substrate removal to couple the radiation and the device without the Silicon lens.

2. DEVICE FABRICATION AND PHYSICS

Our process is fully planar and very reproducible, in order to fabricate monolithic matrixes of radiation detectors which could then be used to acquire real-time terahertz images in a focal plane array configuration (see Fig.1). Starting from highly doped MBE-grown n/n^+ epitaxial layers (100 nm with $N_d = 1\cdot10^{18}$ cm^{-3}on top of 1000 nm with $N_d = 5\cdot10^{18}$ cm^{-3} and semi-insulating substrate,from IQE Inc.), we have fabricated two types of diodes: standard Schottky diodes and ZBDs. As shown in the scanning-electron micrographs of Fig. 1, in both cases the sub-micrometric Schottky junction is achieved by contacting the GaAs surface with the extremity of a free-standing metal bridge[2, 3]. To cut parasitic capacitances, deep mesa isolation was performed between anode and cathode pads, then working as the arms of a planar antenna. The difference between the two types of devices lies only in the three-dimensional geometry of the sub-micron metal-semiconductor junction, which actually allowed us to tune the Schottky barrier thickness and hence the tunneling probability.

In Schottky junctions with high doping levels ($N_d \geq 10^{18}$ cm^{-3} for GaAs) the dominant transport mechanism is the thermionic field emission (TFE) of electrons thermally excited close to the top of the barrier, where the tunneling probability is high. For thinner barriers, the enhanced tunneling probability at all energy levels of the barrier leads to lower nonlinear coefficents and R_d's . For zero-bias rectification at THz frequencies, a low value of R_d at i = 0 is crucial, because it defines the cutoff frequency of the rectifier f_{ci}, which is derived by calculating the radiation power absorbed at the junction[4]:

$$f_{ci} = \frac{(1 + R_s / R_d)^{0.5}}{2\pi C_j (R_s R_d)^{0.5}} \quad (1)$$

If we take the parasitic $R_s \sim 20\ \Omega$ (a typical value for submicron epitaxial *n*-GaAs diodes) and $C_j = 1$ fF, zero-bias rectification at THz frequencies requires $R_d < 100$ kΩ at most. For standard diodes with sub-micron area, $R_d > 1$ GΩ at zero bias, therefore $f_{ci} << f_c$ and the diode needs to be dc forward-biased to work as THz rectifier[5]. As we now explain, we have obtained ZBDs with anode area of 0.4 μm^2 and minimum R_d values at $i = 0$ around 100 kΩ through a modification of the standard flat-junction geometry, resulting in a thinner Schottky barrier.

Using the Electron Beam Lithography we have developed a trilayer resist polymer process to obtain a "T-section" anode of 200 nm, while the lenght is variable from 2 to 10 μm. When the metal Schottky contact is evaporated (30 nm Ti and 400 nm Au on n-GaAs) the wafer is first dipped in a $NH_4OH:H_2O_2$ solution to provide the surface cleaning in order to eliminate the presence of oxide. In this step, approximately 10 to 30 nm of GaAs are anisotropically removed from the area where the junction is to be formed. The additional etching step in $NH_4OH:H_2O_2$ results in a very different behavior of the dc characteristics : standard diodes display the typical exponential behavior (not etched with $NH_4OH:H_2O_2$ solution), while ZBDs display quasi-ohmic *I-V*characteristics around the zero-bias point, which are still non-linear at any *V*, including *V=0*. Since the doping level is the same ($N_d = 1 \cdot 10^{18}$ cm^{-3}), the reduced value of R_d at $i = 0$ in our ZBDs is due to a reduced barrier thickness caused by an increased peak electric field E_{max} in the ZBD junction. Fig. 2a-b shows the section, obtained by Focussed Ion Beam (FEI Helios nanolab 600), of typical "T-shaped" anodes: the anode in Fig. 2a is from a standard diode, while the anode in Fig. 2b is from a ZBD. By careful inspection of the junction profile (the footprint of the "T") one sees that the standard junction is perfectly flat, while in the ZBD it presents a curvature radius r_j of about 20 to 50 nm along the short side (0.2 μm long) of the rectangular footprint. By further sectioning the same anode, we have found that the profile is roughly conserved along the full anode length, resulting in a cylindrical junction profile for the ZBDs. Curved junctions develop a higher E_{max}, since a larger volume of the semiconductor is crossed by the field lines and hence is depleted, resulting in an increase of the total tunneling probability by more than one order of magnitude if compared to the flat junction and hence in a strong decrease of R_d, as demostrated by our calculation summarized in Fig. 2c and Fig. 2d.

3. DEVICE PERFORMANCE

To demonstrate the functionality of our ZBDs as THz rectifiers, we have determined their cutoff frequency by irradiating the devices with free-space beams of variable THz frequency *f*. Selected dies containing one device are mounted in a quasi-optical package, which includes a hyper-hemispherical silicon lens pressed on the back of the diode chip by a teflon spring. The performances at terahertz frequencies (directivity and noise equivalent power) of the lens-coupled detector were measured by a free-space-coupled 0.2-0.7 THz radiation source (by Virginia Diodes Inc.) based on a frequency multiplier chain starting from a 8-20 GHz radiation produced from a YIG oscillator: the Voltage Controlled Oscillator (*VCO*) was amplitude-modulated (AM) up to 10 kHz, and the radiation was emitted in free-space by horn antennas, collected and refocused onto the detector lens by a pair of 90° off-axis parabolic mirrors.

The optical responsivity at zero bias $\beta_0(f)$ is plotted in Fig. 3 for one ZBD with area $S_A = 0.2 \times 10$ μm^2 (red line, diode A) and one with area $S_B = 0.2 \times 2.0$ μm^2 (blue line, diode B). At a first inspection, diode A displays $f_{ci} \sim 0.22$ THz, while the smaller diode B has f_{ci} around 0.5 THz. The Noise Equivalent Power (NEP) of the ZBDs was calculated by dividing the measured noise of 40 nV/Hz$^{0.5}$ by β_0 (ZBD noise spectra as a function of readout frequency are reported in the inset). The NEP of diode B at $f = 0.55$ THz is $5 \cdot 10^{-10}$ W/Hz$^{0.5}$, better thanwhat obtained with our standard Schottky detectors dc-biased at $i = 10$ μA (NEP ~ 10^{-8} W/Hz$^{0.5}$ with AM at 330 Hz).

4. FUTURE IMPROVEMENT: MICROMACHINING

In antenna coupled terahertz rectifiers based on Schottky diodes the radiation is fed to the antenna either by a waveguide (narrow band operation) or by a silicon substrate lens centered on the backside of the detector chip (broadband operation). Both these approaches, however, are clearly single-pixel-oriented, since each diode requires one waveguide or one lens. For imaging applications integrated arrays are to be developed, and different solution must be sought for radiation coupling to each pixel, since guided substrate modes cause the cross-talking among different pixels of an integrated array[6].

The first solution is to realize pyramidal horn antenna by using the Silicon micromachining process by means of wet anisotropic etching. The antenna array and the cavity array will be fabricated on silicon wafer and then paste together with GaAs Schottky Diode array wafer (see Fig.4a).
The second and more interesting solution is to inhibits the propagation of substrate modes (optical cross-talking) by locally remove the substrate below the diode; different antenna geometries require different solution so we can fabricate suspended bridge for bow-tie and dipole antenna pixel or we can dig a trench around the pixel for log-periodic antenna pixel (see Fig.4b, 4c).

5. CONCLUSION

In conclusion, we have studied sub-micron *n*-GaAs Schottky diodes displaying enhanced tunneling current at zero-bias, due to a three-dimensional curvature of the junction, and we have investigated the detection properties in the range 0.15-0.7 THz obtaining a good sensitivity level (NEP < 10^{-9} W/Hz$^{0.5}$ at 0.55 THz).
The goal of the development of a diode array structure not coupled to the radiation through a high resistivity silicon lens is to achieve the same good sensitivity level, and work is ongoing.

REFERENCES

[1] P. H. Siegel et al.: 2.5-THz GaAs Monolithic Membrane-Diode Mixer, *IEEE Transactions on Microwave Theory and Techniques*, vol. 47, no. 5, May 1999.
[2] A. Ketterson, M. Tong, J.W. Seo, K. Nummila, K.Y. Cheng, J. Morikuni, S. Kang, I. Adesida: Submicron modulation□doped field-effect transistor/metal–semiconductor–metal based optoelectronic integrated circuit receiver fabricated by direct-write electron beam lithography, *Journal of Vacuum Science & Technology B: Microelectronics and Nanometer Structures*, vol. 10, no.6, November 1992
[3] H. Xu, G.S. Schoenthal, L. Liu, Q. Xiao, J.L. Hesler: On Estimating and Canceling Parasitic Capacitance in Submillimeter-Wave Planar Schottky Diodes , *IEEE Microwave and Wireless Components Letters*, vol. 19, no.12, 807 – 809, December 2009
[4] A. M. Cowley, H. O. Sorensen: Quantitative comparison of solid-state microwave detectors, *IEEE Trans. Microw. Theory Tech.*, vol. 14 (12), 588 (1966).
[5] O. Cojocari, B. Mottet, M. Rodriguez-Girones , S. Biber , L. Schmidt, H. Hartnagel: A new structural approach for uniform sub-micrometer anode metallization of planar THz Schottky components, *Semicond. Sci. Technol.*, vol. 19, 537, 2004
[6] R. Casini, D. Dominijanni, E. Giovine, M. Ortolani, F. Gatta, A. D'Amico and V. Foglietti, *IEEE Proc. Of IR, milli. and THz Waves IRMMW-THz 2010*, (2010).

FIGURES

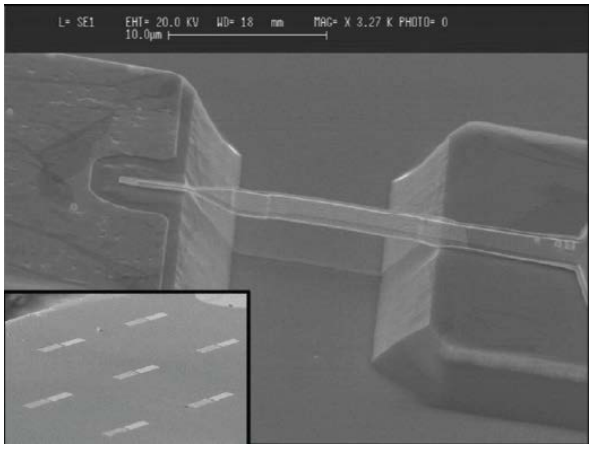

FIG. 1. SEM picture of a Terahertz Schottky diode fabricated at IFN-CNR;inset: Monolithic Schottky Diode Array.

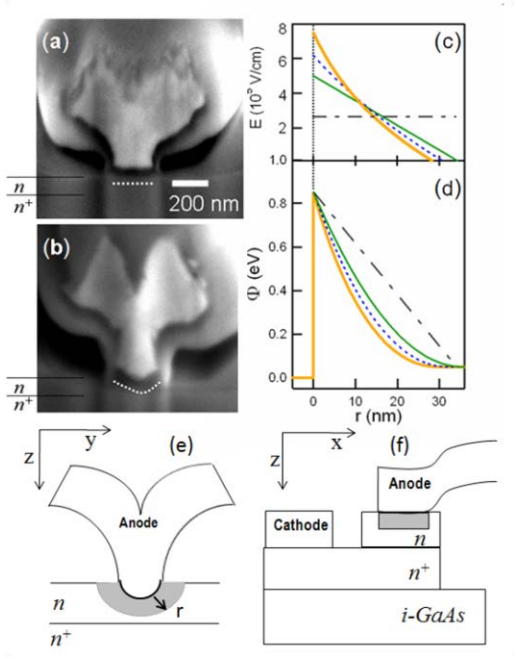

FIG. 2. Section of the anodes realized by focussed ion-beam (a): standard diode. (b): zero-bias detector. Note the junction curvature in (b): the white dotted line roughly represents the depletion region boundary. (c) Electric field and (d) potential energy as a function of distance r from the junction of a cylindrical Au/Ti/n-GaAs Schottky junction with Nd $=10^{18}$ cm^{-3} for two values of the curvature radius r_j, for the flat-junction (thin green line) and in the triangular-barrier approximation (dot-dashed line). (e) Schematic section of the T-shaped anode and (f) sketch of the entire air-bridge Schottky diode. The shaded areas in (e) and (f) represent the cylindrical depletion region of the model used for the calculations in (c) and (d).

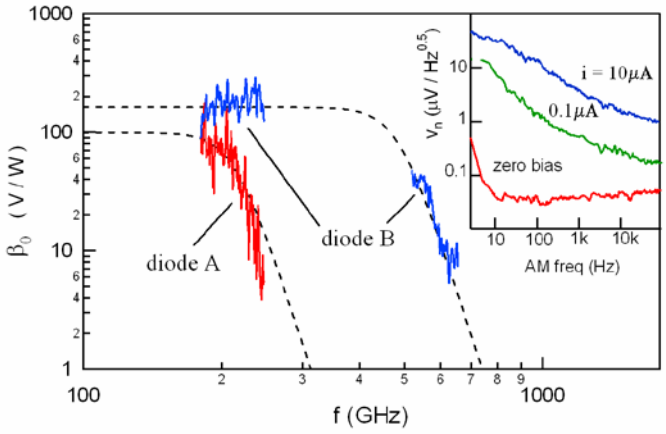

FIG. 3. Experimental determination of the zero-bias video responsivity $\beta_0(f)$ of two ZBD diodes with a quasi-optical setup and a tunable electronic oscillator as the radiation source. Dashed lines are guides to the eye for cutoff frequency evaluation. Inset: noise spectra of a ZBD in the 2 Hz -100 kHz range measured at zero bias and for two dc current bias values.

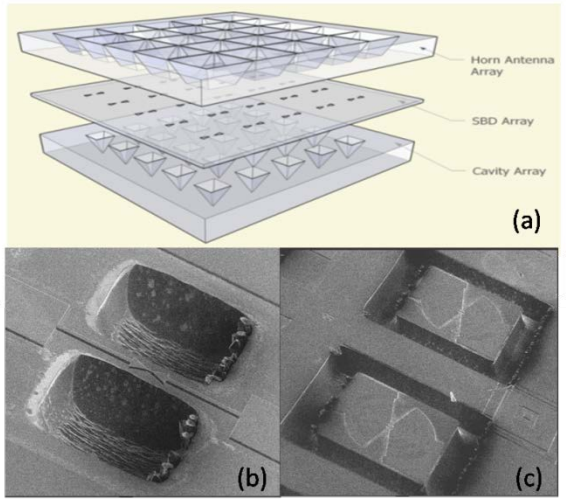

FIG. 4. (a) Pyramidal horn antenna and cavity array realized on Silicon wafer. Array pixel realized with (b) suspended bridge and (c) trench structure.

Photopolymerizable glasses for holographic technologies: performances and challenges

Maria L. Calvo
Department of Optics, Faculty of Physics, Complutense University of Madrid (UCM), 28040 Madrid, Spain
e-mail: mlcalvo@fis.ucm.es

In the material science research field, there is still an open developing area dedicated to the photomaterials. There is a requirement for the designing, synthesis, characterization and development of recording materials exhibiting high dynamic range, high photosensitivity, and excellent optical quality. Moreover, other necessary properties such a slow scattering, thermal stability, low laser damage threshold, low aging factor and dimensional stability may fulfil the main requirements for a wide range of applications. Indeed, this is a challenging achievement to be applied for the purpose of the progress in holographic technologies.
The fulfilment of these requirements shown by photopolymerizable materials has generated an important focus of attention on this family of holographic composites. As a result of the investigation in these materials, the Interdisciplinary Group for Optical Computing (GICO- UCM) has developed in the last decade a new generation of photomaterials [1-2].
The so named photopolymerizable glasses developed withsol-gel techniques were first introduced in 1996 by Cheben et al.[3]. The high performances of this new generation of photomaterials define promising applications for the purpose of holographic and photonic devices. However, some challenges are still open and need to be afforded to assure the expected fulfillment.
We present a critical review of the most significant achievement sand future developments.

REFERENCES

[1]P.Cheben,M.L.Calvo,Appl.Phys.Lett.**78**,1490(2001).

[2]F.DelMonte,O.Martínez-Matos,J.A.Rodrigo,M.L.Calvo,P.Cheben,Adv.Mater.**18**,2014(2006).

[3]P.Cheben,T.Belenguer,A.Nuñez,F. delMonte,D.Levy,Opt.Lett.**22**,1857(1996).

NOTES

Design of High-Performance Lasers and Amplifiers Exploiting Rare Earth Doped Glasses

Marco De Sario, Annalisa Di Tommaso, Pietro Bia, Luciano Mescia, Francesco Prudenzano.

DEE- Dipartimento di Elettrotecnica ed Elettronica, Politecnico di Bari, Via Orabona, 4, 70125 Bari
Phone: +39 080 5963781, e-mail: prudenzano@poliba.it

ABSTRACT
The paper briefly illustrates a few results obtained by simulating lasers and amplifiers based on rare earth doped glasses. Three kinds/configurations of optical couplers have been optimized and compared to highlight the different design strategies which can be followed to enhance the pump absorption in the rare earth doped core of microstructured fiber lasers, by employing suitable cascade of multiple long-period gratings (MLPGs) inscribed in the fiber core region. Moreover, the design of novel chalcogenide glass amplifier, in microsphere configuration, allowing Mid-IR emission, is reported.

Keywords: modelling, laser, grating, microsphere, optical characterization.

1. INTRODUCTION

Fiber lasers enable the construction of compact optical sources, minimizing the cooling system requirements. Their output signal exhibits high beam quality even at high powers and permits the application of the beam combining technique for high energy exploitations. The design flexibility allowed by microstructured optical fibers (MOFs) has accelerated the development of novel fiber lasers, exhibiting ever increasing performance, e.g. in terms of beam quality, peak power, slope efficiency. The employment of suitable long period grating, accurately designed, can further enhance the laser characteristics.Long period gratings (LPGs) have been exploited in many intriguing applications, e.g. filters, gain flatteners, dispersion compensators, sensors, etc. They can be inscribed not only in conventional fibers but even in MOFs [1-10].

LPGs for enhancement of pump absorption in rare earth doped MOF were investigated by the authors in [11-13]. These investigations were focused to obtain efficient high power lasers by minimizing the nonlinear effects and thermal load.

A completely different approach is required if low threshold lasers are needed. Optical processes in microcavities constitute a very interesting and alternative research area with feasible applications in optical sensing, distributed lasing, low threshold lasers. In particular, microspheres attract much interest for the strong confinement of the light into high-refractive-index contrast structures. They allow the construction of compact optical light sources, wavelength filters, optical add-drop devices, optical switches. Also in this case an accurate design, of both the microsphere and the coupled waveguide, can strongly enhance the device behavior.

The paper illustrates the main simulation results obtained in both cases: i) the design of multiple long period gratings to enhance the pump coupling in MOF lasers, ii) the design of Er^{3+} doped chalcogenide microsphere for Mid-IR amplification.

2. DESIGN OF MLPG COUPLERS

Intriguing optical couplers have been designed to enhance the performance of an ytterbium doped, double cladding (DC), microstructured optical fiber (MOF) laser. These couplers are obtained via a cascade of multiple long-period gratings (MLPGs) inscribed in the fiber core region. More precisely, the characteristics of the MLPG couplers have been simulated via an home-made computer code based on both rate equations (RE) and an extended coupled mode theory (CMT).

The designed MPLGs enable the interaction, at the pump wavelength, among the fundamental mode guided in the fiber core (HE_{11}) and the inner cladding modes. The following kinds of couplers have been investigated: a) MLPGs-P, Multiple Long Period Gratings in Passive fibers, i.e. grating cascades inscribed in the undoped region, just outside the laser cavity, b) MLPGs-A, Multiple Long Period Gratings in Active fibers, obtained by a grating cascades inscribed within the laser cavity; c) DS-MLPGs, Double Stage Multiple Long Period Gratings, obtained by a combination of passive grating cascades, inscribed outside the laser cavity, and active ones, inscribed within the laser cavity.The pump and signal wavelengths are λ_p= 976 nm and λ_s =1060 nm, respectively. The MOF optical and geometrical parameters are reported in [11-13]. Other parameters are the ytterbium ion concentration $N_{Yb}=5\times10^{25}$ ions/m^3, the input mirror reflectivity R_1= 0.99,the output mirror reflectivity R_2=0.06,the core refractive index n_c and the cladding refractive n_{cl} at the pump λ_p and signal λ_s wavelengths, $n_c(\lambda_p)$= 1.45172, $n_c(\lambda_s)$= 1.45067, $n_{cl}(\lambda_p)$= 1.45072, $n_{cl}(\lambda_s)$= 1.44967.

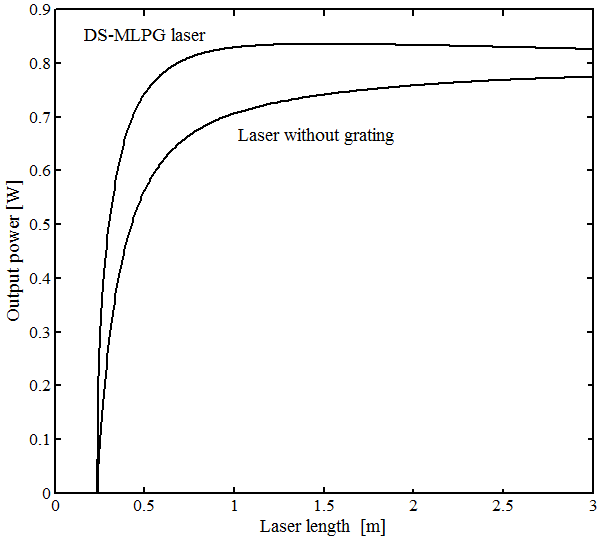

Figure 1. Comparison between the MOF laser without the coupler and with theDS-MLPGs

The pump power considered in the simulations is P_p = 1 W. The three kinds of couplers have been optimized from the point of the grating lengths and periods [11-13]. The couplers have been optimized by following the design strategy as in [11-13].

The simulations indicate that, MLPGs-P cascade before the laser is the most efficient coupler. MLPGs-A inscribed entirely within the laser cavity allows a gradual pump absorption and a minimization of nonlinear effects. Figure 1. illustrates the comparison between the MOF laser without the coupler and with theDS-MLPGs one. The DS-MLPGs coupler exhibits an intermediate behavior between MLPGs-P and MLPGs-A, it allows the simultaneous enhancement of pump absorption by Yb^{3+} ions and the coupling of the cladding modes with the fundamental one at the pump wavelength. These interactions, permit to avoid the deleterious steep increasing of the pump power into the core which could induce strong local heating at the input cavity section. A proper design allows the increasing of the MOF laser output power up to 20 %.

3. DESIGN OF CHALCOGENIDE MICROSPHERES

An optical amplifier constituted by a tapered fibre and an Er^{3+}-doped chalcogenide microsphere has been investigated/designed via an ad-hoc developed 3D numerical model based on CMT and solving the rate equations. The electromagnetic analysis of the microsphere has been performed by finding the solution of the scalar Helmholtz equation in spherical coordinates. By imposing the continuity of the tangential components of electric and magnetic fields at the sphere boundary the characteristic equation is written [14]:

$$\left(\eta_s \alpha_s + \frac{l}{R_0}\right) j_l\left(kn_s R_0\right) = kn_s\, j_{l+1}\left(kn_s R_0\right) \tag{1}$$

where

$$\begin{aligned} \eta_s &= \begin{cases} 1 & \text{TE mode} \\ \dfrac{n_s^2}{n_0^2} & \text{TM mode} \end{cases} \\ \alpha_s &= \sqrt{\beta_l^2 - k^2 n_0^2} \\ \beta_l &= \frac{\sqrt{l(l+1)}}{R_0} \end{aligned} \tag{2}$$

R_0 is the sphere radius, $k=2\pi/\lambda$is the wave number, β_l is the l-th order propagation constant, α_s is the constant describing the evanescent field decay from the microsphere along the radial direction, n_0 is the background refractive index of the medium,n_s is the microsphere refractive index of the medium J_l is the spherical Bessel function of the l-th order.

The main transitions among the erbium energy levels, the amplified spontaneous emission and most important secondary transitions pertaining to the ion–ion interactions have been considered. The taper angle of the optical fiber and the fiber-microsphere gap have been designed to efficiently couple both pump and signal beams and to improve their overlapping with the rare earth doped region.

The feasibility of a microsphere amplifiers of $Ga_5Ge_{20}Sb_{10}S_{65}$ chalcogenide glass has been investigated for operation in the mid-IR wavelength range. In order to perform a realistic design, the simulations have been carried out by taking into account the actual refractive index wavelength dispersion and the actual spectroscopic parameters pertaining to erbium ions [15]. Due to the dense optical spectrum of WGMs, quite small microspheres have been considered. The pump wavelength is λ_p=0.98 μm and the signal one is λ_s=2.7 μm. The device performance has been simulated by changing the fiber-microsphere gap, the thickness of erbium doped region, the fiber taper angle, the erbium concentration and operative parameters such as pump and signal power.

The undoped microspherewith radius R=25 μm is coupled with the tapered fiber. Different values of *g* have been chosen to obtain the critical coupling condition at both wavelengths. The fibre taper has been designed in order to allow the fundamental mode propagation. The considered waist radius and tapered angle are a_0=700 nm and δ=0.03 rad, respectively.

Fig. 2 illustrates the signal transmittance versus the signal power for different erbium concentration N_{Er}=0.1. 0.3, 0.5 [w%] and for the pump power P_p=100 mW, g=560 nm, thickness of doped region S = 3μm. Signal amplification can be obtained for input pump powers higher than 80 mW, and in the small signal operation maximum optical gain of about 7-8 dB has been calculated.

The performed simulations indicate that the proposed Er^{3+}-doped microspheres could be good candidates for an efficient frequency-selective amplification system, to be employed for compensating signal attenuation and for obtaining compact integration of the active optical devices. The simulation results highlight that this scheme could be useful to develop high efficiency and compact Mid-IR amplifiers.

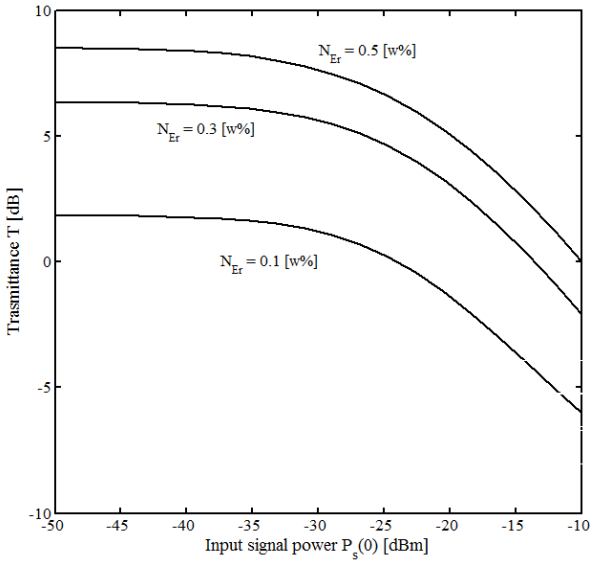

Figure 2. Transmittance versus the signal power for different erbium concentration

4. CONCLUSIONS

The main modelling results pertaining to two different cases, high power laser and low threshold one, are briefly reported. In the former case, three kinds of multiple long-period grating MLPGs couplers have been designed to enhance the high power MOF laser. MLPGs-P is the most efficient coupler, MLPGs-A allows a gradual pump absorption and is suitable for minimizing of nonlinear effects. The DS-MLPGs coupler exhibits an intermediate behaviour. These couplers allow an improvement of the laser performance or a strong reduction of the laser fiber length to parity of output power while to length parity, MLPGs allow to increase the MOF laser output power up to 20 %. Moreover, an Er^{3+}-doped chalcogenide microsphere amplifier evanescently coupled with a tapered optical fiber has been designed. The device performance has been investigated by changing the fiber-microsphere gap, thickness of erbium doped region, fiber taper angle, erbium concentration and operative parameters such as pump and signal power. In the small signal operation maximum optical gain of about 7 dB has been calculated. This indicates that the proposed Er^{3+}-doped microspheres could become good candidate devices to compensate signal attenuation in compact integration of complex optical systems.

ACKNOWLEDGEMENTS

The work has been partially developed within the COST ACTION MP0702.

REFERENCES

1. J.S. Petrovic, H. Dobb, V.K. Mezentsev, K. Kalli, D.J. Webb, I. Bennion, "Sensitivity of LPGs in PCFs Fabricated by an Electric Arc to Temperature, Strain, and External Refractive Index," *J. Lightwave Technol.* 25, pp. 1306-1312, 2007.
2. C.L. Zhao, L. Xiao, J. Ju, M. S. Demokan, W. Jin, "Strain and Temperature Characteristics of a Long-Period Grating Written in a Photonic Crystal Fiber and Its Application as a Temperature-Insensitive Strain Sensor," *J. Lightwave Technol.* 26, pp. 220-227, 2008.
3. B.J. Eggleton, P.S. Westbrook, R.S. Windeler, S. Spalter, T.A. Strasser, "Grating resonances in air-silica microstructured optical fibers," *Opt. Lett.* 24, pp. 1460-1462, 1999.
4. T. Erdogan, "Cladding-mode resonances in short-and long-period fiber grating filters," J. Opt. Soc. Am. A 14, pp. 1760-1773, 1997.
5. L. Mescia, "Design of long-period gratings in cladding-pumped microstructured optical fiber," *J. Opt. Soc. Am. B* 25, pp. 1883-1839, 2008.
6. G. Calò, A. D'orazio, M. De Sario, L. Mescia, V. Petruzzelli, L. Allegretti, T. Palmisano, F. Prudenzano, "Improvement of the pump power coupling in double cladding photonic crystal fiber," *IEEE/LEOS Winter Topical Meeting Series*, pp. 146-147, 2008.
7. S. Baek, S. Roh, Y. Jeong, B. Lee, "Experimental demonstration of enhancing pump absorption rate in cladding-pumped ytterbium-doped fiber laser using pump-coupling long-period gratings," *IEEE Photon. Technol. Lett.* 18, pp. 700-702, 2006.
8. T. Allsop, K. Kalli, K. Zhou, G. Smith, Y. Laia, G. Smith, M. Dubov, D. Webb, I. Bennion, "Long period gratings written into a photonic crystal fibre by a femtosecond laser as directional bend sensors," *Opt. Commun.* 281, pp. 5092–5096, 2008.
9. J. Long, W. Zhi, L. Yange, K. Guiyun, D. Xiaoyi, "Ultraviolet-inscribed long period gratings in all-solid photonic bandgap fibers," *Opt. Express*, 16, pp. 21119- 21131, 2008.
10. L. Shujing, J. Long, J. Wei, W. Dongning, L. Changrui, W. Ying, "Structural long period gratings made by drilling micro-holes in photonic crystal fibers with a femtosecond infrared laser," *Opt. Express*, 18, pp. 5496-5503, 2010.
11. L. Mescia, "Design of long-period gratings in cladding-pumped microstructured optical fiber," *J. Opt. Soc. Am. B* 25, pp. 1883-1839, 2008.
12. G. Calò, A. D'orazio, M. De Sario, L. Mescia, V. Petruzzelli, L. Allegretti, T. Palmisano, F. Prudenzano, "Improvement of the pump power coupling in double cladding photonic crystal fiber," IEEE/LEOS Winter Topical Meeting Series, pp. 146-147, 2008.
13. L.Mescia, T. Palmisano, M. Surico, F. Prudenzano, "Long-period gratings for the optimization of cladding-pumped microstructured optical fiber laser," *Opt. Materials*33, 2 pp. 36–240, 2010.
14. M. L. Gorodetsky, V. S. Ilchenko: Optical microsphere resonators: optimal coupling to high-Q whispering-gallery modes. *J. Opt. Soc. Am. B* vol. 16, pp. 147-154, 1999.
15. F. Prudenzano, L. Mescia, L. Allegretti, V. Moizan, V. Nazabal, F. Smektala: Theoretical study of cascade laser in erbium-doped chalcogenide glass fibers. *Opt. Mat.* vol. 33, pp. 241–245, 2010.

Novel Cross-Relaxation Energy Transfer Calculation Applied on Thulium Highly-Doped Tellurite Glasses

M. Taher[1], H. Gebavi[1], M. Zannin[1], S. Taccheo[1], D. Milanese[2], and Rolindes Balda[3,4]
[1]*College of Engineering, SwanseaUniversity, Singleton Park, SA2 8PP, Swansea, UK*
[2] *PhotonLab - Dipartimento di Scienza dei Materiali ed Ingegneria Chimica, Politecnico di Torino, Torino, Italy*
[3]*Departamento de Fisica Aplicada I, Escuela Superior de Ingenieria, Universidad del Pais Vasco UPV/EHU, Alda. Urquijo s/n 48013 Bilbao, Spain*
[4]*Materials Physics Center CSIC-UPV/EHU and Donostia International Physics Center, 20018 San Sebastian, Spain*
Tel: +44(0)1792602465; e-mail: m.a.taher@swansea.ac.uk

ABSTRACT
In this paper we investigate the cross relaxation parameter of Tm3+ ions in tellurite glasses over a wide range of concentrations: from 0.36 mol% up to 10 mol%. We propose a new measurement approach based on monitoring the steady-state emission spectra. The proposed method is very simple and allows to measure even very highly doped samples. The cross-relaxation parameter shows a linear dependence with respect to dopant concentration over the full investigated interval and the measured slope is 1.81×10^{-17} cm^3 s^{-1} $mol\%^{-1}$. The linear dependence suggests a dipole-dipole interaction.

Keywords: Rare-earth, Cross-relaxation, fibre laser, Thulium, laser modelling

1. INTRODUCTION

Thulium laser is an excellent candidate for infrared domain applications thanks to its broad emission spectrum at around 1.8 micron [1]. This makes this kind of laser very appealing for several application ranging from precise cut and ablation of biological tissues to LIDAR and sensing applications [2-5]. A further advantage relies on pumping process where cross-relaxation mechanism produce two exited Tm ions out of one pump photon absorbed [6]. For this reason the knowledge of cross-relaxation mechanism is of the outmost importance to properly model and design the laser. So far several methods have been proposed to measure the cross-relaxation parameter, usually based on lifetime measurements [7,8] but also on numerical fitting of fluorescence dynamic versus pump power [9]. In all cases was not possible to define the value of cross-relaxation parameter over a wide range of Tm concentration due to the fact that for very high doping level the pump level is strongly quenched by cross-relaxation and fast detectors are needed. In this paper we investigate the cross-relaxation parameter over a wide range of the doping level up to 10 mol%. To overcome limitation of previous measurement methods we suggests a new method to calculate the cross-relaxation parameters based on steady-state fluorescence measurement. The investigation was done using a set of sample of Tm-doped tellurite glasses. The choice of this glass host was based on the facts they have the lowest phonon energies (~ 750 cm-1) of all oxides glasses, which lead to increase in optical efficiency and decrease in probability of non-radiative multiphonon decay as well as an excellent rare earth ions solubility comparing with silicate and germinate glasses. The above advantages explains why Tm-doped tellurite glass fibre lasers are of a great interest [10-12].

2. THEORETICAL MODELLING

Tm has a quite complex system of energy levels [9] but we can consider empty the $^3H_5$ level due to non radiative fast relaxation to $^3F_4$ without losing in model accuracy. The corresponding rate-equation system used to analyze our experimental data is:

$$\frac{dN_0}{dt} = -W_{03}N_0 + \frac{N_3}{\tau_{30}} + \frac{N_1}{\tau_1} - C_R N_3 N_0 \quad (1)$$

$$\frac{dN_1}{dt} = \frac{N_3}{\tau_{31}} - \frac{N_1}{\tau_1} + 2C_R N_3 N_0 \quad (2)$$

$$\frac{dN_3}{dt} = W_{03}N_0 - \frac{N_3}{\tau_{30}} - \frac{N_3}{\tau_{31}} - C_R N_3 N_0 \quad (3)$$

where N_0, N_1, and N_3 are the populations of Tm^{3+} ions in the $^3H_6$, $^3F_4$, and $^3H_4$ levels respectively, W_{03} is the pump rate (s^{-1}) and C_R the cross relaxation parameter, τ_{xy} is the lifetime of the x to y transition and τ_x is the lifetime of level x. Note that $\tau_3=(\tau_{31}^{-1}+\tau_{30}^{-1})^{-1}$. The C_R parameter is a function of the Tm doping level. At steady state the time derivatives in the rate equations are equal to zero. Considering the conservation law of Tm^{3+} ions populations, we can also write $N_t = N_0 + N_1 + N_3$. The methods based on fluorescence lifetime measurements [7,8] uses equation 3 and calculate the cross-relaxation parameter from level 3 lifetime quenching. However lifetime values falls below 1 μm for highly-doped samples and measurements of low level signals is difficult. To overcome the limitation of previous methods we propose to investigate the steady-state emission from $^3H_4$ and the $^3F_4$ levels. In steady-state condition from Eq. 2 follows:

$$C_R = \frac{1}{2N_0}\left[-\frac{1}{\tau_{31}}+\frac{N_1}{N_3\tau_1}\right] \tag{4}$$

The ratio between the population of level 1 and 3 can be rearranged by using the Fuchtbauer-Landenburg rule [13] and the relationship that provides the amount of the spontaneous emission [14]. A final form was found:

$$C_R = \frac{1}{2N_0\,\tau_{31}}\left[kR-1\right] \tag{5}$$

where R is the ratio of the emission spectra from and 'k' contains all other experimental constant. In our case k value was 1.33.

3. RESULTS

All samples hadthe same host composition $75TeO_2$-$20ZnO$-$5Na_2O$ (mol%), labeled as TZN, and were doped with Tm^{3+} concentrations ranging from 0.36 mol% to 10 mol% [15,16]. We measured all relevant lifetime parameters by investigation the lowest doping level samples. To calculate the ratio *R* we excited Tm samples at the wavelength of 785 nm and we observed the emission from the two transition bands centered at 1.47 and 1.8 μm, which corresponding to $^3H_4 \rightarrow {}^3F_4$ and $^3F_4 \rightarrow {}^3H_6$ respectively. Results are shown in Fig. 1 where we normalized all curves to the peak of $^3H_4 \rightarrow {}^3F_4$ transition at 1.47 μm.

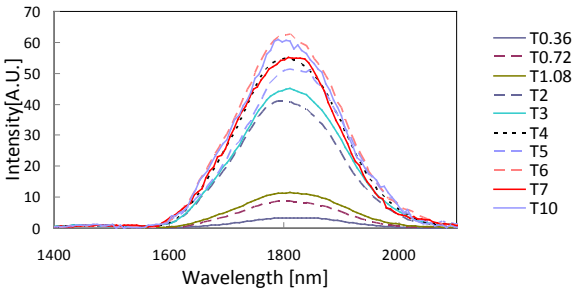

Figure 1.Emission spectra, inset magnifies the of $^3H_4 \rightarrow {}^3F_4$ transition at 1.47 μm.

Figure 2 shows the cross-relaxation parameter values calculated by using Eq. 5. We can note a quite clear linear increase even for highest doped samples where, however the slope is slightly reduced.

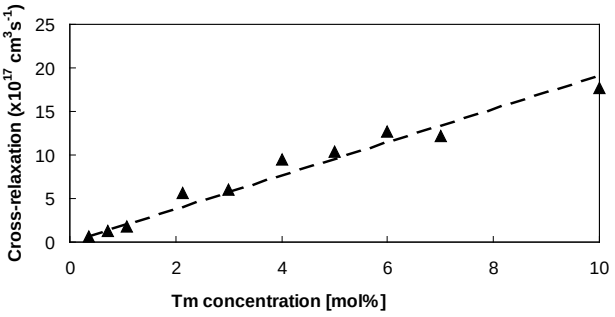

Figure 2. Cross-relaxation parameter versus Tm concentration.

From the experimental data the fitted C_R is $1.81x10^{-17}$ cm^3 s^{-1} $\%mol^{-1}$ is obtained. While this value is below the one previously reported in TZN glass [9] it is consisted with the one used for silica fiber modeling [17]. The observed linear dependence on concentration of the cross-relaxation parameter can be explained with the behavior of the concentration quenching of the lifetimes, as predicted by Auzel in the framework of dipole-dipole interaction processes [18]. We believe that the data here reported will be useful to model and design laser in TZN glasses. This measurement method can be easily extended to other type of glasses.

4. CONCLUSIONS

A new and simple approach based on the emission spectra measurements was developed to investigate cross-relaxation parameter in Tm-doped samples with very high doping levels. Thanks to this new method we were able to experimentally calculate the cross relaxation parameter of Tm3+ ions in tellurite glasses over a wide range of concentrations. This approach demonstrated to be very sensitive and can be used to investigate other kind of Tm-doped glasses. The obtained values of cross-relaxation show a linear dependence with dopant concentration and value of the linear fit slope was $1.81x10^{-17}$ cm^{-3} s^{-1} $\%mol^{-1}$. The knowledge of this value allows a proper modelling of Tm-doped tellurite glass laser by properly comparing the impact of different doping level.

ACKNOWLEDGEMENTS

We acknowledge the support by FP7 LIFT project (Leadership in Fiber Technology, Grant #228587), and the collaboration within COST Action MP0702. R. Balda acknowledges financial support from the Spanish Government under project MAT2009-14282-C02-02.

REFERENCES

1. D. C. Hanna, I. M. Jauncey, R. M. Percival, I. R. Perry, R. G. Smart, P. J. Suni, J. E. Townsend, and A. C. Tropper, "Continuous-wave oscillation of a monomode thulium-doped fibre laser," Electron. Lett. 24, 1222-1223 (1988).
2. S. D. Jackson and A. Lauto, "Diode-pumped fiber lasers: A new clinical tool," Lasers in Surgery and Medicine 30, 184-190 (2002).
3. J. Y. Allain, M. Monerie, and H. Poignant, "Tunable CW lasing around 0.82, 1.48, 1.88 and 2.35 μm in thulium-doped fluorozirconate fibre," Electron. Lett. 25, 1660-1662 (1989).
4. E. R. M. Taylor, L. N. Ng, J. Nilsson, R. Caponi, A. Pagano, M. Potenza, and B. Sordo, "Thulium-doped tellurite fiber amplifier," IEEE Photon.Technol. Lett. 16, 777-779 (2004).
5. M. Yamane and Y. Asahara, "*Glasses for photonics*" (Cambridge: Cambridge University Press, 2004).
6. W. Jianfeng, J. Shibin, L. Tao, G. Jihong, N. Peyghambarian, and N. P. Barnes, "Efficient thulium-doped 2 μm germanate fiber laser," IEEE Photon.Technol. Lett. 18, 334-336 (2006).
7. A. S. S. de Camargo, S. L. de Oliveira, D. F. de Sousa, L. A. O. Nunes, and D. W. Hewak, "Spectroscopic properties and energy transfer parameters of Tm^{3+} ions in gallium lanthanum sulfide glass," J. Phys.: Condens. Matter 14, 9495-9505 (2002).
8. R. R. Petrin, M. G. Jani, R. C. Powell, and M. Kokta, "Spectral dynamics of laser pumped $Y_3Al_5O_{12}$: Tm: Ho lasers," Opt. Mater. 1, 111–124 (1992).
9. C. A. Evans, Z. Ikonic´, B. Richards, P. Harrison and A. Jha, "Theoretical Modeling of a 2 μm Tm^{3+} Doped Tellurite Fiber Laser: The Influence of Cross Relaxation," J. Lightwave Technol. 27, 4026-4032 (2009).
10. J. Wu, S. Jiang, T. Luo, J. Geng, N. Peyghambarian, and N. P. Barnes, "Efficient thulium-doped 2-μm germanate fiber laser," IEEE Photon.Technol. Lett. 18, 334–336 (2006).
11. Q. Huang, Q. Wang, J. Chang, X. Zhang, Z. Liu, and G. Yu, "Optical parameters and upconversion fluorescence in Tm^{3+}/Yb^{3+} co-doped tellurite glass," Laser Physics 20, 865-870 (2010).
12. B. Richards, Y. Tsang, D. Binks, J. Lousteau, and A. Jha, "Efficient 2 μm doped tellurite fiber laser," Opt. Lett. 33, 402–404 (2008).
13. C. R. Giles, C. A. Burrus, D. DiGiovanni, N. K. Dutta, and G. Raybon, "Characterization of erbium-doped fibers and application to modeling 980-nm and 1480-nm pumped amplifiers," IEEE Photon. Technol. Lett. 3, 363 - 365 (1991).
14. C. R. Giles and E. Desurvire, "Propagation of signal and noise in concatenated erbium-doped fiber optical amplifiers," J. Lightwave Technol. 9, 147 - 154 (1991).
15. H. Gebavi, D Milanese, R Balda, S Chaussedent, M Ferrari, J Fernandez, and M Ferraris, "Spectroscopy and optical characterization of thulium doped TZN glasses," J. of Appl. Phys. 43, 135104-135111 (2010).

16. H. Gebavi, D. Milanese, G. Liao, Q. Chen, M. Ferraris, M. Ivand, O. Gamulin, and S. Taccheo, “Spectroscopic investigation and optical characterization of novel highly thulium doped tellurite glasses,” J. of Non Cryst. Solids 355, 548-555 (2009)
17. S. D. Jackson and T. A. King, “Theoretical Modeling of Tm-Doped Silica Fiber Lasers,” J. Lightwave Technol. 17, 948-954 (1999).
18. F. Auzel, G. Baldacchini, L. Laversenne, and G. Boulon, “Radiation trapping and self-quenching analysis in Yb3+, Er3+, and Ho3+ doped Y2O3,” Opt. Mater. 24, 103-109 (2003).

Effect of oxygen content in gas mixtures on luminescence of ZrO2 doped up to 8 mol % with Eu^{3+} ions

Witold Łojkowski[1], Anna Świderska- Środa[1], Agnieszka Opalińska[1], Krzysztof Gałązka[1], Donats Millers[2], Larisa Grigorieva[2], KrisjanisSmits[2], Aharon Gedanken[3], Irena Grigorianis[3], Cristina Leonelli[4]

[1] Institute of High Pressure Physics, PAS, Sokolowska 29/37,01-142 Warsaw, Poland
Tel: +48228880006; e-mail: wl@unipress.waw.pl
[2] Institute of Solid State Physics, Riga University,8 Kengaraga street, Riga, LV-1063, Latvia
[3]Department of Chemistry, Bar-Ilan University, Ramat-Gan 52900, Israel
[4]Dipartimento di Ingegneria dei Materiali e dell'Ambiente, Facolta' di Ingegneria, Universita' degli Studi di Modena e Reggio Emilia, Via Vignolese 905/A, 41100 Modena, Italy

ABSTRACT
We report the results of research carried out by the present international consortium within the OXYNANOSEN project funded under the European ERANET-Matera programme. The main result is demonstration of the effect of oxygen content in gas mixtures on luminescence of nanocrystalline zirconia doped up to 8 mol.% with Eu^{3+} ions. The effect is stable and reproducible in terms of the correlation between oxygen content and luminescence of the nanocrystalline material. The effect of excitation light energy, phase composition of nano-zirconia, testing time, and influence of auxiliary gasses (Argon, CO_2, water vapour) on luminescence will be presented. A plausible mechanism of the effect will be discussed, as well as application of the material in oxygen sensors.

Keywords: zirconia nanoparticles, Europium doping, luminescence, oxygen, sensor

1. INTRODUCTION

Measurements of the oxygen amount is important in such applications as exhaust gases of car engines, control of technological processes, control of the oxygen level in glasshouses, optimization of combustion processes, in-metallurgy and other. Well known are sensors based on a change of electrical conductivity of zirconia contacting gas atmosphere with variable oxygen content (lambda sensor). They request electrical contacts to be connected with the material, and itself being heated to temperatures permitting active ionic conductivity, i.e., several hundred K. There are optical oxygen sensors based on luminescence changes in dye-containing membranes, such as a porphyrin dye, embedded in a polymeric membrane or quantum dots. However optical luminescence oxygen sensors based on inorganic materials were not, to the best authors knowledge, known [1]. However, an optical oxygen sensor based on inorganic sensor material would offer several advantages, such as simplicity of construction, avoiding electrical connections and contacts, and wide range of operating temperatures and chemical stability. In the paper we review the results of investigations of zirconia nanoparticles doped with europium ions as sensor material. The research was carried out by the present international consortium and was funded by ERANET – Matera program within the OXYNANOSEN project.

2. RESULTS

Fig.1. shows the luminescence dependence on oxygen content in the atmosphere surrounding the sample in oxygen nitrogen atmosphere. The luminescent material is nanocrystalline zirconia doped with 8 mol% of Eu^{3+} ions. The effect was obsereved in the temperature range 20-350^{o}C The amplitude of the effect decreases with decreasing specific surface of the material, which occurs when the powder is annealed and the grain size increases from 10 to 100 nm. It increases also with increasing Eu content from 0.5 to about 5 mol.%. The effect of adding CO_2 causes only weak changes in the observed effects, contrary to the effect of water vapours, which cause luminescence quenching. Theoretical considerations and experimental data [2] lead to the conclusion, that the observed luminescence intensity decrease as the oxygen content increase is connected with change of surrounding of Eu ions. A decrease of symmetry when an oxygen ion is missing in the Eu atomic neighbourhood leads to increased probability of optical transitions between the excited Eu electronic levels. The effect is characteristic for a nanocrystalline material, where the contribution of Eu ions situated in the surface layers, where oxygen content can change even at room temperature, to luminescence is measurable and substantial.

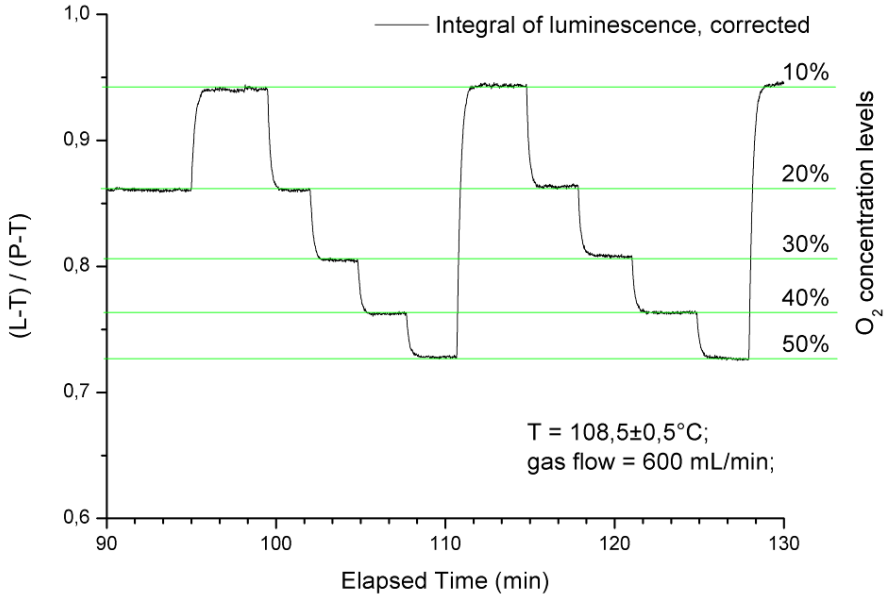

Fig. 1. Effect of O_2 content in nitrogen atmosphere on the luminescence signal. Excitation with LED light at 250 nm. Luminescence L-T is the integral of the luminescence spectrum from 600 to 700 nm with subtracted background. P-T is the integrated background level.

3. CONCLUSIONS

Eu^{3*} ions doped nano crystalline zirconia is a prospective material for an optical oxygen sensor operating in the temperature range up to 350^{o}C

ACKNOWLEDGEMENTS

The work was supported by ERANET-MATERA within the OXYNANOSEN project. The Authors are grateful to Piotr Nyga for luminescence measurements, Ewa Grzanka for XRD investigations, Tomasz Plocinski for TEM investigations, Jaroslaw Kaszewski and Urszula Narkiewicz for XPS studies, Jan Mizeradzki and Adam Presz for SEM work.

REFERENCES

[1] W. Lojkowski,D. Millers,J. D. Fidelus,L. Grigorjeva,A. Opalinska,U. Narkiewicz,W. Strek, "Measurement of Oxygen Partial Pressure Based on Zirconium Dioxide Luminescence", Europ. Pat. EP 1920238 (2006).

[2] K. Smits, L. Grigorjeva, D. Millers, A. Sarakovskis, A. Opalinska, J. D. Fidelus, W. Lojkowski: Europium doped zirconia luminescence, Optical Materials 32 (2010) 827–831

Photoinduced Optical Manipulations with Azo-Polymers

D. Urbonas[1], L. Kucinskaite[1], R. Petruskevicius[1*], G. Navickaite[2], G. Seniutinas[2], R.Tomasiunas[2], V.Getautis[3]

[1]*Center for Physical Sciences and Technology, Savanoriu ave. 231, LT-02300 Vilnius, Lithuania*

[2]*Institute of Applied Research, Vilnius University, Sauletekio ave. 10, LT-10223 Vilnius, Lithuania*

[3]*Kaunas University of Technology, Radvilenu pl. 19, LT-50270 Kaunas, Lithuania*

**e-mail: raimisp@ktl.mii.lt*

ABSTRACT

Models based on kinetic equations and beam propagation method are proposed for simulation of the all-optical poling. These models take into account the overall balance of molecules in cis - trans states and spatial the distribution of induced second order nonlinearities in azo-polymers. We demonstratethatrelaxationkinetics of all-opticalpolingcanbe characterized byshort – and long – time relaxation. The long time relaxationisfullydescribed by orientational diffusioncoefficientof transisomer. The short timerelaxationdepends on the conditions ofmicro-texturegratingwritingand is mainlycaused by the relaxation of cisisomer and parameters for the reorientation probabilities.We find out that the spatial localization and depletion of photo induced second order nonlinearities can be achieved for the all-optical poling by the focused 3D polychromatic Gaussian beams.

Keywords: all-optical poling, azo-polymers, azophenylcarbazole, relaxation kinetics, spatial localization, beam propagation method

1. INTRODUCTION

Photoinduced optical manipulation by optical poling of azo-dye polymers is carried out by inducing the second order nonlinearities by means of polychromatic interference of first and second harmonic waves [1]. The optical poling of azo-dyes in the polymer matrix is going through so-called reorientational hole burning and molecular reorientation mechanisms. This is a complex mechanism consisting of three parts: photo excitation of azo-dye and isomerization of trans to cis state, cis state relaxation back to trans state and molecular thermal induced orientational diffusion [2, 3]. The orientation hole burning is followed by a reversible trans-cis-trans isomerization process, which drives optical orientation motion, finally leading to a net permanent molecular polar order. In contrast to the DC electric field poling, optical poling does not need to use electrodes or corona discharge. It can be carried out at room temperature and automatically produces quasi-phase-matched second order susceptibility micro-pattern for generation of the second harmonic.

In this paper, a theory based on phenomenological kinetic equations and 3D beam propagation method (BPM) are proposed for the all-optical poling. The obtained theoretical results qualitatively well coincide with experimental results on all-optical poling kinetics of azophenylcarbazole type azo-dyes in polycarbonate polymer matrix. In the BPM model of photo induced optical manipulation, two coupled Fresnel equations are used to describe first and second harmonic waves in 3D polymer layer with induced second order nonlinear micro-grating patternby all-optical poling. The BPM equations are solved by finite differences, using Crank-Nicholson difference schemes with ADI (alternating direction implicit) algorithm and transparent boundary condition (TBC) capable of handling wave propagation in the infinite space. The focused 3D polychromatic beams have been used. This model also takes into account optical poling specifics related to the orientational hole burning mechanisms. It was shown that it is possible to achieve spatial localization and depletion of photo induced second order susceptibility $\chi^{(2)}$.

2. MODELING OF KINETICS

The phenomenological kinetic equations for the all-optical poling model were proposed by J.-M. Nunzi [1], where only the trans state of azo-dye was taken into consideration in the optical poling process. Later, this model has been improved by including into the overall balance of kinetics the molecules in cis-state [2]. Our simulations are based on this more general model. We obtained infinite system of coupled differential equations for order parameters $T_j$andC_j, which define 1D all-optical poling model [4, 5]. This system was truncated to 10 equation system and solved for case of CW laser excitation. It is assumed that before poling process, all azo-dye molecules are in unexcited state (trans state) and oriented isotropically. The parameters necessary for modeling of optical poling are found out by fitting close to real parameters of materials used for optical poling experiments [4, 5]. The best fit obtained by theoretical modeling of the measured relaxation of induced second harmonic

generation in the "dark" regime is presented in the Fig.1 for azo phenylcarbazole V-628 dispersed in polycarbonate polymer matrix. Parameters are used for modeling: single photon excitation rate $4*10^{-5}$ s^{-1}, two photon excitation rate $2*10^{-3}$ s^{-1}, azo-dye orientational diffusion coefficient $4*10^{-5}$ s^{-1} and cis isomer relaxation time 167s.

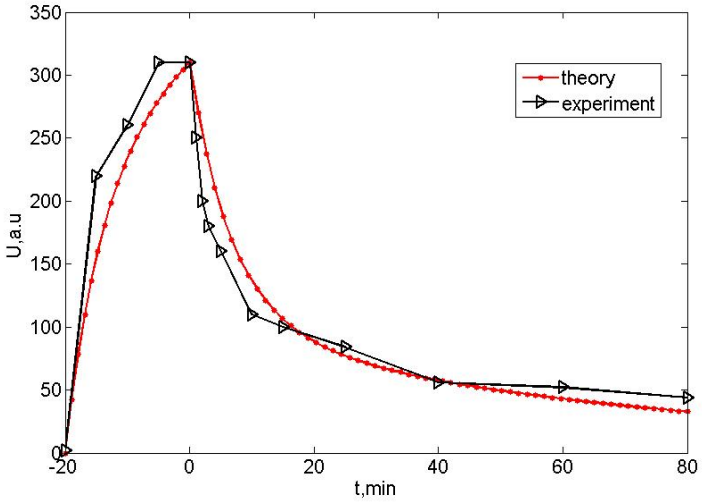

Figure 1. Amplitude of generated second harmonic in phenylcarbazole V-628 versus seeding and reading time in all-optical poling process. Curve with dots corresponds to theoretical modelling, triangles - to experimental results.

It is shownthattherelaxationkinetics of opticalpolingcanbe characterized byshort – and long – time relaxation. The long time relaxationisfullydescribed by diffusioncoefficientD_t forthe transisomer. The short timerelaxationdepends on the conditions ofmicro-texturegratingwritingand is mainlycaused by the relaxation ofthe cisisomer and parameters for reorientation probabilities.

3. SPATIALLY RESOLVED MODEL

The beam propagation method is an approximation technique for simulation of propagation of light in slowly varying optical waveguides. BPM has several key advantages. Besides its effectiveness, the BPM is a quick and easy method of solving for fields in integrated optical devices. It has also been extended to be applicable to analyze: polarization, nonlinearity, nonparaxiality, reflections and other physical phenomena.

Two coupled 3D Fresnel equations are used to describe first and second harmonic waves in polymer layer with second order susceptibility $\chi^{(2)}(x,y,z)$ micro-grating pattern:

$$2jk_0 n_{\omega 0}\frac{\partial E_\omega}{\partial z}=\frac{\partial^2 E_\omega}{\partial x^2}+\frac{\partial^2 E_\omega}{\partial y^2}+k_0^2\left(n_\omega^2(x,y,z)-n_{\omega 0}^2\right)E_\omega+k_0^2\chi^{(2)*}(x,y,z)E_{2\omega}E_\omega^* e^{-j\Delta\beta z} \quad (1)$$

$$4jk_0 n_{2\omega 0}\frac{\partial E_{2\omega}}{\partial z}=\frac{\partial^2 E_{2\omega}}{\partial x^2}+\frac{\partial^2 E_{2\omega}}{\partial y^2}+4k_0^2\left(n_{2\omega}^2(x,y,z)-n_{2\omega 0}^2\right)E_{2\omega}+k_0^2\chi^{(2)}(x,y,z)E_\omega E_\omega e^{j\Delta\beta z} \quad (2)$$

,

where $k_0=k_\omega=\frac{\omega}{c}$, $j=\sqrt{-1}$, $\Delta\beta=2k_0\left(n_{2\omega 0}-n_{\omega 0}\right)$ is phase matching mismatch (determines quasi phase matching(QPM) grating period), $n_{\omega 0}$ and $n_{2\omega 0}$ are the refractive indices of first and second harmonic waves. Induced second-order nonlinear susceptibility is described as follows:

$$\chi^{(2)}(x,y,z)=\chi_{eff}^{(2)}(x,y,z)\cos(\Delta\phi+\Delta kz)\exp\left(-\frac{\alpha_{2\omega}(x,y,z)}{2}z\right) \quad (3)$$

where $\Delta\phi = \phi_{2\omega} - 2\phi_{\omega}$ - phase difference between polychromatic beams, $\alpha_{2\omega}$ is the second harmonic absorption coefficient and induced effective nonlinear susceptibility:

$$\chi^{(2)}_{eff}(x, y, z) = \chi^{(3)}_{eff}(x, y, z)\,\mathrm{Re}(E^2_{\omega}E^*_{2\omega}) \quad (4)$$

and equation (4) means that generation of quasi static electric field is presented by rectification effect [6].

The above system ofequation (1) and (2) concern so called BPM model of electromagnetic optical poling. Equations are solved by finite difference BPM , using the Crank-Nicholson difference schemes with ADI (alternating direction implicit) algorithm. A transparent boundary condition (TBC) capable of handling wave propagation in the infinite space is incorporated in the finite difference algorithm.

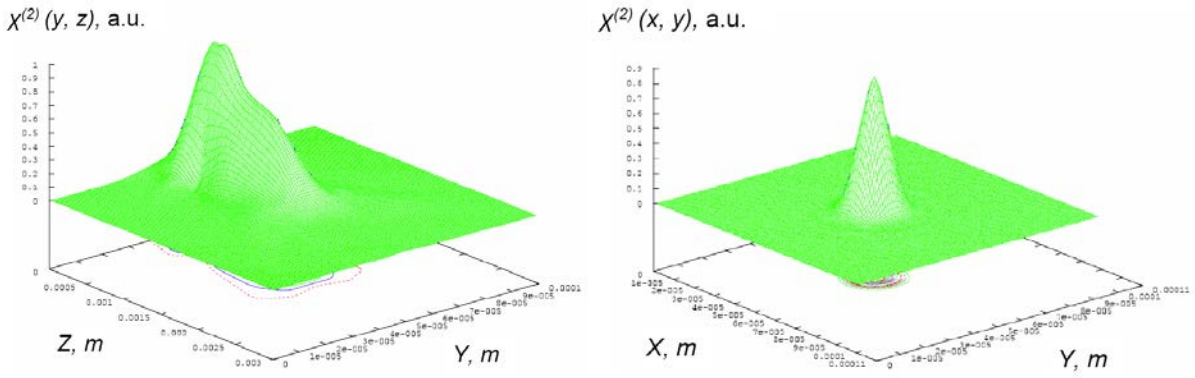

ZY plane *XY plane for z=0.7mm*

(a)

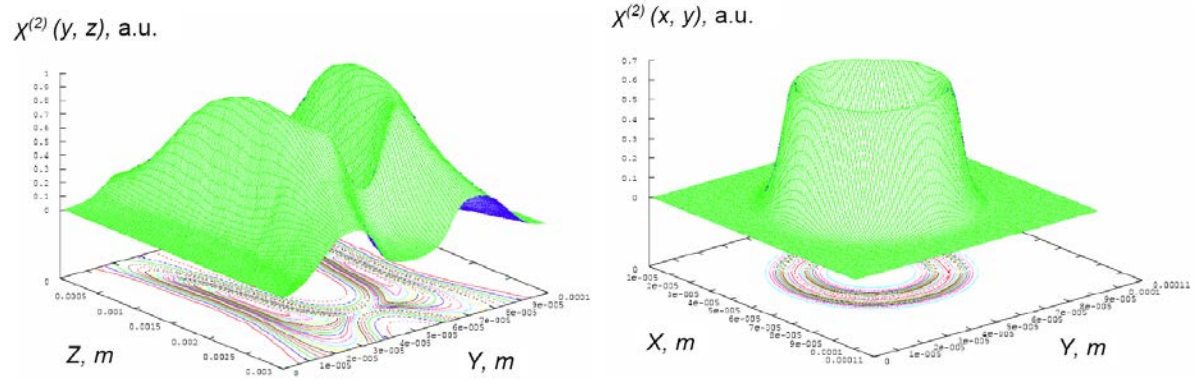

ZY plane *XY plane for z=0.7mm*

(b)

Figure 2. Distribution of induced $\chi^{(2)}$ by focused Gaussian beams in ZY and XY planes. (a) - spatial localization of induced $\chi^{(2)}$, (b) - spatial depletion of induced $\chi^{(2)}$.

3D optical poling results (induced $\chi^{(2)}$ distribution) by two focused polychromatic Gaussian beams are show in Fig. 2, where $\chi^{(3)} = 1.8 * 10^{-23} m^2/V^2$,with the spot size of beams of 20μm and the focus position of 1.33mm. As shown in Fig. 2a, we get localization effect of induced $\chi^{(2)}$. During this work 3D optical poling BPM model for focused polychromatic beams has been modified to take into account all-optical poling specifics related to the orientational hole burning mechanisms. Furthermore, it was shown, that it is possible now to achieve spatial depletion of induced $\chi^{(2)}$ (Fig. 2b).

4. CONCLUSIONS

The kinetic parameters for azophenylcarbazoles are extracted from experimental data using theoretical model. It is shown that large dye molecules have highest poling efficiency and less branched dye structures have higher photoinduced erasure during reading of poled media. It is shown that relaxation kinetics of azo-dye molecules in polymers can be described by two characteristic time intervals: in short term – by writing conditions, relaxation rate of cis isomer and reorientation probability, in long term – by the transisomer orientational diffusion.3D BPM optical poling model for focused polychromatic beams was developed. It was also shown thatspatial localization and depletion of induced $\chi^{(2)}$ in azo-polymers is possible to achieve.

ACKNOWLEDGEMENTS

This work was supported by EU COST Actions MP0702, MP0604 and the Research Council of Lithuania (MULATAS-2, AZOGAN).

REFERENCES

[1] C.Fiorini, F.Charra, J.-M.Nunzi, P.Raimond, Quasi-permanent all-optical encording of noncentrosymmetry in azo-dye polymers, *J.Opt. Soc. Am. B*, vol. 14(8), pp.1984-2003, 1997.

[2] G. Xu, X. Liu, J. Si, P. Ye, Zh. Li, Yu. Shen, Modified theory of photoinduced molecular polar aliggnment in azo polymers, *Opt. Lett.*, vol. 25(5), pp.329-331, 2000.

[3] G. Seniutinas, L. Laipniece, J. Kreicberga, V. Kampars, J. Grazulevicius, R. Petruskevicius, R. Tomasiunas, Orientational relaxation of three different dendrimers in polycarbonate matrix investigated by optical poling, *Journal of Optics A: Pure and Applied Optics*, Vol. 11 (3), 034003 (7pp), 2009.

[4] G.Navickaite, G. Seniutinas, R. Tomasiunas, R.Petruskevicius, V.Kampars, Optical functionalism of azopolymers of different generations: photoinduced orientation and harmonic generation, *Physica Status Solidi A*, vol. 208 (8), pp.1833-1836, 2011.

[5] G.Navickaite, G.Seniutinas, R.Tomasiunas, R.Petruskevicius, V.Getautis, M.Daskeviciene, Photoinduced orientational dynamics of phenylcarbazole molecules in polycarbonate, *Dyes and Pigments*, vol. 92 (3), pp.1204-1211, 2012.

[6] P.S. Weitzman, U. Österberg, A modified beam propagation method to model second harmonic generation it optical fibers, *IEEE Journal of Quantum Electronics*, vol. 29 (5), pp.1437-1443, 1993.

Photonic Bandgap Confinement in an All-Solid Tellurite Glass Photonic Crystal Fibre

Gerardo Scarpignato[1], Joris Lousteau[1], George Athanasiou[2], Emanuele Mura[1], Nadia Boetti[1], Massimo Olivero[1], Trevor Benson[2], Daniel Milanese[1]

[1] *Photonlab, DISMIC, Politecnico di Torino, Corso Duca degli Abruzzi 24 10129 Torino, Italy.*
Tel +39 011 5644707, Fax. +39 011 5644699

[2] *George Green Institute for Electromagnetics Research , University of Nottingham, NG7 2RD Nottingham, Nottingham, UK.*

Author's e-mail: gerardo.scarpignato@polito.it

ABSTRACT

In this paper, the fabrication and optical assessment of an all-solid tellurite glass photonic crystal fibre is discussed. The manufacturing process via a preform drawing approach and the characterization process is described and discussed. The fibre exhibits some minor morphological deformations which do not impair the observed optical confinement by bandgap effect within the fibre. The experimental fibre attenuation spectrum displays clear bandgap confinement regions whose positions are confirmed by modelling the fibre properties using a semi-analytical method similar to the ARROW model. The combination of PBF structures with the particular optical properties of tellurite glasses can lead to the development of optical components with non-conventional characteristics, especially those where chromatic dispersion can be critical.

Keywords: All-solid photonic crystal fibre, tellurite glass, band structure modelling.

1. INTRODUCTION

Photonic bandgap fibres (PBF) present some unique properties that have attracted interest for their application in several fields [1]. Among them, wavelength filtering, chromatic dispersion control, sensing and nonlinear applications have been already demonstrated and it is expected to have an enhanced application prospect in the near future [2, 3].

Currently, hollow core photonic bandgap fibres (HC-PBF) made from silica glass have been a hot research topic. However, this type of structure exhibits some drawbacks not only in terms of manufacturing difficulties but also during the post fabrication implementation. For example, basic operations on these fibres such as fibre cleaving and splicing are technically challenging. Furthermore, as observed for silica glass nanowires [4], long term degradation of the mechanical and optical properties of the thin glass membranes within HC-PCF could also be a concern.

Regarding the glass material, only few publications have focussed on photonic bandgap fibres made from non-silica glasses. The recent report of a high quality HC-PCF made from Schott SF6 glass [5] should be considered among them. Other solutions include the use of composite structures, realised through pumping of tellurite glass or chalcogenide glass into a silica microstructured fibre [6,7]. However, the high thermal expansion mismatch between these glasses produces large mechanical stresses that inevitably lead to detrimental effects. Such stresses not only affect the mechanical integrity of the fibre structure but also the refractive index distribution because of the typical high photoelastic effects occurring in soft glasses [8-9]. Moreover, the dissolution of silica glass in tellurite melt [10] would even deteriorate the optical properties. On the other hand, tellurite glasses possess dispersive and nonlinear optical properties that in combination with PBF structures could produce very interesting optical components.

Here, we report on an all-solid tellurite glass bandgap fibre that has been manufactured to overcome some of the fabrication issues mentioned above. The design of our PBF tellurite glass fibre in terms of refractive indexes and dimensions is based on the approach used and discussed by Birks *et al*. in [11] for all-solid PBF structures.

2. EXPERIMENTAL

2.1 Fibre fabrication

The fibre was made from two tellurite glass compositions namely, TZNGe1 and TZNGe2. The compositions were based on the typical TZN (TeO_2-ZnO-Na_2O) [12] glass matrix where GeO_2 was introduced to improve the thermo-mechanical properties and to reduce the risk of crystallization upon reheating. The glass compositions were also designed to have close glass transition temperatures (Tg), and thus similar thermal expansion coefficients in order to prevent mechanical integrity issues. The glass transition temperatures of the two glasses were measured by Differential Scanning Calorimetry (DSC) and were found to be T_{g1} = 307 ± 3 °C and T_{g2} = 311 ± 3 °C for TZNGe1 and TZNGe2, respectively.

The refractive index of the TZNGe1 and TZNGe2 glass was measured by prism coupling technique at five distinct wavelengths 633, 825, 1061, 1312 and 1533 nm. The results were fitted using a Sellmeier equation [13].

Taking into account the error on measurements, the so-obtained chromatic dispersion curves of the two glasses were found to be quasi parallel, as shown in Fig. 1. The difference between the refractive indices of TZNGe2 and TZNGe1 was measured to be of $\Delta n = 0.029 \pm 0.001$ at 633 nm.

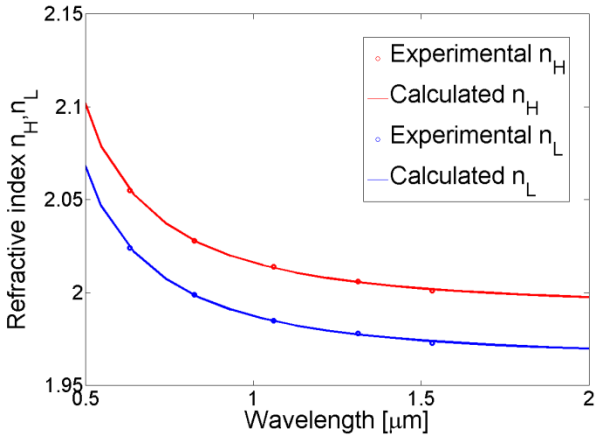

Figure 1. Refractive index dispersion of the two manufactured glasses TZNGe1 and TZNGe2 having n_L and n_H values, respectively. Measured values are indicated by circles.

The fibre was made using the stack and draw technique. The tubes and rods used for the preform were manufactured through a combination of rotational casting and stretching techniques, respectively. Thirty six rods, containing TZNGe2 glass were arranged in three rings around a central rod made from the low index glass TZNGe1. The preform was pulled into 200 m of fibre at a speed of 5 m/min under N2 atmosphere.

Although the fibre did not show any sign of homogeneous crystallization, punctual fibre defects were observed. Since such defects are not detected when drawing standard tellurite glass fibres, it is believed that they arise from impurities present in the preform at the interface between the rods. A photographic image of a cleaved end face of a section of fibre taken with an optical microscope is shown in Fig. 2 a). As it can be observed, the overall hexagonal microstructure has some degree of distortion with respect to the initial preform structure. The rings are slightly offset with regard to the fibre centre and the high index inclusions are not perfectly circular. These morphological defects can be generated by the existence in the preform of an air gap between the hexagonal structure and the inner wall of the surrounding tube. An asymmetrical distribution of the preform temperature acts in combination with the existing gap leading to the deformations described. The dimensional characteristics of the fibre are the following: the mean fibre diameter recorded during drawing was $D_f = 115 \pm 0.5$ μm with maximum fluctuations of ± 4 μm over the whole fibre drawing process. The high index inclusions had a diameter $d = 2.25 \pm 0.20$ μm and the pitch of the micro-structured cladding was $\Lambda = 8.6 \pm 0.2$ μm.

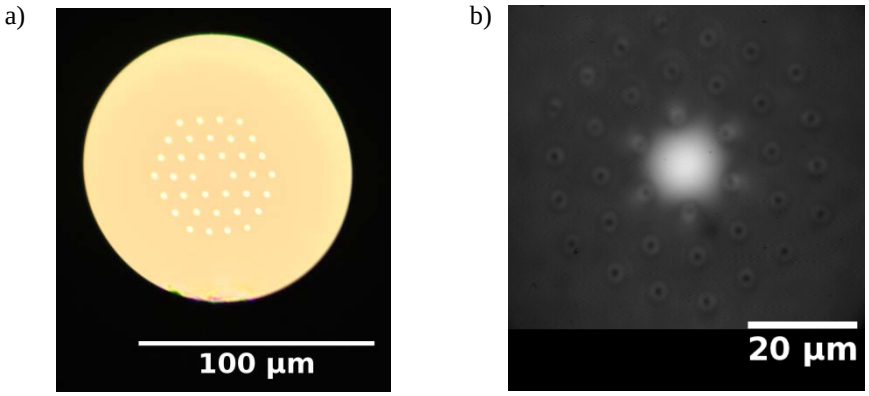

Figure 2 a) Optical micrograph of the end face of the photonic bandgap fibre (PBF) made from tellurite glass. High refractive index inclusions from TZNGe2 glass appear in bright. The remaining area of the fibre is made from low index TZNGe1 glass. b) Near field output image of a 28 cm long section of tellurite glass PBF shown left. In this case the fibre input face is excited in the central low refractive index area using a broadband source that emits from 480 nm up to 2000 nm.

2.2 Fibre loss and guiding characteristics

Optical assessment of the fibre was performed as described by Bouwmans *et al.* in [14]. A commercial supercontinuum source (SuperK from NKT) was focused in a 9 mm core SMF28 optical fibre which was end face coupled to the tellurite glass PBF. The near field image of the fibre output beam was collected on a Grundig electronic SN76 IR videocamera for infrared and on Digital DG-03 videocamera for visible wavelengths. A near field micrograph of the fibre end face illustrating guiding is shown in Fig. 2 b). The output spectra from the fibre were collected through an iris diaphragm, which isolates the beam confined into the low index central area of the fibre from the non-guided light still propagating through the cladding. Two spectrum analysers were used, an Avantes model AvaSpec-2048x14 for the wavelengths ranging from 480 nm to 1100 nm and a HP70951A optical spectrum analyser for wavelengths in the range 700-1700 nm.

The initial length of fibre under test was 28 cm. The loss measurements were performed by a cut-back method where 11 sections of fibre, each 1 to 2 cm long, were successively removed. The fibre output spectra in the visible and in the IR were recorded after each cut to calculate the fibre loss spectrum shown in Fig. 3. For each wavelength the attenuation value was calculated through a linear least square fitting of the experimental data. The typical standard deviation between experimental data and the fitting curve was calculated to be as high as 5 dB/m. The high uncertainty in the measurements is due to the low reproducibility of the end face cleave quality. Actually, it was found difficult to manipulate and to cleave such a short length of fibre without impairing the optical launching conditions at the input end face of the fibre. Another source of error is the measurement methodology, which requires realignment of the output beam with the collecting fibre between each measurement. In spite of the care taken, a full reproducibility of the realignment procedure could not be ensured. Nonetheless, the presence of "low" loss guidance for several wavelength bands (550-650 nm, 810-980 nm and 1100-1700 nm) can be observed in the attenuation spectrum, depicted as clear bands in Fig. 3. On the other hand, for wavelengths within the red bands no confinement occurs. At these wavelengths, the low RI central area of the fibre behaves as a highly lossy core from which all light leaks towards the cladding, i.e. the hexagonal area containing the high index rods.

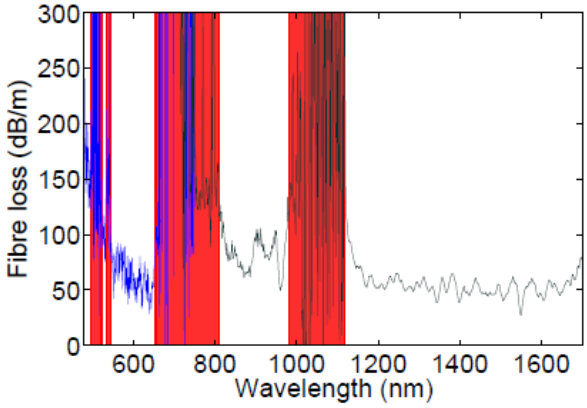

Figure 3. Attenuation spectrum of tellurite glass PCF measured by cutback technique using a supercontinuum source to illuminate the fibre. Bands in red indicate those wavelengths where no confinement occurs.

3. SIMULATION RESULTS

In order to assess the quality of the fiber with respect to theoretical performances, the electromagnetic characteristic behaviour of the fibre was modelled using a semi-analytical model as developed by Birks *et al.* [11]. This method provides an approximated representation of the band structure by means of a dispersion plot in which the different bandgaps and modes can be identified. Thus, the technique supplies a prediction or reference of the bandgap ranges that can be contrasted with those experimentally found using the loss spectrum.

Modelling results are shown in Fig. 4. The modes allowed to propagate with low losses must have a propagation constant $\beta < k * n_L$, where k is the angular wavenumber. They are therefore located inside the white zones of Fig. 4 and below the black line. Thus, theoretical guidance bandgaps are expected to be found: from 560 to 610 nm, from 670 to 940 nm and from 1050 to 1500 nm. By comparing the experimental attenuation of Fig. 3 and the modelling results of Fig. 4, it can be observed that the positions of the real bandgaps have a fairly good agreement with the predicted ones. The small differences are thought to be influenced by the morphological distortion described in the previous section and because the applied method only provides an approximated mapping of the bandgap zones. Moreover, fibre losses present an important degree of inaccuracy, especially at the vicinity of a bandgap, which in turns have an impact in the correct localization of these bands.

Further work is underway using a propietary software (BandSolve from RSOFT). This tool can compute the complex value of the propagation constant β using numerical calculation based on the vector plane-wave method [11]. The results of this work will provide a more accurate identification of the spectral structure of the bandgap

and an accurate evaluation of the loss behaviour of the PCF structure. These values are the subject of a current research that will be published elsewhere.

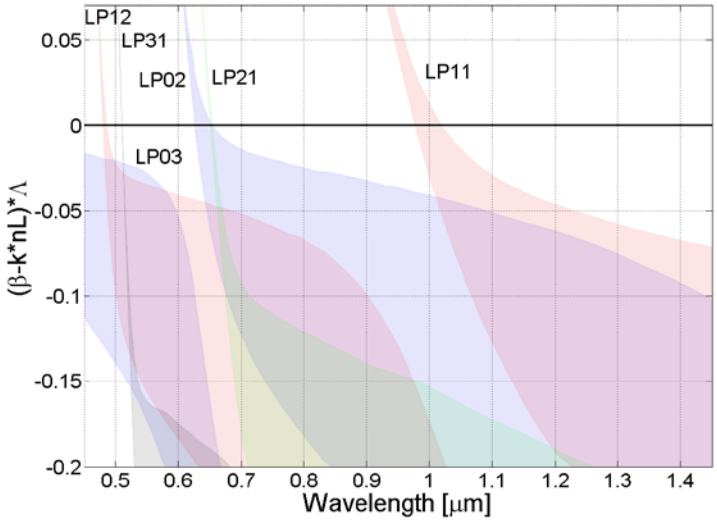

Figure 4. Band structure of the photonic crystal fibre. Zones where leaky modes are situated have a fairly good matching to those found in the attenuation spectrum.

4. CONCLUSIONS

The manufacturing feasibility of an all-solid tellurite glass PBF, that allow combining unconventional properties of tellurite glasses to bandgap confinement effect, has been discussed. It is foreseen that this combination will have a fruitful use in a vast number of applications, in particular in those fields where chromatic dispersions is of interest. In fact, the important amount of fibre geometries that can be created together with the range of refractive index and chromatic dispersion behaviour of tellurite glass will offer a fine tuning of the dispersive behaviour of these fibres. Moreover, all-solid fibre configurations simplifies the integration among existing optical components while allowing to splice PCF tellurite glass fibres to standard silica ones [14]. Clearly, in order to reach this level of integration a higher control of the fibre quality is required. All the steps of the manufacturing processes, from glass synthesis fabrication to fibre drawing, needs to be improved considerably.

REFERENCES

[1] A. Cerqueira: Recent progress and novel applications of photonic crystal fibers, in *Rep. Prog. Phys.,73*, 024401, 2010.
[2] F. Benabid: Hollow-core photonic bandgap fibre: new light guidance for new science and technology, in *Phil. Trans. R.l Soc. A*, 364, pp. 3439, 2006.
[3] V. Pureur, et al: Overview on solid core photonic bandgap fibers, in *Fiber and Int. Optics*, 28, 27, 2009.
[4] G. Brambilla; F. Xu; X. Feng: Fabrication of optical fibre nanowires and their optical and mechanical characterization, in *Electronic Letters*, 42(9), pp. 517, 2006.
[5] X. Jiang, et al: Single-mode hollow-core photonic crystal fiber made from soft glass, in *Opt. Exp.*, Vol. 19 (6), pp. 15438-44, 2011
[6] M.A. Schmidt, et at: All-solid bandgap guiding in tellurite-filled silica photonic crystal fibers, in *Optics Letters*, 34, 13, pp. 1946, 2009.
[7] N. Granzow, et al: Bandgap guidance in hybrid chalcogenide–silica photonic crystal fibers, in *Optics Letters*, Vol. 36, pp. 2432-2434, 2011.
[8] A. Feltz, et al: Optical glasses for IR transmittance, in *Journal of Non-Crystalline Solids*, 129, 31-39, 1991.
[9] T. Nakai, et al: Changes in refractive index of fluoride glass fibers during fiber fabrication processes, in *Appl. Phys. Lett.* 56, 203, 1990.
[10] H. Rawson: Chapter 11 Tellurite and Vanadate Glasses, in *Inorganic Glass Forming Systems*, Ed.: Academic Press Inc. London & New-York, 1967.
[11] T.A. Birks, et al: Approximate band structure calculation for photonic bandgap fibres, in *Opt. Exp.*, Vol. 14, pp. 9483, 2006.
[12] SX. Shen, A. Jha: Raman spectroscopic and DTA studies of TeO2-ZnO-Na2O tellurite glasses, in *Adv. Mat. Res.*, vol. 39-40, 159, 2008.
[13] W. Sellmeier: Zur Erklärung der abnormen Farbenfolge im Spectrum einiger Substanzen, *Annalen der Physik und Chemie*, Vol. 219, 272-282, 1871.
[14] G. Bouwmans, et al: Fabrication and characterization of an all-solid 2D photonic bandgap fiber with a low-loss region (< 20 dB/km) around 1550 nm, *Opt. Exp.*, Vol. 13, pp. 8452-8459, 2005.

Fuse effect dynamics in optical fibers

Paulo André[1,2]
[1] *Instituto de Telecomunicações, Campus de Santiago, 3810-193 Aveiro, Portugal.*
Tel: +351-234377900; e-mail: pandre@av.it.pt
[2] *Departamento de Física, Universidade de Aveiro, Campus de Santiago, 3810-193 Aveiro, Portugal.*

ABSTRACT
In this paper we investigate the dynamics of the fiber fuse effect propagation in optical fibers.

Keywords: Fiber fuse effect, high power signals, optical fibers.

1. INTRODUCTION

Nowadays, the optical power increase in the optical fiber networks, resulting from the growing of the number of optical channels and from the use of high power optical amplifiers (namely, Raman) has lead to an augmented concern about the damage resulting by the fiber fuse phenomenon [1].
This phenomenon was first observed in 1987 and can lead to the destruction of the optical fiber infrastructure along several kilometres [2]. The fiber fuse phenomenon is initiated by a local heating of the optical fiber, causing a strong signal absorption that increases the temperature up to the Silica vaporization value. Due to the heating transferring mechanisms this optical fuse discharge zone [3], produced by the fuse process propagates towards the high-power signal sources [4].
In this paper we review the main characteristics of the phenomenon, such as the fuse zone velocity, threshold power, voids interval for standard single mode fibres and bend insensitive fibres [5-6]. Finally, the aspects related with fuse effect detection and mitigation will be addressed [7].

REFERENCES

[1] P.S. André, et al., Optical Fibers Bending Limits for the Optical Fiber Infrastructures, 9th IEEE Africon Conference,882-884, 2009.
[2] R. Kashyap, K. J. Blow, Observation of catastrophic self-propelled self-focusing in optical fibres, Electronic letters, **24**, 47–49, 1988.
[3] P. S. André, et al., Improved thermal model for optical fibre coating owing to small bending diameter and high power signals, Electronic letters, **46**, 695-696, 2010.
[4] M. Facão, et al., Traveling Solutions of the Fuse Effect in Optical Fibers, IEEE J. Journal of Lightwave Technology, **29**, 109-114, 2011.
[5] P. S. André, et al., Evaluation of the Fuse Effect Propagation in Networks Infrastructures with Different Types of Fibers, Conference on Optical Fiber Communication (OFC)/Collocated National Fiber Optic Engineers (NFOEC), **JWA10**, 2010.
[6] Ana M. Rocha, et al.; Threshold Power of Fiber Fuse Effect for Different Types of Optical Fiber, 13th International Conference on Transparent Optical Networks (ICTON), 2011.
[7] Ana M. Rocha, et al., Detection of Fiber Fuse Effect Using FBG Sensors, IEEE Sensors Journal, **11**, 1390-1394, 2011.

NOTES

Engineering of Quasiperiodic Gratings for Multiple Surface Plasmons Polaritons Couplers

Ido Dolev[1], Michael Miller[1], Gil Porat[1] and Ady Arie[1]
[1] *Department of Physical Electronics, Fleischman Faculty of Engineering, Tel-Aviv University, Tel-Aviv 69978, Israel. e-mail: idodolev@tau.ac.il*

ABSTRACT
In this paper we present a novel method to couple light from multiple wavelengths and angles into surface plasmons polaritons using a single quasiperiodic grating. The quasiperiodic grating can be designed in a systematic manner using the dual-grid method, thereby enabling to control the coupling strength and the grating dimensions. We demonstrated experimentally efficient coupling of light into a surface plasmon from several different illumination angles using a single quasiperiodic grating. This method can also be implemented to couple light from different directions using a 2-D quasiperiodic grating.

Keywords: plasmons, quasiperiodic, gratings, coupler.

1. INTRODUCTION

Surface plasmons polaritons (SPP) are surface electromagnetic waves propagating along the interface of a metal with negative dielectric constant and a dielectric material with positive dielectric constant. In recent years SPP plays a key role in many research applications and devices, mainly as chemical and bio-chemical sensors [1]. Since the wavevector of SPP is larger than the free space wavevector, the main challenge using SPP is coupling them to the metal-dielectric interface. Usually prisms and periodic gratings are used to allow efficient coupling of single free space wave to a single SPP by matching their wavevectors (momentum).These methods are limited to a single process, i.e., a single free space wave into a single SPP, per device. In this paper we propose a new method to couple SPPs by using a quasiperiodic grating [2]. This method allows coupling of several free space wavevectors into either a single SPP or several SPPs simultaneously. The quasiperiodic gratings are designed in a systematic manner, by adopting a well-known method in the field of quasicrystals - the dual-grid method (DGM) [3].

2. THEORY

For efficient coupling between free space wave and SPP in periodic grating momentum conservation must be fulfil:

$$k_0 \sin\theta + m\frac{2\pi}{\Lambda} = \mp \mathrm{Re}\left(k_{sp}\right) \qquad (1)$$

where $k_0=2\pi/\lambda$is the free space wave number, λ is the wavelength,θ is the illumination angle relative to the surface normal, $k_{sp}$is the SPP wave number, $\Lambda$is the grating period, and m = ±1,2,…N. For semi-infinite metal and dielectric mediums k_{sp} is equal to:

$$k_{sp} = k_0\sqrt{\frac{\varepsilon_m \varepsilon_d}{\varepsilon_m + \varepsilon_d}} \qquad (2)$$

where$\varepsilon_m$and$\varepsilon_d$are the permittivities of the metal and the dielectric, respectively. The strength of the coupling of the SPP depends on the value of the Fourier coefficient at the corresponding spatial frequency. It therefore decreases as |m| increases and reaches the maximum value for the first order coefficient (m= ±1). Figure 1 illustrates such a scheme where the dielectric material is $KTiOPO_4$ (KTP) and the metal is silver.

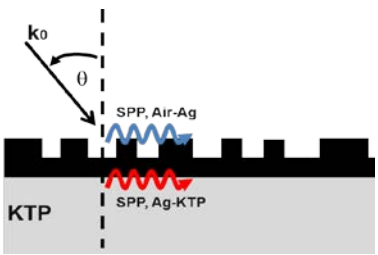

Figure. 1. Illustration of the SPP quasiperiodic grating coupler

SPP can be coupled both to the Ag-KTP and to the Air-Ag interfaces.For coupling of different free space wavevectors, at different illumination angles and into different SPPs, one needs to design a grating that has several well defined Fourier components. The amplitude of each Fourier component will determine the relative coupling strength. With periodic gratings, one can couple only interactions that are described by equation (1), and with limited control on the coupling strength. However, a quasiperiodic grating can provide an arbitrary set of Fourier components and is therefore a good candidate for the multi-coupling task.

Quasiperiodic structures are structures that exhibit long range order, which is manifested by a discrete set of well defined peaks in their Fourier spectra. By using a suitable quasiperiodic grating we can therefore couple different electromagnetic waves into SPPs simultaneously.

3. METHOD

We design the quasiperiodic gratings using the DGM [3]. The DGM is a systematic algorithm that enables to determine the required pattern of the grating so that it will simultaneously couple different interactions with arbitrary wavevector mismatch values. In addition, it also allows us to optimize the amplitudes of the Fourier components for each wavevector mismatch.

To demonstrate the DGM SPP coupling we designed five different structures: three periodic gratings,each supports a single Δk mismatch, i.e. $2\pi/\Lambda_i$, and two quasiperiodic gratings: one supports two different Δk's mismatches (case (1)) and the second supports three different Δk's mismatches simultaneously (case (2)).

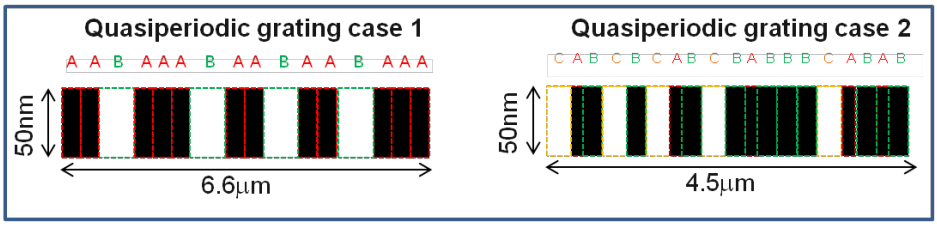

Figure. 2. First few building blocks of the quaisperiodic gratings used for SPP coupling experiments.

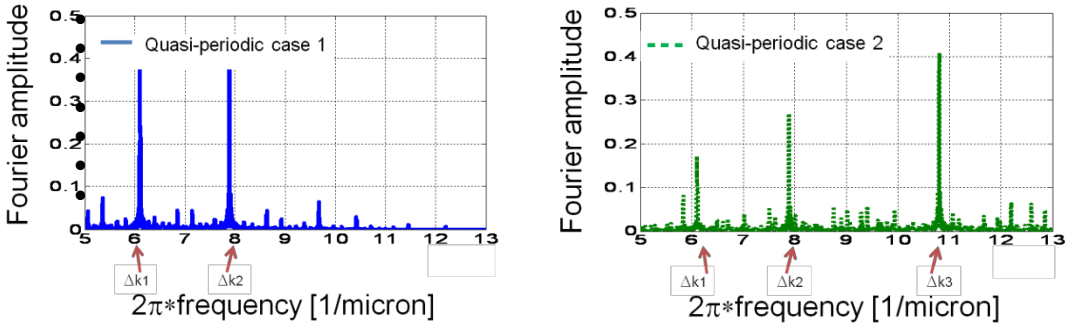

Figure. 3. Fourier spectra of the quaisperiodic gratings used for SPP coupling experiments.

The periodic gratings Λ_1, Λ_2 and Λ_3, were designed to support Air-Ag (Ag-KTP) SPP which are generated by illumination with λ = 1047.5 nm with incidence angles of 1° (62°), 17° (36°) and 51° (6°), respectively.

4. EXPERIMENT

The samples were prepared by evaporating 25nm silver film on top of a KTP crystal followed by a standard e-beam lithography technique to generate the desired structure on PMMA (polymethyl methacrylate) mask. A 50 nm silver layer was then evaporated and the PMMA was removed. The result was 50nm silver grating and 25nm silver film on top of the KTP dielectric crystal (Fig. 1). The size of each grating was 400 μm × 400 μm.We performed a reflection experiment in order to characterizethe coupling into SPP, which manifest as a reflection dip at the coupling angle: a 200 mW, Nd:YLF CW laser (1047.5nm) was focused to a waist of 200 μm. The laser polarization was set by half wave-plate and a polarizer to TM polarization. The gratings were set on a rotating stage and the reflected light was measured at 0.5 degree steps.

5. RESULTS

The results are presented in figure 3. A clear deep appears when SPP is coupled into the device. In figure (4a) we present the measurements of the periodic gratings (Λ_1 and Λ_2) Air-Ag and Ag-KTP SPP, and the case (1) quasiperiodic grating. As predicted, all SPP are coupled in the quasiperiodic grating at the exact angles as the SPP from the periodic gratings. This implies that a single quasiperiodic grating can be used to couple several SPP simultaneously. Figure (4b) presents similar measurements of the Air-Ag SPP for all three periodic gratings and for the case (2) quasiperiodic grating. Again,all Air-Ag SPP appear in the single quasiperiodic grating at identical angles as the SPP in the periodic gratings. Additional dip appears in the case (2) quasiperiodic grating corresponding to the Ag-KTP SPP (Δk_3 mismatch)

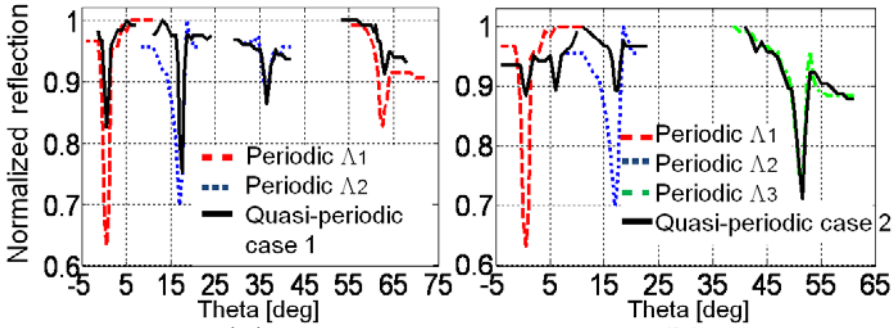

Figure. 4. Experimental results.Normalized reflection vs. illumination angle for the different gratings.

6. CONCLUSIONS

In summary, we have shown a method to couple SPP using quasiperiodic grating [2]. This robust method allows control and optimization on the coupling strength. We demonstrated experimentally coupling of SPP from several different illumination angles using one quasiperiodic grating. This SPP coupling technique can be used for a wide range of applications where multiple coupling conditions are required, such as biochemical SPP sensors, nonlinear optics, and other SPP sub-wavelength optical devices.

ACKNOWLEDGEMENTS

We thank Dr. A. Tsukernik for the e-beam writing. This work was supported by the Israel Science Foundation, Grant No. 774/09.

REFERENCES

[1] S. A. Maier, Plasmonics: Fundamentals and Applications (Springer, 2007).
[2] I. Dolev, M. Volodarsky, G. Porat and A. Arie, Multiple coupling of surface plasmons in quasiperiodic gratings, Optics Letters, **36,** 1584-1586, (2011).
[3] R. Lifshitz, A. Arie, and A. Bahabad,Photonic quasicrystals for nonlinear optical frequency conversion, Phys. Rev. Lett. **95**, 133901 (2005).

NOTES

Hybridization of Plasmons in Coupled Nanowires

Nataliya Sakhnenko, Nadiia Stognii, Alexander Nerukh
Kharkiv National University of Radio Electronics,
pr. Lenina 14, 61166, Kharkiv, Ukraine.
e-mail: n_sakhnenko@yahoo.com

ABSTRACT

Theoretical study of plasmon resonant eigenfrequencies in metal nanowires is presented. Mechanism of the plasmonic mode coupling that can be considered as symmetric and antisymmetric combinations of isolated wires plasmons is investigated. Accurate analysis of the spectrum of different plasmon resonances is presented.

Keywords: plasma, surface plasmons, plasmon eigenfrequency.

INTRODUCTION

Metallic nanostructures are the subject of growing studies in recent years due to the possibility of strong light localization beyond the diffraction limit via the excitation of surface plasmons [1]. Various elements such as plasmonic waveguides [2], subwavelength resonators [3] and optical nanoantennas [4] have been studied recently. Surface plasmons have been explored for their potential in a single molecule detection with surface Raman scattering [5], transmissions through subwavelength apertures [6-7], subwavelength imaging [8]. Plasmonic structures of different shapes (nanowires, nanorods, nanospheres, nanoshells) are provided by various fabrication techniques. The silver nanowire structure is a candidate to key components in future ultracompact photonic devises [9]. It can be considered as a plasmon biosensor to monitor tiny biomolecular interactions [10] and as a novel modulator for control of the intensity of the transmitted surface plasmon polaritons through a nanowire array [11]. Possible future nanophotonic technologies demand devices that can generate stimulated emission of surface plasmons (spaser-based nanolaser). However it is challenging problem due to extremely strong absorption losses in metal at optical frequencies. The suggestion to compensate loss by optical gain using dye molecules in presence of metal nanoparticles [12] or using nanoparticles with gold core and dye-doped silica shell [13] to overcome the loss has been implemented in experiments recently. Therefore, for these applications accurate modeling that provides a valuable insight into fundamental processes is of great importance.

The interaction of metal nanostructures with light leads to the excitation of surface plasmons with different resonance frequencies in the form of propagating waves or localized oscillations that associated with collective oscillations of the electrons. Most metals possess a negative dielectric constant at optical frequency as the plasma frequency of the conduction electron gas lies in this range. The noble metals (silver and gold) have been most closely used in plasmonics because their plasmon resonances lie close to the visible region of the spectrum and can be excited by ordinary optical sources. The plasmon resonances of nanoparticles with dimensions down to 2 nm can be investigated using classical Maxwell's theory [14]. When the illumination frequency passes nearby the plasma frequency of the metal the real part of the dielectric permittivity becomes negative and plasmon resonances can be excited. The plasmon frequencies are strongly dependent on the particle size and shape. The plasmonic modes of coupled nanoobjects can be considered as symmetric and antisymmetric combinations of plasmons of isolated objects with different frequencies and field portraits [14-18].

PROBLEM FORMULATION AND METHOD OF THE SOLUTION

In this paper we solve the eigenvalues problem for a chain of coupled metal nanowires that can be modeled by virtue of plasma cylinders of infinite extent. Radius of each column is a, separation distance between them is d. Fig. 1 represents a schematic diagram of the structure.

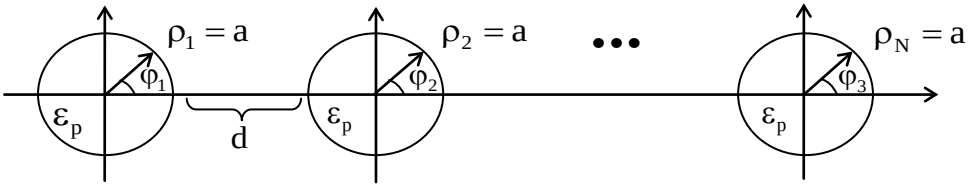

Fig. 1. Schematic diagram of the structure.

Plasma is described by the permittivity ε_p that is given by the Drude model:

$$\varepsilon_p(\omega) = 1 - \omega_p^2 \cdot (\omega(\omega + i\gamma))^{-1} \tag{1}$$

Here ω_p represents the plasma frequency, γ is the material absorption. Sub-wavelength resonances are possible when $\varepsilon(\omega) < 0$ (or equivalently $\omega_p > \omega$), they are called plasmon resonances or surface plasmons. The ambient medium is free space. H-polarized fields are considered. We present the z-component of the internal field as

$$H(\rho_l, \varphi_l) = \sum_{s=-\infty}^{+\infty} K_s^{(l)} J_s(k_p \rho_l) e^{is\varphi_l} \tag{2}$$

and the external field as

$$H(\rho_l, \varphi_l) = \sum_{l=1}^{N} \sum_{s=-\infty}^{+\infty} M_s^{(l)} H_s^{(2)}(k\rho_l) e^{is\varphi l} \,. \tag{3}$$

Here (ρ_l, φ_l) are set of N polar systems of coordinates, associated with each cylindrical columns ($l = 1...N$), $z-$ axis is parallel to the cylinders, $k = \omega \cdot c^{-1}$, $k_p = n_p \omega c^{-1}, c$ is light velocity in a vacuum, $n_p = \sqrt{\varepsilon_p(\omega)}$, $\varepsilon_p(\omega)$ is defined by formula (1), time dependence is $e^{i\omega t}$.

Unknown coefficients K_s and M_s are found from the boundary conditions, requiring the continuity of the tangential components of the total electric and magnetic fields at each cylindrical column's surface. Using the addition theorem for the Bessel functions we arrive to an infinite system of algebraic equations that can be truncated in order to provide a controlled numerical precision.

RESULTS

Eigenvalues of isolated metal nanowire

Fig. 2 (a) illustrates the value of the real part of plasmon eigenfrequency versus normalized frequency (ka) for different values of $w_p = \omega_p a c^{-1}$ that we will call further a normalized plasma frequency. We have to stress that there is no solution for the case $s = 0$ (s is a numbers of angular field variations). It is seen that plasmon resonances for different values of s are closely spaced. Field portraits of the plasmons are shown in the inset of Fig. 2 (a). Fig. 2 (b) presents the scattering cross section of the metal nanowire due to illumination by plane wave. Comparing Fig. 2 (a) and 2 (b) we come up to the conclusion that the peak of the scattering cross section coincides with lowest $s = 1$ plasmon.

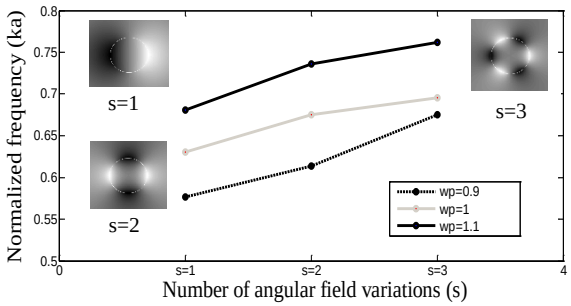

Fig. 2 (a). The dependence of the plasmon eigenfrequency on number of angular field variation.

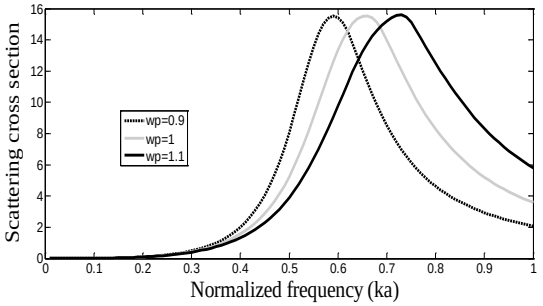

Fig. 2 (b). Scattering cross section of isolated nanowire.

Eigenvalues of a pair of coupled metal nanowires

For the case of two coupled plasma cylinders the structure has two symmetry axis that causes four classes of excited plasmons with different symmetry: EE (even symmetry with respect to x and y axes), EO (x – even; y - odd), OE (x – odd; y - even), OO (x – odd; y - odd) [19]. Fig. 3 shows near field portaraits of different types of plasmons ($s = 2$). The plasmonic modes of coupled nanowires can be considered as symmetric and antisymmetric combinations of plasmons of isolated wires.

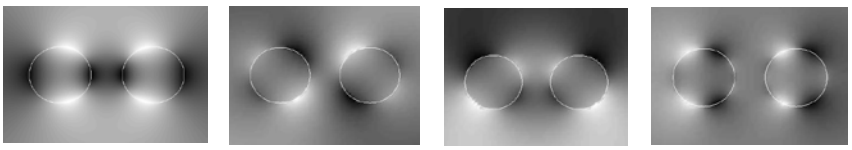

Fig. 3. Nearfieldportraits (from left to right) of EE, OO, OE, EO plasmons ($s = 2$).

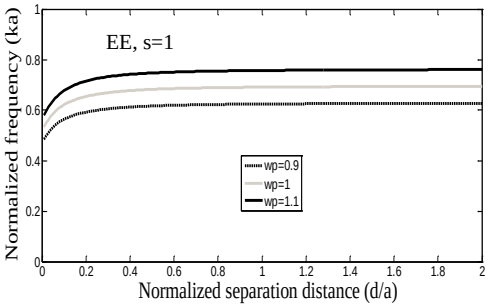

Fig. 4 (a). The normalized frequency versus the normalized separation distance between two coupled metal nanowires for EE plasmon (s=1) for various values of w_p .

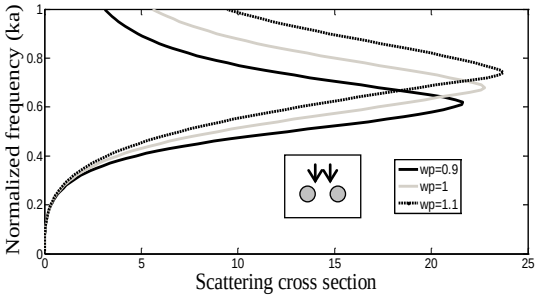

Fig. 4 (b).The scattering cross section of two coupled wires. Direction of the illumination is shown in inset. Separation distance is $d/a = 2$.

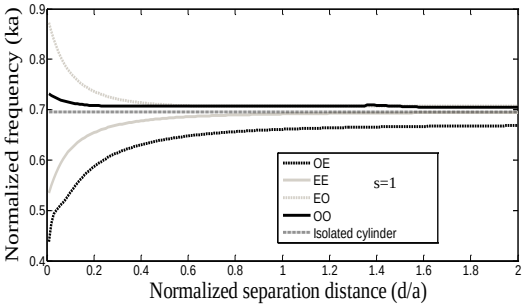

Fig. 5 (a). The normalized frequency versus the normalized separation distance between the two coupled metal nanowires ($w_p = 1$).

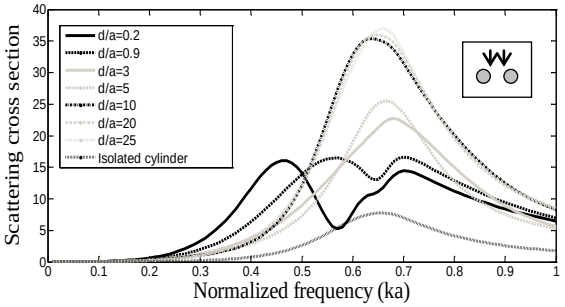

Fig. 5 (b). Scattering cross section of two metal nanowires for various separation distances ($w_p = 1$).

Fig. 4 (a) represents dependence of the normalized frequency of EE plasmon ($s = 1$) on the separation distance between the metal wires. It is seen the decreasing of the frequency when normalized plasma frequency decreases (that is equivalent to the decreasing of the wire radius for fixed plasma frequency). Comparison with scattering cross section graph shows that this plasmon can be excited by plane wave (Fig. 4 (b) when the illumination direction is normal to the main axis of the structure.

Fig. 5 (a) shows the normalized frequencies versus the separation distance between nanowires for all possible types of excited plasmons ($s = 1$). It is clearly seen that for distant cylinders eigenfrequencies are nearly identical for all four symmetry classes. As separation distance d becomes smaller, the frequency shift of the coupled plasmons becomes much stronger. Fig. 5(b) estimates possibility of plasmons to enhance electromagnetic radiation in subwavelength scale ($ka < 1$). It should be mentioned that the strong field enhancement is observable for distant wires (gap is not less than 10 radii).

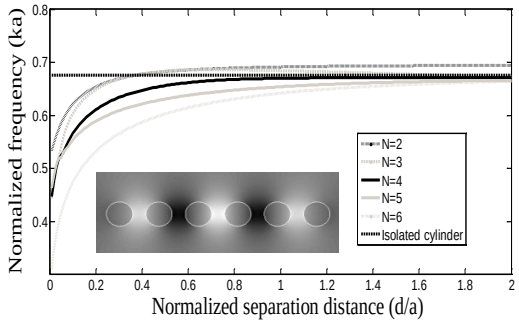

Fig. 6 (a). The dependence of the EE plasmon eigenfrequency on separation distance for different number of wires.

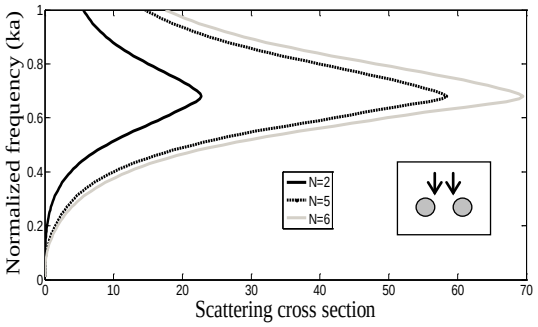

Fig. 6 (b). Scattering cross section of linear chain of metal nanowires for different number of wires. Separation distance is $d/a = 2$.

Eigenvalues of a N coupled metal nanowires

Fig. 6 (a) representseigenfrequencies of EE plasmon (s=1, w_p =1) for different number of coupled metal nanowires. The field distribution of EE plasmon in a chain of six plasma cylinders is shown in the inset in Fig. 6(a). It is seen that eigenfrequencies decrease with increasing the number of coupled plasma cylinders. Fig. 6 (b) presents growing of the amplitude of the excited plasmon with increasing the number of wires.

CONCLUSION

The eigenfrequencies of the coupled metal nanowires that is modeled as cylinders filled with negative permittivity plasma have been analyzed. It has been shown that individual plasmons of isolated wire interact and form symmetric and antisymmetric plasmonic coupled modes of different types. Accurate analysis of the influence of the coupling of metal wires on their spectrum of different plasmon resonances is presented.

ACKNOWLEDGEMENTS

This work was supported by the Ukrainian National Target Program "Nanotechnologies and Nanomaterials" and the State Agency for Science, Ukraine. Ms. N. Stognii acknowledges the support of this research by IEEE AP-Society through Doctoral Award.

REFERENCES

[1] A. Zayats, I. Smolyaninov: Near-field photonics: surface plasmon polaritons and localized surface plasmons, *Journal of Optics A: Pure and Applied Optics*, vol. 5, pp. 16-50, 2003.

[2] S. Bozhevolnyi, V. Volkov, E. Devaux, J. Laluet, and T. Ebbesen: Channel plasmon subwavelength waveguide components including interferometers and ring resonators, *Nature*, vol. 440, pp.508-511, 2006.

[3] J. li, N. Engheta: Ultracompact sub-wavelength plasmonic cavity resonator on a nanowire, *Phys. Rev. B*, vol. 74, 115125, 2006.

[4] L. Novotny and N. Hulst, Antennas for light, *Nature Photonics*, vol. 5, pp. 83-90, 2011.

[5] K.Kneipp, Y. Wang, H. Kneipp, L. Perelman, I. Itzkan, R. Dasari, and M. Feld: Single molecule detection using surface-enhanced Raman scattering (SERS), *Phys. Rev. Lett.*, vol. 78, pp. 1667–1670, 1997.

[6] J. Weiner: The physics of light transmission through subwavelength apertures and aperture arrays, *Reportson Progress in Physics*, vol. 72, 064401, 2009.

[7] T. Thio, K. Pellerin, R. Linke, H.Lezec, T. Ebbesen: Enhanced light transmission through a single subwavelength aperture, *Optics Letters*, vol. 26, pp.1972-1974, 2001

[8] I. Smolyaninov, J. Elliott, A. Zayats, and C. C. Davis: Far-field optical microscopy with a nanometer-scale resolution based on the in-plane image magnification by Surface Plasmon Polaritons, *Phys. Rev. Lett.*, vol. 94, 057401, 2005.

[9] E. Ozbay: Plasmonics: merging photonics and electronics at nanoscale dimension, *Science*, vol. 311, pp. 189-193, 2006.

[10] K. Kim, S.J. Yoon, D. Kim: Nanowire-based enhancement of localized surface plasmon resonance for highly sensitive detection: a theoretical study, *Optics Express*, vol. 14, no. 25, pp. 12419-12431, 2006.

[11] D. Fedyanin, A. Arsenin: Transmission of surface plasmon polaritons through a nanowire array: mechano-optical modulation and motion sensing, *Optics Express*, vol. 18, no. 19, pp. 20115-20124, 2010.

[12] G. Dice, S. Mujumdar, and A. Elezzabi: Plasmonically enhanced diffusive and subdiffusive metal nanoparticle-dye random laser, *Appl. Phys. Lett.*, vol. 86, 131105, 2005.

[13] M. Noginov, *et al.*: Demonstration of a spaser-based nanolaser, *Nature*, vol. 460, pp. 1110-1113, 2009.

[14] J. Kottmann, O. Martin: Plasmon resonant coupling in metallic nanowires, *Optics Express*, vol. 8, pp. 655-663, 2001.

[15] Rolly, B. Stout, N. Bonod: Metallic dimers: When bonding transverse modes shine light, *Phys.Rev. B*, vol. 84, 125420, 2011.

[16] A. Devilez, B. Stout, N. Bonod: Mode-balancing far-field control of light localization in nanoantennas, *Phys. Rev. B*, vol. 81, 245128, 2010.

[17] N. Stogniy (Stognii), N. Sakhnenko, A. Nerukh: Plasmon resonances in linear array of coupled silver nanowires, *Proc. Int. Conf. Transparent Optical Networks (ICTON-11)*, Stockholm, We.P.8, 2011.

[18] N. Stogniy (Stognii), N. Sakhnenko: Theoretical study of plasmon resonances in linear chain of silver nanowires, *Proc. Int. Conf. Laser and Optical Networks Modeling (LFNM-11)*, Kharkiv, 043, 2011.

[19] E.I. Smotrova, *et al.*: Optical Coupling of Whispering-Gallery Modes of Two Identical Microdisks and Its Effect on Photonic Molecule Lasing, *IEEE J. Select. Topics in Quant. Electr.*, vol. 12, pp. 78-85, 2006.

Two-dimensional plasmonic nano-structures for linear and nonlinear regimes

M. Grande[1,*], M. A. Vincenti[2], T. Stomeo[3], G. Bianco[4], G. Morea[1], R.Marani[1], V. Marrocco[1,5], D. de Ceglia[2], V.Petruzzelli[1], M. De Vittorio[3,6], G. Bruno[4], M. Scalora[7], A. D'Orazio[1]

[1] Dipartimento di Elettrotecnica ed Elettronica, Politecnico di Bari, Via Re David 200, 70125 Bari (Italy)
[2]AEgis Technologies Inc., 410 Jan Davis Dr., Huntsville 35806, AL – USA
[3] Italian Institute of Technology (IIT), Center for Bio-Molecular Nanotechnology, Via Barsanti, Arnesano (Lecce), 73010 Italy
[4] Institute of Inorganic Methodologies and of Plasmas, IMIP-CNR, via Orabona 4, 70126 Bari, Italy
[5] Istituto di Tecnologie Industriali ed Automazione ITIA-CNR, Via P. Lembo 38, 70125 Bari (Italy)
[6] National NanotechnologyLaboratory (NNL), CNR-ISTITUTO DI NANOSCIENZE, Dip. Ingegneria dell'Innovazione, Università Del Salento, Via Arnesano, 73100 Lecce, Italy
[7]Charles M. BowdenResearch Center, RDECOM, RedstoneArsenal, Alabama 35898-5000 – USA
Tel: +390805963532; e-mail: grande@deemail.poliba.it

ABSTRACT

In this contribution we provide an overview of our recent research results on the optical properties of 2D array of gold patches immersed in homogeneous and asymmetric environment. The investigated structure acts as a bio-sensing platform that exploits the formation of a plasmonic band gap in the reflection spectrum.

Keywords: nanophotonics, surface plasmon, biosensor, EOT, nonlinear, SERS

MODELLING OF PLASMONIC NANOSTRUCTURES

The fascinating optical properties of plasmonic nanostructures have attained great interest in the last decade since they can be usefully exploited in many emerging applications, such as sensing, spectroscopy, light emitters, optical data storage, and photovoltaics.

In the framework of COST Action MP0702 activities, we performed numerical analysis on plasmonic optical properties of different metal nanostructures. In particular, we put emphasis on back and forward scattering and on the calculation of field enhancement and spectral response of metal nanoparticles having different shape (nanorods, nanospheres, bow-tie, squared and rectangular patches). Theoretical calculations have indicated that the plasmonic absorption strongly depends on the detailed configuration of nanostructures in terms of materials, metals (Ag and Au) and semiconductors, and geometrical parameters, such as length, thickness and width/diameter. Moreover, we evaluated the spectral response of more complex geometries based on one-dimensional array of plasmonic heterostructures able to enhance and focus light [1] and of multiple elementary periodic structures [2], with the aim of understanding how properly tailor the spectral behaviour of periodic plasmonic structures and exploring the possibility of developing light concentrator and back reflectors to assist and optimize solar cells [3], plasmonic platforms for biosensing and optical nanoantennas [4].

In this contribution we will provide an overview of our recent research results on the optical properties of 2D array of gold patches immersed in homogeneous and asymmetric environment [5-6]. The investigated structure acts as a bio-sensing platform that exploits the formation of a plasmonic band gap in the reflection spectrum.

Figure 1 shows the Scanning Electron Microscope (SEM) image of the fabricated device. The gold patches are periodically arranged on a Silicon substrate. The periodicities in the two directions are chosen so that $p_x = p_y = p$ = 630 nm. Several samples with different aperture sizes a were fabricated, while the gold nano-patch thickness w has been fixed equal to 200 nm.

Simulations were performed by means of 2D and 3D Finite Element Method and home-made FDTD codes. Three different states are distinguishable in the reflection spectrum across the plasmonic band gap: V, M and FP states, respectively. The V state corresponds to the excitation of a leaky mode that propagates on the metal grating and causes a sharp dip in the reflection spectrum; the M state corresponds to the coupling and back radiation of a surface plasmon and, hence, corresponds to a maximum in the reflectivity spectrum. Finally, the FP state is a hybrid state related to the availability of a Fabry- Pérot mode inside the cavity. This mode propagates in the metal-insulator-metal (MIM) waveguide that supports a transverse-electro-magnetic TEM-like guided mode only under specific circumstances.

Evidence of the above mentioned states is shown in Fig. 2a, where the V state can be clearly identified on a two dimensional map where reflection is plotted as a function of both incident angle (0° - 90°) in the wavelength range on interest (400 - 700 nm). The map emphasizes how the resonance associated to the V state splits in two arms and linearly shifts with a variation of about 10 nm when the source is tilted by an angle as small as 1°. Furthermore the

high absorption of gold between 400 nm and 500 nm suppresses all features within this wavelength range. Figure 2a also reveals that these geometrical parameters do not allow guided modes in the MIM waveguide for the wavelength range under investigation and, as a consequence, forbid the formation of hybrid modes related to the interference between cavity and surface modes. Figure 2b reports the simulated and experimental reflection spectra showing that the spectral position of the V states is almost identical. The extremely small shift and the broadening of the measured spectrum can be addressed to the roughness of the metal patches.The potential sensitivity of the device has be derived by evaluating the spectral shift when an extremely small change of the refractive index is induced at the top surface of the sensor, leading to sensitivity values up to 1000 nm/RIU and a corresponding Figure of Merit (*FOM*) of 222 RIU^{-1} (*FWHM* of the resonance is only 4.5 nm) that corresponds to a significant advance in the improvement of plasmonic sensor devices.

Moreover we will provide experimental proof of the sensing capabilities of this device by observing colour variations in the diffracted field when the air overlayer is replaced with a small quantity of isopropyl alcohol (IPA).

Finally we will report on the investigation of Surface Enhanced Raman Scattering (SERS) when the 2D array of gold patches is functionalized with thiols molecules. Figure 3 shows the SERS signal when the aperture *a* is varied. As it can be inferred from the plot, the SERS signal decreases when the aperture is narrowed and this is completely consistent with the simulation results. Moreover the SERS performance when different laser wavelengths and numerical apertures are adopted will be discussed highlighting that the geometrical parameters and, in a particular way, the periodicity strongly affect the nonlinear response of these periodic nanostructures.

ACKNOWLEDGMENTS

The authors would like to acknowledge the COST action MP0702 on “Towards Functional Sub-Wavelength Photonic Structures” and “FIRB - Hub di ricercaitalo-giapponesesullenanotecnologie.” M. G. acknowledges partial financial support from the Army Research Office (Grant No. W911NF-11-1-0284_1490-AM-01) and from “Progetto Regione Puglia - Laboratorio Regionale di Sintesi e Caratterizzazione di Nuovi Materiali Organici e Nanostrutturati per Elettronica, Fotonica e Tecnologie Avanzate” fromRegione Puglia.

REFERENCES

[1] R. Marani et al., “*Enhancement of extraordinary optical transmission in a double heterostructure plasmonic bandgap cavity*”, Plasmonics, March 12, 2011, doi 10.1007/s11468-011-9225-4.

[2] V. Marrocco et al., “*Anomalous plasmonic band gap formation in two-dimensional slit arrays with different periods”*, 13th International Conference on Transparent Optical Networks, 26-30 June, 2011, Stockholm, Sweden.

[3] R. Marani et al, “*Plasmonic bandgap formation in two-dimensional periodic arrangements of gold patches with subwavelength gaps*”, Optics Letters, Vol. 36, No. 6, pp. 903-905 (2011).

[4] T. Dattoma, M. Grande, R. Marani, V. Marrocco, G. Morea, A. D’Orazio, “*Resonance wavelength dependence and mode formation in gold nanorod optical antennas with finite thickness”*, Progress in Electromagnetics Research B, vol. 30, 337-353, 2011.

[5] M. Grande, R. Marani, F. Portincasa, G. Morea, V. Petruzzelli, A. D’Orazio, V. Marrocco, D. de Ceglia, M.A. Vincenti, “*Asymmetric plasmonic grating for optical sensing of thin layers of organic materials*”, Sensors and Actuators B, 160, 1 (15 december 2011), pp.1056-1062, doi: 10.1016/j.snb.2011.09.025.

[6] M. Grande, M. AVincenti, T. Stomeo, G. Morea, R. Marani, V. Marrocco, V. Petruzzelli, A. D’Orazio, R. Cingolani, M. De Vittorio, D. de Ceglia, M. Scalora, "*Experimentaldemonstration of a novelbio-sensingplatform via plasmonic band gap formation in gold nano-patch arrays*" Opt. Express 19, 21385-21395 (2011).

FIGURES

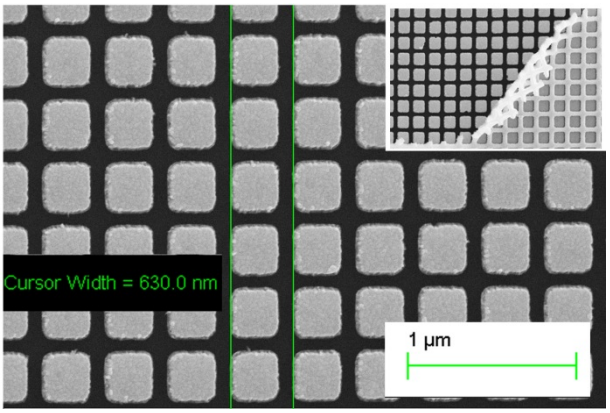

Figure 1: SEM image of the fabricated device (inset: lift-off process).

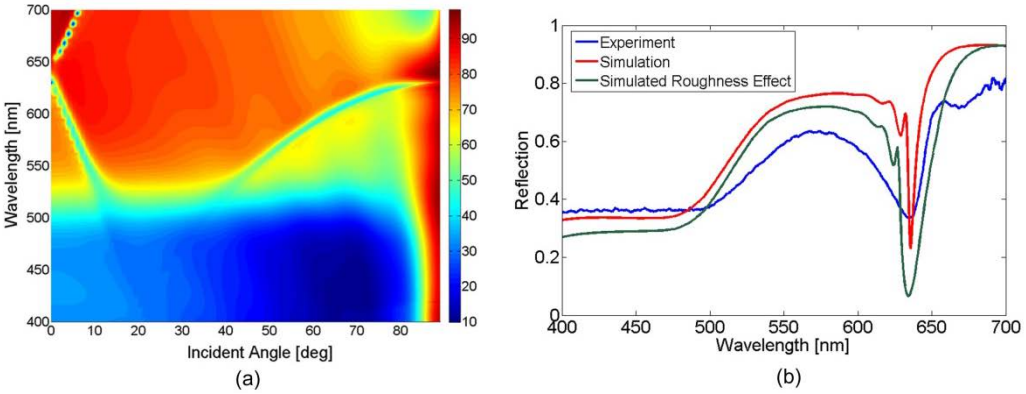

Figure 2: a) Reflection map of the nanostructure characterized by the parameters p = 630 nm, w = 200 nm, a = 120 nmas a function of the incident angle; b) Simulated and experimental reflection spectra.

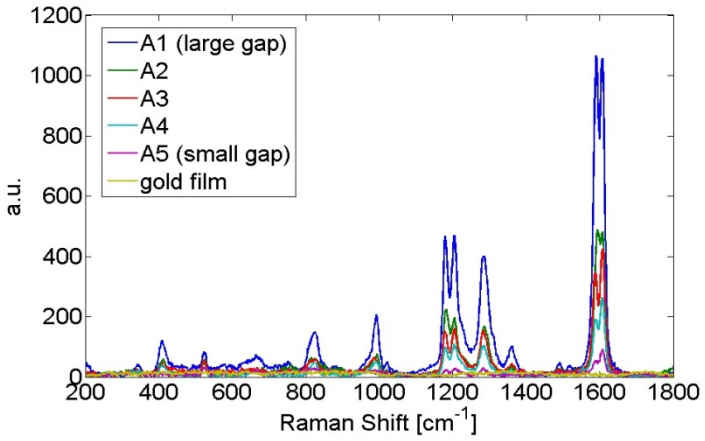

Figure 3: SERS signal when the gap is varied (the yellow curve corresponds to the reference signal of the flat gold film).

NOTES

Analysis of Surface Plasmons Excitation in Kretschmann Structure at Waveguiding, Amplifying and Nonlinear Cover Layer by the Method of Single Expression

Hovik V. Baghdasaryan[1], Tamara M. Knyazyan[1], Tamara T. Hovhannisyan[1], Marian Marciniak[2]
[1] *FOC Lab., State Engineering University of Armenia, Terian 105, Yerevan 0009, Armenia.*
Tel: (374 99) 110 547, e-mail: hovik@seua.am
[2] *National Institute of Telecommunications, Department of Transmission and Optical Technologies, 1 Szachowa Street, 04-894 Warsaw, Poland*

ABSTRACT
Traditional Kretschmann structure with a dielectric covering layer of different thickness is analysed numerically by the method of single expression. Application of thin SiO_2 layer in the Kretschmann structure as a protective cover (of some nanometers thickness) is discussed. Covering layers of some hundred nanometers exhibit waveguiding features and their excitation is possible at angles less than the angle of surface plasmon (SP) excitation. Inclusion of gain in a covering layer is analysed and compensation of intrinsic loss in a metallic layer is discussed. The minimal value of gain for loss compensation is needed for the first waveguide-mode of a covering layer, which is a candidate in application for optical on-chip interconnects.
An influence of intensity-dependent nonlinearity in a cover layer on SP excitation in Kretschmann structure is analysed. Inclusion of nonlinearity in a covering dielectric medium causes the shift of the incident wave angle of surface plasmon excitation and bistable behaviour of the angular dependence of the reflectance. At the fixed amplitude of intense incident wave the hysteresis in the reflectance revealed the proper direction of angular interrogation depending on the sign of nonlinearity.

Keywords: surface plasmon (SP), Kretschmann structure, waveguiding cover layer, nonlinear cover layer, hysteresis, method of single expression (MSE).

1. INTRODUCTION

Nanophotonics is rapidly growing field of science and technology due to its potential in developing compact and fast operating, reliable photonic components for optical communication networks, free-space optical interconnects, spectroscopy, imaging, sensors, security systems, etc. [1]. Nanophotonic devices are wavelength-scale structures consisting of dielectric, semiconductor and/or metallic thin layers or nanoparticles. Traditionally metals are used as mirrors and electric contacts for optoelectronic devices. High intrinsic loss of metals has prevented spreading their application in different photonic components. However metals as media with negative permittivity nowadays attract particular interest in nanophotonics. With the miniaturization of photonic structures, metals start to reveal unique features in manipulating light at distances smaller than the operating wavelength. Particularly, an interface between a dielectricand a metal sustain surface plasmons (SPs), specific light waves propagating along the interfaceand evanescently confined in the perpendicular direction [2,3]. In recent years the field of plasmonics has attracted much interest in the context of highly integrated nanophotonic devices, material science, biological sensing, spectroscopy, medical diagnostics, environmental monitoring, food safety, security, etc. [1-3].

Widely used techniques for plasmonic waves excitation are by means of prism couplers, optical waveguides and diffraction gratings [3]. Excitation of surface plasmons by prism couplers can be realised by two configurations: Kretschmann and Otto. The Kretschmann structure is widely accepted as the superior configuration for sensor operation. It delivers higher sensitivity and is easier in implementation as the metal film can be deposited directly on the prism interface (Fig. 1).

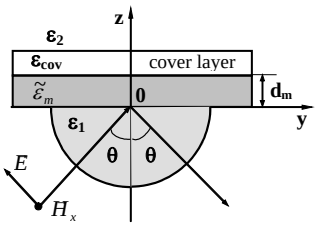

Figure 1. Schematic Kretschmann-type structure with cover layer

At the incidence of TM polarised light wave at a definite angle (in range of total internal reflection (TIR)) and specific thickness of metallic layer SP generation at the metal-dielectric interface takes place. At this angle a deep decrease in reflection is observed and the resonant enhancement of optical field amplitude at the interface takes

place[4]. The light intensity enhancement at the metal-dielectric interface brings to the extreme sensitivity to any change in a dielectric medium where analyte is positioned in sensing applications.

2. METHOD OF RESEARCH

All known theoretical methods for the analysis of SP excitation rely on fulfillment of superposition principle that prevents their application for a strong nonlinear problem solution.As a computational tool for numerical modelling of linear and light's intensity-dependent nonlinear plasmonic structures the method of single expression (MSE) is used in the current work [5-8]. In the MSE loss, gain and intensity-dependent nonlinearity in the multilayer structures can be taken into account without any restrictions on the value and sign. Along with the reflectance, transmittance and absorbance of aconsidered structure the distributions of electric and magnetic field amplitudes and power flow density within and outside a structure can be analysed by the MSE.

3. RESULTS OF NUMERICAL ANALYSIS

3.1 Protective and waveguiding cover layer

For sensing applications different modifications of the conventional Kretschmann structure involving multilayer metal-dielectric structures are used [9,10]. Particularly, deposition of a thin polymer coating film on a metallic layer causes shift of the reflectance dip to a slightly higher angle that permits to find out information on the optical thickness and properties of the coating. Such angular interrogation in the Kretschmann configuration comprising ultrathin film upon a metallic layer is used in surface plasmon microscopy and surface plasmon resonance (SPR) biosensors [9,10]. Except for plasmonic features such a structure starts to reveal also waveguiding properties, so along with a SP-polariton mode guided-wave-polariton modes are observed in the angular reflectance of the multilayer metal-dielectric plasmonic structure [10]. An analysis of influence of a thickness of a cover layer upon a metallic layer can give knowledge about a change of conditions of SP excitation, which is useful for sensing of aggressive matters when the cover layer is used to protect metallic interfaces susceptible to oxidation.

The numerical simulation by the MSE has been performed first for an excitation of SP at the incidence of TM plane EM wave on a Kretschmann structure without a cover layer. The silver layer of thickness $d_m = 47$ nm of permittivity $\tilde{\varepsilon}_m = \varepsilon'_m + j\varepsilon''_m = -11.3 - j0.62$ (at λ_0=530.9 nm) is taken. The permittivities of a prism and medium above metallic layer are $\varepsilon_1 = 3$ and $\varepsilon_2 = 1$, correspondingly. The characteristic sharp resonance dip in the angular reflectance of the structure $R(\theta)$ related to plasmon excitation is observed at the incidence angle $\theta_{dip} = 37.2644^o$ (Fig. 2a). At the metal/air interface an essential field enhancement takes place for both magnetic $\hat{H}$ and electric $\hat{E}$ field amplitudes while on either sides of the interface exponential decaying waves are observedthat indicatesapossibility of SP excitation along the interface (Fig. 2b). Poynting vector P_z sharply decreases in the metallic layer due to intrinsic loss of Ag and is constant on either sides of the layer.

At the thin enough cover layer (~ 2÷4 nm) the location of the dip and its half width are changed slightly compared with the structure without any cover. The behaviour of magnetic and electricfield amplitudes at the Ag/SiO_2 interface is also not changed. This indicates the possibility to use of ultrathin covers of SiO_2 to protect metallic surfaces from aggressive matters at sensing applications.

With the increase of the cover SiO_2 layer the shift of the dip towards greater angles is observed. The behaviour of magnetic and electricfield amplitudes remains almost the same as in the case of thin covers with a slight distortion at the SiO_2/air interface. At further increase of the cover (at 210 nm) in the angular reflectance of the structure along with the dip related to SP excitation a new dip at smaller angle of 36.764^0 appears (Fig. 3a). Outwardly this dip is similar to the plasmonic dip however the distributions of field amplitudes indicate that at this angle the waveguiding-mode is supported by SP at the Ag/SiO_2 interface (Fig. 3b).

At further increase of the cover layer thickness (at 600 nm) in the angular reflectance of the structure along with the plasmonic dip two dips at the angles of 42.76^0 and 54.8^0 related to two waveguide-modes appear (Fig. 4a). Corresponding distributions of field amplitudes confirm this fact (Fig. 4b). Further increase of the cover layer revealed increase of the number of waveguide-modes whereas the plasmonic dip does not change its position and shape.

At the excitation of a single mode in thecover waveguide it is possible to have wave propagation at distances longer than for SP since in the metal the field amplitude is not resonantly enhanced in this case. This waveguide indicated the higher sensitivity to inclusion of modest gain in the cover layer, which promises to have loss compensated waveguide suitable for optical on-chip interconnect applications [8].

(a) (b)

Figure 2. (a) Angular reflectance of the Kretschmann structure without cover layer, (b) distributions of magnetic and electric field amplitudes, Poynting vector and profile of effective permittivity

$\varepsilon_{eff} = \varepsilon_i - \varepsilon_1 \cdot \sin^2\theta$ *(i=1,m, 2)within the multilayer structure at the plasmonic dip [8].*

(a) (b)

Figure 3. (a) Angular reflectance of the Kretschmann structure with a cover layer of thickness 210 nm, (b) distributions of magnetic and electric field amplitudes, Poynting vector and profile of effective permittivity within the structure at the waveguide-mode dip (at the incidence angle 36.764^0) [8].

(a) (b)

Figure 4. (a) Angular reflectance of the Kretschmann structure with a cover layer of thickness 600 nm and (b) distributions of magnetic and electric field amplitudes, Poynting vector and profile of effective permittivity within the structure at the secondwaveguide-mode dip (at the incidence angle 42.76^0) [8].

3.2 Kerr-type nonlinearity in the covering layer

In sensing of some biological objects, organic materials or others inherently possessing nonlinearity, the resonant field enhancement at the interface causes nonlinear phenomena: second harmonic generation and field intensity-dependent nonlinear effects [11,12]. High field intensity at the interface brings to the change of plasmons excitation conditions due to nonlinearity in analyte, and, as a consequence, strong dependence of measurement results on incident field intensity. A relevant computer simulation of SP excitation at high field intensity will be useful for predicting and understanding the measurement results. An influence of a weak nonlinearity in Kretschmann structure has been earlier studied revealing that SP excitation conditions are changed bringing to hysteresis in the reflection spectrum[12].Nowadays for sensing applications an analysis of a strong nonlinearity in analyte is topical.

The numerical simulation by the MSE has been performed for an excitation of a surface plasmon at the incidence of TM plane EM wave on a nonlinear Kretschmann structure having a silver layer of thickness $d_m = 47$ nm with permittivity $\tilde{\varepsilon}_m = \varepsilon'_m + j\varepsilon''_m = -11.3 - j0.62$ (at $\lambda_0 = 530.9$ nm).

The analysis of the case of Kerr-type nonlinearity in the covering dielectric medium with permittivity $\varepsilon_{\text{cov}} = \varepsilon_0 + \varepsilon_{nl} \cdot |E|^2$ (ε_0 is the linear term of permittivity and ε_{nl} is the nonlinear coefficient) is performed for both types of nonlinearity: positive ($\varepsilon_{nl} > 0$) and negative ($\varepsilon_{nl} < 0$). The permittivity of a prism and a dielectric are taken as $\varepsilon_1 = 3$ and $\varepsilon_0 = 2$, correspondingly. Computationsby the MSE have been performed for the fixed value of incident magnetic field amplitude ($\hat{H} = 20$ a.u.) and bistable angular dependences for the reflectance $R(\theta)$ are obtained.The angle of plasmonic dip for $R(\theta)$ in the linear case is $\theta_{SPlin} = 64.0256$. Depending on the sign of nonlinear coefficient of analyte the strong dip ($R(\theta) \approx 0$) in the reflection spectrum is observed only at proper direction of angular scanning (by increasing or decreasing of incidence angle).

(a) (b)

Figure 5. Angular dependences of reflectance at (a) negative $\varepsilon_{nl} = -0.001$*, (b) positive* $\varepsilon_{nl} = 0.001$ *nonlinear coefficient in analyte [7].*

At negative nonlinearity the strong dip is shifted towards lower angles (Fig. 5a) and correspondingly, at positive nonlinearity the shift of the dip towards greater angles takes place (Fig. 5b).

Relevant optical field amplitude localisation and behaviour of power flow density within plasmonic structures are also obtained during the analysis.

4. CONCLUSION

Correct numerical simulation by the MSE of optical properties of the Kretschmann structure with SiO_2 cover layer revealed, that thin cover layer of thickness ~ 2÷4 nm can protect a metallic layer from aggressive matters in sensing applications without affecting sensitivity of such structures. With the increase of the cover's thickness at the definite incident angles, less than the angle of SP excitation, the plasmonic structure can operate as single-mode optical waveguide of thickness ~ 210 nm with loss less than for SP. Such waveguides can find application in optical on-chip interconnects.

Specific angular interrogation characteristics are obtained at the fixed amplitude of illuminated light for a nonlinear analyte. The performed accurate simulation for both signs of nonlinear coefficient will be useful in application of plasmonic sensors on the subject of impact of optical sources' intensity on measurement results at intensity-dependent nonlinearity in analyte.

ACKNOWLEDGEMENTS

The authors thank COST MP0702 action "Towards Functional Sub-wavelength Photonic structures" for stimulating discussions.

REFERENCES

[1] L. Novotny, B. Hecht: *Principles of nano-optics*, Cambridge University Press, Cambridge, 2006.
[2] S. A. Maier: *Plasmonics: Fundamentals and Applications*, Springer, 2007.
[3] J. Homola: *Surface Plasmon Resonance Based Sensors*, Springer-Verlag, 2006, vol.4.
[4] H. Weber, G.W. Ford: Optical electric-field enhancement at a metal surface arising from surface-plasmon excitation, *Opt. Lett.*, vol. 6, No.3, pp. 122 –124, 1981.
[5] H.V. Baghdasaryan, T.M. Knyazyan: Problem of plane EM wave self-action in multilayer structure: an exact solution, *Opt. & Quant. Electron.*, vol. 31, pp. 1059-1072, 1999.
[6] H.V. Baghdasaryan, *et al.:* Development of the Method of Single Expression (MSE) for Analysis of Plane Wave Oblique Incidence on Multilayer Structures Having Complex Permittivity and Permeability, in *Proc. ICTON 2008*, Athens, Greece, June 2008, paper Th.A1.4.
[7] H.V. Baghdasaryan, *et al.:* Wavelength-scale analysis of optical field localization at plasmonic resonance in non-linear Kretschmann structure by the method of single expression, in *Proc. ICTON 2010*, Munich, Germany, June-July 2010, paper Mo.C2.4.
[8] H.V. Baghdasaryan, *et al.:* Peculiarities of Surface Plasmon Excitation in Amplifying Kretschmann Structure: Correct Wavelength-Scale Analysis by the Method of Single Expression, in *Proc.ICTON 2011,* Stockholm, Sweden, June 2011, paper Mo.C2.5.
[9] J.-N. Yih, *et al.:* Angular interrogation attenuated total reflection metrology system for plasmonics sensors, *Appl. Optics*, vol.44, pp. 6155-6162, 2005.
[10] S.P. Frisbie, *et al:* Optical reflectivity of asymmetric dielectric-metal-dielectric planar structures, *Journ. Light. Technol.*, vol. 27, pp. 2964-2969, 2009.
[11] C.-C. Tzeng, J. T. Lue: Optical second-harmonic generation from silver films with long-range surface-plasmon excitation, *Surf. Sci.*, vol. 216, pp. 579–586, 1989.
[12] J.R. Sambles, R.A. Innes: A comment on nonlinear optics using surface plasmon-polaritons, J. Modern Optics, vol.35, pp.791-797, 1988.

Formation of metal nanoparticles studied by high resolution time-resolved Fourier-transform infrared spectroscopy

Svatopluk Civiš, Vladislav E. Chernov
J.Heyrovsky Institute of Physical Chemistry AV ČR, Dolejškova 3, Praha 8, Czech Republic.
Tel: +420 26605 3275; e-mail: civis@jh-inst.cas.cz

ABSTRACT
High resolution time-resolved Fourier-transform infrared spectroscopy is be applied for observations of the emission arising after irradiation of a metal and metal oxides targets with a pulsed nanosecond ArF (λ = 193 nm) laser. The infrared emission spectra will be studied in the 800–8000 cm^{-1} spectral region. Although the spectra of the atoms were studied in various frequency ranges, our study points to the existence of spectral lines, which have not yet been observed. While the visible spectral lines are due to the transitions involving the ground and low-excited states, the IR lines in atoms correspond to the transitions between highly excited (Rydberg) levels. The transition probabilities and oscillator strengths for all transitions involving the reported levels are calculated.
Keywords: Laser-induced breakdown spectroscopy, infrared spectra, Rydberg states.

1. INTRODUCTION

Pulsed laser ablation and depositing processes are currently frequently used techniques. Laser induced plasma at low fluence (typically 10 J/cm^2) has numerous applications, e. g. Pulsed Laser Deposition (PLD) for multi-elemental analysis. The latter technique, known as Laser Induced Plasma Spectroscopy (LIPS) Laser-Induced Breakdown Spectroscopy (LIBS) consists of analyzing the light spectrum emitted from a plasma created on the sample surface by laser pulses. LIPS has many practical advantages over the conventional methods of chemical analysis of elements and is consequently being considered for a growing number of applications [1]. Excimer lasers operating in near-ultraviolet regions with typical laser fluences of 1-30 J/cm^2 are used for many types of ablation.

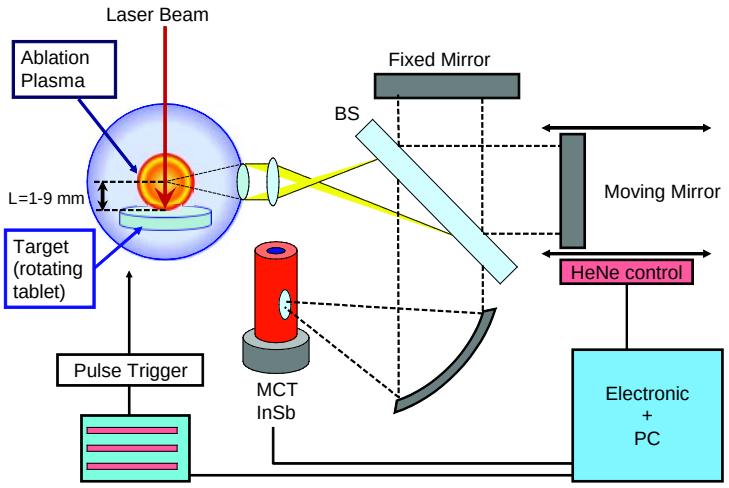

Figure 1. The sketch of the experimental setup.

The ablation plume arising after irradiation with frequencies of nanosecond duration pulses is governed by a great number of very complex physical processes. During the laser pulse (with typical duration of 20 ns), the laser photons heat the sample and bring a part of its surface to the critical temperature. The heated material starts to boil explosively and creates an emission plume consisting of ejected particles, atoms and ions. The particles inside the plume can themselves interact with the laser photons, which leads to a subsequent rise in the temperature of the ablation plume and to photochemical and photodissociation processes. The electrons created in the photodissociation processes can interact with the laser pulse via the electron ion inverse bremsstrahlung, which again causes additional heating of the plume and leads to the fast transition of the plume from ionized gas to plasma. The electrons escaping from the corona region cause a separation of charges, thereby inducing the ionized part of the plasma to accelerate. After the end of the laser pulse, the plume expands adiabatically. The electron-ion

collision inside the plume can create excited ions. The electron-ion collision in the presence of a third body can results in their recombination leading to formation of atoms in highly excited Rydberg states. A radiative cascade of these Rydberg states is then observed as the optical emission of the ablation plume. The properties of the observed plumes obtained by the ablation of different materials can eventually reflect the superposition of the ensemble processes described above.

Here is shortly reported a study focused on time-resolved spectra arising from 193 nm pulsed laser ablation of gold and silver targets in a 10^{-3}Torr vacuum. We report IR spectra of several metal atoms in the 800–8000 cm^{-1} region.

2. METHODS

The sketch of the experimental setup is presented in Fig. 1. For the measurement of the time resolved FTIR spectra the synchronous continuous scanning method was used. After each ArF laser trigger point several data points was sampled while the interferometer's mirror moved continuously. To couple this method with a laser ablation as a source of the registered emission requires a special instrumental approach. In usual time-non-resolved FT measurement the data from the detector are sampled at each zero-cross point of the He-Ne laser fringes. The difficulty of the time-resolved measurement comes from the fact that the repetition rate of the available high repetition lasers (suitable for ablation experiments) is lower than the frequency of the He--Ne laser fringes produced by the interferometer. To solve this problem following method was used. Instead of application of the laser pulse every zero-cross point of the He-Ne laser fringes only *n*-th zero-cross point triggers the laser action. As a result 1/*n* of each time-resolved interferogram is obtained after each scan [2]. The timing diagram is shown in Fig. 2.

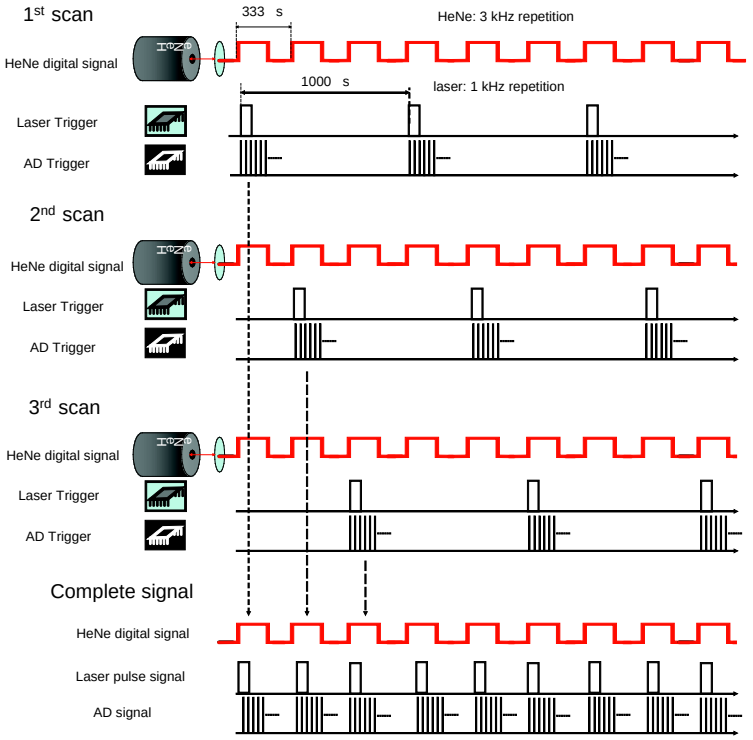

Figure 2. Timing diagram for the interleaved sampling

3. RESULTS

The infrared emission spectra of Au, Ag, Cu, Na, K and Cs resulting from the laser ablation of targets performed as metal plates or alkali metal salts (NaI, NaBr, KCl, KBr, KF, KI, CsCl and CsI) tablets in a vacuum was recorded using time-resolved Fourier-transform spectroscopy in the 800-1000, 1000-1200, 1200-1600, 18003600, 4100-5000 and 5200-7500 cm^{-1} ranges with a resolution of 0.2 cm^{-1}. The majority of the observed lines correspond to transitions between low-excited Rydberg states of metal atoms with a principal quantum number n=4..10; the most prominent lines being due to transitions between the states with high orbital momenta l=3..5.

This study reports 32 new lines of Au, 12 of Ag, 20 of Cu, 17 of Na, 26 of K and 21 of Cs (with uncertainties of 0.00030.03 cm^{-1}). The measured Na and K lines are in agreement with the solar spectra recorded in Atmospheric Chemistry Experiment (ACE). An example of the recorded spectra is given in Fig. 3.

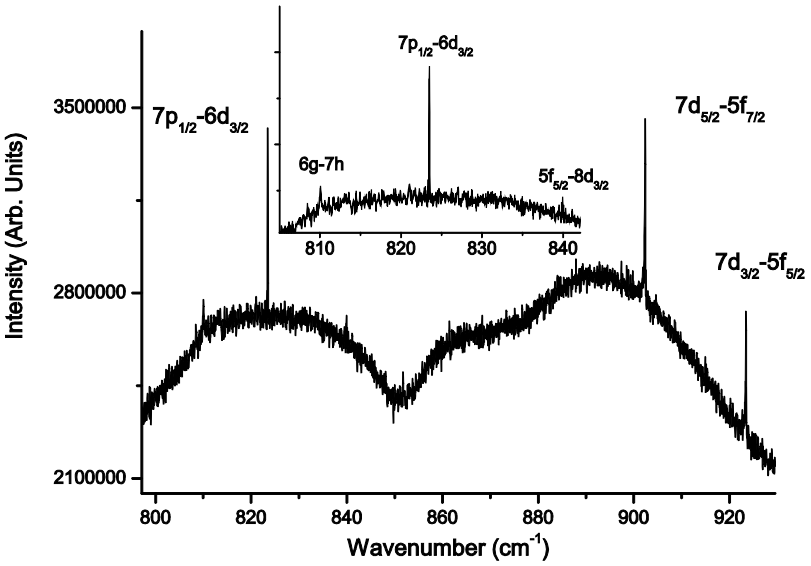

Figure 3. A part of the recorded Cs emission spectrum.

The line classification is performed using relative line strengths expressed in terms of transition dipole matrix elements calculated with the help of the single-channel quantum defect theory (QDT)[4]. We show the results for the transition probabilities and oscillator strengths for transitions between the reported atomic metal states.

For the classification of the observed IR lines, an important role is played by the *f*-, *g*- and *h*-states including those discovered in the present measurements. For all the elements considered, the most intensive emission line in the 800-1000 cm^{-1} and 1200-1600 cm^{-1} region correspond to the 6*g*-7*h* and 5*g*-6*h* transitions respectively.

The investigation of atomic emission in our LIBS experiment is complicated by nonequilibrium and nonstationary conditions of the plasma for the excited states. In particular, the emission intensities of the spectral lines show a complex dependence on the time delay τ after the ArF laser pulse shot (see Fig. 4). So the use of the time-resolved scheme is essential in our experiment.

4. CONCLUSIONS

Using Fourier-transform infrared (FTIR) spectroscopy of a plasma formed by ablation of metallic or salt targets by a pulsed nanosecond ArF laser in a vacuum, we report IR spectrum of several atomsatomic cesium in the 800–8000 cm^{-1} region. No spectra of metals were measured previously the below 2000 cm^{-1}. From the lines observed here and in our previous works we extract revised energy values for more than 150 energy levels (uncertainty 0.01--0.03 cm^{-1}) of which 8 levels of Au, 3 of 23 Ag, 4 of Cu, 1 of K, 3 of Na and 2 of Cs are reported for the first time. These newly-reported levels have high orbital momentum *l*=3,4,5.

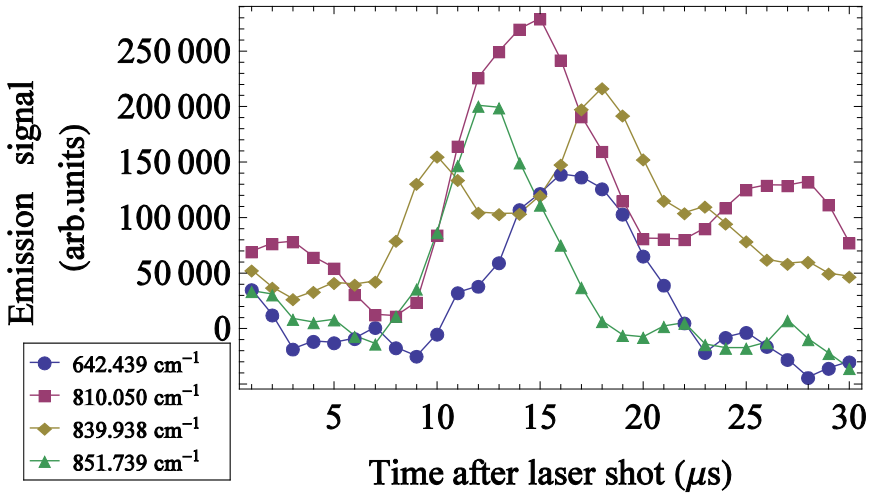

Figure 4. Time profiles of some emission lines observed in CsI ablation.

We also calculate the probabilities of transitions between the observed lines. We show a non-monotonic behavior of the emission intensity as a function of the time delay after the ablating laser shot and of the distance between the probed area and the target surface. These curves are examples of a complex dynamics of the excited state population which is only scarcely available for these states.

ACKNOWLEDGEMENTS

This work was financially supported by the Grant Agency of the Academy of Sciences of the Czech Republic (Grant No. IAA400400705).

REFERENCES

[1] D. Babánkova, S. Civiš, L. Juha: Chemical consequences of laser-induced breakdown in molecular gases, *Progress in Quantum Electronics*, vol.30, pp. 75-88, 2006.

[2] K. Kawaguchi, Y. Hama and Sh. Nishida: Time-resolved Fourier transform infrared spectroscopy: Application to pulsed discharges, *J. Mol. Spectr.*, vol.232, pp. 1-13, 2005.

[3] S. Civiš, I. Matulková, J. Cihelka, P.Yu. Buslov and V.E. Chernov: Time-resolved FTIR emission spectroscopy of Au in the 800--000 cm^{-1} region: new Rydberg transitions, *Phys. Rev. A*, vol.81, p. 012510, 2010

[4] V.E. Chernov, D.L. Dorofeev, I.Yu. Kretinin and B.A. Zon: Method of the reduced-added Green function in the calculation of atomic polarizabilities, *Phys. Rev. A*, vol.75, p.022505, 2005.

Theoretical study of loss compensation in long-range dielectric loaded surface plasmon polariton waveguides

Sonia M. García-Blanco[1], Markus Pollnau[1] and Sergey I. Bozhevolnyi[2]
[1]*Integrated Optical MicroSystems Group, MESA+ Institute for Nanotechnology, University of Twente, P.O. Box 217,7500 AE Enschede, The Netherlands*
s.garciablanco@utwente.nl
[2]*Institute of Technology and Innovation, University of Southern Denmark, DK-5230 Odense, Denmark*

ABSTRACT
In this paper, a theoretical study of loss compensation in long-range dielectric loaded surface plasmon waveguides (LR-DLSPPs) is presented. Although extendable to other gain materials, rare-earth doped double tungstates are used as gain material in this work. Two different structures are studied and the effect of the different waveguide geometrical parameters on the material gain required to fully compensate the propagation losses are reported. The simulations were performed at 1.55 μm wavelength. A material gain as low as 12.5 dB/cm was determined as sufficient to obtain complete loss compensation in one of the proposed waveguide structures supporting sub-micron lateral mode dimension.

Keywords: plasmonic waveguides; gain material; rare-earth ions; double tungstates.

1. INTRODUCTION

Surface plasmon polaritons (SPPs), evanescent electromagnetic waves propagating along metal-dielectric interfaces, have been the subject of numerous studies due to their unique properties. Promising applications in a variety of fields include optical biosensing, data storage, photovoltaic cells, and highly integrated photonic circuits [1]-[3]. Many different plasmonic waveguiding configurations have been proposed and demonstrated over the past few years [4]-[9]. In general, SPP waveguides are subject to a trade-off between mode-field confinement and propagation loss, exhibiting either good optical confinement but short propagation distances [6], or long propagation distances necessitating large mode profiles [7]. Recently, a novel type of plasmonic waveguide configuration was proposed, long-range dielectric-loaded surface plasmon polariton (LR-DLSPP) waveguides that combine the millimeter-range propagation with a relatively strong mode confinement [8], [9]. Reduced propagation losses provided by this novel structure permit enlarging the range of gain materials that can be selected for loss compensation.

Many efforts have been directed towards compensating propagation losses in plasmonic waveguides by use of different gain materials [10]-[13]. In this work, we proposed the use of rare-earth (RE) doped double tungstates, which have been recently reported to provide elevated gain [14] with very interesting characteristics, such as amplification without distortion of very-high-rate signals in the small-signal-gain regime and large gain bandwidth up to a few tens of nanometers, interesting for broadband optical amplification and the generation of ultra-short laser pulses.

In this work, loss compensation in LR-DLSPP waveguides by optical gain provided by a RE-doped double tungstate material incorporated into the LR-DLSPP configuration is theoretically studied. Two structures are presented. The effect of different waveguide parameters on the efficiency of the material gain to compensate propagation losses is evaluated. Lossless propagation is predicted for material gain as low as 12.5 dB/cm, with a mode size comparable to conventional dielectric-loaded surface plasmon polariton waveguides [15].

2. DESCRIPTION OF THE PROPOSED STRUCTURES

The generic LR-DLSPP structure includes a low-refractive-index substrate material, a buffer layer of a high-refractive-index material, a metal stripe and a dielectric ridge, the dimensions and refractive index of which should be chosen to balance the electric fields at both sizes of the gold stripe to ensure long-range propagation [8]-[9].

In this study, the substrate material chosen is SiO_2 (n ~ 1.46) and the metal selected is gold (n_{gold} = 0.55+j11.5 [16]). The wavelength utilized is 1.55 μm. The dimensions of the gold stripe were fixed in all cases to a thickness of 15 nm and a width of 200 nm. The gain material utilized is RE-doped double tungstate with refractive index ~2.05. In Structure 1 the gain material is added as the buffer layer while the ridge is made of polyimide (n ~ 1.9). In Structure 2, the buffer layer chosen is Si_3N_4 (n_{Si3N4} ~2.05) and the gain is added to the ridge. A 100 nm-thin BCB adhesive layer is introduced between the buffer layer and the ridge as part of the integration procedure of the gain material to the structure. Figure 1 shows the two structures under study.

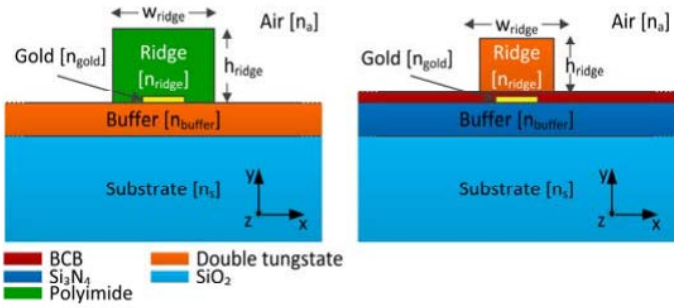

(a) *(b)*

Figure 1.Proposed LR-DLSPP structures: (a) Gain material as the bufferlayer; (b) Gain material as the ridge.

3. FINITE DIFFERENCE CALCULATIONS

Finite difference (FD) calculations with perfect magnetic conductor (PMC) and perfectly matched layers (PML) were carried out using the PhoeniX B.V. The size of the calculation window was chosen as 20 μm by 20 μm to ensure that the field at the boundaries of the window was zero. Since the simulated structures present regions with different sizes, these thinner structures were artificially divided in the required number of sublayers to ensure that enough grid points were assigned to these critical areas. The number of sublayers was selected so that the addition of more layers only produced negligible variation in the results. Figure 2 shows the mesh utilized in the simulations for Structure 2. In the metal, a grid size of 0.75 nm was utilized (i.e., the metal stripe of 15 nm thickness was represented by 20 sublayers).

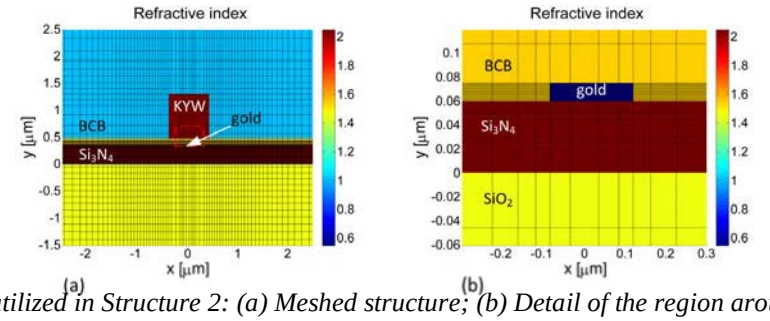

Figure 2. Mesh utilized in Structure 2: (a) Meshed structure; (b) Detail of the region around the gold layer.

4. RESULTS

The two structures proposed in Section 2 were simulated as described in Section 3. The net propagation loss of the structures was calculated as a function of the buffer thickness for different ridge dimensions. It is well known that in a LR-DLSPP waveguide, the electric fields above and below the gold stripe should be as balanced as possible in order to minimize propagation losses [8]. Furthermore, in order to enhance the effectiveness of loss compensation by the gain material, the confinement of the mode into the gain region should be maximized. Both effects can be related as

$$\alpha_{net} = \alpha_{loss} - \Gamma g_{mat} \quad (1)$$

where α_{net} is the net modal loss in dB/cm, α_{loss} is the propagation loss of the passive structure in dB/cm, Γ is the fraction of optical power overlapping with the gain region, and g_{mat} is the material gain provided by the material utilized in the gain region. α_{loss} finds a minimum at the point of electric field balance. Figure 3 (a) shows this effect applied to Structure 1. For each ridge size, there is a thickness of the buffer layer that minimizes the losses. In the case of Structure 1, as the ridge height is increased for a given ridge width, a thicker buffer is required to balance the electric field above and below the gold stripe. The power confinement to the active gain region (Figure 3 (e)), which in this case is the buffer layer, follows the opposite trend. The thinner the ridge, the more the mode is pushed towards the active buffer layer. Figures 3 (b)-(d) shows the combined effect for different values of the material gain of the buffer layer. Figure 3 (f) shows the evolution of the lateral mode dimension as a function of buffer thickness for different ridge dimensions.

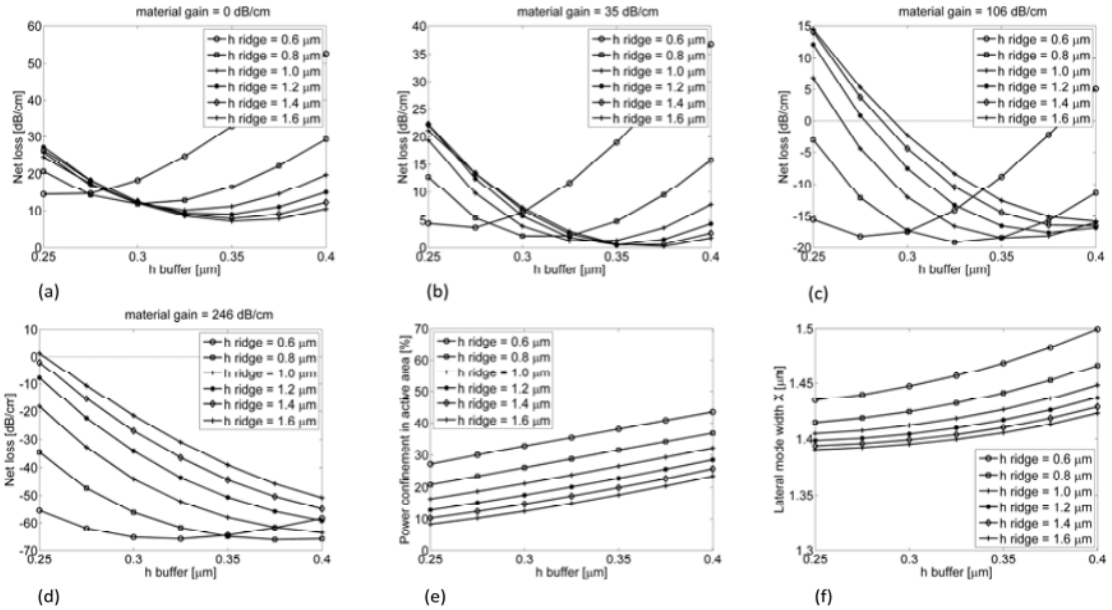

Figure 3. Effect of different geometrical parameters on the performance of Structure 1: (a)-(e) Net loss versus buffer thickness for a ridge width of 1.6 μm and different ridge heights. Material gain investigated are 0, 35, 106 and 246 dB/cm; (e) Power confinement in active area; (f) Lateral mode width.

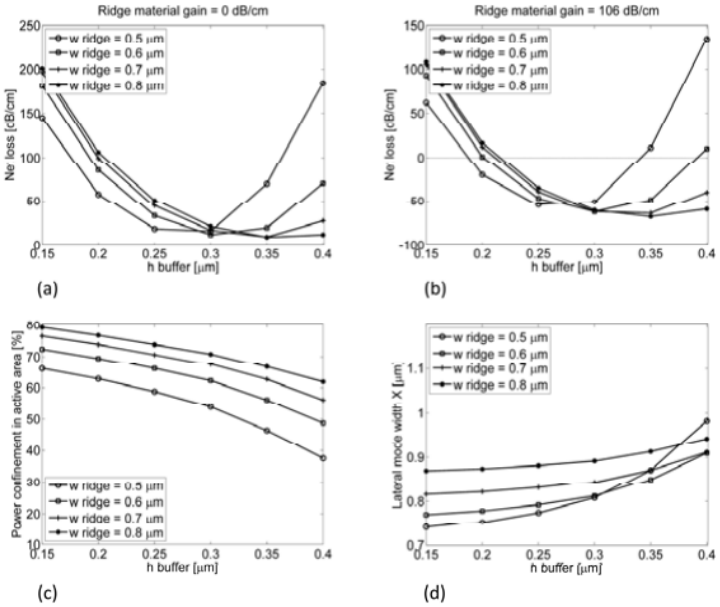

Figure 4. (a) Net loss for Structure 2 with no gain, ridge height of 0.8 μm and several ridge widths; (b) Net loss when using material gain of 106 dB/cm; (d) Power confinement in active area; (d) Lateral mode width.

Similar set of simulations were carried out for Structure 2 (Figure 4). The much larger confinement to the active region, in this case the waveguide ridge, permits a much more efficient utilization of the material gain for plasmonic loss compensation. Figure 5 shows the mode profiles of the waveguide geometries requiring the smallest material gain to achieve full loss compensation. A minimum material gain of 37 dB/cm is required for Structure 1 (ridge dimensions 1.6x1.6 μm^2 and buffer thickness 0.37 μm). A gain as small as 12.5 dB/cm suffice to fully compensate propagation losses in Structure 2 (ridge dimensions 0.8x0.8 μm^2 and buffer thickness 0.35 μm). This latter structure supports a propagation mode with sub-micron lateral dimension (0.92 μm).

5. CONCLUSIONS

The structures considered in this paper show a great potential to reach the goal of loss compensation in plasmonic waveguides and are promising for plasmon amplification and lasing. The low material gain required to compensate propagation losses, 37 dB/cm in Structure 1 and 12.5 dB/cm in Structure 2 broadens the range of gain materials that can be utilized. RE-doped double tungstate gain materials were selected in this study due to

their very good match of refractive index with the materials utilized in the structure and the interesting characteristics of the gain they can provide. Experimental demonstration of the considered structures will constitute the next milestone on the way towards lossless plasmonic waveguides.

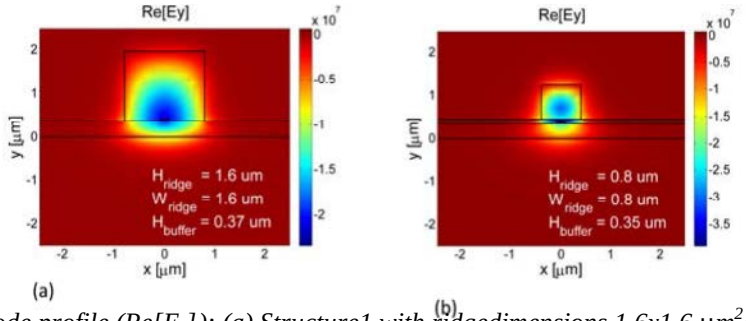

Figure 5.2-D mode profile (Re[E_y]): (a) Structure1 with ridgedimensions 1.6x1.6 μm^{2}and buffer height of 0.37 μm;(b)Structure2 with ridge dimensions 0.8x0.8 μm^{2}and buffer height of 0.35 μm.

ACKNOWLEDGEMENTS

The authors acknowledge support from the COST Action MP0702: Towards functional sub-wavelength photonic structures. Support from the FP7 Marie Curie Career Integration Grant PCIG09-GA-2011-29389 (SMGB) and. Danish Council for Independent Research FTP-project No. 09-072949 ANAP (SIB) is also appreciated.

REFERENCES

[1] Q. Min, C. Chen, P. Berini, and R. Gordon, "Long range surface plasmons on asymmetric suspended thin film structures for biosensing applications," Opt. Express **18**, 19009-19019 (2010).

[2] M. Mansuripur, A. R. Zakharian, A. Lesuffleur, S.-H. Oh, R. J. Jones, N. C. Lindquist, H. Im, A. Kobyakov, and J. V. Moloney, "Plasmonic nano-structures for optical data storage," Opt. Express **17**, 14001-14014 (2009).

[3] H. A. Atwater and A. Polman, "Plasmonics for improved photovoltaic devices," Nat. Mater. **9**, 205-213 (2010).

[4] R. F. Oulton, V. J. Sorger, D. A. Genov, D. F. P. Pile, and X. Zhang, "A hybrid plasmonic waveguide for subwavelength confinement and long-range propagation," Nat. Photonics **2**, 496-500 (2008).

[5] J. A. Dionne, L. A. Sweatlock, H. A. Atwater, and A. Polman, "Plasmon slot waveguides: Towards chip-scale propagation with subwavelength-scale localization," Phys. Rev. B **73**, 035407 (2006).

[6] T. Holmgaard and S. I. Bozhevolnyi, "Theoretical analysis of dielectric-loaded surface plasmon-polariton waveguides," Phys. Rev. B **75**, 245405 (2007).

[7] P. Berini, "Plasmon-polariton waves guided by thin lossy metal films of finite width: Bound modes of symmetric structures," Phys. Rev. B **61**, 10484-10503 (2000).

[8] T. Holmgaard, J. Gosciniak, and S. I. Bozhevolnyi, "Long-range dielectric-loaded surface plasmon polariton waveguides," Opt. Express **18**, 23009-23015 (2010).

[9] J. Gosciniak, T. Holmgaard, and S. I. Bozhevolnyi, "Theoretical analysis of long-range dielectric-loaded surface plasmon polariton waveguides," J. Lightwave Technol. **29**, 1473-1481 (2011).

[10] J. Grandinier, G. Colas des Francs, S. Massenot, A. Bouhelier, L. Markey, J.-C. Weeber, C. Finot, and A. Dereux, "Gain-assisted propagation in a plasmonic waveguide at telecom wavelength," Nano Lett. **9**, 2935-
2939 (2009).

[11] I. De Leon and P. Berini, "Amplification of long-range surface plasmons by a dipolar gain medium," Nat. Photonics **4**, 382-387 (2010).

[12] A. V. Krasavin, T. P. Vo, W. Dickson, P. M. Bolger, and A. V. Zayats, "All-plasmonic modulation via stimulated emission of copropagating surface plasmon polaritons on a substrate with gain," Nano Lett. **11**, 2231-2235 (2011).

[13] I. P. Radko, M. G. Nielsen, O. Albrektsen, and S. I. Bozhevolnyi, "Stimulated emission of surface plasmon polaritons by lead-sulphide quantum dots at near infra-red wavelengths," Opt. Express **18**, 18633-18641 (2010).

[14] D. Geskus, S. Aravazhi, S. M. García-Blanco, and M. Pollnau, "Giant optical gain in a rare-earth-ion-doped microstructure," Adv. Mater., in press (2011).

[15] S. M. García-Blanco, M. Pollnau, and S. I. Bozhevolnyi, "Loss compensation in long-range dielectric-loaded surface plasmon-polariton waveguides", Opt. Express **19**, 25298-25311 (2011).

[16] M. L. Theye, "Investigation of the optical properties of Au by means of thin semitransparent films," Phys. Rev. B **2**, 3060-3078(1970).

Design of photonic system for energy assisted magnetic recording

John Donegan
School of Physics and CRANN, Trinity College Dublin, Dublin 2, Ireland
jdonegan@tcd.ie

ABSTRACT
The density in magnetic recording media continues to increase strongly. New technologies are now under investigation including energy assisted magnetic recording (EAMR). Using a near-field optical probe, a spot size of less than 50 nm x 50 nm can be created on the surface of the magnetic media. The E-field intensity at the surface is such as to strongly heat the medium above the Curie temperature with a large temperature gradient.
Details of our recent modeling studies using FEM analysis will be presented in which we will show the design of the near-field transducer that can produce a very significant temperature increase while preserving a long lifetime of the transducer, a very necessary condition for this technology to become a reality.

NOTES

Some Basic Aspects of Computational Photonics

Alexander Quandt[1], Robert Warmbier[1], George S. Manyali[1] and Heinrich A. M. Leymann[2]
[1] *School of Physics and DST/NRF Centre of Excellence in Strong Materials, University of the Witwatersrand, Private Bag 3, 2050 Johannesburg, South Africa.*
Tel: +27-11-717-6956; e-mail: alex.quandt@wits.ac.za
[2] *InstitutfuerTheoretischePhysik, Universitaet Magdeburg, Postfach 4120, 39126 Magdeburg, Germany.*

ABSTRACT
With modern simulation methods, it is possible to model photonic crystals and photonic devices from the bottom up, starting with the atomic and electronic structure of the underlying dielectrics. To this end, one has to combine the fastest and most accurate modern ab initio simulation methods based on Density Functional Theory (DFT) with programs that directly solve either Maxwell's equations or the related wave equations for a given complex combination of dielectrics. This leads to some sort of multi-scale approach to computational photonics. We present various technical aspects of the underlying simulation methods, and give some illustrative examples.

Keywords: Dielectric properties, density functional theory, photonic band structure, photonic crystals.

1. INTRODUCTION

Although our general knowledge of photonics is pretty advanced [1], one often realizes in practice that the basic materials aspects cause most of the difficulties in achieving certain functionalities within a given frequency range. Stresses/strains, cracks, diffusion, impurities, dislocations accompany any production process that aims at the layout of a complex dielectric matrix for a given application. Sometimes we do not even know the best possible materials for given frequency range, because any combination of standard materials for other frequency ranges will not show the required dielectric contrast, or be plagued by massive losses in that specific frequency range. And also from a purely structural point of view, while searching for a rather specific functionality, we might even want to deviate from standard photonic matrices, and give up periodicity to a certain extent.

Therefore it is clear that the optimization of the fabrication processes will also require a proper modelling of the dielectric matrix, which amounts to perform some sort of computer experiments on a given system, changing the arrangement of real and photonic atoms (layers, columns, spheres). In this sense numerical simulations might actually serve as some sort of guiding line for real experiments and synthesis processes, because without a proper optimum layout of the dielectric matrix, the whole process of creating a specific photonic device might turn out to be far too costly and time consuming.

As many of the physical or chemical processes that accompany the synthesis and layout of a dielectric matrix have their causes in the atomic structure of the dielectric components, it is crucial to have a detailed understanding of the optical properties of materials already at the atomic scale. The method of choice are modern ab initio methods based on Density Functional Theory (DFT) ([2]-[3]), as described and illustrated in Section 2.

Once the dielectric tensor is known for various dielectric components, we can include this information into the macroscopic Maxwell equations, and solve them for a given scenario. Some of the most important applications are photonic crystals and their related photonic band structures [4], which will be described and illustrated in Section 3. We will close with a short summary and outlook.

2. AB INITIO DETERMINATION OF THE DIELECTRIC TENSOR

The most direct approach to determine the dielectric tensor ε within the framework of DFT is the evaluation of ε in the basis of Kohn-Sham orbitals, as described below. However, such a straightforward approach will exclude local field effects. The latter may nevertheless be included using advanced numerical techniques like Density Functional Perturbation Theory (DFPT) [5]. We will give a short summary of the basic formalism, and discuss some illustrative examples for cubic diamond and rhombohedral α-boron using a plane-wave based ab initio package called VASP [6]-[9].

2.1 Density Functional Theory and Dielectric Properties.

Within DFT, the electronic part of a complex molecular or solid system is represented by an energyfunctional $E[n]$, which depends on the one-particle density n. Within the Kohn-Sham approximation, $E[\psi_i,n]$ is also supposed to depend on the one-electron orbitals ψ_i from which n is built [3]:

$$E[\psi_i, n] = \sum_{i}^{occ} \langle \psi_i | T + V_{ext} | \psi_i \rangle + E_{HXC}[n] \quad (1)$$

The first term in equation (1) denotes the matrix elements of the kinetic energy T and the external potential V_{ext}, whereas the density dependent part E_{HXC} includes the classical electron-electron interactions, as well as exchange

and correlation effects. The art of doing DFT is to somehow guess the most accurate *approximate* form of this important last term E_{HXC} [3].

Once a proper approximation for E_{HXC} is in place, the ground state of the electronic system is obtained by minimization the energy functional $E[\psi_i,n]$ with respect to the orbitals, which leads to a system of coupled one-particle equations (Kohn-Sham equations [3]):

$$H|\psi_i\rangle = \varepsilon_i|\psi_i\rangle \text{ with } H = T + V_{ext} + \frac{\delta E_{HXC}}{\delta n} \tag{2}$$

This system of Kohn-Sham equations has to be solved self-consistently, and the best numerical strategy consists of mapping equation (2) on a system of linear equations, simply by expanding the orbitals ψ_i into various suitable basis sets, in particular Gaussians and plane waves. The latter are very popular for simulating solid systems, as they are a natural choice for representing Bloch states. But a plane wave basis set also allows for an efficient use of FFT techniques [8]-[9], as well as an easy implementation of pseudopotentials and related concepts [10].

Once the orbitals ψ_i have been determined by solving equation (2) self-consistently, one may directly evaluate the imaginary part of the frequency-dependent dielectric tensor ε for a given plane wave basis set as follows (see [11]):

$$\varepsilon^I_{\alpha,\beta}(\omega) = \frac{4\pi^2 e^2}{\Omega} \lim_{q\to 0} \frac{1}{q^2} \sum_{c,v,\mathbf{K}} 2w_{\mathbf{K}} \delta(\varepsilon_{c\mathbf{K}} - \varepsilon_{v\mathbf{K}} - \omega) \times \langle u_{c\mathbf{K}+\mathbf{e}_\alpha q} | u_{v\mathbf{K}} \rangle \langle u_{c\mathbf{K}+\mathbf{e}_\beta q} | u_{v\mathbf{K}} \rangle^* \tag{3}$$

Here Ω is the volume of the unit cell, the indices *c* and *v* refer to conducting and valence states respectively. Furthermore within the **K**-space related to the plane wave basis, the $w_{\mathbf{K}}$ represent integration weights, and $u_{c\mathbf{K}}$ is the cell-periodic part of the orbital Bloch states. From the knowledge of the imaginary part of ε described in equation (3), the real part of ε may be determined with the help of the Kramers-Kronig relations, as described in [11]. Note that expressions like equation (3) will not include local field effects. But the latter may be included using Density Functional Perturbation Theory (DFPT, see [5], [11]), or using the so-called GW method [12].

2.2 Examples: First Principles Dielectric Tensors for Diamond and α-Boron.

In Fig. 1 we show some examples for a first principles determination of the frequency-dependent dielectric tensor using VASP. We used the PAW method [10] for the representation of the ionic cores, and excluded local field effects [11]. Our results are nevertheless in good agreement with previous measurements and simulations.

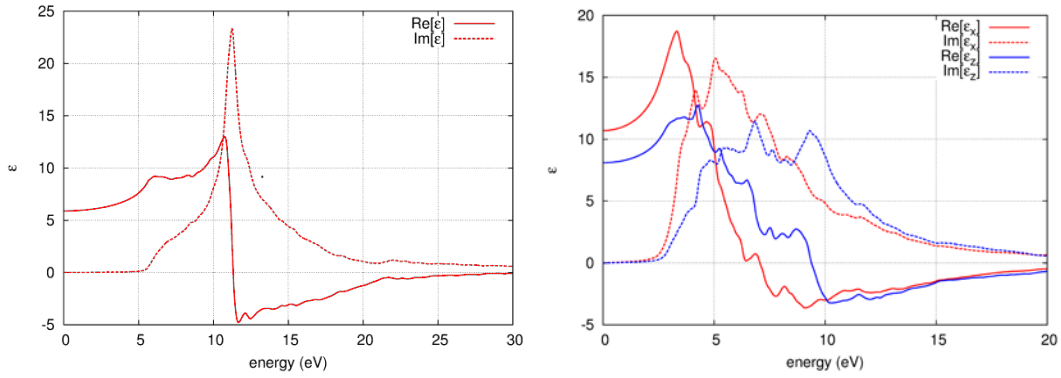

Figure 1. Real and imaginary parts of the dielectric tensor ε for cubic diamond (left) and rhombohedral α-boron (right). The calculated values span a technologically interesting energy range from the UV to the IR.

Note that diamond has cubic symmetry, and therefore the diagonal elements of the dielectric tensor ε are all equal. Whereas in the case of rhombohedral α-boron, the orientation of the main axes for the dielectric tensor are different from the orientation of the three lattice vectors, which results in an anisotropic dielectric tensor. The general behaviour of the dielectric properties is also in agreement with the Lorentz oscillator model [1]. The real part of ε is positive for frequencies below resonance, zero at resonance, and negative above resonance, and also the imaginary part of ε still resembles the Lorentzian predicted by the oscillator model model [1].

Furthermore the oscillator model also tells us about the asymptotic behaviour of the dielectric tensor. The real part of ε is supposed to go to a constant ε_∞ at low frequencies, and ε should approach a value of 1 from below at higher frequencies (i.e. the typical realm of x-ray diffraction!). On the other hand the imaginary part of ε should go to zero for low as well as high frequencies. We see that the numerical simulations are also able to reproduce this general behaviour in a reasonable fashion.

3. PHOTONIC BAND STRUCTURE CALCULATIONS

After a first principles determination of the dielectric tensor ε the next step of the multi-scale approach consists of plugging that tensor into Maxwell's equations, and solve the latter for certain scenarios. In most cases, the solution to Maxwell's equations can only be found numerically, and sometimes the non-idealized (i.e. complex) numerical ε may actually lead to rather surprising results that challenging common textbook wisdom [13]. In this section however we only focus on lossless homogeneous dielectric materials, and explore the photonic band structures of complex photonic crystals made of such components. Our methods of choice are frequency domain methods [4] based on a plane-wave basis set [14]-[15]. In the following, we will sketch the basic formalism, and discuss an illustrative example from a detailed study of complex 2D Archimedean photonic crystals [16].

3.1 Frequency Domain Methods

Frequency domain techniques are a popular approach to predict the optical behaviour of photonic crystals and related photonic devices. The materials properties of the underlying complex dielectric matrix will enter Maxwell's equations through a position dependent and periodic ε(**r**), whereas we assume μ ≈ 1 for most applications. The fluctuating ε(**r**) may be pictured as a periodic dielectric matrix made of various homogeneous components, each of them characterized by a specific ε. Light within such a periodic dielectric medium tends to form standing Bloch waves, and the major numerical task consists of the determination of these Bloch waves by solving the wave equation for the related magnetic field **H**(**r**), subject to a transversality condition (no free charges and currents):

$$\nabla \times \left(\frac{1}{\varepsilon(\mathbf{r})} \nabla \times \mathbf{H}(\mathbf{r}) \right) = \left(\frac{\omega}{c} \right)^2 \mathbf{H}(\mathbf{r}) ; \qquad \nabla \cdot \mathbf{H}(\mathbf{r}) = 0 \tag{4}$$

It must be pointed out that the **H**(**r**) are Bloch waves, in analogy to electronic Bloch states within solid systems. Therefore the eigenvalues of equation (4) imply a dispersion relation ω(**K**), and thus a photonic band structure. Of particular interest are the band gaps within a given photonic band structure, because the band gaps correspond to decaying optical states, and ultimately lead to omnidirectional total reflection for a certain frequency range.

By expanding the photonic Bloch waves into a plane-wave basis set, one may map the eigenvalue problem of equation (4) onto a system of linear equations. A proper discretization of ε(**r**), the implementation of FFT techniques as well as band-by-band conjugate-gradient minimization techniques are the key features for the development of fast and memory efficient algorithms to determine **H**(**r**) [14]-[15]. However, none of these numerical algorithms is really restricted to real and lossless ε(**r**) [4], and some of the more general cases are actually implemented in the software package MPB [15] issued by MIT.

Note that once we know the magnetic field **H**(**r**), the corresponding electric field **E**(**r**) may easily be determined from:

$$\mathbf{E}(\mathbf{r}) = \left(\frac{-ic}{\omega \varepsilon(\mathbf{r})} \right) \nabla \times \mathbf{H}(\mathbf{r}) \tag{5}$$

3.2 Example: Gap Maps for 2D Archimedean Photonic Crystals.

For many technological applications like photonic wave guides or photonic fibres (see [1] and [4]), it is important to have a way of predicting the size of the photonic band gap as a function of important structural parameters (gap maps). In Fig. 2 we reproduced such a photonic gap map for a complex Archimedean tiling, where the band structure calculations has been performed using our own domestic software package [14].

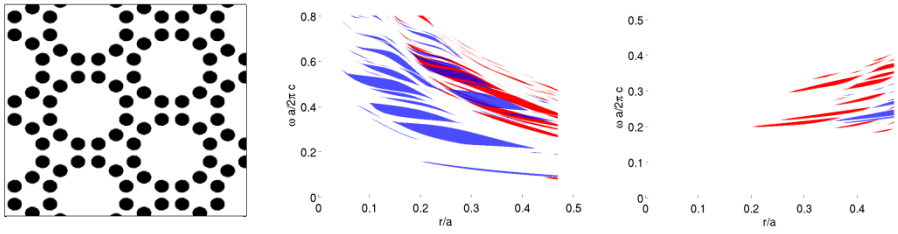

Figure 2. Archimedean tiling 4621 (left) and the corresponding gap maps (i.e. size of gap vs. radius) for columns in air (middle), and air holes drilled into a dielectric matrix. For our simulations we chose ε=11.3 for the dielectics, and ε=1 for air. Blue colors indicate TM band gaps, red colors indicate TE band gaps.

Our results reveal a number of overlapping regions for band gaps, which corresponds to in-plane and out-of-plane polarizations of the photonic Bloch waves. As the band gap for each of the polarization of a given Bloch

wave implies omnidirectional total reflection within the plane, the overlap regions actually indicate omnidirectional total reflection for all polarizations.
The purpose of such studies is to understand the appearance of robust and wide omnidirectional band gaps as a function of structural complexity. This knowledge should become most useful for frequency ranges, where the only available dielectric materials show a rather narrow range of dielectric contrasts. As small dielectric contrast implies rather narrow photonic band gaps for the known standard systems with photonic band gaps (for a survey see [4]), the only promising strategies to develop working photonic devices within these frequency ranges could be the introduction of structural disorder to localize propagating optical modes within a certain frequency ranges, and/or modifications of the basic dielectric components on the atomic scale, already. Both approaches are perfectly covered by the multi-scale approach described above.

4. CONCLUSIONS

We discussed the key numerical elements of a multi-scale approach to model complex photonic structures and devices. One component is the proper numerical determination of dielectric properties from first principles, based on modern ab initio DFT methods. The second component is a numerical solution to Maxwell's equations and/or the related wave equations, as exemplified for plane wave based frequency domain methods to determine the band structure of photonic crystals. We sketched the theoretical background of both numerical components, and discussed some illustrative examples.
We believe that the multi-scale approach should become most useful in frequency ranges, where there is little dielectric contrast, and where only a proper combination of suitably nanostructured materials and a very specific layout of the resulting complex dielectric matrix might actually lead to functional photonic devices.

ACKNOWLEDGEMENTS

A.Q., R.W. and G.S.M. would like to thank the School of Physics and the DST/NRF Centre of Excellence in Strong Materials at the University of the Witwatersrand for financial and hardware/software support. A. Q. also likes to thank the National Institute for Theoretical Physics (NITheP) for financial support, and Profs. A. Every (Wits) and M. Ferrari (Trento) for many valuable discussions.

REFERENCES

[1] B.E.A. Saleh, M.C. Teich: *Fundamentals of Photonics*, Hoboken: Wiley-Interscience, 2007.
[2] P. Hohenberg, W. Kohn: Inhomogeneous Electron Gas, *Phys. Rev.*, vol. 136. pp. B864, 1964.
[3] R.G. Parr, W. Yang: *Density-Functional Theory of Atoms and Molecules*, Oxford: Clarendon Press, 1989.
[4] J.D. Joannopoulos, S.G. Johnson, J.N. Winn, R.D. Meade: *Photonic Crystals, Molding the Flow of Light (2nd ed.)*, Princeton: Princeton University Press, 2008.
[5] S. Baroni, S. de Gironcoli, A. Dal Corso: Phonons and related crystal properties from density-functional perturbation theory, *Rev. Mod. Phys.*, vol. 73. pp. 515, 2001.
[6] G. Kresse, J. Hafner: Ab initio molecular dynamics for liquid metals, *Phys. Rev. B.*, vol. 47. pp. 558, 1993.
[7] G. Kresse, J. Hafner: Ab initio molecular dynamics simulation of the liquid- metal amorphous semiconductor transition in germanium, *Phys. Rev. B.*, vol. 49. pp. 14251, 1994.
[8] G. Kresse and J. Furthmueller: Efficiency of ab initio total energy calculations for metals and semiconductors using a plane-wave basis set, *Comp. Mat. Sci.*, vol. 6. pp. 15-50, 1996.
[9] G. Kresse and J. Furthmueller: Efficient iterative schemes for ab initio total-energy calculations using a plane-wave basis set, *Phys. Rev. B.*, vol. 54. pp. 11169, 1996.
[10] G. Kresse, J. Joubert: From ultrasoft pseudopotentials to the projector augmented-wave method, *Phys. Rev. B.*, vol 59. pp. 1758, 1999.
[11] M. Gajdos, K. Hummer, G. Kresse, J. Furthmueller, F. Bechstedt: Linear optical properties in the projector-augmented wave methodology, *Phys. Rev. B.*, vol. 73. pp. 045112, 2006.
[12] M. Shishkin and G. Kresse: Implementation and performance of frequency-dependent GW method within PAW framework, *Phys. Rev. B.*, vol. 74, 025101, 2006.
[13] R. Warmbier, A. Quandt, G.S. Manyali: About surface plasmon polaritons in uniaxial anisotropic materials, submitted to *Phys. Rev. B.*, 2011.
[14] A. Quandt and H.A.M. Leymann: Simulation of Complex Dielectric Materials, *Adv. Sci. Tech.*, vol. 71. pp. 58, 2010.
[15] S.G. Johnson, J.D. Joannopoulos: Block-iterative frequency domain methods for Maxwell's equations in a planewave basis, Optics Express, vol. 8. pp. 173, 2001.
[16] H.A.M. Leymann: *Theorie und Simulation OptischerEigenschaftenKomplexerDielektrischerMaterialien* (Theory and simulation of optical properties for complex dielectric Materials), diploma thesis, InstitutfuerPhysik der Universitaet Greifswald, Germany, 2010.

Peculiarities of the Electric Field Controlling of Goos-Hänchen Effect in 1D Magnetic Photonic Crystal

Yuliya S. Dadoenkova[1], Igor L. Lyubchanskii[1,2], YoungPak Lee[3], Theo Rasing[4]
[1] *Donetsk Physical & Technical Institute of the NAS of Ukraine, R.Luxemburg str. 72, 83114, Donetsk, Ukraine*
Tel: +38062 3115227; e-mail: igorl@fti.dn.ua
[2] *Department of Physics and Technology, Donetsk National University, 83000, Donetsk, Ukraine*
[3]*Quantum Photonic Science Research Center (q-Psi) and Department of Physics, Hanyang University, Seoul 133-791, Republic of Korea*
[4]*Radboud University Nijmegen,Institute for Molecules and Materials, 6525 AJ Nijmegen, the Netherlands*

ABSTRACT
The Goos-Hänchen effect at light transmission through a one-dimensional magnetic photonic crystal with a complex defect layer composed of an electro-optic and magneto-optic material is investigated theoretically. The influence of the position of the defect layers as well as the presence of a permanent external electric field on the Goos-Hänchen shift is investigated, taking into account the frequency dispersion of the permittivities of the system.

Keywords: Goos-Hänchen effect, magnetic photonic crystal, electro-optics.

1. INTRODUCTION

During the last decades photonic crystals (PCs) are intensively investigated because of their promising applications in modern photonics [1]. The PCs are artificial structures composed of materials with different refractive indices and periodic in one-, two-, or three dimensions, with periods comparable to the wavelength. If the periodicity of a PC is destroyed via the introduction of an extra element inside the periodic structure, a new narrow peak called “defect mode” arrives inside the photonic band gap (PBG).

In this communication, we investigate a one-dimensional PC composed from finite-size magnetic PCs spaced by complex defect composed of MO and EO sublayers. The transmittivity of the EO/MO bilayer is very sensitive to the action of an external electric field [2, 3]. It should expect that such EO/MO bilayer embedded into the magnetic PC will demonstrate new peculiarities in optical and MO effects in transmitted light, for example, Goos-Hänchen (GH) effect.

2. MODEL AND NUMERICAL RESULTS

Please check spelling in your paper and do not use automatic hyphenation. Additionally, be sure your sentences are complete and that there is continuity within your paragraphs. Check the numbering of your graphics and make sure that all appropriate references are included.

We consider a finite size 1D periodic photonic system composed of three PCs of structure $(NM)^n$ with a period $D=d_N+d_M$, where layer N is gadolinium-gallium garnet (GGG) $Gd_3Ga_5O_{12}$ with thickness d_N, and layer M is yttrium-iron garnet (YIG) $Y_3Fe_5O_{12}$ with thickness d_M, and two defect layers placed between these PCs, as shown in Fig. 1. The layers of the PC are located in the *xy*-plane and the *z*-axis is normal to the interfaces. The defect layers consist of an EO ZnSe film of thickness d_{EOL} and a MO film of bismuth-iron garnet (BIG) $Bi_3Fe_5O_{12}$ of thickness d_{MOL}. Between these defect layers *m* periods of the PC are placed. We assume that the magnetization vectors **M** in the YIG and BIG films are parallel to the *z*-axis. A DC external electric field $\mathbf{E}_0$ is applied to the system in an arbitrary direction.

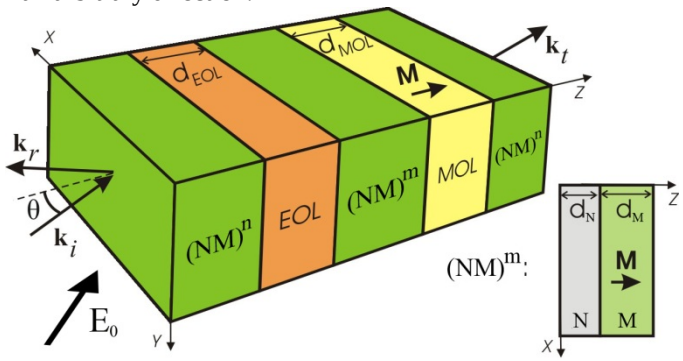

Figure 1. Schematic picture of 1D PC with two defect layers: $(NM)^n(EOL)(NM)^m(MOL)(NM)^n$. Here $\mathbf{k}_i$, $\mathbf{k}_r$ and $\mathbf{k}_t$ denote wave vectors of the incident, reflected and transmitted light, respectively, θ is the incidence angle.

The EO effects consist of a change in the optical properties of a material in response to an electric field. The tensor of the dielectric permittivity of the EO materialcan be represented as a power series on the applied electric field strength $\mathbf{E}_0$as $\varepsilon_{ij}^{(1)} = \varepsilon_{0ij}^{(1)} + r_{ijk}E_{0k} + R_{ijkl}E_{0k}E_{0l} + \ldots$, where $\varepsilon_{0ij}^{(1)}$ is the permittivity without external electric field, r_{ijk} and R_{ijkl} are linear and quadratic EO tensors, respectively. The form of the EO tensors and the nonzero components of r_{ijk} and R_{ijkl} for ZnSe can be found in [4]. The transmittivity in the photonic structure described above is calculated by means of a 4×4 transfer matrix method with taking into account the frequency dispersion of the dielectric permittivities $\hat{\varepsilon}^{(i)}$ of the PC constituents in the near infrared regime.

The GH effect consists in a lateral shift of the reflected and transmitted light relatively to the position followed from the geometry optics. The transmitted beam demonstrates a space shift relatively to the incident wave packet on the length $\Delta\hat{X} = \dfrac{\partial\hat{\psi}}{\partial k_z}$, where $\hat{\psi} = \arctan\left(\mathrm{Im}\left(\hat{T}\right)/\mathrm{Re}\left(\hat{T}\right)\right)$ is phase difference of the transmitted and incident light.

Results of the numerical calculations are presented in Figs. 2, 3, and 4. Thicknesses of the layers in the PC are taken to be d_N=0.25μm, d_M=0.33μm, d_{EOL}=6.42μm, and d_{MOL}=0.58μm. The total number of periods of the PC is fixed to 24. An external electric field is of magnitude E_0~10 MV/m.

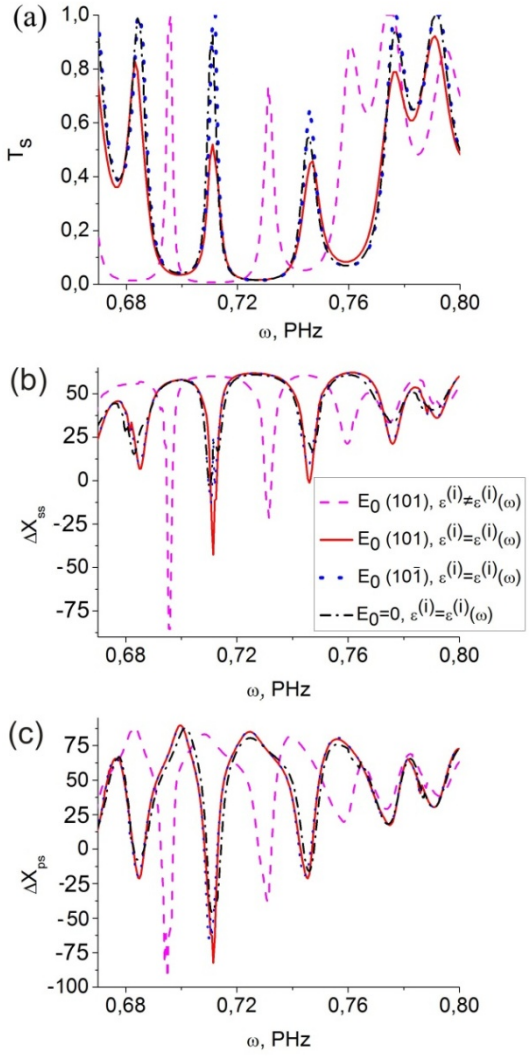

Figure 2. Transmittivity spectra of p-polarized light for PC $(NM)^{12}(EOL)(MOL)(NM)^{12}$ *(a), normalized GH shifts* ΔX_{ss} *(b) and* ΔX_{ps} *(c) with incidence angle* 30°*, in the absence of* $\mathbf{E}_0$*, andin the cases of an external electric field* $\mathbf{E}_0$ *applied in directions (101) and* $(10\bar{1})$ *with and without taking into account the frequency dispersion of* $\hat{\varepsilon}^{(i)}$

Transmittivity spectra in the first PBG for *s*- (p-)-polarized incident light, normalized GH shifts $\Delta X_{ss} \cdot k_0$ (ΔX_{pp}) and ΔX_{ps} (ΔX_{sp}) for the PC $(NM)^{12}(EOL)(MOL)(NM)^{12}$ at the incidence angle 30° are plotted in Fig. 2 (Fig.3) as functions of the frequency ω taking into account the frequency dispersion of $\hat{\varepsilon}^{(i)}$ without $\mathbf{E_0}$, and for $\mathbf{E_0}$ along the (101) and $(10\bar{1})$ directions (dash-dotted, solid and dotted lines, respectively), and without taking into account the frequency dispersion of $\hat{\varepsilon}^{(i)}$ with $\mathbf{E_0}$ along the (101) direction (dashed curve).

The application of an external electric field leads to an increase of the DMs for *s*-polarized incident light. For *p*-polarized light, $\mathbf{E}_0$ results in a transmittivity shift towards the higher frequencies without sufficient increase of the DMs (see Fig. 3(a)).

As one can observe from Figs. 2 and 3, two sharp minima of ΔX_{ij} occur at frequencies which correspond to the DMs. Application of $\mathbf{E_0}$ leads to small enhancement of ΔX_{ij} . Comparing Figs. 2(b), 2(c) and 3(b), 3(c) one can see that the reversal of the *z*-component of $\mathbf{E_0}$ results in significant decrease of minima and increase of maxima of GH shift of *p*-polarized transmitted light, whereas change of GH shift of *s*-polarized transmitted light is relatively small. It should be noted that ΔX_{sp} and ΔX_{ps} are equal only for $\mathbf{E_0}$ absence (see Figs. 6(b) and (d)). External electric field acts on *s*- and *p*-polarized EMWs in diverse way because of different changes of $\hat{\varepsilon}^{(EOL)}$ components, which results in unequal GH shifts of cross-polarized transmitted light. One can see that taking into account the frequency dispersion of $\hat{\varepsilon}^{(i)}$ results in a PBG's, as well as ΔX_{ij} shift towards higher frequencies (see Figs. 2 and 3).

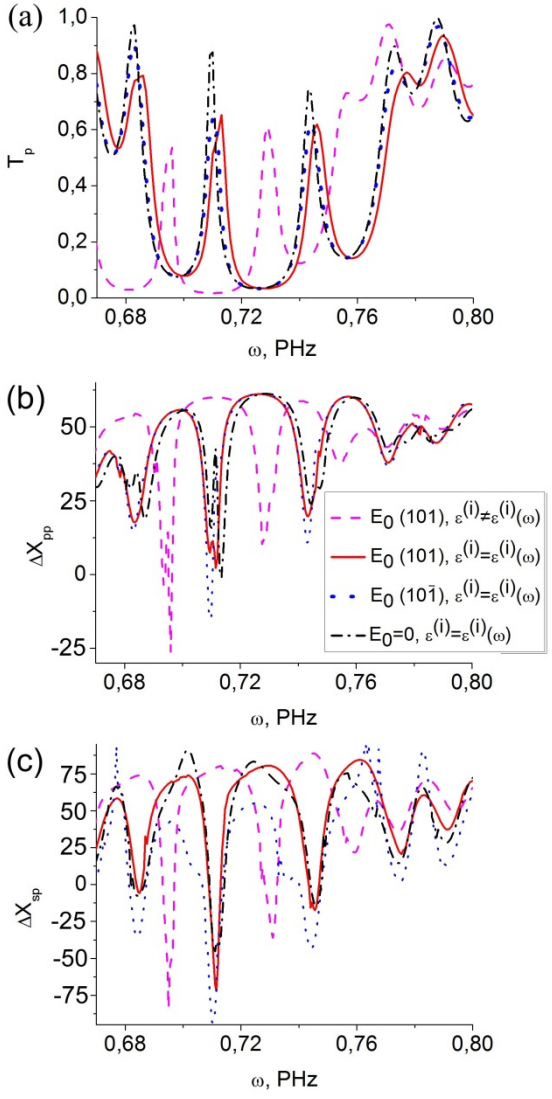

Figure 3. The same as in Fig. 2 except for p-polarized light and ΔX_{pp} (b) and ΔX_{sp} (c).

Figs. 4(a) and 4(b) show T_s and ΔX_{ss} for *s*-polarized incident light as function of ω, at $\theta = 30^\circ$, for different positions of the defect layers. Here $\mathbf{E_0}$ is applied along the (101) direction. One can see that the more periods of the PC are present between the defect layers, the lower are the DMs values. The high-frequency DM vanishes at a smaller number of periods between the defect layers in comparison to the low-frequency one. From Fig. 4(b) one can see that varying the defect layers position it is possible to damp or enhance ΔX_{ss}. The largest negative GH shift can be obtained for the PC $(NM)^{12}(EOL)(MOL)(NM)^{12}$ at ω of the low-frequency DM. The behavior of all ΔX_{ij} ($i,j=s,p$) is similar to one depicted on Fig. 4(b).

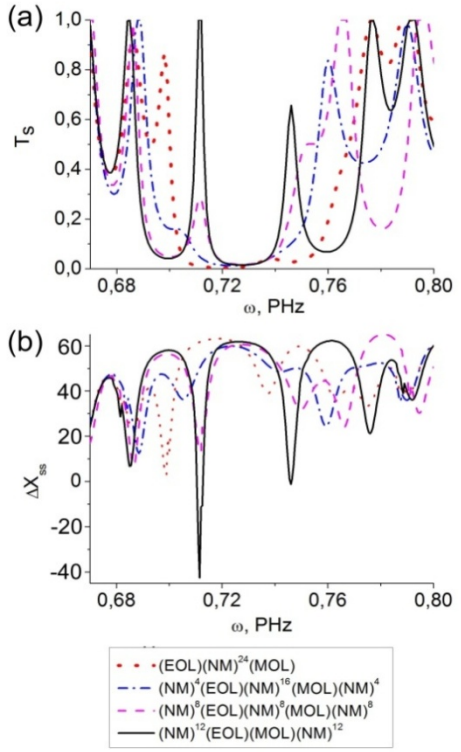

Figure 4. Transmittivity spectra T_s for s-polarized incident light (a) and normalized GH shifts ΔX_{ss} (b) at incidence angle equal to 30° for different positions of the defect layers in the presence of an external electric field.

3. CONCLUSIONS

We have calculated the GH shifts of the light transmitted through a 1D magnetic PC's composed of GGG and YIG layers with electro-optic and magneto-optic defect layers. We have analyzed the influence of the defect layers position on the DM values as well as on GH shifts in the presence of an external electric field. Taking into account the frequency dispersion of the permittivities of the system leads to transmittivity and GH shift spectra drifts towards higher frequencies.

ACKNOWLEDGEMENTS

This work was supported partly via project FP7-People-2009-IRSES, No. 247556 "NoWaPhen" and COST Action MP0702 "Towards Functional Sub-Wavelength Photonic Structures" (Yu.S.D. and I.L.L.), partly by National Research Foundation Koreathrough q-Psi (Y.P.L.) and partly by NWO – the Netherlands Organization for Scientific Research (Th.R.).

REFERENCES

[1] J. D. Jannopoulos, S. G. Johnson, J. N. Winn, and R. D. Meade, *Photonic Crystals: Molding the Flow of Light (Second Edition)*, Princeton, New Yourk: Princeton University Press, 2008.

[2] Yu. S. Dadoenkova, I. L. Lyubchanskii, Y.P. Lee, and Th. Rasing: *Appl. Phys. Lett.*, vol. 97, 011901, July 2010.

[3] Yu. S. Dadoenkova, I. L. Lyubchanskii, Y.P. Lee, and Th. Rasing: *AIP Conf. Proc.*, vol.1291, pp. 106-108, Oct. 2010.

[4] A. Yariv and P. Yeh, *Optical Waves in Crystals*, New York: Wiley, 1984.

One-Dimensional Photonic Crystal with Two Combined Superconducting Defect Layers

Lyubchanskii I.L.[1, 2], Dadoenkova N.N.[1], Lee Y.P.[3], Th. Rasing [4]
[1] *Donetsk Physical & Technical Institute of the National Academy of Sciences of Ukraine, 83114, Donetsk, Ukraine*
Tel: +380 62 3427763; e-mail: igorl@fti.dn.ua
[2] *Department of Physics and Technology , Donetsk National University, Donetsk 83000, Ukraine.*
[3] *Quantum Photonic Science Research Center (q-psi) and Department of Physics, Hanyang University, Seoul 133-791, Republic of Korea*
[4] *Radboud University Nijmegen, Institute for Molecules and Materials, Heyendaalseweg 135, 6525 AJ, Nijmegen, The Netherlands.*

ABSTRACT
In this paper we present the theoretical investigation of the one-dimensional dielectric photonic crystals with two complex defect layers. Both defect layers consist of ultrathin superconducting and dielectric sublayers symmetrically imbedded into the regular photonic structure. The influence of the position of the defect layers with respect to the center of the crystal on the photonic band gap spectra was theoretically investigated at different temperatures. The behaviour of the defect modes with different polarizations as a function of the superconducting sublayer thickness, is studied numerically at temperatures below the critical temperature of the superconducting sublayer. The pronounced contrast in behaviour of the transmittivity spectra of the x- and y-polarized modes was demonstrated. Possibility of a governing the defect modes of the photonic crystals with two complex superconducting defects by changing the temperature and the incident light polarization is shown numerically.

Keywords: photonic crystal, photonic band gap, defect mode, superconducting defect layer, transmittivity.

1. INTRODUCTION

During last years different photonic crystals (PCs) on the basis of the superconducting (SC) materials have being studied intensely both theoretically and experimentally [1]. The interest to the SC PCs is due to their applications in a new type of resonators [2] and microstrip filters based on $YBa_2Cu_3O_7$ which work in the gigahertz regime [3]. By tuning the temperature of the superconductor, the refractive index of the SC component can be changed, and as a consequence, the photonic band gap (PBG) can be controlled. The advantage of the SC PCs is a large tunability of the PBG, as it was demonstrated in the wide temperature interval in the SC state [4].
The majority of papers about the SC PCs are devoted to study of the regular, i.e. non-defect, structures [Anlage]. In the recent papers [5] – [7] the influence of the complex defect layer consisting of the dielectric and SC sublayers leading to appearance of the narrow transmittivity peak inside the leading to appearance of the narrow transmittivity peak inside the photonic band gap (PBG) was studied theoretically. In present article we consider the peculiarities of the PBG spectra of the one-dimensional (1D) PC with two combined SC defect layers symmetrically embedded into the regular periodic structure.

2. PHOTONIC CRYSTAL WITH SYMMETRICALLY IMBEDDED COMBINED SUPERCONDUCTING DEFECT LAYERS

We consider finite-size 1D PC of the structure $(BA)^N D(BA)^M D(BA)^N$ in vacuum, where the layer A is the strontium titanate $SrTiO_3$ with thickness d_1, the layer B is the aluminium oxide Al_2O_3 with thickness d_2. Each complex defect layer D consists of the $SrTiO_3$ sublayer A_{def} of thickness d_{1def} and the SC defect sublayer $YBa_2Cu_3O_7$ of thickness d_s. The period of the regular structure is $D = d_1 + d_2$. The PC's layers are located in the xy - plane and the z -axis is perpendicular to the interfaces. Two positions of the SC sublayers with respect to the dielectric defect sublayers are destinguished: the right-handed (RH) position, when the defect layer has the form $D = A_{def}\, SC$ and left-handed (LH) position with $D = SC\, A_{def}$. In present paper we consider the finite PCs with symmetrical positions of the combined defect structures with respect to the PC's center, referring them as RH - LH and LH - RH geometries, as shown in Figs. 1 (a) and 1 (b), respectively.

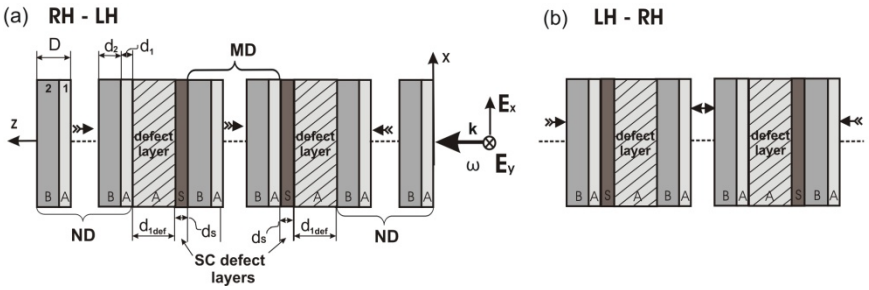

Figure 1. The schematic of the PCs with two complex SC defect layers: (a) RH-LH defect sublayers, and (b) the central part of the PC with LH-RH structure.

We consider the case of normal incidence of the electromagnetic waves (EMWs) linearly polarized (with the electric field component along x- or y-directions) on the right-hand surface of the PC and calculate the transmittivity spectra by means of the transfer matrix method [8]. The details of the method are given in our previous paper [6]. In our consideration we used the frequency- and temperature-dependent dielectric permittivity tensor for $YBa_2Cu_3O_7$ with nonzero diagonal components $\varepsilon_{xx}(\omega,T)$ and $\varepsilon_{yy}(\omega,T)=\varepsilon_{zz}(\omega,T)$, introduced in Ref. [9]. In the optical and near infra-red regimes the electrodynamic properties of $YBa_2Cu_3O_7$ can be described by a dielectric permittivity only with the magnetic permeability of $YBa_2Cu_3O_7$ $\mu_s=1$.

3. NUMERICAL RESULTS

For the numerical calculations we chose the unit cell numbers $N=5$, $M=2$, and the PC's period $D=5\ \mu m$ and the dielectric layer thicknesses $d_1=0.42\,D$, and $d_2=0.58\,D$. The thickness of the dielectric defect sublayer we choose to coincide with the regular layer thickness: $d_{1def}=d_1=2.1\ \mu m$. The refractive indices for the PC's components are $n_1=2.437$ (for $SrTiO_3$), and $n_2=1.767$ (for Al_2O_3) [5, 6].

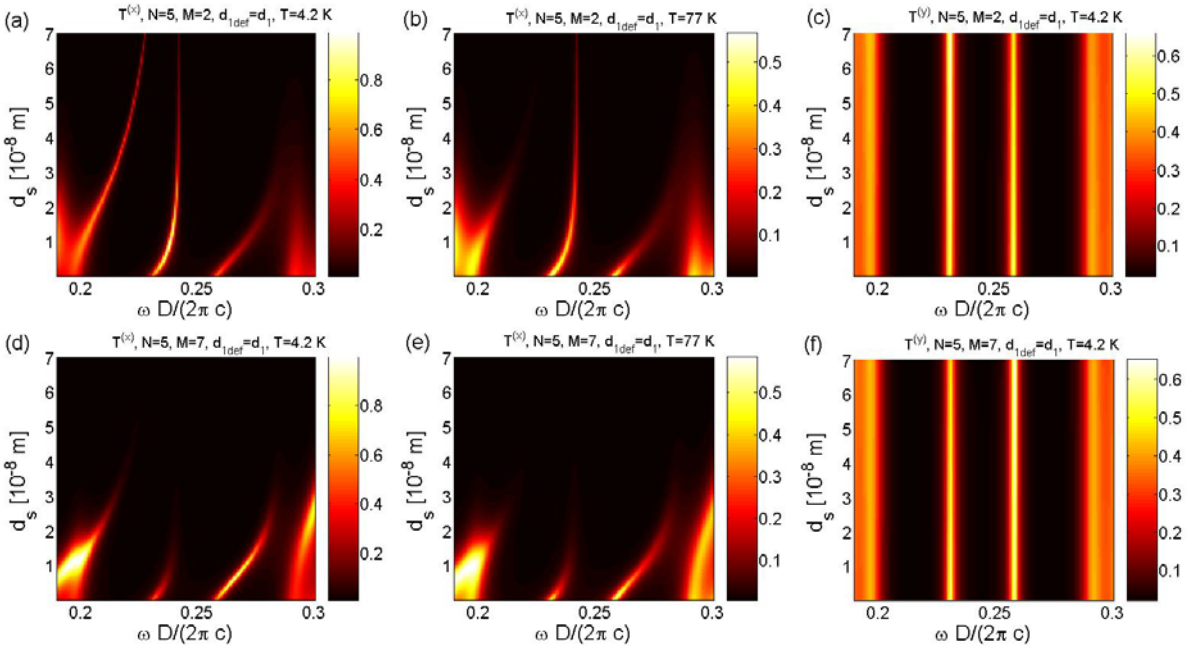

Figure 2. The transmittivities $T^{(x)}$ and $T^{(y)}$ vs the normalized frequency and the defect SC sublayer thickness d_{s} for T=4.2 K (a)-(c), (d) and for T=77 K (b), (d). The upper (a) - (c) and lower (d) - (f) Figs. correspond to RL – LH and LH – RH geometries, respectively.

In Figs. 2 we show the dependence of the transmittivity $T^{(x)}$ for the x-polarized EMWs on the normalized frequency $\omega D/(2\pi c)$ within the first PBG and its vicinity and the SC sublayer thickness d_s for the case of PC with RH - LH combined defects (Figs. 2 (a) and 2 (b)) and with LH - RL ones (Figs. 2 (d) and 2 (e)) calculated for the temperatures $T=4.2\ K$ and $T=77\ K$, respectively. In Figs. 2 (c) and 2 (f) one can see the corresponding dependence for the y-polarized light for the RL - LH and LH - RH geometries, respectively. We consider the variation of the SC sublayer thickness d_s in the range of $[0\div 70]\,nm$. The case of $d_s=0\ nm$

corresponds to the case of pure dielectric defect layers. In Figs. 2(a)- 2(f) there are two transmittivity peaks inside the PBG corresponding to two combined defect layers, which we refer as low-frequency (LF) and hight-frequency (HF) defect modes. From Figs 2(a), 2(b), 2(d) and 2(e) one can see that the variation of the SC sublayer thickness in ranges of several tens of nanometers influence considerably on the PBG spectra of the x-polarized EMWs, leading to the significant shift of both defect modes and the LF PBG edge to the higher frequencies in both RL - LH and LH - RH geometries. The HF edge's shift is pronounced in the case of LH – RL geometry, while in the RH-LH one its position practically does not change. In difference from the x-polarized EMWs, the change in the spectra of y- polarized EMWs is not essential with variation of d_s within the considering range for both geometries (see Figs. 2(c) and 2(d)).

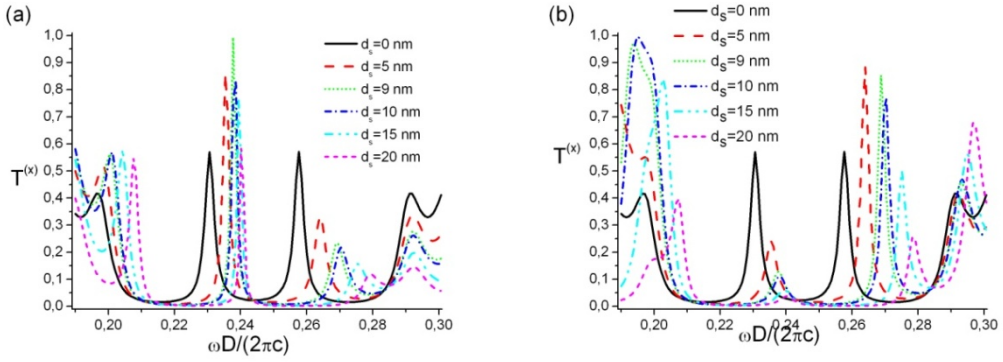

Figure 3. The transmittivity spectra for the x-polarized EMWs for RL-LH (a) and LR-RL(b) structures calculated for T=4.2 K .

In Figs 3(a) and 3(b) we demonstrate the transmitivity profiles, calculated for the set of values of the SC sublayer thickness: $d_s = 0, 5, 9, 10, 15, 20\, nm$ calculated at the temperature $T = 4.2\, K$. The case of the pure dielectric defect layers ($d_s = 0\, nm$) is characterized by presence of two symmetric transmitivity peaks $T^{(x)} \approx 0.6$ inside the PBG at $\omega_{LF} D/(2\pi c) \approx 0.232$ and $\omega_{HF} D/(2\pi c) \approx 0.558$, shown with the solid lines in Figs 3(a) and 3(b). The shifts of the LF and HF defect modes from their positions at $d_s = 0$ are different. For example, for the RH - LH geometry $\Delta\omega_{LF} D/(2\pi c) \approx 0.008$ (which corresponds to 3.01 THz) , while $\Delta\omega_{HF} D/(2\pi c) \approx 0.013$ (4.78 THz) or $d_s = 10\, nm$. In the case of LH – RH geometry the corresponding shifts are approximately of the same values.

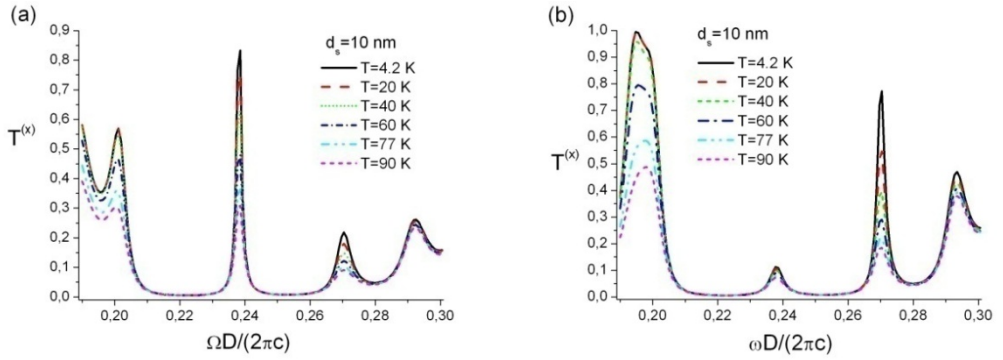

Figure 4. The transmittivity spectra variation with growth of temperature for RL-LH (a) and LR-RL(b) structures for the case of $d_s = 10$ nm .

The presence of the SC defect sublayers results not only the shift of the defect modes to the higher frequencies, but the deformation of the spectra, which becomes unsymmetrical. For example, in the case of RL - LR geometry the increase of d_s leads to the sharp growth of the LF defect mode's magnitude up to $T_{LF}^{(x)} \approx 0.99$ for $d_s = 9\, nm$. The further increase of d_s results the reduction of $T^{(x)}$, as seen in Fig. 3(a). The HF defect mode decays monotonically with the increase of d_s. In the case of LH – RH geometry the defect modes exhibit the opposite behaviour: the LH defect mode monotonically decays and the HF one reaches the maximal value of $T_{LF}^{(x)} \approx 0.88$ for $d_s = 5\, nm$ and drops down with further increase of the SC defect sublayer thickness. At the SC

thickness $d_s = 20\,nm$ the LF defect mode practically vanishes in LH – RH geometry, while in the RH – LH geometry it remains large enough: $T_{LF}^{(x)} \approx 0.58$.

Comparing the PBG spectra in Figs 2 (a) and 2 (b) (as well as in Figs. Figs 2 (d) and 2 (e)), one can see, that the temperature has a strong effect on the transmittivity values of the defect modes and the PBG edges.

In Figs 3 (a) and 3(d) we present the PBG spectra calculated for the set of temperatures, including the temperatures of liquid helium $T = 4.2\,K$, liquid nitrogen $T = 77\,K$ and the critical temperature of $YBa_2Cu_3O_7$ $T_c = 90\,K$ for the SC defect layer thickness fixt to be $d_s = 10\,nm$. As one can see from Figs. 3 (a) and 3(d), the positions of the defect modes and the PBG edges do not shift with the temperature increase. Nevertheless, the magnitude of the defect modes changes essentially. In the RH - LH geometry the LF defect mode peak drops from $T_{LF}^{(x)} \approx 0.85$ at $T = 4.2\,K$ to $T_{LF}^{(x)} \approx 0.32$ at $T = 90\,K$. In the case of LH - RH geometry, the HF peak diminishes from $T_{LF}^{(x)} \approx 0.75$ at $T = 4.2\,K$ to $T_{LF}^{(x)} \approx 0.2$ at $T = 90\,K$. The spectra of y-polarized modes do not exhibit essential modifications with temperature growth in the considered interval.

4. CONCLUSIONS

In conclusion, we have investigated two geometries of the 1D PCs with two combined SC - dielectric defects. The behaviour of the transmittivity of x-polarized defect mode within the first PBG as a function of the normalized frequency and SC sublayer thickness is studied numerically. We showed that the change of position of the SC defect sublayer with respect to the dielectric defect sublayer, leads to serious modification of the PBG spectra of the x-polarized EMWs, in contrast to the y-polarized EMWs. The pronounced contrast in behaviour of x- and y-polarized modes is based on the in-plane anisotropy of dielectric tensor components of the SC sublayer. Our calculations are in agreement with the results obtained in Refs. [5, 6].

ACKNOWLEDGEMENTS

This research is supported partly via projects FP7-PEOPLE-2009-IRSES "NoWaPhen" No. 247556 (N.N.D., I.L.L.) and COST Action MP0702 "Towards Functional Sub-Wavelengts Photonic Structures", partly via NRF grant through q-Psi, Korea (Y.P.L.), and partly via grants from NWO - the Netherlands Organization for Scientific Research (Th.R.).

REFERENCES

[1] S. M. Anlage, The physics and applications of superconducting metamaterials, *J. of Optics*, vol. 13, No.2, p. 024001, Febr. 2011.

[2] E. D. Gennaro, *et al.*, Hibrid photonic – bandgap accelerating cavities, *New Journal of Physics*, Vol. 11, 113022, Nov. 2009.

[3] H.-F. Huang, J.-F. Mao, X.-C. Li, and Z. Li, A photonic bandgap microstrip filter based on YBCO superconducting film, *IEEE Transactions on Applied Superconductivity*, Vol. 15, p. 3827-3826, March 2005.

[4] T.-H. Pei and Y.-T. Huang, A temperature modulation photonic crystal Mach-Zehnder interferometer composed of copper oxide high-temperature superconductor, *J. Appl. Phys.* Vol. 101, 084502, Apr. 2007.

[5] I. L. Lyubchanskii, *et al*, A one-dimensional photonic crystal with a superconducting defect layer, *J. Opt. A: Pure Appl. Opt.*, Vol. 11, p. 114014, Sept. 2009.

[6] N. N. Dadoenkova, *et al*, A one-dimensional photonic crystal with a superconducting defect layer, *J. Appl. Phys.*, Vol. 108, 093117, Nov. 2010.

[7] J. Barvestani, Analytical investigation of one-dimensional photonic crystals with a dielectric-superconducting pair defect, *Optics Communications*, Vol. 284, no. 1, pp. 231-235, Jan. 2011.

[8] D. W. Berreman, "Optics in Stratified and Anisotropic Media: 4 x 4-Matrix Formulation", *J. Opt. Soc. Am.*, vol. 62, pp. 502-510, Apr. 1972.

[9] H. Rauh and Y. A. Genenko, The effect of the superconducting surface layer on optical properties of a dielectric photonic composite, J. Phys. Cond. Mat., Vol. 20, 145203, March 2008.

Thin-film solar cells with combined metallic enhancements

Honghui Shen[1], Aimi Abass[2], Marc Burgelman[2], Bjorn Maes[1,3]
[1] *Photonics Research Group (INTEC), Ghent University-IMEC, Sint-Pietersnieuwstraat 41, B-9000 Gent, Belgium.*
[2] *Department of Electronics and Information Systems, Solar Cells Group, Ghent University, B-9000 Ghent, Belgium.*
[3] *Micro- and Nanophotonic Materials Group, University of Mons, Faculty of Science, Avenue Maistriau 19, B-7000 Mons, Belgium.*
e-mail: bjorn.maes@umons.ac.be

ABSTRACT
Plasmonic elements, such as metallic gratings, in thin solar cells have a strong potential to increase the solar light absorption. Here, we numerically describe devices where multiple elements are combined, to create a more broadband and spatially distributed absorption. For organic solar cells, we introduce both a front and a back metallic grating, and show that both features act independently to create enhancement pathways. For amorphous silicon solar cells we introduce a metallic back grating and a dielectric front structure. By choosing different periods for these separate gratings, coupling to guided modes with plasmonic or photonic character is strongly optimized.

Keywords: Solar energy, surface plasmons, gratings.

1. INTRODUCTION

Thin absorbing layers in solar cells are desired to decrease the material costs, but also to enhance the electronic properties. Unfortunately thinner cells means that light has a greater probability to not be absorbed, therefore the field of light-trapping was created. Nowadays, active layers become so thin that traditional refractive elements become impractical. Therefore wavelength-scale dielectric features and subwavelength scale plasmonic features are introduced, in order to scatter light in more absorbing modes [1]. The inclusion of single elements already received much attention. However, the ultimate trapping structures will probably include various effects, and may therefore necessitate multiple scattering features.

We propose combined devices both for the organic and amorphous silicon platform. The particular implementations depend on the modelled platform, as the material properties and thicknesses vary, but the techniques are more generally applicable. In the organic case we insert metallic gratings on both the front and back side of the cell. For the amorphous silicon cell we introduce a dielectric and a metallic grating, with varying periods.

2. COMBINED PLASMONIC GRATINGS

Our proposed structure with metallic gratings on the front surface and on the back metallic electrode is shown in Fig. 1(a). The integrated absorption versus angle of incidence is shown in Fig. 1(b). A strong enhancement with respect to the planar case is observed, which is kept even for relatively large angles of incidence.

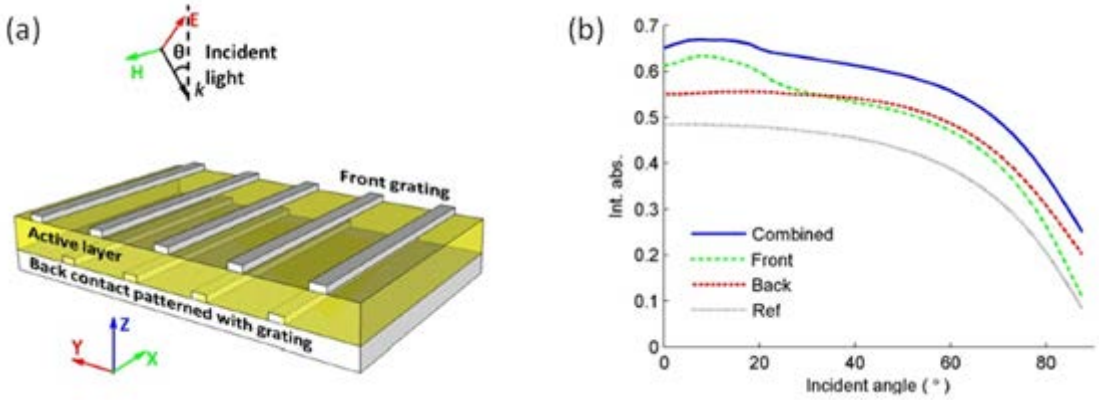

Figure 1 (a) Double grating geometry for an organic structure. (b) Integrated absorption versus angle of incidence in the case of combined grating (blue), front grating only (green), back grating only (red) and flat reference structure (grey).

The operation of the device is elucidated by comparing the absorption spectra with the dispersion of Bloch modes of the structure [2]. Strong absorption peaks appear for the coupling to Bloch plasmonic modes, which in

this structure have a mixed localized (around the grating teeth) and propagating (along the back surface) character. Particular angular dependence stems from the tuning of so-called 'bright' (symmetric) and 'dark' (anti-symmetric) modes [3].

By superimposing the spectrum for single grating and double grating cases, we observe that the particular offset structure here provides an independent operation of both gratings. The offset creates resonances in separate wavelength areas that ultimately provide a broadband enhancement.

3. MULTIPERIODIC GRATINGS

Previously, we reported the combination of dielectric and metallic gratings in an amorphous Si context [4], leading to different functionality for both gratings. Here, we further optimize this structure by using different periods for both gratings, see Fig. 2.

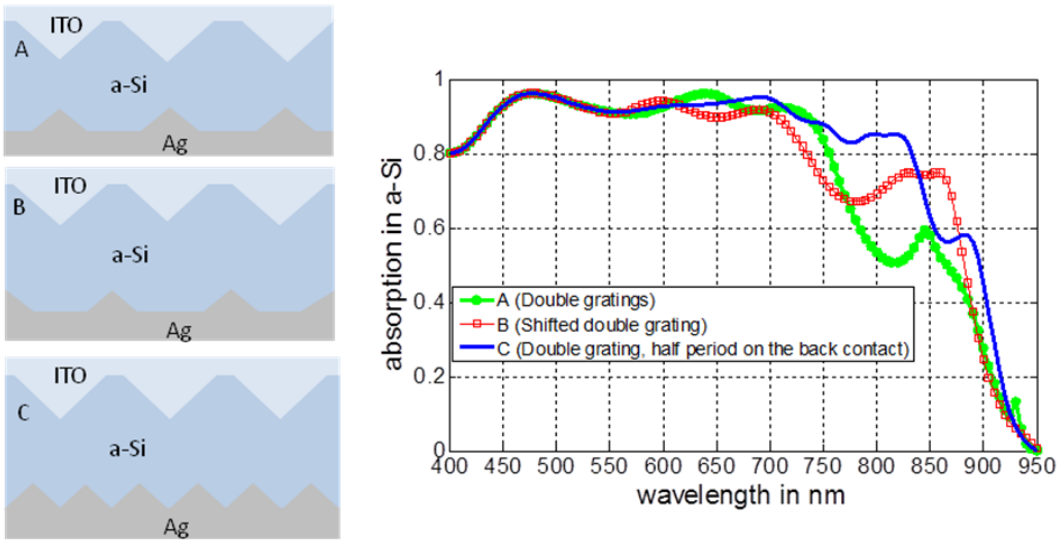

Figure 2 (left) Geometry with A: same period front and back; B: same period but offset; C: doubled period for the back grating.

A clear absorption enhancement of the double grating structure (C, blue curve in Fig. 2) is observed. A main contribution is that the doubled period bottom grating couples well to the *plasmonic* mode, giving a first order diffraction. In contrast, the top ITO front grating couples well to the *photonic* mode, again as first order. Dispersion calculations and period optimizations therefore lead to clear diffraction enhancements.

4. CONCLUSIONS

The inclusion of multiple elements is the next step towards ideal, broadband light-trapping devices. Here we introduce two pathways. First, the combination of front and back metallic gratings provides superimposed enhancements. Second, the optimisation of periods for dielectric and back gratings optimizes the coupling to modes of different character. These general techniques are useful for multiple thin-film solar platforms.

ACKNOWLEDGEMENTS

This research was supported by the IWT (Institute for the Promotion of Innovation by Science and Technology in Flanders) via the SBO-projects 'Polyspec' and 'Silasol', by the Interuniversity Attraction Poles program of the Belgian Science Policy Office IAP P6-10 'photonics@be' and by COST action MP0702.

REFERENCES

[1] H.A. Atwater, A. Polman; Plasmonics for improved photovoltaic devices, *Nature Materials*, vol. 9, pp. 205–213, 2010.

[2] H. Shen, B. Maes; Combined plasmonic gratings in organic solar cells, *Optics Express*, vol. 19, p. A1202, 2011.

[3] A. Abass, H. Shen, P. Bienstman, B. Maes; Angle insensitive enhancement of organic solar cells using metallic gratings, *J. Appl. Phys.*, vol. 109, p. 023111, 2011.

[4] K.Q. Le, A. Abass, B. Maes, P. Bienstman, A. Alù; Comparing plasmonic and dielectric gratings for absorption enhancement in thin-film organic solar cells, *Optics Express*, accepted.

Concentrator of Longitudinal Magnetic Field Generated from Azimuthally Polarized Light

Piotr Wróbel[1], Tomasz J. Antosiewicz[2], Tomasz Szoplik[1]
University of Warsaw, Faculty of Physics, Pasteura 7 Str., 02-093 Warsaw, Poland
Tel: +48 22 55 46 896; e-mail: piotr.wrobel@igf.fuw.edu.pl
[2] Chalmers University of Technology, Department of Applied Physics, SE-412 96 Goteborg, Sweden.

ABSTRACT
Recent years have seen an expansion of research on metamaterials with engineered permeability different from unity. Metamaterials fabricated from components with large values of dielectric permittivity exhibit susceptibilities larger than existing in natural materials. Existence of metamaterials composed of subwavelength elementary cells creates a need for an analog of a scanning near-field optical microscope where the cell is illuminated with a concentrated longitudinal component of magnetic field of electromagnetic wave.
We present two types of probes for a future scanning near-field magnetic microscope useful for measurements of magnetic responses of elementary cells within the visible 400-800 nm range. The first one is a tapered silica fiber with radial metal stripes separated by equidistant slits of constant angular width. The second probe is a radially corrugated, tapered, metal-coated fiber with aperture at the apex. Generation of the longitudinal magnetic field component is possible due to internal illumination with azimuthally polarized light. In FDTD simulations we examine performance of the probes, that is their properties in terms of a full-width at half-maximum of the focus versus energy throughput efficiency.

Keywords: optical magnetism, plasmonics, magnetic metamaterials, scanning microscopy, corrugated probes.

1. INTRODUCTION

Pendry *et al.* [1] have shown that artificial materials composed of elementary cells fabricated from nonmagnetic conducting elements have effective magnetic permeability different from unity. Urzhumov and Shvets [2] presented theoretical formulas for the frequencies and strengths of electric and magnetic resonances valid for any periodic metallodielectric nanostructures operating in the plasmonic regime. More recently, Merlin [3] considered a metamaterial composed of split rings and spherical inclusions. He showed that if a metamaterial is made of substances with the imaginary part of permittivity $\sqrt{\varepsilon''} > > \lambda/d$, where $\lambda >> d$ is the wavelength in vacuum and d is the characteristic length of the particles, then strong diamagnetic or paramagnetic behaviour characterized by susceptibilities whose magnitude is significantly larger than that of natural substances is possible. According to Merlin, the strength of magnetic effects diminishes with decreasing wavelength. Existence of metamaterials composed of subwavelength elementary cells made of materials with large values of the permittivity creates a need for an analogue of a scanning near-field optical microscope (SNOM) where in search of a magnetic response the cell is illuminated with a concentrated longitudinal component of magnetic field of electromagnetic wave.

The idea of scanning near-field magnetic microscope (SNMM) can be realized in different ways. Burresi *et al.* [4] have reported on near-field detection of the magnetic field of light using an aperture SNOM probe with a split ring resonator (SRR) in the aperture plane. Aperture probes without an SRR at the tip end were used for passive measurements of the magnetic component of modes excited in photonic crystal cavities coupled to waveguides [5-6]. The electric and magnetic resonances of a properly oriented SRR can be independently tested by means of a y-polarized TEM_{10} mode (y-polarized HG_{01} mode) with a strongly focused on-axis longitudinal magnetic field H_z and off-axis E_y components as proposed by Banzer *et al.* [7].

In this technical note we present two types of tapered along the z direction dielectric probes with discrete [8] or continuous metal coating which concentrate longitudinal magnetic field of light in the near field of their apexes. Cross sections of the probes are shown in Figure 1a and b – the larger pictures show cross sections far away from the apex, while the smaller ones at the apex. The probes have internal azimuthally polarized illumination coupled to plasmons due to momentum matching on radial gratings. The gratings have continuously changing period what allows for efficient coupling within a wide spectral range. Plasmons with a strong azimuthal component propagate towards the apex where they form an azimuthal current in the metal which results in generation of a strong longitudinal magnetic field Hz.

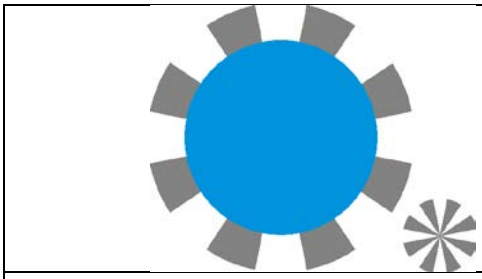

Fig. 1a. Cross section of a tapered silica fiber with radial metal stripes separated by equidistant slits of constant angular width.

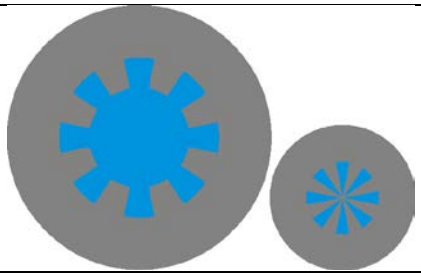

Fig1b. Cross section of radially corrugated, tapered, metal-coated fiber with aperture at the apex.

2. TAPERED DIELECTRIC PROBES WITH RADIAL STRIPES

Magnetic concentrators of the first type are made of dielectric dispersionless fibers with core diameter equal 3.2 μm which taper smoothly from their regular diameter to the apex. In the simulations we accept a taper half-angle equal to 40°. The metal lands and the slits have constant angular width equal $\pi/8$ (eight periods total). The metal lands are made of Ag or Al with thicknesses h varied from 0 to 100 nm. They are modeled using Drude dispersion $\varepsilon(\omega) = \varepsilon_\infty - \omega^2_p/[\omega(\omega + i\Gamma)]$ fitted to experiental data obtained by Johnson and Christy [9] for Ag with parameters equal $\varepsilon_\infty = 3.70$, $\omega_p = 13673$ THz, and $\Gamma = 27.35$ THz. For Al we use data from Ordal et al. [10] with fitting parameters $\varepsilon_\infty = 4.39$, $\omega_p = 12062$ THz, and $\Gamma = 1009$ THz.

Figures 2 and 3 show full-width at half-maximum (FWHM) of the longitudinal magnetic field component H_z calculated 10 nm from the apexes of probes with Ag and Al stripes, respectively. In both cases the stripe thickness changes from 0 to 100 nm. For the largest thickness considered FWHM values are better than half a wavelength. In the case of thin metal stripes plasmons radiate into an azimuthally polarized beam before reaching the apex and diffraction enlarges the spot size considerably. In the whole range of wavelengths FWHM values available with Al stripes monotonically grow with increasing wavelength. This regularity suggest that aluminum is a better choice for stripe metal than silver.

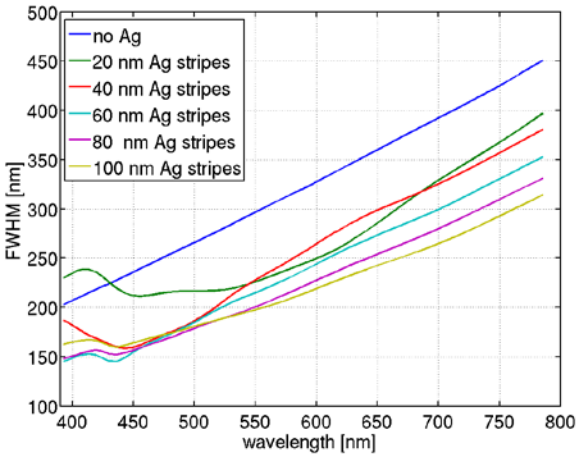

Fig. 2. A tapered dielectric probe with radial Ag stripes. Full-width at half-maximum of the longitudinal magnetic field component H_z calculated 10 nm from the apex for Ag stripe thicknesses $h \in [0, 100]$ nm.

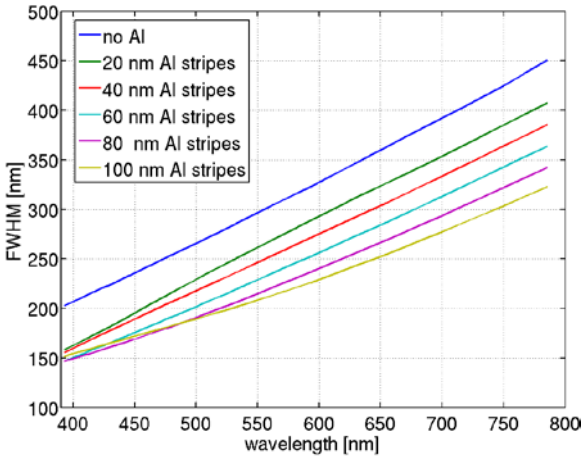

Fig. 3. A tapered dielectric probe with radial Al stripes. Full-width at half-maximum of the longitudinal magnetic field component H_z calculated 10 nm from the apex for Al stripe thicknesses $h \in [0, 100]$ nm.

In near-field of probe apexes not only the longitudinal, accumulated at the z-axis, component of magnetic field is present but also an azimuthal component of the electric field with its energy density increasing away from the z-axis. Figures 4 and 5 present a comparison of magnetic energy density of H_z and electric energy density of E_φ integrated over an area of diameter equal to the FWHM of H_z. In probes with silver stripes this magnetic-to-electric energy density ratio is higher than in those with Al stripes. It is because a narrow H_z needle is generated by azimuthal currents J_φ flowing through the set of stripes and virtual displacement currents in grooves. Those currents are larger in silver which is less lossy than aluminum. For both metals the optimum stripe thickness is within the range from 40 to 100 nm.

Fabrication of probes with radial metal stripes completely separated by narrowing along the probes grooves is not an easy task. The use of focused ion beam etching is still possible in well equipped laboratories only. Below we propose another geometry of a concentrator of longitudinal magnetic field component of light.

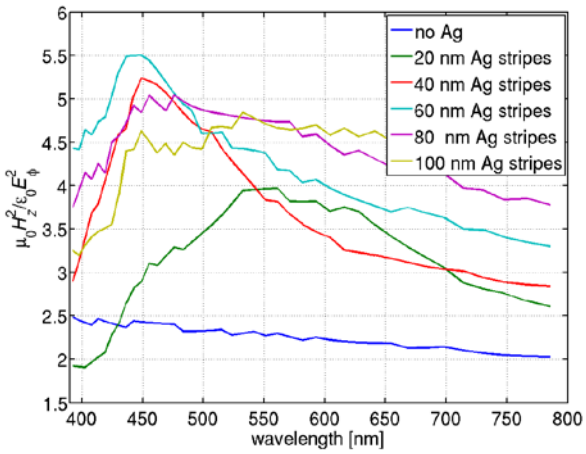

Fig. 4. A tapered dielectric probe with radial Ag stripes. Integrated magnetic energy density of H_z *to integrated electric energy density of* E_φ *ratio for Ag stripe thicknesses* $h \in [0, 100]$ *nm.*

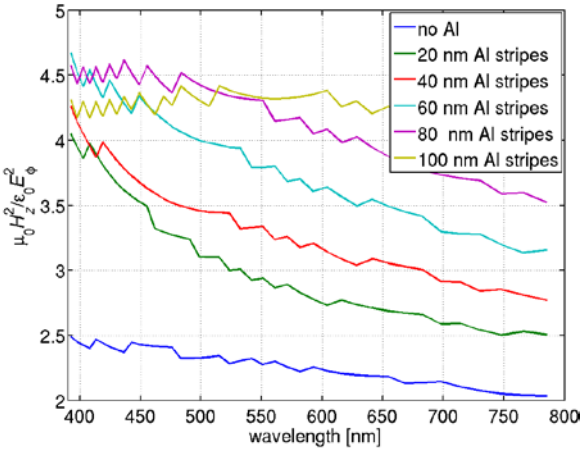

Fig. 5. A tapered dielectric probe with radial Al stripes. Integrated magnetic energy density of H_z *to integrated electric energy density of* E_φ *ratio for Al stripe thicknesses* $h \in [0, 100]$ *nm..*

TAPERED DIELECTRIC METAL COATED RADIALLY CORRUGATED PROBE

Currently we fabricate SNOM probes in the form of apertured metal-coated tapered fibers where light propagating in the fiber core is coupled to surface plasmons on corrugated core-metal coating interface [11-13]. When corrugations are made along the cone surface, internal linearly polarized illumination allows for energy throughput enhancement with respect to that possible in probes without grating coupling.

To generate the longitudinal magnetic field component H_z we need azimuthal current J_φ on the edge of a tip with continuous metal coating of thickness 60 nm. This is possible when internal azimuthally polarized illumination is coupled to plasmons on radially corrugated core-metal coating interface (Figure 1b). Simulated performance of such a probe with Al coating in presented in Figures 6 and 7. FWHM of the longitudinal magnetic field component H_z calculated 10 nm from the apex becomes narrower than that of uncorrugated probes for grooves 40 nm deep and more. In comparison with results shown in Figures 2 and 3 the radially corrugated probes gives better FWHM values especially for short wavelengths. Ratio of magnetic energy density of H_z to electric energy density of E_φ integrated over an area of diameter equal to the FWHM of H_z is is virtually independent on depth of grooves. The ratio reaches values one order of magnitude bigger than those possible with probes with radial stripes.

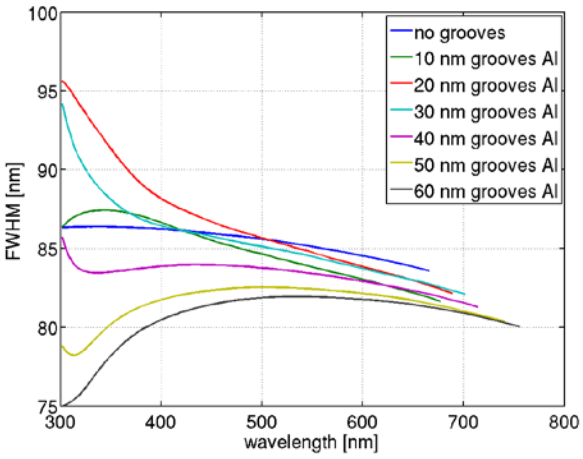

Fig. 6. A tapered dielectric probe with continuous Al coating and radial corrugations $h \in [0, 60]$ *nm deep. Full-width at half-maximum of the longitudinal magnetic field component* H_z *calculated 10 nm from the*

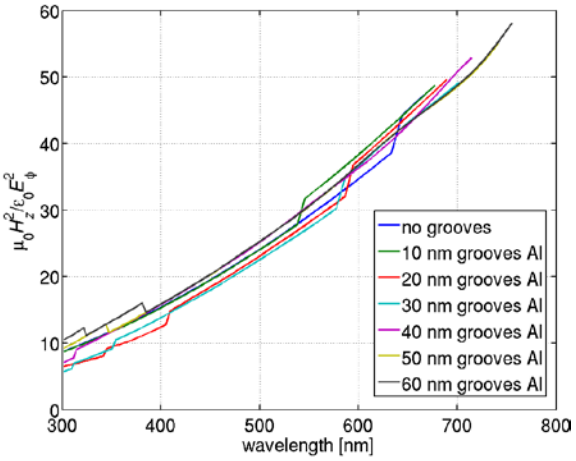

Fig. 7. A tapered dielectric probe with continuous Al coating and radial corrugations $h \in [0, 60]$ *nm deep. Integrated magnetic energy density of* H_z *to integrated electric energy density* of Eφ ratio.

apex.

Recently, in an effort to find an easy method to fabricate magnetic field concentrators other geometries were proposed [14]. Lee *et al.* [14] use external illumination and grating-coupling to surface plasmons onto metallic tips. Concentration of H_{apex}-field and at the same time strong suppression of E_z-field is achieved for double-sided illumination in the the H-symmetric (E out-of-phase, H in-phase) or E-antisymmetric (E field out-of phase, H field in-phase) surface plasmon excitation schemes.

CONCLUSION

An advantage of the proposed magnetic field concentrator is that it may be employed as a scanning near-field probe with shear force control of the probe-sample distance. This distance of single tens of nanometers allows for illumination of individual elementary cells of an arrayed metamaterial. Linear dimensions of those cells should be slightly smaller than FWHM values 160 nm and 80 nm achievable for dielectric probes with radial metal stripes and dielectric probes with continuous metal coating and radial corrugations, respectively. Near-field illumination excites resonances in an elementary cell and $|E|^2$ of scattered light is recorded with a square detector in the far-field.

ACKNOWLEDGEMENTS

This work was sponsored by Polish grants from the National Science Centre # 2011/01/M/St3/05734 and the National Centre for Research and Development # N R15 0018 06/2009.

REFERENCES

[1] J. Pendry, A. Holden, D. Robins, W. Stewart: Magnetism from conductors and enhanced nonlinear phenomena, *IEEE Trans. on Microwave Theory and Tech.* vol. 47, pp. 2075-2084, 1999.

[2] Y.A. Urzhumov, G. Shvets: Optical magnetism and negative refraction in plasmonic metamaterials, *Solid State Commun*. vol. 146, pp. 208–220, 2008.

[3] R. Merlin: Metamaterials and the Landau-Lifshits permeability argument: large permittivity begets highfrequency magnetism, *Proc. Natl. Acad. Sci. U.S.A.* vol. 106, pp. 1693–1698, 2009.

[4] M. Burresi, D. van Oosten, T. Kampfrath, H. Schoenmaker, R. Heideman, A. Leinse, L., L. Kuipers: Probing the magnetic field of light at optical frequencies, *Science* vol. 326, pp. 550-553, 2009.

[5] M. Burresi, T. Kampfrath, D. van Oosten, J. Prangsma, B. Song, S. Noda, S., L. Kuipers: Magnetic light-matter interactions in a photonic crystal nanocavity, *Phys. Rev. Lett.* vol. 105, p. 123901, 2010.

[6] S. Vignolini, F. Intonti, F. Riboli, L. Balet, L. Li, M. Francardi, A. Gerardino, A. Fiore, D. Wiersma, M. Gurioli: Magnetic imaging in photonic crystal microcavities, *Phys. Rev. Lett.* vol. 105, p. 123902, 2010.

[7] P. Banzer, U. Peschel, S. Quabis, G. Leuchs: On the experimental investigation of the electric and magnetic response of a single nano-structure, *Opt. Express* vol. 18, pp. 10905-10923, 2010.

[8] T.J. Antosiewicz, P. Wróbel, T. Szoplik: Magnetic field concentrator for probing optical magnetic metamaterials, *Opt. Express* vol. 18, pp. 25906-25911, 2010.

[9] P. Johnson, R. Christy: Optical constants of the noble metals, *Phys. Rev. B* vol. 6, pp. 4370-4379, 1972.

[10] M.A. Ordal, L.L. Long, R.J. Bell, R.R. Bell, R.W. Alexander, C.A. Ward: Optical constants of themetals Al, Co, Cu. Fe, Pb, Ni, Pd, Pt, Ag, Ti, and W in the infrared and far infrared, *Appl. Opt.* Vol. 22, pp. 1099-1119, 1983.

[11] T.J. Antosiewicz, T. Szoplik: Corrugated SNOM probe with enhanced energy throughput, *Opto-Electron. Rev*. vol. 16, pp. 451-457, 2008.

[12] T.J. Antosiewicz, P. Wróbel, T. Szoplik: Performance of scanning near-field optical microscope probes with single groove and various metal coatings, *Plasmonics* vol. 6, pp. 11-18, 2011.

[13] P. Wróbel, T. Stefaniuk, T.J. Antosiewicz, A. Libura, G. Nowak, T. Wejrzanowski, R. Slesinski, K. Jedrzejewski, T. Szoplik: Fabrication of corrugated probes for scanning near-field optical microscopy, in *Proc. of SPIE* Vol. 8070, pp. 80700I-1-7.

[14] J. S. Lee, S. Han, J. Shirdel, S. Koo, D. Sadiq, C. Lienau, N. Park: Superfocusing of electric or magnetic fields using conical metal tips: effect of mode symmetry on the plasmon excitation method, *Opt. Express* vol. 19, pp. 12342-12347, 2011.

Simulation of photonic crystal nanocavities using a bidirectional eigenmode propagation algorithm: a comparative study.

Jiří Petráček[1], Jaroslav Luksch[1], Bjorn Maes[2], Sven Burger[3], Pavel Kwiecien[4], Ivan Richter[4]
[1] *Institute of Physical Engineering, Brno University of Technology*
Technická 2, 616 69 Brno, Czech Republic, e-mail: petracek@fme.vutbr.cz
[2] *Micro- and Nanophotonic Materials Group, University of Mons, Faculty of Science,*
Avenue Maistriau 19, B-7000 Mons, Belgium
[3] *Zuse Institute Berlin (ZIB), Takustraße 7, D– 14 195 Berlin, Germany*
[4] *Department of Physical Electronics, Faculty of Nuclear Sciences and Physical Engineering, Czech Technical University in Prague, Břehová 7, 115 19 Praha 1, Czech Republic*

ABSTRACT
A new implementation of bidirectional eigenmode expansion and propagation algorithm for the modeling of three-dimensional waveguide structures is presented. The eigenmodes, which are used for expansion of unknown field, are searched numerically using a full vector finite-difference or finite-element modesolver. The technique is applied to the modeling of high-*Q* one-dimensional photonic crystal nanocavity and its results are compared with results obtained by three other independent techniques.

Keywords: eigenmode expansion, numerical modeling, photonic crystals, high-*Q* nanocavities

1. INTRODUCTION

Currently, as photonic and/or plasmonic nanostructures are becoming very attractive components for photonics devices, among other important experimental and technological aspects, new modeling activities are of high interest in connection towards their direct application to realistic 3D problems to be solved and optimized. Clearly, such demands necessitate very efficient and reliable computational methods. One possibility is to perform rigorous simulation in the frequency domain using analytical modal techniques, such as the bidirectional eigenmode propagation [1] (BEP, also known as the mode matching method), which are based on the expansion of the unknown field into a set of the orthogonal waveguide modes. This approach is particularly advantageous for the structures composed of longitudinally uniform waveguides ("sections"). In principle, the modal methods can deal with the structures of arbitrary length (the number of the sections can influence only the total computational time) and readily provide device characteristics such as transmission, reflection or radiation loss. Recently, this approach has been extended to 3D structures [2,3]. Waveguide modes have been calculated using the finite-difference technique under the semi-vector approximation [2] or in the full-vector formulation [3].

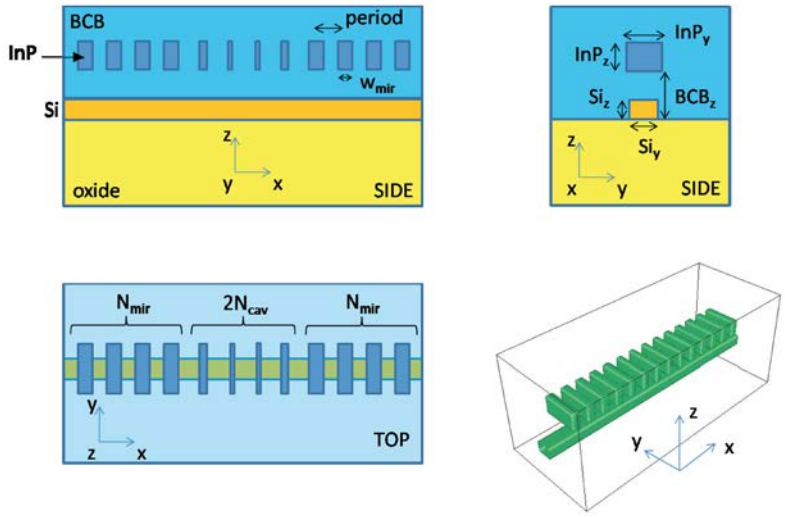

Figure 1. The photonic crystal cavity device coupled to a waveguide. The cavity is formed by the InP sections, the waveguide functions as input/output coupler. The 3D view only shows the Si and InP sections. The structural parameters are described in the text.

In this work, we briefly report about simulation of photonic crystal nanocavities using our own implementation of full-vector BEP for 3D structures. Moreover, we present comparison with other established techniques. Short description of the all techniques is the following.

- Bidirectional eigenmode expansion and propagation algorithm (BEP) was implemented at Brno University of Technology. We have used two different full vector techniques for searching of eigenmodes: a freely available finite-difference modesolver [4] and/or a finite-element commercially available software COMSOL Multiphysics. The techniques were effectively combined with the propagation algorithm of numerically-stable scattering matrices where the interface matrices were determined from overlap integrals of modal fields [2,3,5]. Resonance wavelength and *Q* factor are calculated from eigenvalues of reflectivity matrix.
- The finite-difference time-domain (FDTD) method, using a freely available software package [6].
- The time-harmonic, higher-order 3D finite element (FE) solver JCMsuite with adaptive meshing has been used to compute resonance modes and corresponding complex eigenfrequencies of the cavity [7]. From the complex eigenvalues, resonance wavelength and *Q* factor are derived [8].
- Aperiodic rigorous coupled wave analysis (aRCWA). This is Fourier expansion scheme which uses in-house robust 3D tool which effectively combines both 2D mode solver (based on 2D periodic RCWA tool in a combination with the isolating boundary conditions, either complex coordinate transforms or PMLs [9,10]), with the help of both ASR technique [11] and/or the application of structural symmetries [12], again combined with advanced "grating-oriented" schemes of scattering matrix formalism. Altogether, this efficient tool has been already successfully applied to both subwavelength [13] and plasmonic 3D nanostructures [14]. Resonance wavelength and *Q* factor are calculated from transmission spectra.

For the simulation we used a hybrid cavity structure which research has been conducted within the European Action COST MP0702. Note, that the full results of the study will be published elsewhere [15]. Here, the cavity serves as an example of novel and promising structure used for presentation of BEP and comparison of the numerical techniques. The structure, which is illustrated in Fig. 1, consists of a size-modulated 1D stack cavity coupled with the waveguide. It has been shown that such stack cavities (a simple periodic array of dielectric blocks) can reach ultrahigh *Q* factors provided widths of the blocks (i.e. here the widths of InP sections in *x* direction) are properly modulated near the cavity center [16].

2. RESULTS

Referring to Fig. 1, we used the following parameters for the calculation: InP_y = 0.7 μm, InP_z = 0.35 μm, Si_z = 0.22 μm and BCB_z = 1.0 μm. Refractive indices in various materials are 3.46 (Si), 1.45 (silicon oxide), 3.17 (InP) and 1.54 (benzocyclobutene, BCB).

Center positions of the InP sections are regularly spaced with period a = 0.35 μm. We use 10 unmodulated 'mirror' sections (N_{mir} = 10) with width w_{mir} = 0.2 μm. The number of modulated sections on each side of the center is N_{cav} and we consider modulation of section widths of the form

$$w(i) = (0.15\,\mu\mathrm{m})\left[1 + \frac{(i-1)^2}{3N_{\mathrm{cav}}^2}\right], \quad i = 1...N_{cav} \tag{1}$$

We searched for the fundamental cavity quasi-TE mode (electric field parallel with *y*). In Fig. 2, we show cavity characteristics and compare results of BEP, FDTD and FE techniques. (Note, that in the scale of the graphs the FD and FE based BEP techniques provide identical results. Therefore we present results of the FE based BEP only.) It is seen that the different methods generate results which give the same qualitative picture; showing their good applicability. However, results differ significantly on an absolute scale. This demonstrates that accurate computation of 3D resonators remains a challenging problem.

As the second alternative modal technique, we have applied the aRCWA method based on the free-space Fourier harmonic expansions, rather than on waveguide eigenmode expansions, as in the BEP case. Figure 3 hence shows, as an example here, the convergence *Q* factor behavior of BEP and aRCWA techniques for N_{cav} = 11. As can be seen, although *Q* factor values are not again directly comparable, similar agreement as reached with other two methods has been obtained. Note that the mode numbers in the two figures are, in fact, not directly comparable due to the different nature of the expansion modes. Furthermore, as was expected, the effectively needed number of modes is much larger in aRCWA as compared to waveguide modes applied directly to BEP. The origin of these discrepancies will be discussed and further investigated.

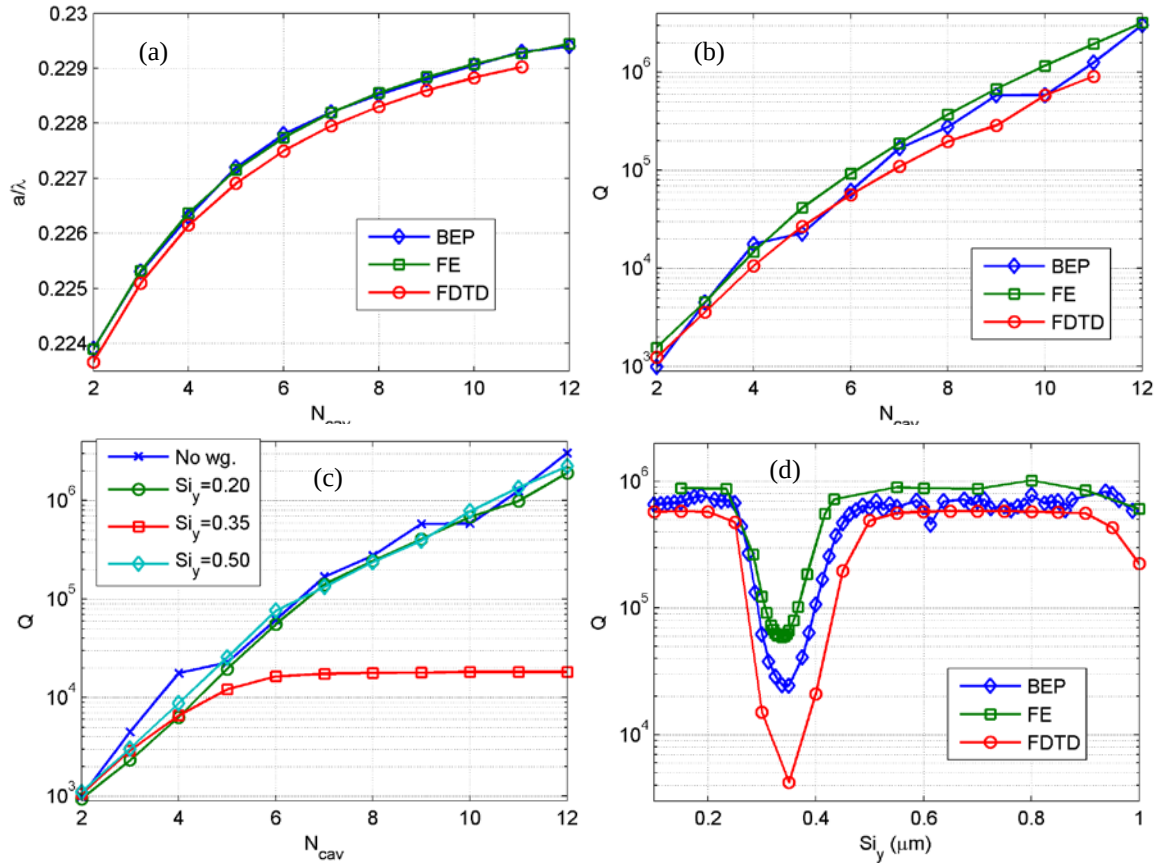

*Figure 2. Q-factor and normalized resonance frequency a/λ provided by three numerical techniques for the cavity shown in Fig. 1. (a) and (b) show results for single cavity without waveguide. (c) BEP results for single cavity (*No wg.*) and hybrid cavity with various values of* Si_y *(in* μm*). (d) Hybrid cavity with* $N_{cav} = 10$.

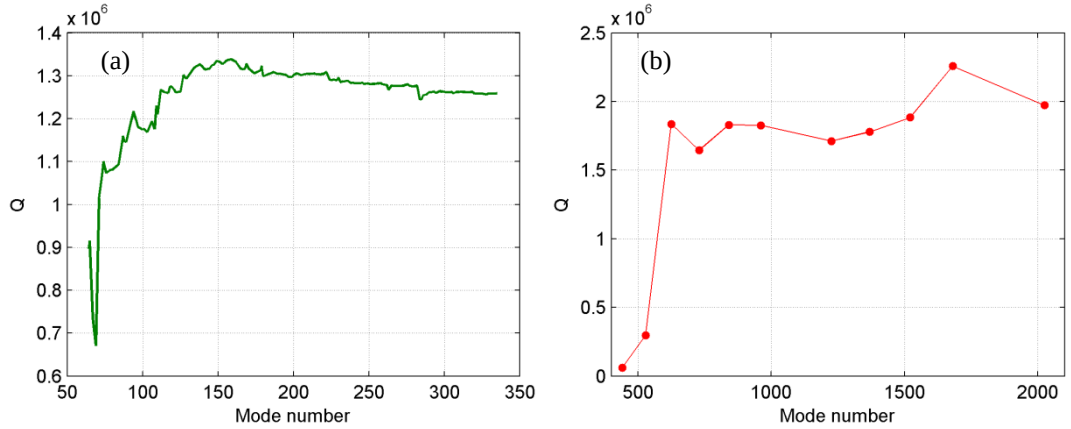

Figure 3. Convergence behavior of BEP (a) and (b) aRCWA . The structure is as in Fig. 1 with $Si_y = 0.50$ μm *and* $N_{cav} = 11$.

3. CONCLUSIONS

In summary, we have developed a bidirectional eigenmode expansion algorithm for the modeling of 3D waveguide structures. The technique has been applied to the novel and promising structure, high-*Q* one-dimensional photonic crystal nanocavity, which research has been conducted within the European Action COST MP0702. Simulations results have been compared with results obtained by three other independent techniques. The all techniques have appeared efficient in providing the important cavity characteristics, with their advantages and disadvantages. Presented results indicate that accurate computation of 3D resonators remains a challenging problem which should be further investigated.

ACKNOWLEDGEMENTS

The work was conducted within the European Action COST MP0702. J.P., J.L, P.K. and I.R. acknowledge supports of this work by Ministry of Education, Youth, and Sports of the Czech Republic under contracts OC09005 and OC09038, and by Czech Science Foundation under contract P205/10/0046.

REFERENCES

[1] G. Sztefka, H.-P. Nolting: Bidirectional eigenmode propagation for large refractive index steps, *IEEE Photon. Technol. Lett.*, vol. 5, no. 5, pp. 554-557, May 1993.

[2] K. Jiang, W.-P. Huang: Finite-difference-based mode-matching method for 3-D waveguide structures under semivectorial approximation, *J. Lightwave Technol.*, vol. 23, no. 12, pp. 4239-4248, Dec. 2005.

[3] J. Mu, W.-P. Huang: Simulation of three-dimensional waveguide discontinuities by a full-vector mode-matching method based on finite-difference schemes, *Opt. Express*, vol. 16, no. 22, pp. 18152-18163, Oct. 2008.

[4] A. B. Fallahkhair, K. S. Li, T. E. Murphy: Vector finite difference modesolver for anisotropic dielectric waveguides, *J. Lightwave Technol.*, vol. 26, no. 11, pp. 1423-1431, May 2008.

[5] P. Bienstman, R. Baets: Optical modelling of photonic crystals and VCSELs using eigenmode expansion and perfectly matched layers, *Opt. Quantum Electron.*, vol. 33, no. 4-5, pp. 327-341, Apr. 2001.

[6] A.F. Oskooi, D. Roundy, M. Ibanescu, P. Bermel, J. D. Joannopoulos, S. G. Johnson: MEEP: A flexible free-software package for electromagnetic simulations by the FDTD method, *Computer Physics Communications*, vol. 181, pp. 687–702, Jan.2010.

[7] J. Pomplun, S. Burger, L. Zschiedrich, F. Schmidt: Adaptive finite element method for simulation of optical nano structures, *Phys. Stat. Sol. (b),* vol. 244, pp. 3419-3434, Oct. 2007.

[8] S. Burger, J. Pomplun, F. Schmidt, L. Zschiedrich: Finite-element method simulations of high-Q nanocavities with 1D photonic bandgap, *Proc. SPIE*, vol. 7933, p. 79330T, Jan. 2011.

[9] E. Silberstein, P. Lalanne, J.-P. Hugonin, Q. Cao: Use of grating theories in integrated optics, *JOSA A*, vol. 18, no. 11, pp. 2865-2875, Nov. 2001.

[10] J.-P. Hugonin, P. Lalanne: Perfectly matched layers as nonlinear coordinate transforms: a generalized formalization, *JOSA A*, vol. 22, no. 9, pp. 1844-1849, Sep. 2001.

[11] J. Čtyroký, P. Kwiecien, I. Richter: Fourier Series-Based Bidirectional Propagation Algorithm With Adaptive Spatial Resolution, *J. Lightwave Technol.*, vol. 28, no. 20, pp. 2969-2976, Oct. 2010.

[12] Z. Y. Li, K. M. Ho: Application of structural symmetries in the plane-wave-based transfer-matrix method for three-dimensional photonic crystal waveguides, *Phys. Rev. B*, vol. 68, no. 24, pp. 245117-1, Dec. 2003.

[13] P. Kwiecien, I. Richter, J. Čtyroký: Comparison of 2D and 3D Fourier modal methods for modeling subwavelength-structured silicon waveguides, *Proc. SPIE*, vol. 8306, p. 83060Y, Oct. 2011.

[14] P. Kwiecien, I. Richter: Efficient three dimensional aperiodic rigorous coupled wave analysis technique, *Proc. ICTON 2011* (13th International Conference on Transparent Optical Networks, June 2011, Stockholm, Sweden), pp. 1-5, June 2011.

[15] B. Maes, J. Luksch, J. Petráček, S. Burger: Numerical method comparison for high-Q optical nanocavities. Under preparation.

[16] M. Notomi, E. Kuramochi, H. Taniyama: Ultrahigh-Q Nanocavity with 1D Photonic Gap, *Opt. Express*, vol. 16, no. 15, pp. 11059-11102, Jul. 2008.

Mini and micro-resonators for the generation of high spectral purity microwave signals.

Loic Morvan[1], Aude Bouchier[2], Yanne Chembo[3], Daniel Dolfi[1], Yannick Dumeige[4], Patrice Féron[4], Maurizio Ferrari[5], Laurent Larger[3], Elodie Le Cren[4], Olivier Llopis[2], Jérémy Maxin[1], Pierre-Henri Merrer[2], Gualtiero Nunzi Conti[6], Gregoire Pillet[1], Khaldoun Saleh[2], Patrice Salzenstein[3], Frederic Van Dijk[7], Gilles Cibiel[8]

[1] THALES Research and Technology , 1 Avenue A. Fresnel, 91767 Palaiseau, France.
Tel: +33169415538; e-mail: loic.morvan@thalesgroup.com
[2] CNRS LAAS, 7 avenue du colonel Roche, F-31077 Toulouse, France.
[3] FEMTO-ST Institute (UMR CNRS 6174), 16 Route du Gray, 25030 Besançon Cedex, France.
[4] ENSSAT-FOTON (CNRS-UMR 6082), ENSSAT-Université de Rennes 1, 6 rue de Kerampont, BP 80518, 22300 Lannion, France.
[5] IFN – CNR, CSMFO Lab., Via alla Cascata 56/C, Povo, 38123 Trento, Italy.
[6] IFAC – CNR, MDF Lab., Via Madonna del Piano 10, 50019 Sesto Fiorentino, Italy.
[7] III-V Lab, Campus Polytechnique, 1, Avenue A. Fresnel, 91767 Palaiseau, France.
[8] CNES, 18 avenue Edouard Belin, F-31401 Toulouse, France.

ABSTRACT

Optoelectronic Oscillators (OEOs) are an attractive alternative to electrical solutions for the generation of high spectral purity signals at high frequency. Indeed, carrying the microwave signal on an optical carrier offers the opportunity of long storage time, with almost no dependence on signal frequency. For example, classical OEOs are based on kilometre long fiber delays and, in a relatively simple setup, their performances exceed the ones of most microwave oscillators. However, the most promising OEOs architectures, in term of performances and integration level, are based on high Q optical resonators. After an introduction on the principle of OEOs and their various potential applications in advanced microwave systems, we will present recent results that we have obtained in this field.

First, the realization and characterization of silica, CaF_2, MgF_2 and $LiNbO_3$ Whispering Gallery Modes (WGM) resonators with Q factors in the 10^8-10^9 range will be presented, together with related light coupling techniques for their practical use in OEOs demonstrations. Then the realization and characterization of fiber-ring resonators, that present Q factors exceeding 10^9 in a relatively simple architecture will be highlighted. Finally, dual-frequency laser sources that have been specifically realized for OEOs will be described.

Keywords: optoelectronic oscillators, optical resonator, whispering gallery mode (WGM), fibre ring, dual-frequency laser source, microwave photonics.

ACKNOWLEDGEMENTS

The authors acknowledge the financial support from European Defense Agency (EDA, project « ARAMOS »), Centre National d'Etudes Spatiales (CNES), and the French national research agency (ANR, project « ORA »).

NOTES

Modification of Spontaneous Radiation in the Presence of a 3-D Thin Dielectric Microdisk and Partial Justification of the 2-D Effective Index Model

Alexander I. Nosich[1], Mikhail V. Balaban[1], Ronan Sauleau[2]
[1] *Institute of Radio-Physics and Electronics NASU, Kharkov, Ukraine.*
Tel: +380-57-720-3782; e-mail: anosich@yahoo.com
[2] *IETR, Universite de Rennes 1, Rennes 35042, France.*

ABSTRACT
The spontaneous emission of a molecular dipole in the presence of a thin dielectric microdisk is studied as a 3D solution of Maxwell's equations with two-sided generalized boundary conditions, local energy finiteness, and a radiation condition at infinity. Results show the radiative and non-radiative decay rates display resonance maxima associated with the disk natural frequencies which can be well explained through the effective- refractive-index approximation.

Keywords: dielectric disk, generalized boundary conditions, analytical regularization, dual integral equations

1. INTRODUCTION

The term "Purcell effect" comes from quantum optics and labels resonant enhancement or, in more a general sense, modification of the spontaneous emission of an atomic or molecular dipole in non-homogeneous environment. Today's interest, in optics, in this phenomenon is explained by the ability of various nano- and micro-size particles to increase spontaneous emission by many orders of magnitude; such enhancement leads directly to applications connected to microlasers and cavity quantum electrodynamics [1-3]. More precisely the study of this effect deals with the radiated and absorbed powers associated with elementary dipoles near various resonant objects. As a rule the Purcell effect has been estimated using the so-called "Purcell factor" which is proportional to the ratio of the resonant mode quality factor to the mode volume. However, it has been recently convincingly argued that this factor, originally derived for closed cavities with imperfectly conducting walls, cannot be used in the case of open resonators such as dielectric or semiconductor microdisks. The reasons are twofold: here the natural modes do not form a complete orthogonal set of field functions and the resonance does not lead to one-term representation of the spontaneous emission rate. Therefore for an accurate estimation of the Purcell effect for open resonators it is mandatory to use full-wave modelling methods and convergent computational techniques.

2. FORMULATION

We consider the problem of finding the electromagnetic field emitted by an elementary electric dipole (EED) parallel to a thin dielectric disk and located as depicted in Fig. 1.

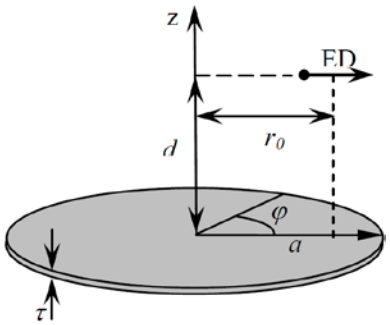

Fig. 1. Geometry of microdisk

If the disk thickness is small, as typical for microcavity lasers, one can neglect the field inside the disk and shrink its volume to the median section, at the expense of introduction of two-side generalized boundary conditions (GBC). We expand the field into Fourier series in the azimuth coordinate and use scalar and vector Hankel integral transforms in the radial coordinate. Substituting these functions into GBC, we obtain a set of dual IEs for each azimuth order *m*. Then we use the method of analytical regularization to invert IE static parts and reduce them to two pairs of coupled Fredholm second kind IEs with smooth kernels [4]. The features of the latter IEs guarantee the convergence of numerical solution if the order of discretization is increased.

3. NUMERICAL RESULTS

As computations have shown, the radiated and absorbed powers display resonances which correspond to the disk eigenmodes of different azimuth orders (see Fig. 2). Note that the Q-factors of these resonances become higher with increasing the azimuth order as typical to the whispering gallery modes (WGM). The resonances revealed in the normalized powers can be explained using the effective refractive index model of the disk. They are caused by the standing waves formed due to the reflections of the guided wave of the dielectric slab at the disk rim. This observation can serve as a *de-facto* justification of the empirical 2-D model of disk cavity with effective refractive index, from the viewpoint of rigorous Maxwell theory.

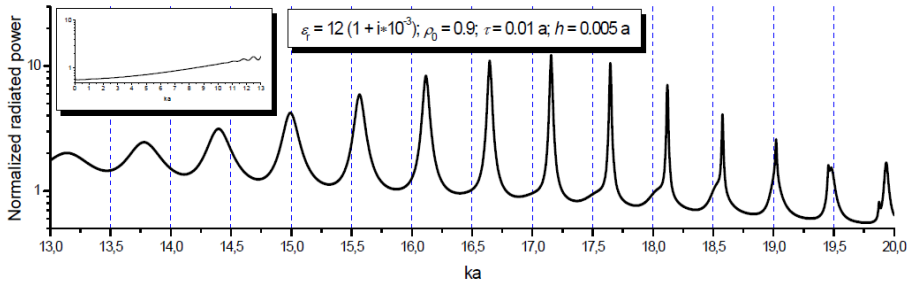

Fig. 2. Normalized radiated power for off-axis EED in the disk presence versus frequency ka.

The 3-D far field pattern corresponding to one of the maxima on the plot in Fig. 2 is presented in Fig. 3.

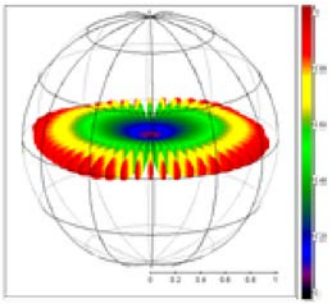

Fig. 3. Total far field pattern for the same disk and dipole as in Fig. 2 with ka = 19.4544318

This in-resonance pattern clearly displays two features: first, the radiation is concentrated in the disk plane and, second, in that plane the pattern shows 50 almost identical lobes characteristic for WGM with $m = 25$.

4. CONCLUSIONS

We have accurately quantified the Purcell effect or, equivalently, the modification of powers radiated and absorbed due to horizontal EED in the presence of a thin dielectric microdisk, by studying it from first principles. This has been done over a wide range of the normalized wavelengths. Thus, the analytical-numerical method which has been applied here places thin material disks in the same position as spherical scatterers in the sense that they can be computed very economically and with controlled accuracy.

ACKNOWLEDGEMENTS

This work was supported by the National Academy of Sciences of Ukraine via the program “Nanotechnologies and Nanomaterials” and the European Science Foundation via the Networking Program “Newfocus”.

REFERENCES

[1] J. Vukovic, *et al.*: Finite-difference time-domain calculation of the spontaneous emission coupling factor in optical microcavities, *IEEE. J. Quantum Electron.*, vol. 35, no 8, pp. 1168-1175, 1999.

[2] L. Rogobete and C. Henkel: Spontaneous emission in a subwavelength environment characterized by boundary integral equations, *Phys. Rev. A*, vol. 70, Art. No. 063815, 2004.

[3] W. Ding, *et al.*: Understanding near/far-field engineering of optical dimer antennas through geometry modification**,”** *Optics Express*, Vol. 17, No 23, pp. 21228-21239, 2009.

[4] M. V. Balaban, *et al.*: Dual integral equations technique in electromagnetic wave scattering by a thin disk, *Progress in Electromagnetic Research B*, vol. 16, pp. 107-126, 2009.

Photonic quantum ring laser structures investigated by laser scanning microscopy techniques

Radu Hristu[1], Stefan G. Stanciu[1], George A. Stanciu[1*]
[1] Center for Microscopy-Microanalysis and Information Processing, University Politehnica of Bucharest, 313 Splaiul Independentei, 060042, Bucharest, Romania.
*Tel: +4021 4029110; e-mail: stanciu@physics.pub.ro

ABSTRACT
We report on the optical beam induced current of photonic quantum ring lasers using Ti:Sapphire femtosecond pulsed laser. By using optical beam induced current microscopy we were able to compare the lasing and the photoinduced current images of the structures and analyze their behavior when changing the excitation wavelength. We report the optimal excitation conditions in terms of excitation laser wavelength for collecting the highest photocurrent signal and hence highlighting the photonic quantum ring behavior of the lasers.

Keywords: photonic quantum ring laser, optical beam induced current, vertical-cavity surface-emitting laser.

1. INTRODUCTION

Photonic quantum ring (PQR) lasers [1] are a new generation type of semiconductor lasers similar to whispering gallery (WG) mode lasers. While WG lasers are based upon 2D total internal reflection (TIR), the PQR laser is more like a whispering cave mode laser, based upon 3D TIR [2]. These devices, with a structure similar to vertical-cavity surface-emitting lasers (VCSELs), exhibit a two threshold behavior of successive lasings. The first is the PQR lasing that occurs at μA threshold currents with the structure emitting on its circumference and the second is the usual VCSEL mode at currents in the range of mA.
In a PQR laser, photons generated in the active region are vertically confined by the top and bottom distributed Bragg reflectors (DBRs) and in-plane annular confinemened by TIR along the lateral boundaries of the active disk. There results a 3D confinement of photons that generates a Rayleigh toroid along the circumferential region of the active area. According to Chin et al. [3] the Rayleigh toroid is limited by the active disk's physical radius R as outer boundary and as inner boundary it has the inner reflection point $r_{in} = Rn_M/n$, where n is the refractive index of the active medium and n_M is the effective refractive index in azimuthal direction $n_M \sim n_{eff}$. Hence, in the active area plane, the PQR region is defined by the Rayleigh's bandwidth: $n_{Rayleigh} = R(1 - n_{eff}/n)$.
PQR laser structures need non-destructive optical and electrical investigation techniques in order to be characterized with good spatial resolution. One such technique is optical beam induced current (OBIC) microscopy which represents a wide-spread method with applications for the characterization of many semiconductor and optoelectronic devices. It has been previously shown that OBIC imaging is more sensitive and specific than photoluminescence (PL) imaging in characterizing different semiconductor devices such as LEDs [4, 5]. It has also been used for diodes to determine carrier lifetime [6], photovoltaic devices to estimate the diffusion length of carriers [7], laser diodes to investigate the uniformity and quantum efficiency of the active region [8, 9], and also for VCSELs characterization [10].
We report here on the imaging of GaAs/AlGaAs PQR laser structures by using OBIC microscopy. Starting from a comparison between the OBIC and lasing images we also show that the properties of the active layer in the PQR circumferential region can be investigated from both the lasing and OBIC images. Additionally, the dependence of the photoinduced current with the excitation wavelength highlights a VCSEL-like behavior of the central region different than the behavior of the circumferential region.

2. EXPERIMENTAL

PQR devices of various diameters were grown on a single chip on n-type (100) GaAs substrate by metal-organic vapor-phase epitaxy method. The structure (fig. 1) consists of two DBR mirrors surrounding a one-λ cavity, which has three 8 nm GaAs quantum wells, $Al_{0.3}Ga_{0.7}As$ barriers and spacers. The thickness of the active region is 269.4 nm. There are 38.5 periods in the n-type bottom mirror and 21.5 periods in the p-type top mirror. The mirrors consist of alternating 41.98 nm $Al_{0.15}Ga_{0.85}As$ and 48.82 nm $Al_{0.95}Ga_{0.05}As$ layers. Between these layers, a 20 nm thick linearly graded AlGaAs additional layer was grown. The p- and n-DBR mirrors were doped with C and Si, respectively. The thicknesses of the quantum wells and their compositions are tuned to yield a resonance wavelength of 850 nm in the vertical direction.
More details regarding the fabrication of similar structures can be found in [11, 12].

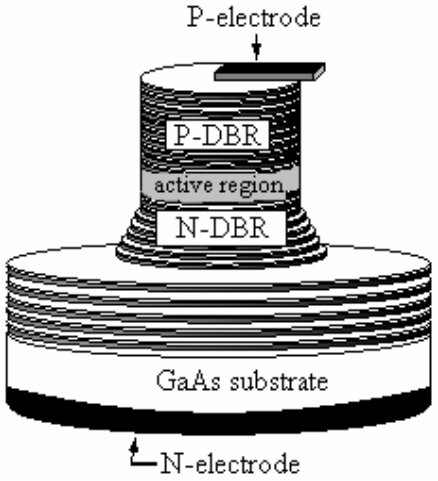

Figure 1. PQR laser structure.

The samples were studied by using pulsed optical excitation provided through the top DBR mirror. A mode- locked Ti:sapphire laser (Spectra Physics Tsunami-S fs, 5 W pump) with a ~80 fs pulse width at a 80 MHz repetition rate and a tunable output between 690 and 850 nm was used as excitation source. A Leica TCS SP confocal laser scanning microscope (CLSM) with a 40X 0.75 NA objective has been used to focus the laser beam and to scan it across the sample. For OBIC imaging, the photocurrent signal (in the range of tens of nA) is pre-conditioned by a current preamplifier (SR-570, Stanford Research) before being fed into the synchronized A/D converter of the CLSM. Lasing images were collected by biasing the PQR lasers and scanning the structures without an excitation laser.

3. RESULTS AND DISCUSSIONS

Using the setup described in the previous section reflection, lasing and OBIC images were acquired (Fig. 2).

Figure 2. Laser scanning microscopy images: from top left to right reflection, lasing and OBIC images of a 32 µm PQR laser.

The lasing image highlights a laser emission on the circumference of the PQR laser as expected. The OBIC image shows the same ring shape pattern on the peripheral region of the laser and an uniform distribution of the photocurrent in the central region. We would like to stress out that if we overlap the reflection, lasing and OBIC images a strong resemblance between them can be observed, especially when looking at the peripheral ring. Hence, OBIC images show a non-uniform distribution of the photocurrent with a higher intensity on the circumference of the device, proving a different behavior of the peripheral ring-shaped region compared to the central area of the structure, similar to the PQR and VCSEL modes in the case of lasing.

Using the tunability of the Ti:Sapphire laser the dependence between the photoinduced current and the wavelength of the exciting laser is investigated. For optoelectronic devices in general, the shape of the photocurrent spectrum is closely connected to the absorption of the whole structure. There are also other contributions that should be taken into consideration like those related to defect or impurity absorption [8].

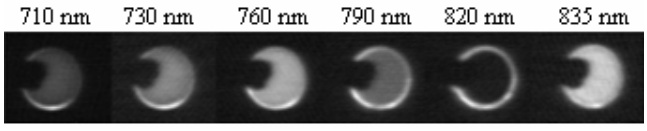

Figre 3. A series of OBIC images from a 32 µm diameter PQR laser with the corresponding excitation wavelengths.

For VCSEL-like structures, including PQR lasers, the influence of the cavity formed by the upper and lower DBRs must additionally be taken into account. Basically, these laser structures are resonant cavities formed between the two DBR mirrors. The mirror pattern affects the entire photocurrent spectrum including the spectrum around the lasing wavelength as well as the spectral region situated below the emission wavelength [9].

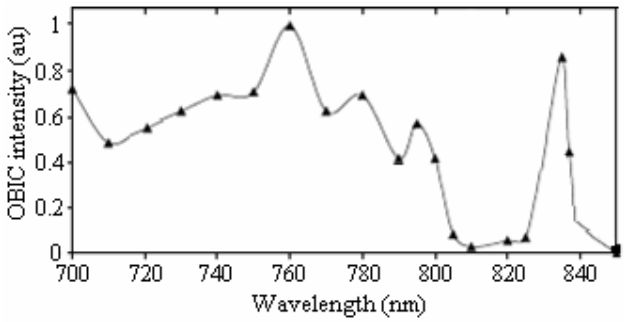

Figure 4. OBIC spectrum for the central region of the PQR laser.

Looking at the OBIC spectra for the central region of the PQR laser (fig. 4) a typical VCSEL behavior [13] can be observed. For wavelengths lower than 710 nm (1.74 eV) the absorption in the upper $Al_{0.3}Ga_{0.7}As$ barrier, with a band-gap energy E = 1.8 eV, influences the OBIC spectrum. Starting with 750 nm the influence of the upper and lower DBR mirrors on the OBIC spectrum is higher. The peak at λ = 760 nm (1.63 eV) is due to transmission maxima of the upper DBR and can also be due to the absorption within the $Al_{0.15}Ga_{0.85}As$ layer in the upper DBR that has a band-gap energy E = 1.61 eV. The main photocurrent feature at 836 nm is in good correspondence with the measured emission wavelength of the device at 835 nm and spectrally lies in the reflectance stop band of the resonant cavity that extends from 800 nm to over 850 nm.

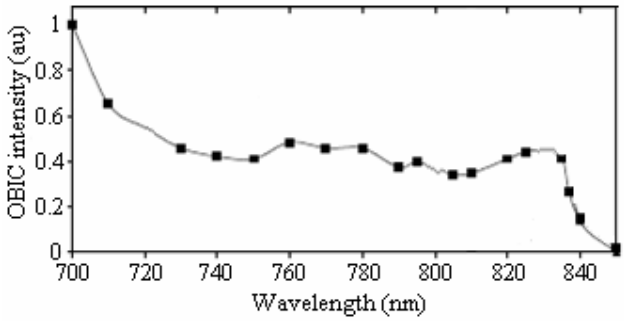

Figure 5. OBIC spectrum for the peripheral region of the PQR laser.

The OBIC spectrum for the peripheral (fig. 5) ring is constantly decreasing from 700 nm to 810 nm due to the decrease in absorption, same as in the case of a multiple quantum well structure [14]. The influence of the DBR mirror and resonant cavity to the spectrum is minimal, being visible between 760 nm and 800 nm where the spectrum slightly increases similar to the OBIC spectrum for the central region, similar to the situation in fig. 4. At wavelengths close to the emission wavelength (835 nm) the dominant excitonic contribution to the GaAs bandedge absorption is visible. It is slightly moved to higher energies than the bulk GaAs band-gap energy (1.42 eV) due to the quantum well effect. When the excitation wavelength is higher than the emission wavelength, the OBIC spectrum drops to zero.

4. CONCLUSIONS

We have investigated PQR lasers using laser scanning microscopy techniques. We have shown that OBIC can be used to investigate these structures proving a VCSEL-like behavior of the central region different from the behavior of the peripheral ring that correspond to the PQR lasing in lasing images.

ACKNOWLEDGEMENTS

This work was supported by CNCSIS–UEFISCDI, project number PNII–IDEI 1566/2008, contract number 726/2009 and by the European Program COST MP0702. The authors are grateful to professor O'Dae Kwon for providing the PQR laser samples.

REFERENCES

[1] J.C. Ahn, et al.: Photonic quantum ring, Phys. Rev. Lett. vol. 82 pp. 536-539, Jan. 1999.
[2] O'D. Kwon, et al.: Photonic quantum ring laser of 3D whispering cave mode, Microelectron. J. vol. 40 pp. 570-573, Mar. 2009.
[3] M. K. Chin, et al.: Estimation of the spontaneous emission factor for microdisk lasers via the approximation of whispering-gallery modes, J. Appl. Phys. vol. 75 pp. 3302-3307, Apr. 1994.
[4] F. J. Kao, et al.: Two-photon optical-beam-induced current imaging of indium gallium nitride blue light-emitting diodes, Opt. Lett. vol. 24 pp.1407-1409 Oct. 1999.
[5] E. Esposito, et al.: Confocal optical beam induced current microscopy of light-emitting diodes with a white-light supercontinuum source, Appl. Phys. B vol. 88 pp. 551-555 Sept. 2007.
[6] C. Raynaud, et al.: OBIC analysis for 1.3 kV 6H-SiC p(+)n planar bipolar diodes protected by Junction Termination Extension, Diam. Relat. Mater. vol. 13 pp.1697-1703 Sept. 2004.
[7] Y. Sayad, et al.: Determination of diffusion length in photovoltaic crystalline silicon by modelisation of light beam induced current, Superlattice. Microst. vol. 45 pp. 393-401 Apr.-May 2009.
[8] G. Stanciu, D. Botez, Microscopy and Analysis, 88, 5 (2002)
[9] A. Richter, et al.: Optical near-field photocurrent spectroscopy: A new technique for analyzing microscopic aging processes in optoelectronic devices, Appl. Phys. Lett. vol. 69 pp. 3981-3983 Dec. 1996.
[10] J.W. Tomm, et al.: Near-field photocurrent spectroscopy of laser diode devices, J. Cryst. Growth vol. 210 pp. 296-302 Mar. 2000.
[11] J. Y. Kim, et al.: Fabrication of Photonic Quantum Ring Laser using Chemically Assisted Ion Beam Etching, J. Vac. Sci. Technol. B vol. 19 pp. 1334-1338 Jul. 2001.
[12] J. C. Ahn, et al.: High-order transverse mode characteristics of 790nm vertical cavity surface emitting lasers, Jpn. J. Appl. Phys. vol. 36 pp. 2134 Apr. 1997.
[13] A. Jaeger, et al.: Angle-dependent photocurrent spectroscopy of oxide-apertured vertical-cavity surface-emitting lasers during aging, Appl. Phys. Lett. vol. 78 pp. 3012-3014 May 2001.
[14] M. Bugajski, K. Reginski: Opto-Electr. Rev. vol. 4 pp. 83 1996.

Transport properties of MOPhC/metal one-way waveguide in the presence of a time-dependent external magnetic field

Vladimir Kuzmiak[1], Sergey Eyderman [1]
[1] *Institute of Photonics and Electronics AS CR, v.v.i., Chaberská 57, 18251 Prague 8, Czech Republic.*
Tel: +420 266773445; e-mail: kuzmiak@ufe.cz

ABSTRACT

We have studied numerically transport and spectral properties associated with the unidirectional propagation of the surface plasmon polariton mode along the interface between metal and uniformly magnetized 2D photonic crystal(PC) fabricated from a transparent dielectric magneto-optic(MO) material. To explore both the transport and spectral properties of such unidirectional device we employed the FDTD method which enables calculating propagation of EM waves through media with full tensorial MO permittivity. We found that the behaviour of a one-way waveguide is strongly affected and the modulation of the external magnetic field implies a number of new and interesting features associated with the redistribution of the EM field that have been interpreted in terms of the spectral analysis by using of the Fourier transform of the EM energy density.

Keywords: magneto-optic photonic crystal, symmetry breaking, nonreciprocity, surface plasmon polariton, optical waveguide.

1. INTRODUCTION

Several concepts that can form one-way waveguide that allow EM energy to flow in one direction only have been proposed recently[1-7]. In order to ensure a spectral non-reciprocity $\omega(-k) \neq \omega(k)$ a breaking of both space- and time-reversal symmetry [8] has to occur. Based on the latter principle, it has been demonstrated one can employ a proper 1D periodic arrangement of magnetic and dielectric components that give rise to strong spectral asymmetry [2]. A new and potentially promising design of one-way waveguide was recently proposed by Yu [1], where the structure is formed by the interface between a photonic crystal and a metal subject to an externally applied static magnetic field. Such a waveguide provides a frequency range where only one propagating direction is allowed and with the bandwidth that is proportional to the strength of the external magnetic field. To overcome the major drawback of the configuration considered in Ref. 1, namely unrealistically high external field to be applied to achieve sizable one-way bandwidth, we proposed a modified waveguide formed between photonic crystal fabricated from a transparent dielectric magneto-optic (MO) material and metal region [9]. A nonreciprocity at the interface is introduced by the MO properties of the photonic crystal material, specifically we considered Bismuth Iron Garnet (BIG, $Bi_3Fe_5O_{12}$), a ferrimagnetic oxide which is easily magnetically saturated by fields of the order of tens of mT. To investigate transport properties of the structure we have implemented finite-difference time-domain (FDTD) method [10,11], that allows calculating the propagation of electromagnetic waves through media with full tensorial magneto-optic permittivity. To explore dynamical properties of a one-way waveguide we studied its behaviour in the presence of the time-dependent external magnetic field. We found that the modulation of the external magnetic field leads within both linear and nonlinear regimes to a number of new and interesting features associated with the redistribution of the EM field. We considered both a harmonic and a transient-like modulation and to interpret new features observed in the spectrum obtained by means of the Fourier transform of the EM energy density.

2. ONE-WAY WAVEGUIDE MODEL

We consider the waveguide which is formed by the interface between a metal characterized by Drude free-electron model and magneto-optic photonic crystal subject to an externally applied magnetic field that is perpendicular to the plane of propagation – see Fig. 1(a). We have shown that such a configuration constitutes non-reciprocal system provided that the frequency of the surface plasmon frequency propagating at the interface between metal and MOPhC lies within the band gap of the photonic crystal. The design of the structure relies on both the presence of the surface plasmon polariton which is independent of time-reversal symmetry breaking and 2D magneto-optic photonic crystal under a static magnetic field. The role of MOPhC is two-fold: non-reciprocity that is induced by magneto-optic material which photonic crystal is fabricated of, while the periodicity gives rise to the band gap where the radiation modes are eliminated and such waveguide suppresses disorder-induced backscattering. The presence of the band gap is a key feature of the studied one-way waveguide since it prevents backscattering via reciprocal radiation continuum. Therefore, information on the spectrum of the Bloch modes is essential in the theoretical description of the system. To describe underlying dispersion relation of the one-way EM waveguide we previously implemented MO aperiodic Fourier Modal Method that has been described in Ref. 9. We have shown that by using eigenmode scattering matrix technique one can deduce the response of arbitrary

finite system by solving generalized eigenvalue problem. After benchmarking of this method using the structure proposed in Ref. 1 we have calculated dispersion relation for the structure shown in Fig. 1 and we found that within the frequency range $0.366 < \omega/\omega_p < 0.376$, where ω_p is the plasma frequency modes the wave can propagate only along one direction. To validate the results obtained by MO aperiodic Fourier Modal Method

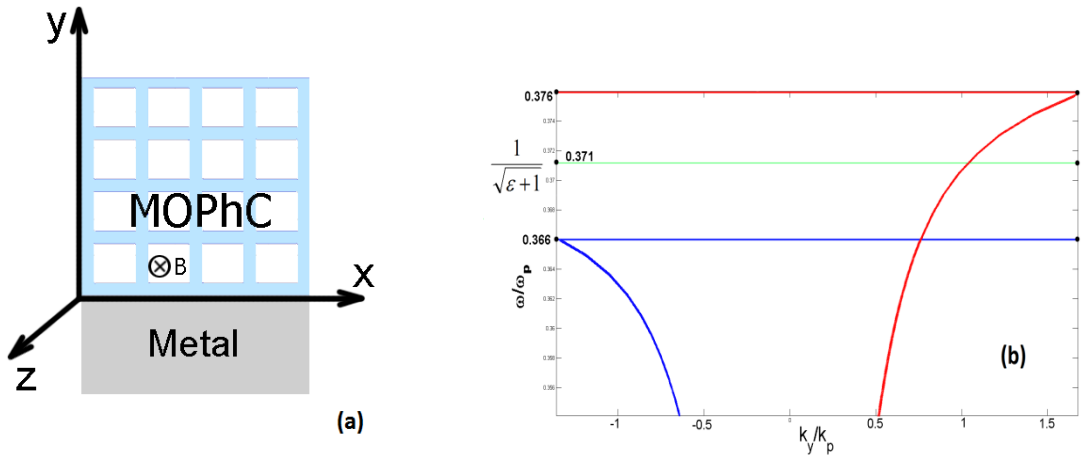

Figure 1. (a) One-way waveguide structure (b) Nonreciprocal surface wave dispersion relation for SPP propagating at between metal and BIG which possesses one-way frequency range $0.366 < \omega/\omega_p < 0.376$.

to obtain deeper physical insight into the underlying mechanisms associated with one-way property we examine the band structure of the one-way waveguide shown in Fig. 1(a) by using a simple theoretical model and plane-wave method which treat both key mechanisms assuring the functionality of the one-way waveguide i.e. time-reversal symmetry breaking which gives rise to one-way frequency range and a suppression of disorder-induced backscattering to the periodicity, separately. The theoretical model which we use in the first step is based on the analysis of non-reciprocal surface wave in the Voigt transverse configuration [12]. We assume a simplified waveguide where we replace the photonic crystal by an uniform MO medium and we evaluate the dispersion relation for a surface plasmon polariton propagating at the interface between metal and MO material. In the second step the dispersion relation is superimposed on the underlying band structure associated with the two-dimensional PhC that is calculated by using a standard plane wave method. In Fig. 1(b) we present part of the dispersion relation which possesses one-way frequency range within that SPP can only propagate in one direction. The frequency associated with the center of the one-way frequency range $0.366 < \omega/\omega_p < 0.376$ corresponds to the frequency of the SPP propagating along the interface in the absence of the external magnetic field. We note that this one-way frequency range coincides with that obtained by Fourier modal method reported by us previously [9]. The theoretical model confirms that the time-reversal symmetry giving rise to magnetic-induced non-reciprocity and the existence of one-way frequency range solely relies on the material properties of magnetic medium and implies unidirectional propagation of the surface plasmon polariton. On the other hand, one has to keep in mind that periodicity of the MO medium plays key role in the system since functionality of the one-way waveguide is based on the presence of the band gap where the radiative modes are eliminated when the metal is placed to close vicinity of the photonic crystal and such a waveguide suppresses disorder-induced backscattering.

3. TRANSPORT PROPERTIES IN THE PRESENCE OF THE TIME-DEPENDENT MAGNETIC FIELD

We also examined dynamical properties of one-way waveguide structure in the case when the magnetic field is time-dependent, namely when it is harmonically oscillating and when it is switched off at some time t_0 i.e. possessing the Heaviside step function behaviour. The amplitude of the external field ΔB corresponds to the magnetic field associated with the off-diagonal term $g = 1$ belonging to the permittivity of the MO medium. The modulation frequency of the external magnetic field ω_e in the former case is chosen to be order of magnitude smaller than that of the frequency of the oscillating dipole that has been chosen to coincide with midgap frequency $\omega_c = 0.396 \times 2\pi c/a$ in normalized units. To study the behaviour of the propagating light in the waveguide shown in Fig. 1 in the presence of sinusoidal time-dependent external magnetic field shown in the inset of the Fig. 2(a) we choose a specific time that is indicated by the full circle on the curve displayed in the same inset. The magnetic field shown in the Fig. 2(a) can be divided into three regions which represent separated domains of the field distributions associated with the mode which arise due to the modulation of the external magnetic field. The upper and central parts within the panel above and below the position of the oscillating

dipole, respectively, correspond to the fractions of the mode which start to propagate in the reverse direction due to the opposite sign of the external magnetic field. We claim that the central part of the energy density shown in Fig. 2(a) correspond to trapped light which is confined via localized modes within the band gap. This feature takes place in the case of sinusoidal modulation while it does not appear in the case of step-like modulation. This effect will be discussed below within in the context of the results related to its spectral properties. The field distribution at the bottom of the panel in Fig. 2(a) corresponds to the part of the wave which curiously enough continues to propagate in the forward direction and, therefore, can be assigned to an induced mode which we inspect in more detail hereafter. Namely, we carry out series of numerical experiments in which we study the spectrum of the field within the structure when the amplitude of the alternating magnetic field is varied. The results shown in Fig. 2(a) correspond to the case of sinusoidal external magnetic field and the spectrum is evaluated after 10 periods of modulation. When the external magnetic field has the Heaviside step function form the spectrum is in comparison with sinusoidal case significantly different, namely it does not contain the localized states within the stop band and this feature is consistent with the absence of the central part of the distribution of the energy density shown in Fig. 2(a). The results presented in Fig. 6 are summarized in Fig. 2(b). The left panel in Fig. 2(b) shows part of the band structure which contains intrinsic PhC band gap (light shaded region) which accommodates unidirectional frequency range (dark shaded range). On the right panel we display Fourier transforms of the EM energy density of the modes which characterize spectra as they depend on the amplitude of the modulation of the external magnetic field ΔB in units related to the off-diagonal term g belonging to the permittivity tensor of the MO medium. The spectrum on the left side of the right panel which corresponds to a small modulation ~1% reveals a single peak and thus indicates that unidirectional propagation is not affected. When the magnitude of the modulation ΔB is increased in the range $0.01g < \Delta B < g$ a number of replicas of the modes appear in the spectrum. We note that when number of the induced modes exceeds two side lobes the system enters nonlinear regime characterized by an increasing number of induced modes. Simultaneously, the induced modes mutually interact and give rise to temporally varying behaviour of their amplitudes. Properties of the Fourier spectra shown in the Fig. 2(b) can be used in the interpretation of the induced modes shown in Fig. 2(a). For the specific case considered that is defined by the ratio between the modulation frequency of the external magnetic field and that of the oscillating dipole i.e. $\omega_e = 0.1\omega_c$ there exists only a single mode with the central frequency which falls inside to the unidirectional frequency range. All other induced modes can be identified either as exponentially decaying waves with frequency within the intrinsic PhC gap which correspond to localized modes or extended-like modes with frequencies within allowed bands. The latter modes represent the induced modes shown at the bottom of the right panel of the Fig. 2(a).

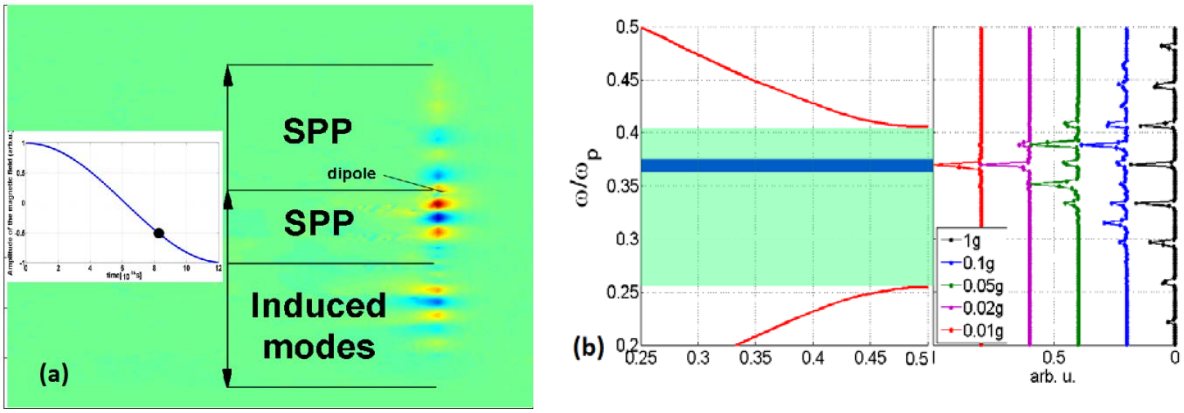

Figure 2 (a)) Snapshot of the magnetic field which shows redistribution of the EM energy density(right panel) at time $t = t_0$ indicated by the full circle in the inset of the left pane (b) The photonic band and structure of the MOPhC with one-way frequency range(left panel) vs. Fourier transforms of the EM energy density of the modes as a function of the magnitude of the modulation of the time-dependent external magnetic field ΔB.

4. CONCLUSIONS

We have studied transport properties of one-way device which can be used for the design of compact integrated analogues of one-way electronic devices such as diodes and transistors. The configuration which we consider allows in comparison with the previously reported system[1] substantially reduction of the external magnetic field. In order to accomplish the design that would be fully competitive with standard electronic counterparts one needs to scale frequencies to telecom range. To explore dynamical properties of a one-way waveguide we studied its behaviour in the presence of the time-dependent external magnetic field, we discovered new and

interesting features arising from the redistribution of the EM density and interpret them on the basis of the spectral analysis carried out by means of the Fourier transform of the EM density.

ACKNOWLEDGEMENTS

V.K. acknowledges support of the Grant No.OC09060 of Czech Ministry of Education within COST Action MP0702. V.K. and S.E. acknowledge support of the National Science Foundation of the Czech Republic by the Grant No. P205/10/0046.

REFERENCES

[1] Z. Yu *et al*.: One-Way Electromagnetic Waveguide Formed at the Interface between a Plasmonic Metal under a Static Magnetic Field and a Photonic Crystal, *Phys. Rev. Lett.* **100**, 023902 (2008).
[2] A. Figotin and I. Vitebsky,: Nonreciprocal magnetic photonic crystals, Phys. Rev. E 63, 066609, 2001.
[3] V. V. Konotop and V. Kuzmiak: Nonreciprocal frequency doubler of electromagnetic waves based on a photonic crystal, *Phys. Rev. B* **66**, 235208, 2001.
[4] F. D. M. Haldane and S. Raghu "One-way Waveguides": Analogs of Quantum Hall Edge-States in Photonic Crystals, arXiv:cond-mat/0503588v1; F. D. M. Haldane and S. Raghu, Possible realization of Directional Optical Waveguides in Photonic Crystals with Broken Time-Reversal Symnmetry, *Phys. Rev. Lett.* **100**, 013904 (2008).
[5] Z. Wang, Y. D. Chong, J. D. Joannopulous, and M. Soljacic, Reflection free One-Way Edge Modes in a Gyrotropic Photonic Crystal, *Phys. Rev. Lett.* **100**, 013905 (2008).
[6] H. Takeda and S. John: Compact optical one-way waveguide isolators for photonic-band-gap microchips, *Phys. Rev. A* **78**, 023804 (2008).
[7] Z. Yu and S. Fan: Complete optical isolation created by indirect interband transitions, *Nat. Photon*. **3**, 91(2009).
[8] I. Vitebsky, J. Edelkind, E. Bogachek, and Uzi Landman: Electronic energy spectra in antiferromagnetic media with broken reciprocity, *Phys. Rev. B* **55**, 12566, 1997.
[9] S. Eyderman, V. Kuzmiak, and M. Vanwolleghem:, One-way waveguide formed at the interface between metal and uniformly magnetized two-dimensional photonic crystal fabricated from magneto-optic photonic crystal, in *Proc. SPIE Photonics Europe*, Brussels, Belgium, April 2010, paper 7713-24.
[10] Ardavan F. Oskooi, David Roundy, Mihai Ibanescu, Peter Bermel, J. D. Joannopoulos, and Steven G. Johnson, "MEEP: A flexible free-software package for electromagnetic simulations by the FDTD method," *Computer Physics Communications* **181**, 687–702 (2010).
[11] Y. Zhao, Ch. Argyropuolos, and Y. Hao, Full-wave finite-difference time-domain method for simulation of electromagnetic cloaking structures, *arXiv:0803.2063v1*.
[12] A. Boardman, N. King, Y. Rapoport, and L.Velasco: Gyrotropic impact upon negatively refracting surfaces, *New J. Phys*. **7**, 191(2006).

Scaled projection of sub-wavelength objects through diffraction-free layered media

Marcin Stolarek , Rafał Kotyński
Faculty of Physics, University of Warsaw, Pasteura 7,02-093 Warsaw, Poland.
Tel: +48225546888; e-mail: rafalk@fuw.edu.pl

ABSTRACT
We demonstrate numerically the scaled projection of sub-wavelength objects through diffraction-free layered metamaterials. The structure operates in a similar way like a hyperlens, however the projection occurs in between flat surfaces, while the hyperlens included curved surfaces. The scaling allows to project sub-diffraction-sized objects into a wave-front that can further propagate to the far-field and vice versa. Potential applications include lithography with dimensions down-scaled as compared to the resolution of the mask, or microscopic imaging of sub-wavelength objects. We discuss the requirements on the surface roughness of the layer boundaries. The RMS of the layer boundaries should remain lower than 0.5nm in order to observe the diffraction-free propagation in the metamaterial.

Keywords: superlens; super-resolution; metal-dielectric multilayer; surface roughness.

1. INTRODUCTION

The development of plasmonics opens the way for a joint use of propagating and evanescent waves in future photonic elements. Such elements will no longer be restricted by the diffraction limit in a straightforward way. Such a possibility was first indicated with the introduction of the concept of the perfect lens [1]. However it was the experimental investigation of the far-field hyperlens [2] that became probably the first realistic super-resolving plasmonic component of practical importance. In the meantime, the asymmetric superlens was demonstrated experimentaly [3], then it was shawn that multilayers operating within the approximation of an effective medium [4] may be used to extend the size of the lens.
There still exists an ongoing effort to design diffraction-free structures with low losses, a large total thickness, and sub-wavelength resolution [4-13]. In a recent work [10] our group has optimised Ag-TiO_2, Ag-GaP and Ag-$SrTiO_3$ multilayers in terms of the resolution and transmission coefficient. It is intriguing that the optimised structures are dissimilar to those designed using the effective medium theory in terms of both the filling fraction and the internal distribution of the field. This is a strong argument for using numerical optimisation instead of simplified theoretical models when designing layered superlenses for practical applications. In [11] we have proposed a low-loss layered metamaterial for the construction of shaped (slanted or prism-shaped) diffraction-free structures with limited reflections, and with impedance matched to air. In [12] it is shown how to use the framework of linear shift-invariant (LSI) systems, widely used in the past within Fourier optics, to construct a polarisation-dependent point spread function (in a matrix form), which enables to express the layered system in an easily tractable form. This formalism has also been used to propose and study a diffraction-free non-planar imaging device. In [13], an analysis of the sensitivity of the superlens towards the fabrication uncertainties is presented, with the main conclusion that the imaging properties are extremely sensitive to the values of material permittivity as well as layer thickness of particular layers. Therefore, it remains a challenge to fabricate a super-resolving multilayers with an overall large thickness.
Although it is convenient to treat a multilayer as an LSI, the analogy to classical imaging systems may be misleading in some respects. For instance, its point spread function (PSF) is not always similar to a Gaussian function and may include a strong phase modulation. In such a case the width of PSF can not be simply interpreted as a measure of resolution. Instead, the actual resolution depends on the feature size of the object and may be even better than the width of PSF [7]. Another issue is that due to reflections, a near-field source and the LSI stack can not be regarded as completely independent systems. Nevertheless, in the two limiting cases of tight coupling (a hard source model) and no coupling (a soft source) the LSI model remains valid [14], and in practice it proves to be an efficient tool for the design of multilayers.
In the present paper, we present a prism-like element for projecting sub-wavelength wavefronts without diffraction, and with a magnification originating from non-parallel external surfaces of the device.
It is well known that surface roughness is a major limiting factor for reaching the theoretical performances in plasmonic components and that it is utmost important to achieve ultraflat surfaces [15]. We will therefore estimate the surface roughness required in the layered systems considered here for diffraction-free propagation.

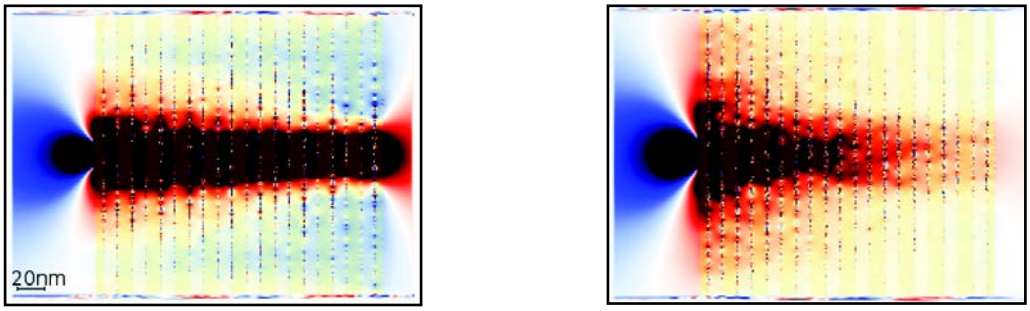

(a) (b)

Figure 1. Influence of surface roughness on diffraction-free propagation in a layered metamaterial. The FDTD simulation presents the horizontal component of the time-averaged Poynting vector obtained for the propagation of a wavefront with a sub-wavelength width through an Ag-TiO_2 stack consisting of layers with the surface roughness of (a) RMS=0.2nm; (b) RMS=0.8nm.

2. SURFACE ROUGHNESS OF METAL-DIELECTRIC METAMATERIALS FOR DIFFRACTION-FREE IMAGING

Surface roughness changes the way, in which surface plasmon polaritons propagate on plain metal-dielectric boundaries. Non-uniformity of the surface results in decoupling of plasmons to propagating waves, and in the excitation of localised plasmons. In a layered structure, where plasmon modes at the neighbouring layer boundaries are strongly coupled, this coupling is extremely sensitive to the geometry of the system.

We have conducted FDTD simulations, which allow us to quantify the degradation of imaging through the metal-dielectric layered metamaterial caused by surface roughness. For this purpose, we have introduced a noise model that characterises rough surfaces. We assumed that the layer surfaces are realisations of correlated Gaussian noise. The autocorrelation function of the noise was estimated from the measurement of the power spectrum of the silver surface deposited with electron beam evaporation and measured with AFM. Then the realisations of the Gaussian noise were obtained by spatial filtering of the samples of white Gaussian noise. Finally, they were used to adjust the definition of the multilayer in the FDTD simulation. The RMS of the noise was taken as a free paprameter.

In Fig. 1. we compare the diffraction-free propagation in two layered structures differing with the RMS of the surface roughness. Remarkably, the RMS of just 0.8nm is already too large to give a chance for a successful experimental realisation of the element. It is necessary to assure that the RMS does not exceed 0.5nm, and possibly to keep it at the level of 0.2nm.

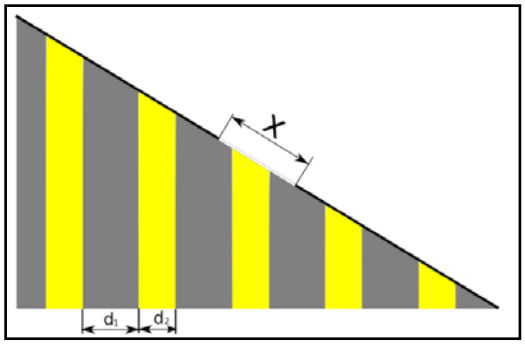

Figure 2. Layered metamaterial with an inclined edge. An aperture of size x in a chromium mask is used to form a sub-wavelength wavefront

3. SCALED IMAGING OF SUB-WAVELENGTH OBJECTS WITH LAYERED METAMATERIALS

In Fig. 2 we show the schematic of an element that we use for scaled sub-wavelength imaging. A diffraction-free multilayer is used to project the image of an aperture of size x onto the other side of the prism. The change of scale is assured by the geometry, and depends on the apex angle of the structure. The crucial point in the operation of the structure is to avoid resonances that depend on the width of the multilayer. Transmission

through the multilayer should not depend on its total thickness and on the width of the external layers. This can be accomplished with very thin layers in the order of 10nm, and by assuring that the multilayer has the impedance matched to the external medium [11].

In Fig. 3. we demonstrate the FDTD results of imaging with a change of scale. Three aperture sizes are shown - x= 2 λ, x= 1λ, x= λ/4. We compare the theoretical magnification calculated based on the apex angle – which is varied in the simulations – with the measured width of the image of the aperture. Their relation is not exactly linear. However the results prove that the structure can be successfully applied for scaled imaging of objects with sizes in the vicinity of the wavelength.

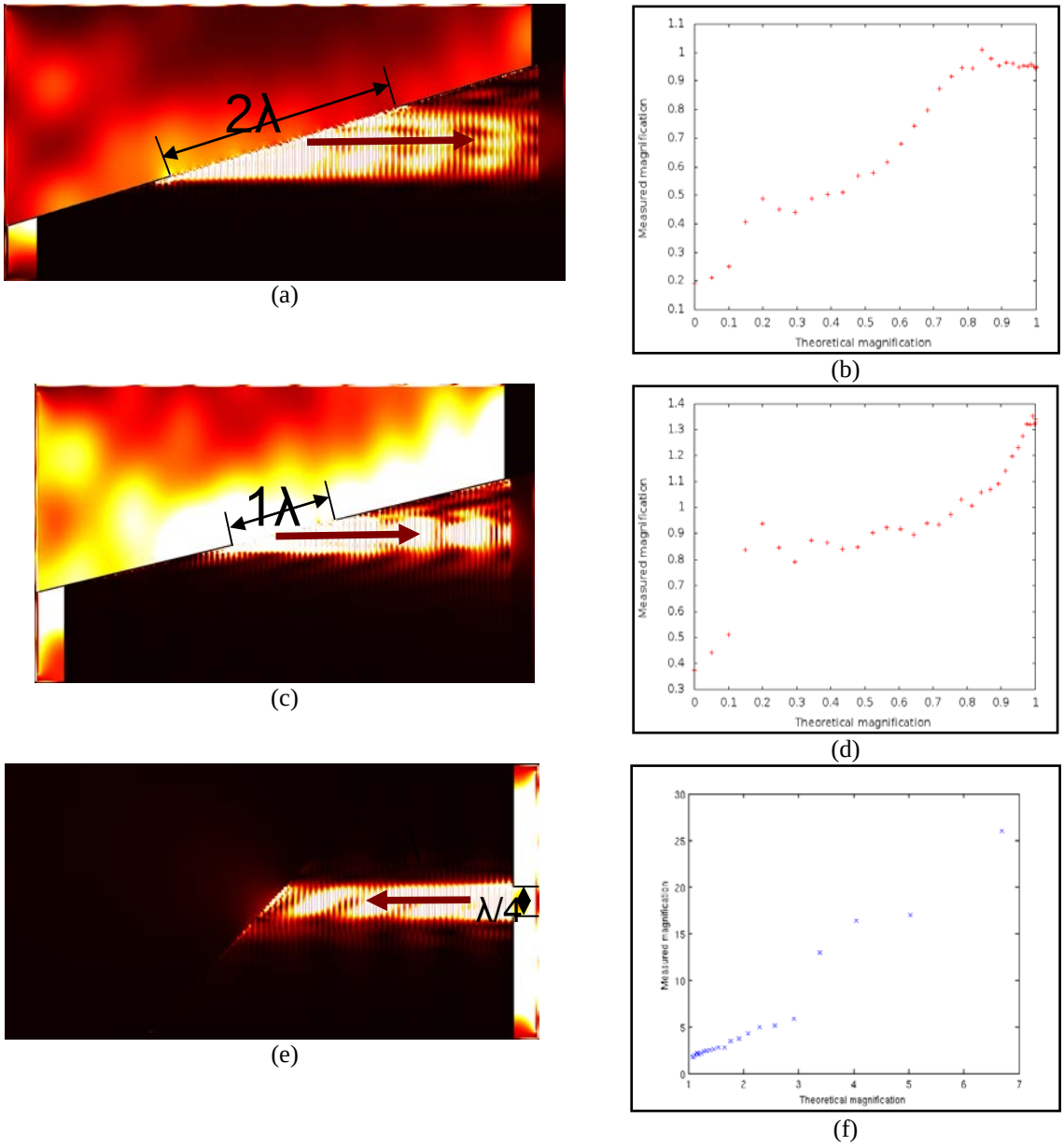

Figure 3. Imaging through the layered structure with a change of scale – FDTD simulation results illustrating the length of the time-avereaged Poynting vector (left), and the theoretical versus the measured change of scale (right). (a,b) The beam incident from the left side is limited with an aperture of x= 2λ, while its image at the right side is sub-wavelength; (c,d) same as in (a) but the aperture is x= 1λ; (e,f) The beam incident from the right side is sub-wavelength-sized and is limited by an aperture of x= λ/4, while its image at the left side is broader than the wavelength;

4. CONCLUSIONS

We have analysed the influence of surface roughness on imaging quality of layered metal-dielectric diffraction-free metamaterials. The roughness is included in FDTD simulations using the realisations of correlated Gaussian noise with varying RMS. Its autocorrelation was determined from AFM measurements, while the RMS is a free parameter. As a result, we conclude that the RMS needs to be kept below 0.5nm in order to achieve superresolution.

We have also investigated imaging with scaling through the layered metamaterial with an inclined surface. Such imaging allows to project sub-diffraction-sized objects into a wave-front that can further propagate to the far-field and vice versa. Potential applications include lithography with dimensions down-scaled as compared to the resolution of the mask, or microscopic imaging of sub-wavelength objects. The magnification partly results from the geometrical projection, and partly from diffractive broadening.

ACKNOWLEDGEMENTS

We acknowledge support from the (Polish) national Science Centre project DEC-2011/01/B/ST3/02281, and from the National Centre for Research and Development project N R15 0018 06, and the framework of European Cooperation in Science and Technology - COST action MP0702.

REFERENCES

[1] J. B. Pendry: Negative refraction makes a perfect lens, *Phys. Rev. Lett.* vol. 85, pp. 3966-3969, 2000.

[2] Z. Liu, H. Lee, Y. Xiong, C. Sun, X. Zhang: Far-Field Optical Hyperlens Magnifying Sub-Diffraction-Limited Objects, *Science* Vol. 315, 1686, 2007.

[3] D. O. Melville and R. J. Blaikie: Super-resolution imaging through a planar silver layer, *Opt. Express*, vol. 13, pp. 2127–2134, 2005.

[4] B. Wood, J. B. Pendry, and D. P. Tsai: Directed subwavelength imaging using a layered metal-dielectric system, *Phys. Rev. B*, vol. 74, 115116, 2006.

[5] D. de Ceglia, M. A. Vincenti, M. G. Cappeddu, M. Centini, N. Akozbek, A. D'Orazio, J. W. Haus, M. J. Bloemer, and M. Scalora: Tailoring metallodielectric structures for superresolution and superguiding applications in the visible and near-ir ranges, *Phys. Rev. A*, vol. 77, 033848, 2008.

[6] M. Conforti, M. Guasoni, and C. De Angelis: Subwavelength diffraction management, *Opt. Lett.*, vol. 33, pp. 2662-2664, 2008.

[7] R. Kotyński, T. Stefaniuk: Multiscale analysis of subwavelength imaging with metal-dielectric multilayers, *Opt. Lett.* vol. 35, pp. 1133-1135, 2010.

[8] N. Mattiucci, D. Aguanno, M. Scalora, M. J. Bloemer, and C. Sibilia: Transmission function properties for multi-layered structures: Application to superresolution, *Opt. Express*, vol. 17, pp. 17517-17529, 2009.

[9] P. A. Belov, C. Simovski, and P. Ikonen: Canalization of subwavelength images by electro-magnetic crystals, *Phys. Rev. B*, vol. 71, 193105, 2005.

[10] A. Pastuszczak, R. Kotyński: Optimised low-loss multilayers for imaging with sub-wavelength resolution in the visible wavelength range, *J. Appl. Phys.*, vol. 109, 084302, 2011.

[11] R. Kotyński, T. Stefaniuk, and A. Pastuszczak: Sub-wavelength diffraction-free imaging with low-loss metal-dielectric multilayers, *Applied Physics A*, doi: 10.1007/s00339-011-6286-3, 2011.

[12] R. Kotyński, T. J. Antosiewicz, K. Król, and K. Panajotov: Two-dimensional point spread matrix of layered metal–dielectric imaging elements, *J. Opt. Soc. Am. A*, vol 28, pp. 111-117, 2011.

[13] R. Kotyński, H. Baghdasaryan, T. Stefaniuk, A. Pastuszczak, M. Marciniak, A. Lavrinenko, K. Panajotov, T. Szoplik: Sensitivity of imaging properties of metal-dielectric layered flat lens to fabrication inaccuracies, *Opto-Electron. Rev.*, vol. 18, pp. 446-457, 2010.

[14] R. Kotyński: Fourier optics approach to imaging with sub-wavelength resolution through metal-dielectric multilayers, *Opto-Electron. Rev.*, vol. 18, pp. 366-375, 2010.

[15] P. Nagpal, N. C. Lindquist, S.-H. Oh, D. J. Norris : Ultrasmooth Patterned Metals for Plasmonics and Metamaterials, *Science* Vol. 325, 594, 2009.

Waveguides based on chalcogenide films: a review of their preparation and applications in infrared integrated optics

C. Vigreux and A. Pradel
ICGM cc1503, Université Montpellier II, Place Eugène Bataillon, 34095 MONTPELLIER cedex 5, France
cvigreux@lpmc.univ-montp2.fr

ABSTRACT

Chalcogenide glasses are inorganic glassy materials which contain one or more of the chalcogen elements: S, Se or Te, but not O, in conjunction with more electropositive elements like for example As, Ge, Sb, Ga or Sn. They are infrared transmitting and easy to put in thin film form, so that they are particularly attractive materials for the realization of micro-components for infrared integrated optics. Different applications can be considered for such micro-components, like environmental metrology with the fabrication of micro-sensors, biology with the realization of immunosensors for example, space with the elaboration of nulling interferometers, etc. Different groups were thus interested in the realization of channel waveguides based on chalcogenide films, since they constitute the building blocks of IR micro-components. Different approaches were studied, like laser writing, silver photodoping, ion implantation, embossing or film stacking and etching, that will be described and discussed. To end, the light-guiding structures for [6-11µm] and [10-20 µm] spectral bands prepared in the laboratory by film stacking and etching will be presented and showed to be potential candidates for modal filtering in nulling interferometers.

NOTES

Circular Dichroism of self-organized metal nanowires arrays in the second harmonic field

A. Belardini[1], M. C. Larciprete[1], M. Centini[1], E. Fazio[1] and C. Sibilia[1], D. Chiappe[2], C. Martella[2], A. Toma[2], M. Giordano[2], F. Buatier de Mongeot[2]

[1] *Dipartimento di Scienze di Base ed Applicate per l'Ingegneria, Sapienza Università di Roma,Via A. Scarpa 16, I-00161 Roma, ITALY; e-mail: alessandro.belardini@uniroma1.it*

[2] *Dipartimento di Fisica, Università di Genova and CNISM,Via Dodecaneso 33, 16146 Genova, ITALY.*

ABSTRACT

Here we report the experimental observation of circular dichroism induced by optical extrinsic chirality in the second harmonic field (800nm-400nm) of self-organized nanowires arrays with sub-wavelength periodicity (160nm). In the measurements, the second harmonic signal generated by the curved nanowires was recorded as a function of the incidence angle for left- and right-handed impinging pump fundamental light; the results show more than 50% of visibility of the extrinsic optical nonlinear circular dichroism.

Keywords: extrinsic optical chirality, second harmoni generation, self assembled nanowires, nonlinear circular dichroism.

1. INTRODUCTION

Metal nanostructures supported on dielectric substrates have attracted great interest as building blocks of nanoscale optical devices such nano-plasmonic devices or planar metamaterials. In this framework artificial circular dichroism [1] is investigated for developing novel devices for active polarization controllers, like rotators and modulators and high efficient molecular sensors. Here we report the experimental observation [2] of nonlinear extrinsic chirality [3] (circular dichroism) of the second harmonic (SH) field generated by self-organized gold nanowire arrays with sub-wavelength periodicity [4,5]. In this material the chirality arises from the curvature of the self-assembled wires, producing a lack of symmetry at oblique incidence [3]. Such circular dichroism in the SH field is the evident signature of the sample morphology and can be used in order to develop more efficient molecular sensors, based on metal enhanced fluorescence or surface enhanced Raman scattering.

2. DISCUSSION

In Figure 1 some experimental results are shown with pumping light at 800nm (second harmonic signal at 400nm); in Figure1a is evident the dichroic behavior of the sample with curved wires, between right-ended circular polarizer light (red squares) and left-ended circular polarizer light (blue disks). On figure1b the same measurements on a flat gold (20nm) reference sample, where the dichroism is absent.

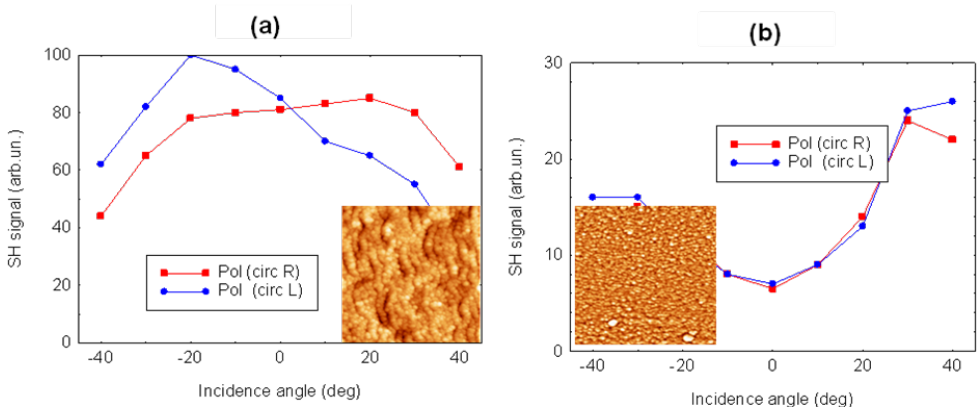

Figure 1. (a) Second harmonic signal from curved nanowires, for circular polarized light (Right-handed polarization, red squares; Left-handed polarization, blue disks). (b) Second harmonic signal from flat gold (20nm), for circular polarized light (Right-handed, red squares; Left-handed, blue disks). In the insets the morphology of the samples are shown (the areas are 2 micron x 2 micron).

The measurements highlight (as expected [3]) that extrinsic chirality arises when the wave vector direction $\hat{k}$, the normal to the sample surface $\hat{n}$ and the direction of the curvature $\hat{R}$ form a non-planar triad [4].
The handedness of the chirality can be expressed by the sign of the triple product of the former three vectors [4]:

$$\frac{1}{R}\hat{R} \cdot \hat{k} \times \hat{n} \quad . \qquad (1)$$

From the measurements it is possible to retrieve a important dimensionless parameter: the nonlinear circular dichroism that is the difference between the generated SH field intensity (at s- or p-polarization state) obtained from the left-handed circular polarized pump light and the right-handed one divided by the average total generated intensity [4,6]

$$\frac{I_L^{2\omega} - I_R^{2\omega}}{(I_L^{2\omega} + I_R^{2\omega})/2} \quad . \tag{2}$$

This parameter is the sign of resonant optical activity [6] that gives rise to the possibility of negative refraction [3,7]. From the nonlinear optical point of view the second harmonic signal is generated from the wires mainly by the magnetic dipole term or Lorentz term [2,4,8]

$$\vec{P}_{2\omega} = \frac{e}{m\omega}\left(\frac{i}{2i\omega - \gamma_{2\omega}}\right)\vec{J}_{\omega} \times \vec{B}_{\omega} \tag{3}$$

where *e* is the modulus of the electron charge, *m* is the electron effective mass, γ is a damping coefficient taking into account ohmic losses. When the light impinges on a tilted sample with the radius of curvature pointing down and with negative angles, the curved wire can be seen as an element of a conductive left-handed helical coil providing a preferential path for the induced electronic current density *J*. Thus, the SH signal show a larger generation when is excited by a left-handed circularly polarized light (see the blue disks in figure 1a). On the other hand, if the tilting incidence angle is of the opposite sign (i.e. the vectorial product $\hat{k} \times \hat{n}$ in formula 1 changes the sign), the right-handed circularly polarized pump produces a larger SH signal (see the red squares in figure 1a). Measurements performed on flat reference sample shows only negligible differences in the left-handed and right-handed signal as reported in figure 1b. In ref.4 we reported also measurements performed on a reference sample constituted by straight nanowires; even in this case the extrinsic circular dichroism results to be negligible due to the absence of a curvature that could break the symmetry.

3. CONCLUSIONS

We present the evidence of nonlinear circular dichroism in curved gold nanowire. Such dichroism give the possibility to have a self-assembled effective extrinsic chiral optical medium with potential anomalous refraction capability.

CONCLUSIONS A

REFERENCES

[1] A. S. Schwanecke, A. Krasavin, D.M. Bagnall, A. Potts, A.V. Zayats, and N. I. Zheludev, Phys. *Rev. Lett*. **91**, 247404 (2003).

[2] A. Belardini, M. C. Larciprete, M. Centini, E. Fazio, C. Sibilia, D. Chiappe, C. Martella, A. Toma, M. Giordano, F. Buatier de Mongeot, accepted on Phys. Rev. Lett. (2011).

[3] E. Plum, X.-X. Liu, V. A. Fedotov, Y. Chen, D. P. Tsai, and N. I. Zheludev, Phys. *Rev. Lett*. **102**, 113902 (2009).

[4] A. Belardini, M. C. Larciprete, M. Centini, E. Fazio, C. Sibilia, M. Bertolotti, A. Toma, D. Chiappe, F. Buatier de Mongeot, Optics Express **17**, 3604 (2009).

[5] A. Toma, D. Chiappe, D. Massabò, C. Boragno, and F. Buatier de Mongeot Applied Physics Letters 93, 163104 (2008).

[6] T. Verbiest, M. Kauranen, A. Persoons, M. Ikonen, J. Kurkela, H. Lemmetyinen, J. Am. Chem. Soc. 116, 9203 (1994).

[7] J. B. Pendry, Science 306, 1353 (2004).

[8] M. C. Larciprete, A. Belardini, M. G. Cappeddu, D. de Ceglia, M. Centini, E. Fazio, C. Sibilia, M. J. Bloemer, and M. Scalora, Phys. Rev. A 77, 013809 (2008).

Second-harmonic Microscopy of Individual Single-walled Carbon Nanotubes

Mikko J. Huttunen[1], Olli Herranen[2], Andreas Johansson[2], Hua Jiang[3], Prasantha R. Mudimela[3,4], Pasi Myllyperkiö[5], Godofredo Bautista[1], Albert G. Nasibulin[3], Esko I. Kauppinen[3], Markus Ahlskog[2], Martti Kauranen[1] and Mika Pettersson[5]

[1] *Department of Physics, Tampere University of Technology, P.O. Box 692, FI-33101 Tampere, Finland.*
[2] *Department of Physics, Nanoscience Center, P.O. Box 35, FI-40014 University of Jyväskylä, Finland.*
[3]*Department of Applied Physics and Center for New Materials, Aalto University, Puumiehenkuja 2, FI-00076 Aalto University, Finland.*
[4]*IACQER Center for Research and Development on Nanotechnology, Malla Reddy Engineering College, Secunderabad-500014, India.*
[5]*Department of Chemistry, Nanoscience Center, P.O. Box 35, FI-40014 University of Jyväskylä, Finland.*
e-mail: mikko.j.huttunen@tut.fi

ABSTRACT

Single-walled carbon nanotubes (SWNTs) are promising for new applications in optoelectronics and nanotechnology due to their extraordinarily tuneable electronic properties. Depending on the indices of the roll-up vector, SWNTs can for example act either as a semiconductor or a metal. For the future applications to emerge, more reliable fabrication and characterization techniques for individual as well as for larger quantities of SWNTs are needed. Optical techniques are suitable for characterization of even larger quantities of SWNTs, and for example fluorescence and Raman scattering techniques have been found useful. Nonlinear optical techniques for SWNT characterization have so far been scarce, but can offer new capabilities.

Here we demonstrate that second-harmonic generation (SHG) can be observed even from an individual SWNT. To confirm the individuality of the SWNT, it was first characterized by transmission electron microscopy and electron diffraction, and then imaged by SHG microscopy. We also attribute the probable origin of the SHG signal to be the non-zero chiral angle of the SWNT. This opens possibility of optically and *in-situ* determining the handedness of individual chiral SWNTs. The results demonstrate the potential of SHG microscopy as a fast, non-destructive and a simple method for studying of carbon nanomolecules.

Keywords: carbon nanotubes, single-walled carbon nanotubes, second-harmonic generation, chirality.

1. INTRODUCTION

The physical properties of carbon nanotubes (CNTs) and single-walled carbon nanotubes (SWNTs) greatly depend on the very small changes in how their graphene layers are rolled up into tubes. For example the electronic and thus optical behavior of a SWNT can be changed from a semiconductor to a truly metallic by simply changing the indices denoting the roll-up vector from (10,9) to (10,10). The wide variety of electronic structures in combination with a strong nanoscale lattice and an exceptionally high thermal conductivity are the main reasons for the large interest in using SWNTs in future electronic and optical devices [1]. Unfortunately, controllable and scaled-up production of SWNTs is still very challenging. In order to fabricate devices based on the properties of individual SWNTs, there is a need for further advancement of characterization methods that are fast, cheap and precise.

Optical micro- and spectroscopies can provide valuable tools for characterization of nano-objects, including individual SWNTs [2,3]. The main benefits of optical techniques are the possibilities to study also larger quantities of SWNTs and *in-situ* capabilities. Single-photon excitation processes, such as Raman spectroscopy [4] and fluorescence [5] have been used to study the dynamics and electronic structure of SWNTs. In addition to linear processes, nonlinear optical techniques can provide complementary information, ideally also label-free, and are especially suitable for studying nano-objects, which typically have large nonlinear optical responses [3]. For example four-wave mixing (FWM) has been used for imaging of CNTs [3].

In contrast to third order-processes, second-order processes are very sensitive to the symmetry of the system, and are within the electric-dipole approximation of the light-matter interaction forbidden in centrosymmetric materials. This sensitivity has made second-order techniques widely used tools to study systems with broken symmetry, such as surfaces, interfaces, and molecular films [6]. Chiral objects lack mirror symmetry, and thus necessarily lack centrosymmetry allowing second-order processes such as second-harmonic generation (SHG). And since most of the SWNTs are chiral, SHG has been proposed as a suitable probe of their structure [7]. Ideal achiral SWNTs are centrosymmetric and should not produce SHG. Introduction of defects, however, might break the centrosymmetry of even achiral SWNTs and allow SHG response, which would make SHG microscopy a new tool to visualize defects in SWNTs. So far, SHG has been observed from thin films or ensembles of SWNTs

[7], and has been associated with chirality and large second-order susceptibility on the order of 10^{-6} esu, but it has not been clear whether an individual SWNT could generate a measurable SHG response.

Here we report a SHG response from an individual SWNT, and demonstrate that even SHG microscopy is feasible. The fabricated sample consisted of suspended SWNT across an air slit. This configuration facilitated transmission electron microscopy (TEM) and electron diffraction measurements from the same sample, which were performed to confirm the individuality of the SWNTs and the chiral roll-up indices (*n*,*m*) of the tubes. Our results demonstrate the potential of SHG microscopy as a new tool to study SWNTs and their structural properties.

2. SAMPLE FABRICATION AND EXPERIMENTAL SETUP

The SWNT sample was fabricated on a 500 µm thick, double side polished <100> Si wafer with the 300 nm thick dielectric layer of Si_3N_4 on both sides. First, a µm 750 x 750 µm opening in the bottom Si_3N_4 layer was made, using optical lithography followed by reactive ion etching at a pressure of 55 mTorr and 150 W power with a gas flow of 50 sccm of CHF_3 and 5 sccm of O_2. This was followed by wet etching through the Si wafer in 35 % KOH at 97 º C, with an etch rate of ~180 µm/h. The etching process was anisotropic with an etching angle of 54.7 º, resulting in a ~50 µm x 50 µm Si_3N_4 membrane window on the front side. A slit opening with the dimensions 1.2 µm x 40 µm was made in the Si_3N_4 membrane, using electron beam lithography followed by a second reactive ion etching step. The bottom of the sample was then covered by a 25 nm thick layer of tantalum, chosen for its high melting point, which enables it to survive during the deposition of CNTs by chemical vapour deposition (CVD). The metal layer supported the membrane and could be used for gating purposes. SWNTs were grown across the membrane in a vertical CVD reactor. CO was used as the carbon source, Ni as the catalyst material and the CNT growth temperature was 750 °C. The SWNT synthesis is described in more detail elsewhere [8].

A schematic of the sample geometry and the used characterization techniques are shown in Fig. 1(a). For SHG microscopy, a home-built setup (Fig. 1(b)) was used. A mode-locked Nd:Glass laser emitting an 82-MHz train of 200 fs pulses centered at the wavelength of 1060 nm was used with an average input power of around 1 mW to avoid sample damage. The input beam was expanded to a diameter of 7 mm, spatially filtered, collimated and polarized before entering the focusing objective (NA=0.8). Since the linear and nonlinear optical responses of SWNTs depend on the polarization of the incident beam, a polarizer was used to clean up the linear polarization of the beam and a subsequent quarter-wave plate was used to change the polarization to circular.

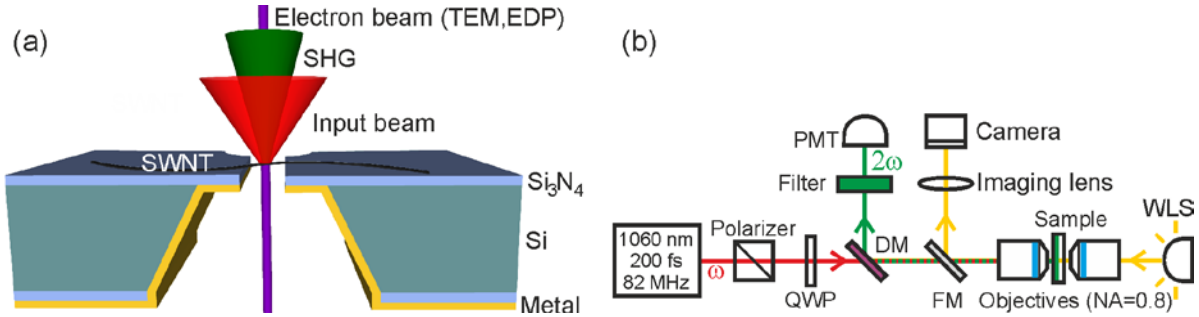

Figure 1. (a) *The SWNTs were suspended across an air slit opening to facilitate TEM, EDP and SHG from the sample.* (b) *A home-built SHG microscope setup was used in epi-configuration, where reflected SHG was separated from the fundamental beam by a dichroic mirror (DM) and an interference filter and detected by a photomultiplier tube (PMT). A white-light source (WLS), flip mirror (FM) and consecutive bright-field imaging arm were used for approximate alignment of the sample for SHG measurements.*

The SHG light was collected only in reflection by the focusing objective and separated from the fundamental and by a long-pass dichroic mirror and a narrowband interference filter (16.5 nm bandwidth centered at 532 nm), and detected by a cooled photomultiplier tube connected to a photon counting unit. To ease the sample positioning, a white-light imaging arm was implemented in the microscope. To avoid changes to the input polarization of the laser beam due to the imaging arm, a flip mirror was used to steer the white light to the imaging lens and a consecutive camera when needed. SHG imaging was done by raster scanning the sample at the focal plane of the microscope objective using a 3-axis piezo-actuated translation stage. The pixel dwell time was 150 ms, averaged twice, and for the 5 µm x 5 µm scanning area, 100 x 100 pixels were used.

3. RESULTS

First we imaged the sample by TEM, which revealed two SWNT structures (Fig. 2(a)). Then we characterized the observed SWNT structures (Fig.2(a-c)) by measuring their electron diffraction patterns (EDPs) (data not shown). The first SWNT structure (I) consisted of a bundle of CNTs and the second (II) was confirmed to be an

individual SWNT. The roll-up indices of the individual SWNT were determined to be (42,1) through a method based on intrinsic layer line distance analysis of its EDP making the SWNT chiral [9]. Then we performed SHG microscopy on the sample and saw the suspended SWNT structures (Fig. 2(d)). Due to a strong background SHG signal from the used Si_3N_4 membrane, we were not able to visualize the SWNTs on top of the substrate. Finally we verified the presence of SWNTs by imaging the sample by TEM after the SHG experiment.

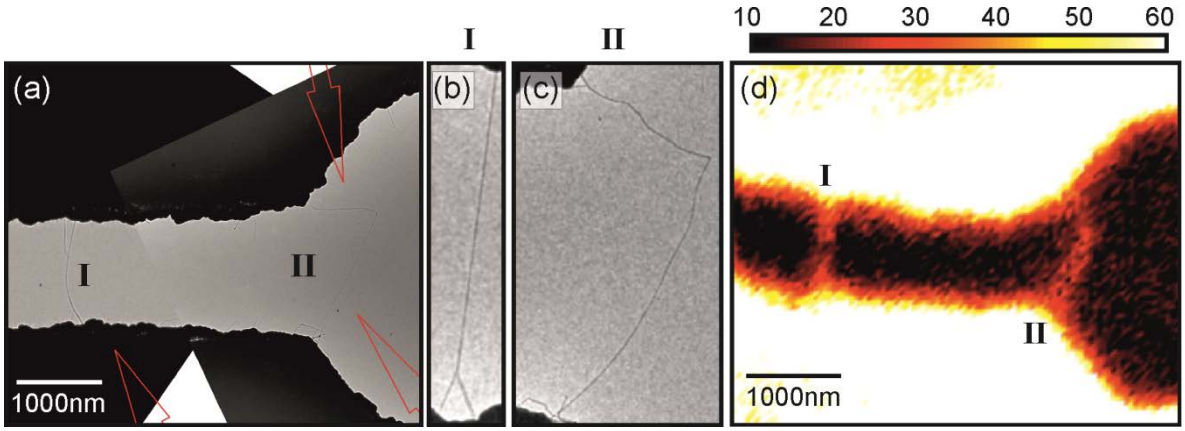

Figure 2. (a) *TEM image of the sample featuring (b) a bundle of 4-5 CNTs and (c) an individual SWNT (II).* (b) *SHG image of the sample showing the two SWNT structures (I and II).*

4. DISCUSSION AND CONCLUSIONS

Within the electric-dipole approximation, chirality, defects or both can be the source of SHG. And since the observation of a distinct EDP established the tube as being chiral and having a low defect concentration, chirality is the most probable source. This opens interesting possibilities to measure the handedness of SWNTs non-destructively and *in situ*. This has so far been only possible by scanning probe microscopy [10] or high-resolution TEM imaging [11], which are both are time consuming and potentially damaging to the SWNT.

In the future, it would be interesting to develop a SHG-based technique to probe the absolute handedness of SWNTs. As known, SHG as a second-order process is sensitive to symmetry properties of the system. This sensitivity arises from the structure of the second-order susceptibility tensor, the components of which can be classified as achiral or chiral. The latter components are non-vanishing only for a chiral system and reverse signs when the handedness of the system is reversed. The chiral signatures in SHG responses arise from a complex interplay between these achiral and chiral components and usually lead to changes in the SHG field amplitudes depending on the handedness of the sample and the probing beam [12]. But a defect-free SWNT possesses only chiral components leading only to phase changes in the SHG responses. Therefore to determine the handedness of the SWNTs, a phase sensitive SHG technique would have to be implemented [13].

In addition to chirality, also defects can play an important role in the properties of SWNTs. Since SWNTs are ideally one dimensional structures, defects can seriously hinder electron transport [14]. Thus a possibility to visualize them with an optical resolution and label-free would be important for future optoelectronic applications. Currently defects can be visualized by several techniques, for example by electroluminescence [14]. Since ideal SWNTs have very high symmetry, defects are expected to decrease the overall symmetry and introduce new non-vanishing susceptibility components changing the local SHG response. This could in future facilitate SHG microscopy as a complementary non-destructive and label-free technique for visualizing defects in SWNTs.

To conclude, we have demonstrated to our knowledge the first observation of SHG from an individual SWNT. The most probable origin of the SHG is the chirality of the SWNT. We also propose that SHG microscopy could be utilized in measuring the handedness of SWNTs and visualizing defects in SWNTs.

ACKNOWLEDGEMENTS

M.J.H. acknowledges the support from Modern School of Optics and Photonics in Finland and Emil Aaltonen foundation, O.H. from Jenny and Antti Wihuri foundation. We also acknowledge the Academy of Finland (128445, 134973 and 7122008) and CNB-E project of Aalto University MIDE program for funding.

REFERENCES

[1] P. Avouris, Z. Chen, V. Perebenios: Carbon-based electronics. *Nature Nanotech.* **2**, 605-615 (2007).
[2] M. Y. Sfeir, *et al.*: Optical spectroscopy of individual single-walled carbon nanotubes of defined chiral structure. *Science* **312**, 554-556 (2006).
[3] Y. Wang, *et al.*: Four-wave mixing microscopy of nanostructures. *Adv. Opt. Photon.* **3**, 1-52 (2011).

[4] A. Hartschuh, *et al*.: High-resolution near-field raman microscopy of single-walled carbon nanotubes. *Phys. Rev. Lett.* **90**, 095503 (2003).
[5] M. J. O'Connell: Band gap fluorescence from individual single-walled carbon nanotubes. *Science* **297**, 593-596 (2002).
[6] Y. R. Shen: Surface properties probed by second-harmonic and sum-frequency generation. *Nature* **337**, 519-525 (1989).
[7] L. De Dominicis, *et al*.: Analysis of the chiral composition of a carbon nanotube surface by means of second harmonic generation. *J. Raman Spectrosc.* **36**, 165-170 (2005).
[8] P. R. Mudimela, *et al*.: Incremental variation in the number of carbon nanotube walls with growth temperature. *J. Phys. Chem. C* **113**, 2212-2218 (2009).
[9] H. Jiang, *et al*.: Unambiguous atomic structural determination of single-walled carbon nanotubes by electron diffraction. *Carbon* **45**, 662-667 (2007).
[10] C. Lieber, *et al*.: Atomic structure and electronic properties of single-walled carbon nanotubes. *Nature* **391**, 62-64 (1998).
[11] Z. Liu, *et al*.: Determination of optical Isomers for left-handed or right-handed chiral double-wall carbon nanotubes. *Phys. Rev. Lett.* **95**, 187406 (2005).
[12] J. J. Maki, M. Kauranen, A. Persoons: Surface second-harmonic generation from chiral materials. *Phys. Rev. B* **51**, 1425-1434 (1995).
[13] L. Le Xuan, *et al*.: Balanced homodyne detection of second-harmonic generation from isolated subwavelength emitters. *Appl. Phys. Lett.* **89**, 121118 (2006).
[14] M. Freitag, *et al*.: Electrically excited, localized infrared emission from single carbon nanotubes. *Nano Lett.* **6**, 1425-1433 (2006).

Analysis and Design of Diffractive-Optical and Photonic Band-Gap Elements: Activities during the COST Action MP0702

L. Pajewski, C. Ponti, G. Schettini

Roma Tre University, Appl. Electron. Dept., via della Vasca Navale 84, 00146 Rome Italy:schettin@uniroma3.it.

ABSTRACT

Two main lines have been explored: diffractive optical and photonic band-gap elements. In the first line, work has been focused on the optimization of the power coupled to equally intense output beams: following our previous results on three- and four- beam elements, we have derived an optimum-efficiency multiplier, with an arbitrary number of output beams, and have given its phase transmittance in an analytic form. For the second line the possibility of enhancing the directivity of a planar antenna has been explored, in particular we designed, fabricated, and tested a woodpile PBG and a patch antenna, obtaining more than 10 dB of gain increase.

Keywords: Diffractive Optical Elements, Beam Multipliers, Photonic Band-Gap Materials, Woodpile, Gain-Enhancement of Antennas, Fourier Modal Method.

INTRODUCTION

The research activity of our group, in the framework of the 2007–2012 Cost Action MP0702 *Towards Functional Sub-Wavelength Photonic Structures*, has been mainly devoted to the design of Diffractive Optical Elements (DOE) and Photonic Band-Gap (PBG) metamaterials.

A DOE is, in general, a complex pattern of micro- and nano-scale structures modulating and transforming light in a predetermined way. DOEs open new degrees of freedom in electromagnetic field transformation, can be designed to handle a number of simultaneous tasks, and offer basically new opportunities for optical systems and devices. They are key components for applications where small dimensions, compactness and light weight are demanded.

PBGs, also called photonic crystals, are artificial media of great interest for their applications both in the microwave and infrared wavelength ranges, with sub-wavelengths implants embedded in a homogeneous background. The main feature is the presence of frequency bands within which the waves are highly attenuated and do not propagate.

Both the DOEs and the PBGs studied by us are passive and periodic dielectric structures, with a finite-thickness and one, two, or three, periodicity directions. We design them, and analyze their electromagnetic behavior, by using in-house codes implementing the Fourier Modal Method (FMM) [1-5].

In the field of diffractive optics, we mainly focused on beam multipliers. In [6] the profile of a DOE producing four equi-intense diffraction orders with the maximum efficiency was derived; moreover, a full-wave electromagnetic analysis was performed to study the behaviour of the device in the resonance domain. During the last years, we worked on the generalization of the procedure presented in [6] and, in this work, we prove that an optimum-efficiency beam multiplier with an arbitrary number of equi-intense diffraction orders exists, deriving its phase transmittance in an analytic form. Once the number of output beams is fixed, the electromagnetic behaviour, performances, and limits, of the synthesized device can be rigorously predicted by using the FMM codes.

As far as the design of PBGs is concerned, we studied their application to improve the performances of antennas. When used as planar reflectors, as substrates, or as high-impedance ground-planes, these periodic media are able to eliminate the drawbacks of conducting ground-planes, to prevent the propagation of surface waves also allowing a lowering of the antenna profile, and to improve the radiation efficiency. In PBG resonator antennas, an electromagnetic crystal is employed as a superstrate on a primary radiator, backed with a ground plane, and its effect is a considerable increase in the directivity. Moreover, embedding a source in a PBG working near its band-gap edge, it is possible to obtain a highly-directive antenna. In particular, we focus on PBG resonator antennas. We present the synthesis, realization, and experimental characterization of a woodpile covered patch-antenna: the main effect of the periodic structure on the antenna performances reveals to be an enhancement of about 10 dB in maximum gain [7], [8].

DIFFRACTIVE OPTICAL ELEMENTS

Beam multipliers are very popular components which divide an input beam into a certain number of output beams with equal power. They are used in many applications, as in optical signal processing, laser manufacturing optical interconnections (one-to-many array coupling, beam path switching, etc.). Maximization of the diffraction efficiency (fraction of the incident beam power that is converted into the power of the desired output beams) is a fundamental target in designing a beam multiplier, and optimal methods for the design and analysis of diffracting structures have been developed.

In this Section, we present the analytical prove that an optimum-efficiency multiplier, with an arbitrary number of output beams, exists, and we give its phase transmittance in an analytic form.

Let us consider a grating having the transmission function $\tau(x)=\exp[i\,\Phi(x)]$, where $\Phi(x)$ denotes the phase profile. Without loss of generality, in the following formulas we assume a unitary value (in suitable units) of the period d. Due to its periodicity, the following Fourier series expansion holds:

$$\tau(x)=\sum_{n=-\infty}^{+\infty}\tau_n\exp(i2\pi nx) \tag{1}$$

where

$$\tau_n=\int_{-1/2}^{1/2}\tau(x)\exp(-i2\pi nx)dx \tag{2}$$

The first variation of the square of the Fourier-coefficient magnitude is:

$$\begin{aligned}\delta|\tau_n|^2 &= i\int_{-1/2}^{1/2}\varepsilon(x)\exp[i\,\Phi(x)]\exp(-i2\pi nx)dx\int_{-1/2}^{1/2}\exp[-i\,\Phi(y)]\exp(i2\pi ny)dy+\\ &-i\int_{-1/2}^{1/2}\varepsilon(y)\exp[-i\,\Phi(y)]\exp(i2\pi ny)dy\int_{-1/2}^{1/2}\exp[i\,\Phi(x)]\exp(-i2\pi nx)dx=\\ &=i\int_{-1/2}^{1/2}\varepsilon(x)\{\tau_n^*\exp[i\,\Phi(x)-i2\pi nx]-\tau_n\exp[-i\,\Phi(x)+i2\pi nx]\}dx\end{aligned} \tag{3}$$

Let us now consider the functional

$$\mathrm{I}=\sum_{n=-\infty}^{+\infty}\beta_n|\tau_n|^2 \tag{4}$$

where β_n are suitable positive multipliers. On imposing that the first variation of I vanishes, the following equations are found:

$$\sum_{n=-\infty}^{+\infty}\beta_n|\tau_n|\sin[\alpha_n-\Phi(x)+2\pi mx]=0 \tag{5}$$

$$\cos[\Phi(x)]\sum_{n=-\infty}^{+\infty}\beta_n|\tau_n|\sin[\alpha_n+2\pi nx]=\sin[\Phi(x)]\sum_{n=-\infty}^{+\infty}\beta_n|\tau_n|\cos[\alpha_n+2\pi nx] \tag{6}$$

being α_n the argument of τ_n. Assuming that

$$R(x)=\sum_{n=-\infty}^{+\infty}\beta_n|\tau_n|\cos[\alpha_n+2\pi nx],\qquad \Gamma(x)=\sum_{n=-\infty}^{+\infty}\beta_n|\tau_n|\sin[\alpha_n+2\pi nx] \tag{7}$$

Eqs. (5) and (6) can be satisfied if

$$\cos[\Phi(x)]=g(x)R(x),\qquad \sin[\Phi(x)]=g(x)\Gamma(x) \tag{8}$$

being $g(x)$ a real arbitrary function. Therefore, the function $\Phi(x)$ maximizing the functional I assumes the form

$$\Phi(x)=\arctan\left[\frac{\Gamma(x)}{R(x)}\right]+\pi\ \mathrm{step}\,[R(x)] \tag{9}$$

where $\mathrm{step}(\cdot)$ denotes the Heaviside function. The parameters α_n and β_n have to be chosen in such a way that all the Fourier coefficients have the same magnitude. Although the expression in Eq. (9)seems to be quite complicated, the optimum profile assumes, eventually apart for discontinuities, a simple and regular shape. In Fig. 1, the optimum profile is shown for 4, 5, and 6 equi-intense output beams. The beam uniformity is 0.001.

As is well known, in the paraxial domain the vectorial nature of light can be neglected and the influence of the diffractive element on the illuminating wavefront can be described by its transmission function. In the resonance domain, instead, when grating-profile features have transverse dimensions comparable with the wavelength of the impinging radiation, the scalar diffraction theory fails. To study the element properties correctly, a rigorous application of the electromagnetic theory becomes necessary. Such a treatment of the problem allows, for

example, to understand the operational limits of the DOE and to study its angular response. Numerical results of the full-wave analysis of the beam multipliers, performed by using the FMM codes, are not shown here, for brevity reasons, and will be presented during the Conference.

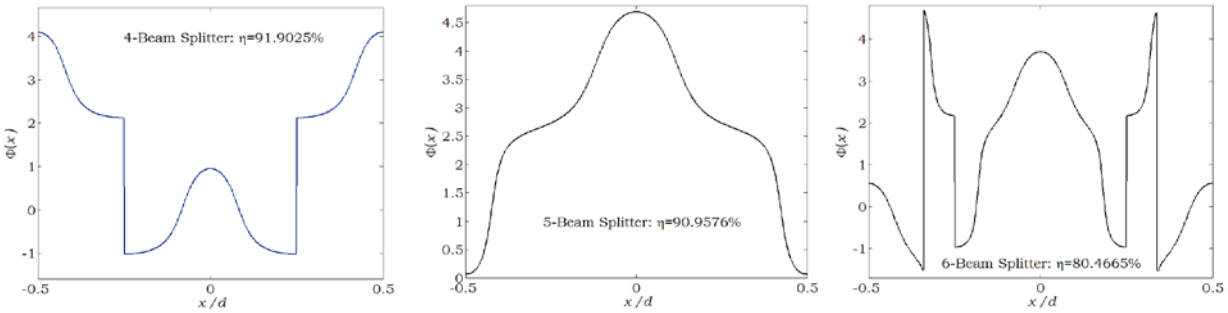

Figure 1. Optimum profile for 4, 5, and 6 equi-intense output beams.

PHOTONIC BAND-GAP ELEMENTS

A Photonic Band-Gap material with woodpile unit cell of square cross-section rods, of side w = 3.18 mm, periods $d_x = d_y$ = 8 mm, and $d_z = 4w$, has been designed [7]. Its band-gap is centred on 12 GHz, and extends from 10 to 14 GHz.

Two identical alumina prototypes have been fabricated and characterized by experimental measurements in a shielded anechoic chamber. With transmission measurements on a single or two consecutive woodpile layers, the band-gap has been determined. Measurements have been carried out also with the two layers arranged to form a cavity of length h, i.e. introducing a spacing h between the two layers along the z direction in order to obtain an interruption in the periodicity. The effect is the introduction of transmission peaks inside the band-gap, which can be employed to filter the electromagnetic waves in the allowed directions. Transmission properties of both asymmetric and symmetric have been measured, considering different values of the cavity length h and of the polarization of the excitation electric field.

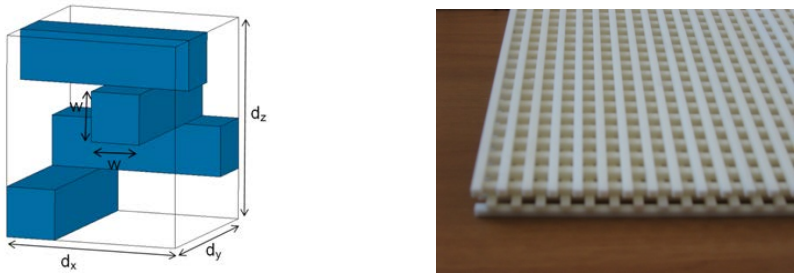

(a) *(b)*

Figure 1. The woodpile unit cell (a) and a detail of the woodpile prototype (b).

Symmetric cavities are the most interesting with a view to their use in a class of antenna applications. In fact, symmetric cavities can be modelled with an electromagnetically equivalent structure made of a halved cavity of length $h/2$, with a perfectly-conducting plate in the symmetry plane. In particular, a resonator antenna made of a microstrip patch and a woodpile cavity has been devised [7], [8]. Cavities with transmission peaks centred at the resonant frequency of the patch, which is of 10.3 GHz, have been used as superstrates of the basic radiator. Two different orientations of the woodpile with respect of the antenna polarization have been considered, together with different values of the spacing $h/2$. Experimental measurement pointed out a gain enhancement in of 10 dB with respect to the microstrip patch alone.

Results are here reported for a cavity of length h = 90 mm, with electric field polarization parallel to the most internal rods of the cavity. A first peak is displayed inside the band-gap, at 10.3 GHz, as shown in Figure 2, where the measured transmission efficiency is reported.

When such a cavity is applied as superstrate of the patch antenna, at the halved distance $h/2$ = 45 mm, the gain enhancement is of 10.17 dB. The HPBW is 12◦ in the E-plane, 14◦ in the H-plane; the side-lobe level (SLL) is -9.84 dB in the E-plane, -13.15 dB in the H-plane (Figure 3).

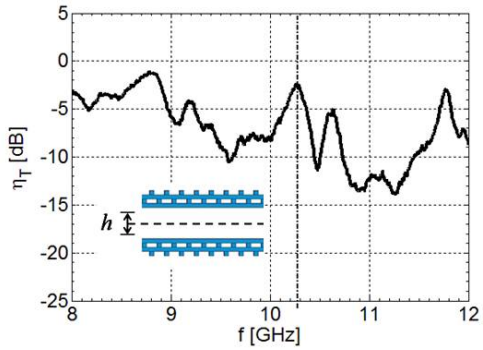

Figure 2. Measured transmission efficiency through a symmetric woodpile cavity of length h = 90mm.

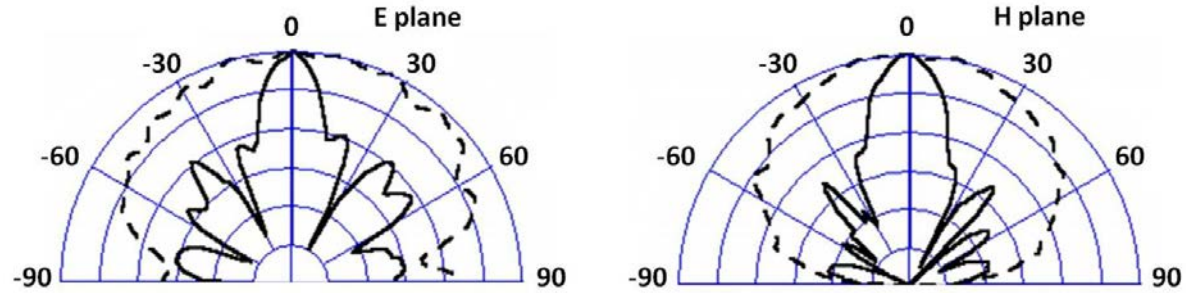

Figure 3. Measured radiation patterns for a patch antenna covered by a woodpile cavity with h/2 = 45 mm (solid line), and without woodpile (dotted line).

CONCLUSIONS

An optimum-efficiency multiplier with an arbitrary number of output beams exists, its phase transmittance is presented. Moreover a designed, realized, and tested PBG-covered patch antenna is shown.

In the future, for what pertains to DOEs, we plan to apply the theory developed for beam multipliers to the design of optical components to be realized and possibly tested with the help of an experimental group; moreover we intend to extend the activity done on PBGs to new structures with the aim of exploring new effects and of reaching accurate results for the realization of devices both in microwave and optical regimes.

REFERENCES

[1] L. Pajewski, *et al.*: Analysis and Design of Diffractive-Optical and Photonic Band-Gap Elements, in *Proc. COST MP0702 Kick-off Workshop*, Warszawa, Poland, April 2008.

[2] L. Pajewski, *et al.*: Fourier Modal Method for the Analysis of Two- and Three-Dimensional PBGs, in *Proc. COST MP0702 Kick-off Workshop*, Warszawa, Poland, April 2008.

[3] L. Pajewski and G. Schettini Photonic Band-Gap Structures with Periodicity Interruptions: theory and applications in *Proc. of the 9th International Conference on Transparent Optical Networks (ICTON)*, Rome, pp. 88-91, July 1-5 2007.

[4] F. Frezza *et al.*: Characterization and Design of Two-Dimensional Electromagnetic Band-Gap Structures by Use of a Full-Wave Method for Diffraction Gratings, *IEEE Transactions on Microwave Theory and Techniques*, vol. 51(3), pp. 941-951, March 2003.

[5] L. Pajewski and G. Schettini: Three-dimensional Electromagnetic Band-Gap Structures: Theory and Applications, in *Advanced Techniques for Microwave Systems*, G. Schettini, Editor, Research Signpost, Trivandrum, India, 2011, in press.

[6] R. Borghi *et al.*: Optimum Even-phase Four-beam Multiplier, *Optical Engineering*, vol. 41(11), pp. 2736-2742, Nov. 2002.

[7] F. Frezza *et al.*: Design and Fabrication of a 3D-EBG Superstrate for Patch Antennas, in *Proc. 39th European Microwave Conference (EuMC)*, Rome, Sept. 29 –Oct.1 2009.

[8] F. Frezza *et al.*: Analysis and Experimental Characterization of a Woodpile-Covered Patch Antenna, in *Proc. 40th European Microwave Conference (EuMC)*, Paris, Sept. 28-30 2010.

Review of Electromagnetic Wave Properties of Periodic Arrays of Metallic Carbon Nanotubes

Igor S. Nefedov and Sergei A. Tretyakov
Aalto University, School of Electrical Engineering, Dept. of Radio Science and Engineering, SMARAD Center of Excellence, P.O. Box 13000, 00076 Aalto, Finland
Tel: +3589470 22139; e-mail: igor.nefedov@aalto.fi

ABSTRACT
In this paper we present results of our theoretical studies of electromagnetic waves in periodic arrays of metallic carbon nanotubes (CNTs). Two models have been developed for the analysis of CNT arrays: a numerical model, based on Green's function method, and an effective medium model. We demonstrate that CNT arrays exhibit properties of indefinite media, characterized by hyperbolic dispersion in an ultra-broadband frequency range. Finite-thickness slabs of vertically standing CNTs support propagation of backward waves in a very wide frequency range.

Keywords: carbon nanotubes, hyperbolic media, backward waves

1. INTRODUCTION

Interest to electromagnetic properties of carbon nanotubes is caused by their potential applications in nanoelectronics [1], nanoantennas [2-4], polarizers [5], free electron lasers [6], and devices for THz sensing and imaging [7]. Carbon nanotubes (CNTs), possessing metallic properties, are of special interest for nanoelectronics due to their high conductivity at THz frequencies compared to metal nanowires [2]. For this reason, their applications appear to be promising in THz and infrared ranges due to noticeably lower losses compared to other conductive materials.

One of the most important electromagnetic properties of metallic CNTs is a capability to support propagation of strongly delayed surface waves [8]. It is caused by a very high kinetic inductance of thin single-wall CNTs [9] and it makes electromagnetic (EM) wave propagation in CNTs strongly different compared to transmission lines made of usual bulk metals. For description of electromagnetic properties of metallic CNTs the model of impedance cylinder and effective boundary conditions is used very often [8]. The model of impedance cylinders takes into account quantum properties of CNTs via the complex frequency-dependent surface conductivity. This model was applied for theoretical study of CNT transmission lines and interconnects [1] and structures composed of closely packed bundles of parallel identical metallic CNTs [10]. In [11] it was applied to two-dimensional periodic arrays of single-wall metallic CNTs.

2. NUMERICAL AND EFFECTIVE MEDIUM MODELS

2.1 Numerical model

Let us consider EM waves, propagating along a two-dimensional volumetric array of infinitely long metallic zigzag CNTs, having the radius R and forming a hexagonal lattice with the lattice constant d, see Fig. 1. For eigenwaves

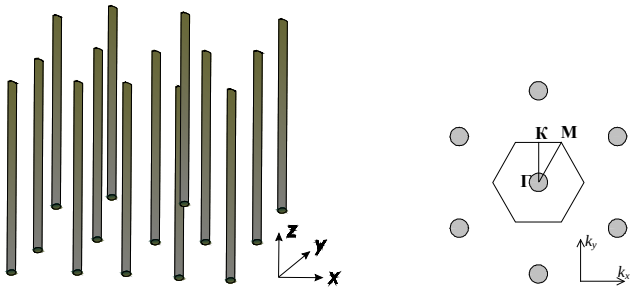

Figure 1. Left: Geometry of the CNT array. Right: Hexagonal lattice in space of wave vectors.

in arrays of infinitely long carbon nanotubes we assume the space-time dependence of fields and currents as $\exp[j(\omega t-\beta z-\mathbf{k}_\perp\cdot\mathbf{r}_\perp)]$, where $\mathbf{k}_\perp$ is the wave vector of Floquet-Bloch waves propagating in the plane of periodicity $\mathbf{r}_\perp$ (the z-axis is directed along carbon nanotubes). Carbon nanotubes are classified by the dual index (m,n) and for zigzag CNTs n=0. If m=3q (q is an integer), zigzag CNTs possess metallic properties. The radius of such a nanotube can be expressed via m and it is equal to $R=\sqrt{3}\,mb/2\pi$, where b=0.142 nm.

As a model of the individual metallic zigzag nanotube, we take an impedance cylinder, characterized by the complex dynamic conductivity. For frequencies below the optical transition band the following simple expression for the axial surface conductivity can be used [8]:

$$\sigma \cong -j\frac{2\sqrt{3}e^2\Gamma_0}{m\pi\hbar(\omega - j\nu)}, \qquad m = 3q, \tag{1}$$

where e is the electron charge, Γ_0=2.7 eV is the overlapping integral, τ=1/ν is the relaxation time. We neglect the azimuthal currents at the carbon nanotube surface compared to the axial one, which is fully justified for the parameters of CNTs chosen below and, consequently, we can consider TM_z waves with the axial component of the magnetic field H_z=0. This approximation is adequate because of the strong anisotropy of the conductivity of CNTs [9] resulting from quantum effects. It follows from (1) that the impedance of one CNT per unit length reads

$$z_i = \frac{1}{2\pi R\sigma} = \frac{m\hbar^2\nu}{4\sqrt{3}e^2\Gamma_0 R} + j\omega\frac{m\hbar^2}{4\sqrt{3}e^2\Gamma_0 R} = R_{cnt} + j\omega L_{cnt}\,. \tag{2}$$

The inductance L_{cnt} has a quantum nature and it is actually the kinetic inductance [9]. Namely the positive imaginary part of the surface impedance, i.e. the kinetic inductance, determines such a property of CNTs as a capability to support propagation of strongly delayed waves. The same relates to graphene in the intraband region [12]. We use the integral representation of the electric field induced by currents on the surface of CNT. We can neglect the non-homogeneity of the current distribution on the contour of the nanotube due to its extremely small radius. The electric field at the CNT surface can be expressed via the current and the surface conductivity. Finally, we obtain a an integral equation with respect to the surface current density J_z. Integrating this equation over the contour of CNT we come to the dispersion equation which is solved numerically.

2.2. Effective medium model

In the framework of the effective medium model CNT arrays can be considered as uniaxial materials with the permittivity dyadic

$$\bar{\bar{\varepsilon}} = \varepsilon_{zz}\boldsymbol{z}_0\boldsymbol{z}_0 + \varepsilon_0(\boldsymbol{x}_0\boldsymbol{x}_0 + \boldsymbol{y}_0\boldsymbol{y}_0), \tag{3}$$

where ε_0 is the permittivity of vacuum (we consider CNTs placed in vacuum). As was shown in [13],

$$\frac{\varepsilon_{zz}}{\varepsilon_0} = 1 - \frac{k_p^2}{k^2 - j\zeta k - k_z^2/n^2}, \quad k_p^2 = \frac{\mu_0}{d^2 L_{cnt}}, \tag{4}$$

where k is the wave number in free space; k_p is the effective plasma wave number; parameter $n^2 = L_{\text{cnt}}C_{\text{cnt}}/(\varepsilon_0\mu_0)$ measures the strength of spatial dispersion in the medium; L_{cnt}, C_{cnt} are the effective inductance and capacitance of CNTs per unit length, respectively; μ_0 is the permeability of vacuum; and the parameter $\zeta = (R_{\text{cnt}}/L_{\text{cnt}})\sqrt{\varepsilon_0\mu_0}$ is responsible for losses. Estimations of CNT parameters show that the value n^2 is very high and the term k_z^2/n^2 can be neglected. Physically it is caused by a very high value of the kinetic inductance of carbon nanotubes. For waves, propagating along CNTs, the effective medium model gives a very simple expression for the z-component of the wave vector [14]:

$$k_z^2 = \frac{k^2(k^2 - k_\perp^2 - k_p^2)}{k^2 - k_p^2}, \tag{5}$$

where $k_\perp$ is the transversal wavenumber.

3. HYPERBOLIC DISPERSION

Obviously, relation (5) describes a typical *hyperbolic* dispersion. Dispersion diagram in form of the slow-wave factor (the ratio of the speed of light in vacuum to the phase velocity) over the transversal wave vector plane is shown in Fig. 2. A zigzag CNT (21,0) is taken as an example, so R≈0.822 nm. Calculations were implemented at 27 THz. The slow-wave factor for the surface wave in a single CNT with such a radius equals to 70 [9] and it is shown by the dashed line. It is remarkable, that the slow-wave factor strongly depends on the transversal wavenumber. Namely, at the Γ-point ($|k_\perp|$=0) k_z/k=1, but for larger $|k_\perp|$ the slow-wave factor can strongly exceed this value for asingle CNT. This result is in agreement with [10], where bundles of closely packed metallic CNTs were considered and it was found, that the slow-wave factor for azimuthally symmetric guided waves decreases (tending to unity) with increasing of the number of nanotubes. It takes place even for the ratio $d/(2R)$≈12, where the term “closely packed” is not applicable. Evidently, this feature is inherent for waves in large arrays of electromagnetically coupled CNTs (which is infinite in the considered case) independently on their assembling, if the currents in all tubes are in phase. Reduction of the lattice period causes an increase of the electromagnetic interaction between nanotubes whichresults in an increase of the slow-wave factor k_z/k. The densiest packing of CNTs in arrays takes place in bundles, where the distance between nanotubes is 0.334 nm, so the lattice constant

d=1.978 nm. In this case the maximal value of $k_z/k \approx 250$ is achieved near the K-point. The most remarkable property of hyperbolic

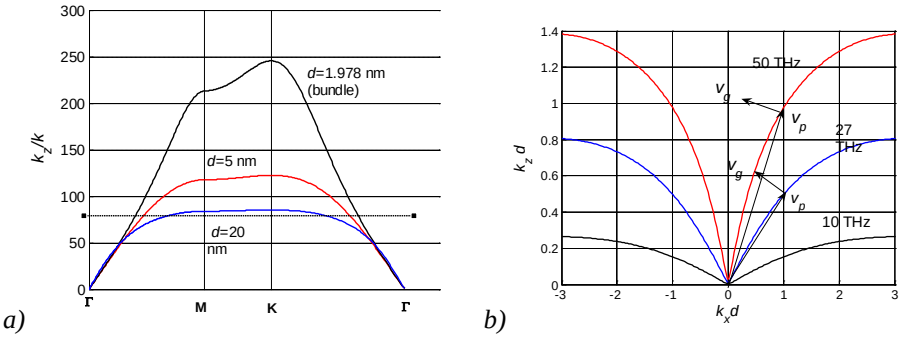

Figure 2. a) Real part of the slow-wave factor Re(k_z/k)*, calculated for different lattice constants d. b) Isofrequencies in plane of wave vectors. The lattice constant d=15 nm. Arrows show directions of the phase velocity v_p and the group velocity v_g.*

media is the capability to support propagating waves with any transversal component of the wave vector. The hyperbolic dispersion is inherent in *indefinite* metamaterials in which the axial and tangential components of the permittivity tensor have different signs [15]. In contrast to other known hyperbolic media, arrays of metallic CNT exhibit this property in an ultra-broad frequency range, see Fig. 2b.

4. BACKWARD WAVES IN A FINITE-THICKNESS SLAB

Using the effective medium model it is possible to show analytically that a finite-thickness slab of vertically standing carbon nanotubes (see Fig. 3a) supports propagation of backward waves [16]. Let us assume for simplicity that the slab is placed between PEC and PMC planes, where the PMC boundary models the open-ended interface with free space. The relation between the transversal wave-vector components and the wave number in free space is

$$k_\perp^2 = \frac{(k^2-k_p^2)(k^2-k_z^2)}{k^2}, \tag{6}$$

where $k_z=\pi/(2h)$. One can easily show that the derivative $dk^2_\perp/dk^2<0$ if $k_z/k>1$ and $k_p/k>1$. Indeed,

$$\frac{dk_\perp^2}{dk^2} = \frac{k_\perp}{k}\frac{dk_\perp}{dk} = 1 - \frac{k_z^2 k_p^2}{k^4} < 0, \tag{7}$$

since $k_z/k>1$ and $k_p/k>1$. Thus, in this regime, finite-thickness slabs support propagation of backward waves because the group velocity is in the opposite direction to the phase velocity.

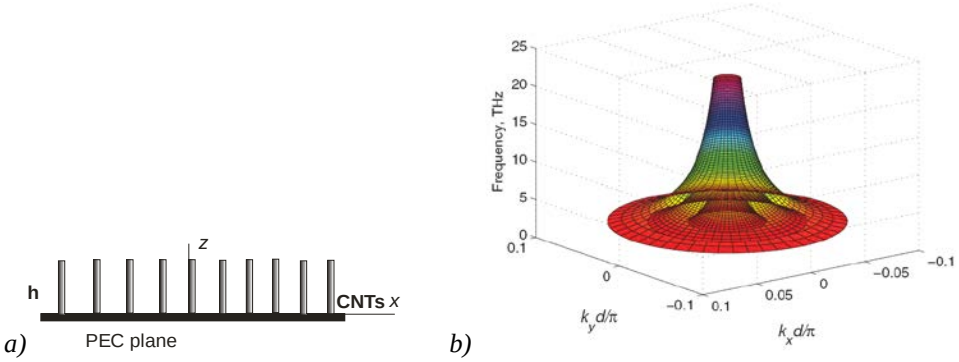

Figure 3. a) Geometry of the finite-thickness CNT slab. b) Frequency as a function of the normalized wave numbers in the transverse plane $k_x d/\pi$, $k_y d/\pi$. d = 15 nm and h = 1.5 μm.

Let us fix the normalized axial wave number $k_z d$ (see Fig. 2b). This can be done by taking a finite-thickness slab with any boundary conditions at the interfaces perpendicular to the z axis. The dispersion equation for the CNT array placed between two perfect electric conductor (PEC) planes is $k_z(k_x,\omega)h = l\pi$, where h is the thickness of the slab and l is the integer defining the mode number. For CNTs between the PEC and perfect magnetic conductor (PMC) planes, it reads $k_z(k_x,\omega)h = l\pi/2$. It is clear from Fig. 2b that k_x always decreases with an increase of the frequency under fixed k_z. Fig. 3b illustrates the dispersion properties of three modes, propagating in a CNT slab placed between PEC and PMC planes. There are three embedded hyperbolic surfaces. The internal

cone corresponds to l= 1, and the external one to l = 3. The top and bottom parts of these surfaces are cut out. One can see that backward waves propagate in the slab in a very wide frequency range. Their properties are quite isotropic in the *x-y* plane due to a very small period of the CNT lattice.

5. CONCLUSIONS

In summary, we have shown that arrays of single-wall metallic carbon nanotubes behave as indefinite media in ultra-broad frequency ranges (in the THz band). Arrays of vertically standing finite-length CNTs support propagation of backward waves, which are characterized by low levels of losses in the terahertz and mid infrared ranges. Note that, in contrast, finite-thickness arrays of horizontally aligned CNTs support propagation of forward waves [14]. Finite-thickness slabs of vertically standing carbon nanotubes can be considered as perfect planar isotropic, backward-wave metamaterials. The properties of this structure were explained in two ways: analyzing isofrequency diagrams, calculated numerically on the basis of the Green's function method, and using the effective medium theory. The model of an epsilon-negative crystal explicitly demonstrates that these effects are consequences of a very high kinetic inductance of thin carbon nanotubes.

ACKNOWLEDGEMENTS

This work has been partially funded by the Academy of Finland and Nokia through the Center-of-Excellence program.

REFERENCES

[1] A. Maffucci, G. Miano, F. Villone: A transmission line model for metallic carbon nanotube interconnects, *Int. J. of Circuit Theory and Appl.*, vol. 36. pp. 31-51, 2008.
[2] G.V. Hanson: Fundamental transmitting troperties of carbon nanotube antennas, *IEEE Trans. on Ant. Prop.*, vol. 53. pp. 3426-3434, 2005.
[3] Y. Wang, *et al.*: Receiving and transmitting light-like radio waves: Antenna effect in arrays of aligned carbon nanotubes, *Appl. Phys. Lett.*, vol. 85. pp. 2607-2609, 2004.
[4] S.A. Maksimenko, *et al.*: Carbon nanotube antenna: Far-field, near field and thermal-noise properties, *Physica E*, vol. 40. pp. 2360-2364, 2008.
[5] L. Ren, *et al.*: Carbon nanotube terahertz polarizer, *Nano Lett.*, vol. 9. pp. 2610-2613, 2009.
[6] K.G. Batrakov, *et al.*: Carbon nanotube as a Cherenkov-type light emitter and free electron laser, *Phys. Rev. B*, vol. 79. p. 125408, 2009.
[7] K. Fu, *et al.*: Terahertz detection in single wall carbon nanotubes, *Appl. Phys. Lett.*, vol. 92. p. 033105, 2008.
[8] G.Y. Slepyan, *et al.*: Electrodynamics of carbon nanotubes: Dynamic conductivity, impedance boundary conditions, and surface wave propagation, *Phys. Rev. B*, vol. 60. p. 17136, 1999.
[9] P. J. Burke: Lüttinger liquid theory as a model of the gigahertz electrical properties of carbon nanotubes, *IEEE Trans. on Nanotechnol.*, vol. 3. pp. 129-144, Sept. 2002.
[10] M. V. Shuba, S.A. Maksimenko, A. Lakhtakia: Electromagnetic wave propagation in an almost circular bundle of closely packed metallic carbon nanotubes, *Phys. Rev. B*, vol. 76. p. 155407, 2007.
[11] I. S. Nefedov: Electromagnetic waves propagating in a periodic array of parallel metallic carbon nanotubes, *Phys. Rev. B*, vol. 82. p. 155423, 2010.
[12] G.W. Hanson: Dyadic Green's functions and guided surface waves for a surface conductivity model of graphene, *J. of Appl. Phys.*, vol. 103. p. 064302, 2008.
[13] S. I. Maslovski, M. G. Silveirinha: Nonlocal permittivity from a quasistatic model for a class of wire media, *Phys. Rev. B*, vol. 80. p. 245101, 2009.
[14] I.S. Nefedov, S.A. Tretyakov: Effective medium model for two-dimensional periodic arrays of carbon nanotubes, *Photonics. Nanostr.*, vol. 9. pp. 374-380, Oct. 2011.
[15] D. R. Smith, D. Schurig: Electromagnetic wave propagation in media with indefinite permittivity and permeability tensors, *Phys. Rev. Lett.* Vol. 90. p. 077405, 2003.
[16] I.S. Nefedov, S.A. Tretyakov: Ultrabroadband electromagnetically indefinite medium formed by aligned carbon nanotubes, *Phys. Rev. B*, vol. 84. p. 113410, 2011.

Combination of analog and computer generated holography used to produce complex optical structures

Svetlana Savić-Šević[1], Dušan Grujić[1], Dejan Pantelić[1], Boban Zarkov[1], Srećko Ćurčić[2], Branislav Jelenković[1]

[1] *Institute of Physics, University of Belgrade, Pregrevica 118, 11080 Zemun, Belgrade, Serbia*
Tel: +38111 3713063; e-mail: branaj@ipb.ac.rs

[2] *Institute of Zoology, Faculty of Biology, University of Belgrade, Studentski Trg 16, 11000 Belgrade, Serbia*

ABSTRACT

Combination of an analog and computer generated holography is used to produce complex diffraction gratings. As a result, a combination of volume and surface relief grating is obtained. We used this to mimic vortex structures found on the butterfly wing scale.

Keywords: computer generated holography, Bragg gratings, photonic structures, Lepidoptera, biomimetics

1. INTRODUCTION

Complicated micro- and nano- structures are omnipresent in nature, especially in the world of insects. Microlenses, surface and volume diffraction gratings, photonic crystals, nanoparticles, antireflection layers – all of them can be found on the eyes, cuticle or wings of insects [1]. Simple structures are rarely found – they are a rather intricate involving combination of several different types of micro and nano-patterns.

Take a lepidopteran (butterfly or moth) wing scale as an example. It is a thin hollow plate (several tens of microns wide, more than hundred micron long, and several micron thick) whose upper surface has a number of ridges which produce a surface relief diffraction grating. However, each individual ridge is a complicated structure which consists of a number of slanted lamellas. In that respect it looks quite like volume Bragg grating. In some butterflies interior of the scale is packed with tiny-particles which, if regular, function as a photonic crystal [2]. In others, interior contains irregular array of particles which strongly and selectively scatter the incoming radiation [3].

Even though regular structures predominate, certain amount of irregularity can be observed too. We are particularly amazed by dislocations that can be observed on the butterfly scales – i.e. at certain positions single ridge either bifurcates or. Observed feature looks almost exactly like a fork-hologram [4] whose main characteristic is that it produces a vortex beams in its diffraction orders. “Fork holograms” on the wing scales can be numerous - almost 1000 vortex generating structures per square millimeter - in the *Apatura iris* and *Apatura ilia* butterfly species which we previously studied [5]. High density of dislocations might suggest that they are not there by chance. It is our hypothesis that vortex light generated on the butterfly wing improves the visibility necessary for communication of individuals of the same species.

It seems interesting and rewarding to investigate how nature solved complicated problems of mimicry (imitation), aposematism (warning coloration) and camouflage. In that respect we are investigating the possibility of using combination of analog and computer generated holography to produce complex structures.

2. RESULTS

It is our aim to manufacture a structure which is a combination of surface relief and volume grating - similar to butterfly wing scale. This is a two step process. First, we have generated fork- hologram using direct laser writing, and then volume grating by interfering counter-propagating beams. Thus, two exposures were made on the same photosensitive material.

We used dichromated pullulan [6] as a photosensitive material. Its main feature is that both surface relief [7] and volume gratings can be recorded, in that respect being ideal for our purpose. Material is prepared as a thin layer on a glass substrate. After exposure material is further processed by immersion in several isopropyl alcohol – water baths. This serves to amplify the recorded gratings.

Direct laser writing overexposes the material and locally destroys the volume grating. Due to the polymerization pullulan shrinks in overexposed locations. Also, at the center of the laser drawn line the beam burns the material to a certain depth. Between the fork hologram lines, volume grating is preserved and brightly colored, due to the spectral selectivity of the Bragg grating.

The diffraction pattern on the fork hologram was recorded using green (532 nm) laser light for which Bragg grating is highly reflective. We have simultaneously recorded transmitted and reflected diffraction and observed that the reflected intensity is much higher than transmitted.

Further research is necessary in order to improve the overall quality of the resulting hologram. As can be seen, there is a large amount of stray radiation which is a consequence of parasitic beams during the volume hologram

recording. This should be corrected by immersing a hologram plate in an immersion liquid during chemical processing. Another source of noise is a consequence of discrete steps of coordinate table during direct laser writing. At the end of each step, the table stops producing increased irradiation of photosensitive material and slight widening of the produced line.

3. CONCLUSIONS

We have used a combined digital-analog technique to produce a combination of volume and surface diffraction grating. As a proof-the principle we have manufactured vortex-beam (fork) hologram with spectral selectivity induced by intrinsic Bragg grating. The resulting hologram is spectrally selective (as a consequence of volume Bragg grating), while producing multiple diffraction orders just like ordinary surface relief grating.

ACKNOWLEDGEMENTS

This research was financially supported by the Serbian Ministry of Education and Science (projects 45016, 171038, 173038, and 173055)

REFERENCES

[1] P. Vukusic: Advanced Photonic Systems on the Wing-Scales of Lepidoptera, in *Functional Surfaces in Biology - Little Structures with Big Effects*, Stanislav N. Gorb Ed., Springer Science+Business Media B.V. (2009),

[2] G.E. Schröder-Turk, S. Wickhamc, H. Averdunk, F. Brink, J.D. Fitz Gerald, L. Poladian, M.C.J. Large, S.T. Hyde: The chiral structure of porous chitin within the wing-scales of Callophrys rubi, *Journal of Structural Biology*, Vol. 174. pp. 290–295, 2011.

[3] A.L Ingram, A.R Parker: A review of the diversity and evolution of photonic structures in butterflies, incorporating the work of John Huxley (The Natural History Museum, London from 1961 to 1990) , *Phil. Trans. R. Soc. B*, Vol. 363. pp. 2465-2480, 2008.

[4] A. Bekshaev, O. Orlinska, M. Vasnetsov: Optical vortex generation with a “fork” hologram under conditions of high angle diffraction, Opt. Commun. Vol. 283 pp. 2006-2016, 2010.

[5] D. Pantelić, S. Ćurčić, S. Savić-Šević, A. Korać, A. Kovačević, B. Ćurčić, B. Bokić: High angular and spectral selectivity of purple emperor (Lepidoptera: Apatura iris and A. ilia) butterfly wings, *Opt. Express* Vol. 19. pp. 5817-5826, 2011.

[6] D. Pantelić, S. Savić, D. Jakovljevic: Dichromated pullulan as a novel photosensitive holographic material, *Opt. Lett.* Vol. 23 pp. 807-809, 1998.

[7] S. Savić-Šević, D. Pantelić: Relief hologram replication using a dental composite as an embossing tool, *Opt. Express* Vol. 13 pp. 2747-2754, 2005.

Investigation of Small *V* and High *Q* SOI Optical Resonators

D. Urbonas[2], M. Gabalis[2], P. Seidler[1], R.Petruskevicius[2], T. Stoeferle[1], G. Raciukaitis[2]
[1]*IBM Research – Zurich, Säumerstrasse 4, 8803 Rüschlikon, Switzerland*
[2]*Center for Physical Sciences and Technology, Savanoriu ave. 231, Vilnius LT-02300, Lithuania*
Tel: +37069633953; e-mail: darius.urbonas@ff.stud.ff.vu.ltt

ABSTRACT
Recently, various wavelength-sized 1D, 2D or 3D cavities with theoretical *Q* of 10^5 and ultra small modal volume *V* of 0.04 $(\lambda/2n)^3$ have been reported, however in most of these cavities air is used as low dielectric material (λ is the wavelength, and *n* is the refractive index). Here we implement three-dimensional finite-difference time-domain simulations to investigate physical phenomena in more detail and demonstrate that it is possible to achieve a high *Q* over *V* ratio by employing 1D periodicity and various types of materials as low dielectric material.

Keywords: integrated optical devices, photonic crystals, hybrid optical cavities, bowtie resonators.

1. INTRODUCTION

Optical micro cavities with small modal volume and high quality factor are required for many optical applications, including cavity quantum electrodynamics, nonlinear optics, low threshold lasers and optical switches. Despite difficulties to localize light in wavelength-sized optical cavities with strong light confinement, recently rapid progress has been made on this issue by employing photonic band gaps and total internal reflection in well-designed photonic crystals. Cavities with *Q* of 10^5 and modal volume of 0.04 $(\lambda/2n)^3$ have been theoretically demonstrated. This means that we can store photons for longer than one nanosecond in a smaller than wavelength-sized volume. However such cavities, as far as we know, with high *Q* and low modal volume have only been achieved in cavities, which use air as the low-dielectric-constant material. Therefore it is unclear how these cavities will perform if we use media with higher refractive index (for example nonlinear material) as the low-dielectric-constant material.

In contrast to the above, here we present a theoretical investigation of cavities with different low-dielectric-constant materials (i.e. SiO_2, polymers and other materials).

2. PRINCIPLE OF LOW MODAL VOLUME AND HIGH Q CAVITIES

There are two different methods to store photons for longer than one nanosecond in a wavelength-sized volume. One way is to rely on total internal reflection (ring or disc resonators), and the second is to employ strong light confinement of a photonic band gap in a well-designed structure [1, 2]. A combination of, these effects may also be employed, e.g. use of a photonic band gap in one dimension and total internal reflection in the other two dimensions. Total internal reflection only holds for a certain restricted range of wave vectors, and thus it becomes ineffective when the cavity size becomes small because localization in real space leads to delocalization in *k*-space (example Fig. 1), which eventually breaks the total internal reflection condition. Photonic band gap confinement works regardless of the wave vector range, and thus it is essentially better for confining light in a small volume than total internal reflection.

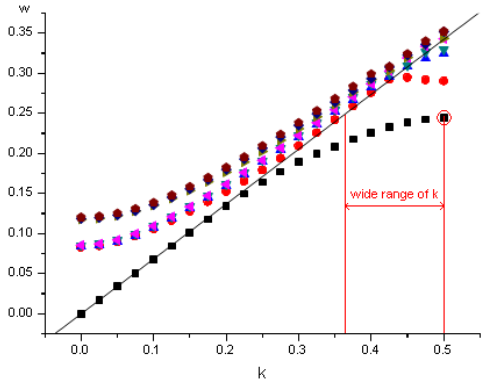

Figure 1. Photonic band structure of a 1D photonic crystal. The horizontal axis is the k-vector along the crystal in units of 1/a and the vertical axis is the eigen frequency in units of c/a where c is the speed of light and a is the periodicity of the photonic crystal. The solid line denotes the light line, below which the frequencies are guided and can be confined by the cavity. The range of confined k-vectors depends on the lower band edge frequency.

If we abruptly modify the waveguide to form a cavity, we will cause a large perturbation in the originally loss-free mode profile, which will result in significant radiation loss for the cavity modes. That is why we have to gradually modify the waveguide (Fig. 2) to create a local modulation of the gap position. The use of gradual width modulation produces light confinement with minimum mode profile perturbation. If the modulation is sufficiently gradual, the delocalization in *k*-vectors space can be minimized. Since the position of the mode band edge is very sensitive to the structural parameters, we can introduce gradual confinement, which is required if we are to achieve a high Q.

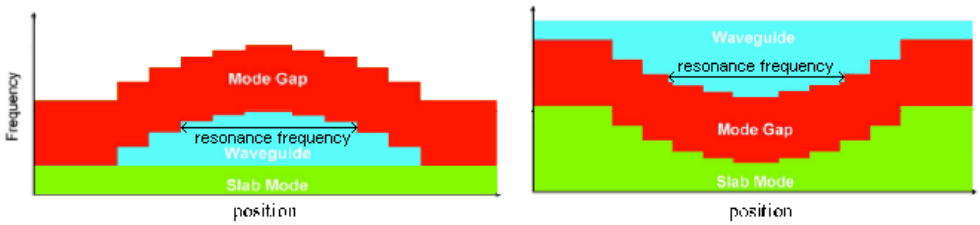

Figure 2. Band gap gradual shift and minimization of lower band edge frequency.

If we introduce a slit [3] or channel [4] into the waveguide we will be able to decrease modal volume by almost two orders of magnitude. We use a slit in the center of the structure (Fig. 3) and we have two dielectric materials with different dielectric constants ε_1 and ε_2, where $\varepsilon_2 > \varepsilon_1$. Two media are parallel to each other and form an interface. Here we can implement boundary conditions for Maxwell's equations:

$$\mathbf{D}_1 - \mathbf{D}_2 = \rho \tag{1}$$

The tangential components of the ***E***-field are continuous across the interface. In many interface problems, there are no externally applied surface charges ρ or currents on the boundary. In such cases, the boundary conditions may be stated as $\mathbf{D}_1 = \mathbf{D}_2$. Then we introduce $\mathbf{D} = \varepsilon\mathbf{E}$, which gives $\varepsilon_1\mathbf{E}_1 = \varepsilon_2\mathbf{E}_2$. Dividing the equation by ε_1 leads to $\mathbf{E}_1 = \frac{\varepsilon_2}{\varepsilon_1}\mathbf{E}_2$. Taking into account the assumptions for the dielectric constants gives $\mathbf{E}_1 > \mathbf{E}_2$ ($\mathbf{E}_1$is the electric field located in the low dielectric material and $\mathbf{E}_2$ the electric field in the high dielectric material).

The equation for modal volume is:

$$V = \frac{\int \varepsilon |\mathbf{E}|^2 dV}{\varepsilon_{max} |\mathbf{E}_{max}|^2}, \tag{2}$$

In this case, $\mathbf{E}_{max}$ is located in the low-dielectric material with dielectric constant $\varepsilon_{max} = \varepsilon_1$. This means that we can achieve a jump in the electric field (Fig. 3) when going from high dielectric material to low dielectric material. From equation (2), we will see that introducing this jump in electric field helps us to decrease the modal volume by a factor of $\frac{\varepsilon_2{}^2}{\varepsilon_1}$.

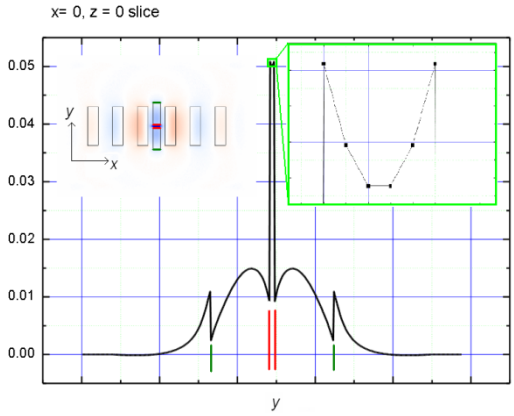

Figure 3. Achieving high local E-fields using a deep subwavelength-sized slit.

However, such an embedded slit is not a gradual structure modification and leads to delocalization in *k*-vector space, which actually means that we will have a scattered field. These scattered components are almost equal to the magnitude of the excitation field and are the main reason for high losses and low *Q*. One way to decrease these losses is to use a channel instead of a slit. A channel helps to confine more light because for two reasons. First it lowers the frequency of the band edge, which means we will have a larger range of *k*-vectors confined under the light line (Fig. 1). Second, it helps to confine light in the z direction because of total internal reflection. Introducing a channel that goes all the way through the structure (not only the central defect) in the x direction also helps to increase the *Q* factor because of the more gradual band gap shift.

Using air as the low-dielectric-constant material helps to increase the jump in dielectric field by a factor of $\frac{\varepsilon_2{}^2}{\varepsilon_1}$, but air is not useful for many optical devices. That is why it is important to use materials that have a higher refractive index as the low-dielectric-constant material, for example silicon dioxide. Optimizing the 1D cavity where the high-dielectric-constant medium is silicon and the low-dielectric-constant material has a refractive index higher than 1 is one of our goals. Using various types of materials instead of air ($n > 1$) as the low-dielectric-constant material for ladder type and block cavities (Fig 4.) decreased Q by several orders of magnitude. This is mainly because of the narrower range of k-vectors that is confined in the structure (the light line is lower).

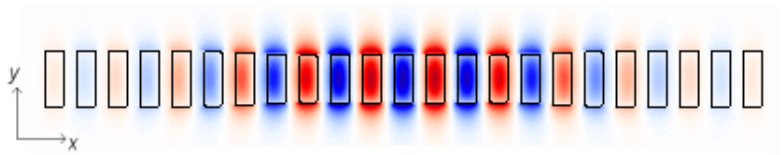

Figure 4. Modification of block-stack cavity (Si/SiO_2 cavity, Q ~ 24000 and V ~ 1 a^3).

A modification of the original bowtie structure [4] is suggested in Fig. 5. Here we use a buried channel instead of a slit that goes all the way through the structure in the z direction. To excite our cavity we use an $\mathbf{E}_y$ field. However, because of the scattering element in the center of the structure (in this case a channel), other **E** field components appear ($\mathbf{E}_x$ and $\mathbf{E}_z$). These two additional **E** field elements are not confined in the structure and are radiated away. Therefore, $\mathbf{E}_x$ and $\mathbf{E}_z$ components in the center of a cavity are very small compared to the $\mathbf{E}_y$ field.

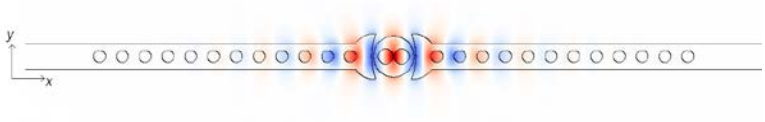

a) $\boldsymbol{E}_y$ field.

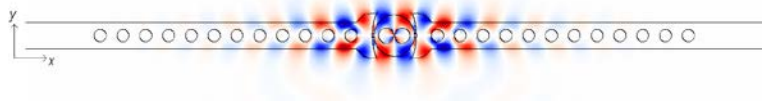

b) $\boldsymbol{E}_x$ field.

c) $\boldsymbol{E}_y$ field (x = 0 cut)

d) Bowtie structure with a channel (x = 0 cut)

e) $\boldsymbol{E}_y$ field (x = 0 cut)

f) Bowtie structure with a slit (x = 0 cut)

Figure 5. Bowtie structure with implemented channel or slit in the center. The field strength is shown in blue and red shades, where the saturation is normalized to the respective E-field maximum.

In Fig. 6 (pictures a and b), all three **E** field components are shown ($\frac{\mathbf{E}_x{}^2}{\mathbf{E}_{x(\max)}{}^2}$, $\frac{\boldsymbol{E}_y{}^2}{\mathbf{E}_{y(\max)}{}^2}$ and $\frac{\mathbf{E}_z{}^2}{\mathbf{E}_{z(\max)}{}^2}$). It is clearly visible that $\mathbf{E}_y$ (solid red line) component in the bowtie structure with a channel instead of a slit is confined better due to total internal reflection. In this case, we use SiO_2 instead of air as a low-dielectric-constant material. The condition for total internal reflection is:

$$Q_i = \arcsin\left(\frac{n_2}{n_1}\right) \tag{3}$$

where Q_i is the incident angle, n_2 and n_1 are the refractive indices of the low-dielectric-constant and high-dielectric-constant materials, respectively. From equation 3 we can see that light incident at an interface with an angle less than Q_i would be partially transmitted, while light incident at an interface at larger angles with respect to the normal would be totally internally reflected. That is why we need to make the ratio $\frac{n_2}{n_1}$ as low as possible. Thus, using SiO_2 instead of air decreases the total internal reflection effect (lower range of Fourier components can be confined).

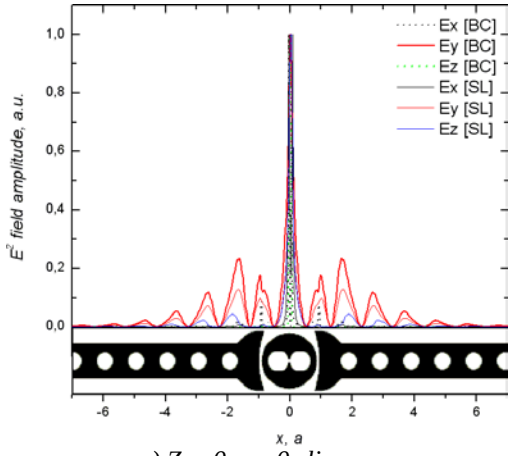

a) Z = 0, y =0 slice.

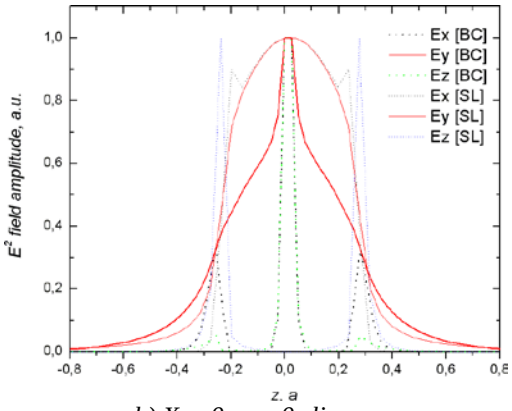

b) X = 0, y = 0 slice.

Figure 6. Bowtie structure with implemented channel or slit in the center. In pictures a and b localization of $\boldsymbol{E}^2$ *is shown. Here BC stands for buried channel and SL – slit.*

3. CONCLUSIONS

High *Q* and low *V* structures were simulated. Different designs of photonic crystal micro cavities were investigated and it was shown in more details that it is possible to get low modal volume by introducing a channel or a slit in the center of the micro cavity which however in turn causes delocalization in *k*-vector space and a low quality factor. It was demonstrated that a channel is better than a slit because of guiding by total internal reflection in the z direction. In addition to this, it was shown that cavities which have silicon dioxide as the low dielectric material are worse compared to cavities with air because of reduced total internal reflection. This drawback, however, has to be taken into account when considering devices with cladding instead of air bridges, because the latter are not useful for integrated devices.

ACKNOWLEDGEMENTS

This work was supported by Lithuania-IBM joint project NANO1 and EU COST Action MP0702.

REFERENCES

[1] M. Notomi, E. Kuramochi, H. Taniyama: Ultrahigh-Q Nanocavity with 1D Photonic Gap, OPTICS EXPRESS, Vol. 16, No. 15, pp. 11095-11102, 2008.

[2] Eiichi Kuramochi, Hideaki Taniyama, Takasumi Tanabe, Kohei Kawasaki,Young-Geun Roh, and Masaya Notomi: Ultrahigh-Q one-dimensional photonic crystal nanocavities with modulated mode-gap barriers on SiO2 claddings and on air claddings, OPTICS EXPRESS, Vol. 18, No. 15, pp.15859-15869, 2010.

[3] Ping Yu, Biao Qi, Xiaoqing Jiang, Minghua Wang, and Jianyi Yang: Ultrasmall-V high-Q photonic crystal nanobeam microcavities based on slot and hollow-core waveguides, OPTICS LETTERS, Vol. 36, No. 8, pp.1314 – 1316, 2011.

[4] A. Gondarenko, M. Lipson: Low modal volume dipole-like dielectric slab resonator, OPTICS EXPRESS, Vol. 16, No. 22, pp.17689-17694, 2008 .

Functionalized gold nanostars for enhanced FT-Raman spectroscopy

Emilia Giorgetti [1], Silvana Trigari[1], Giancarlo Margheri [1], Angela Zoppi [1], Alessio Rindi [2], Giovanna Dellepiane [2], Giovanna Brusatin [3], Laura Brigo [3], Iljiana Timtcheva [4] and Maurizio Muniz-Miranda [5]

[1] ISC-CNR, Via Madonna del Piano 10, 50019 Sesto Fiorentino (Firenze), Italy.Tel: +390555226691; e-mail: emilia.giorgetti@fi.isc.cnr.it

[2] Department of Chemistry and Industrial Chemistry, University of Genova, Genova, Italy.

[3] Department of Mechanical Engineering, University of Padova, Padova, Italy.

[4] Institute of Organic Chemistry with Centre of Phytochemistry BAS, Sofia, Bulgaria.

[5] Department of Chemistry "Ugo Schiff", Università di Firenze, Sesto Fiorentino (Firenze), Italy.

ABSTRACT

Stable gold nanostars (AuNSs) with tunable extinction properties were obtained by chemical reduction. The theoretical computations put in evidence the existence of hot spots located on the tips of the nanostars up to 1200 nm wavelength and beyond, which opens the way to applications to enhanced FT Raman spectroscopy. The FT Raman enhancing capability of such nanostructures was validated by preliminary experiments through functionalization with thiol-terminated fluorescent compounds.

Keywords: gold nanostars, FT Raman spectroscopy, fluorescence

INTRODUCTION

The ultra fast development of the possibilities of matter manipulation down to the nanoscale, which occurred in the past 20 years, makes now available several types of metal/dielectric nanostructured materials (nanohybrids), which are based on coinage metals in the form of nanoparticles (MeNPs) in colloidal suspensions. Excitation of localized surface plasmons can enhance significantly both the extinction cross section and the local electromagnetic field, up to many orders of magnitude. These properties constitute the fundament of Surface Enhanced Raman Spectroscopy (SERS), with enhancements of the Raman response of molecular adsorbates which can reach values up to 10^{14}–10^{15} in single-molecule experiments [1]. In particular, large SERS enhancements are obtained when incident and scattering radiations match the localized surface plasmon resonance (LSPR) maximum of the metallic nanostructure, which can vary in spectral position, intensity and width when the metal particles change size, shape and dielectric environment or - if they cannot be considered isolated as it occurs in the case of MeNIFs - when the interaction among neighbouring nanoparticles causes strong field localizations in the gaps. In many applications, such as those involving biological samples or fluorescent adsorbates, it is important to perform the Raman investigations at long wavelengths, that is in the Near Infrared (NIR) spectral region. For this purpose, several metal nanostructures have been proposed, ranging from nanorods to nanoprisms or nanocages. Such structures are quite effective around 700-900 nm. However, when the use of longer Raman exciting wavelength is required, nanostars, i.e. highly branched metallic nanostructures seem more promising [2].

In this framework, this contribution reports on results of a theoretical and experimental investigation carried out on gold nanostars, with emphasis on the possibility of tuning their morphology in a controlled way, so that they can behave as active materials for SERS tests at NIR wavelengths. Although the presence of CTAB as stabilizing agent makes particle functionalization difficult [2], preliminary SERS experiments performed with a fluorescent dye bearing end thiol groups seem to confirm functionalization of the nanostructures and their field enhancing ability in the 1000-1200 nm range.

RESULTS

A feasible approach to move the LSPR above 700-900 nm spectral windows is that of using branched NPs, commonly known as nanostars (NSs). Ref. 2 describes a simple procedure to fabricate randomly branched Au nanostructures with predetermined extinction properties, which can be tuned from the visible at least up to 1800 nm. The protocol, which is a seed-less one, makes use of $AgNO_3$ and of small amounts of NaOH as a control parameter for tuning nanoparticles morphology.

Fig. 1a shows a TEM micrograph of NSs obtained without NaOH. They have the biggest size among the batches obtained with different NaOH concentrations and exhibit an extinction band which extends up to

1800 nm. The average geometrical features of this sample are: (224±14) nm core diameter, (114±48) nm branch length and (36±7) ^{o} tip angle.

Theoretical simulations by a Finite Element Modelling (FEM)-based code permitted to calculate the electromagnetic field distribution around the typical nanostar tip belonging to this batch. The results are reported in Fig. 1b, which clearly shows formation of an intense hot spot at 1200 nm wavelength. A similar distribution is obtained with 1064 nm wavelength, suggesting that such structures can be conveniently employed inn FT-Raman experiments.

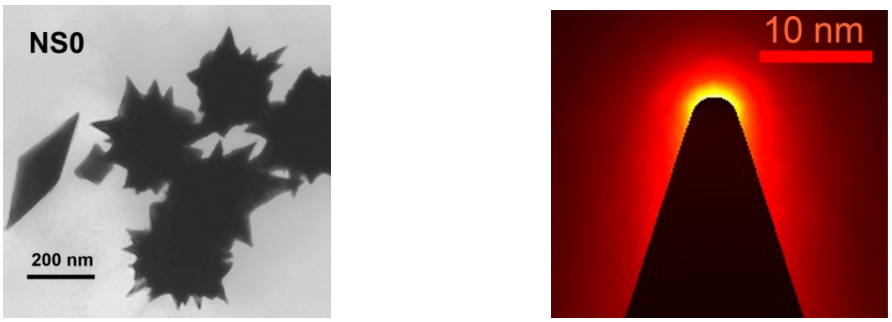

[1] *b)*

Figure 1. a) TEM image of gold nanostars and b) theoretical simulation of the distribution of electromagnetic field at typical nanostar tip for 1200 nm impinging wavelength.

We tested the potentialities of NSs of Fig. 1 as FT Raman intensifiers by functionalizing them with the fluorescent compound of Fig. 2, the 2-(8-mercaptohexyl)-6-methoxy-1H-benzo[de]isoquinoline-1,3(2H)-dione (hereafter named Nafta6) [3]. The main photophysical characteristics of Nafta6 in $CHCl_3$ are: $\lambda_{Absorption}$ = 363 nm; $\lambda_{Fluorescence}$ = 430 nm; Fluorescence Quantum Yield = 0.92; fluorescence life time = 6.6 ns.

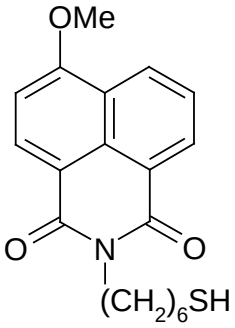

Figure 2. Chemical structure of 2-(8-mercaptohexyl)-6-methoxy-1H-benzo[de]isoquinoline-1,3(2H)-dione (Nafta6).

Its Raman spectrum in the powder state, obtained with 785 nm excitation, is reported in Fig. 3 (red line). The most prominent Raman bands detected in the spectrum of powders correspond to vibrational modes of naphthalene [4]. In particular, the bands observed at 510, 615, 1402, 1586 cm^{-1} are related to those of naphthalene at 514, 619, 1380 and 1578 cm^{-1}, respectively. The two low-frequency bands (510, 615 cm^{-1}) are attributable to ring bending modes and the others (1402, 1586 cm^{-1}) to ring stretching modes. Lastly, the Raman band at 1694 cm^{-1} is due to C=O stretching mode.

The NSs are obtained in aqueous solutions and stabilized by CTAB, which also behaves as templating agent. Although the presence of CTAB makes particle functionalization difficult [2], the small dimensions of Nafta6 and the strong affinity of the thiol group for the gold surface are expected to favour it. For this purpose, the NSs were centrifuged twice (5 min @ 2500 rpm) to remove the CTAB excess. Each time the AuNS were redispersed in pure water. Then, they were incubated overnight with a 7.9 mM solution of Nafta6 in acetone. Lastly, three centrifugation cycles (5 min @ 2500 rpm) were performed to remove the excess of Nafta6 with subsequent redispersion in pure acetone.

FT-Raman spectroscopy of Nafta6-functionalized AuNSs was performed at 1064 nm exciting wavelength by using a JASCO RFT-600 FT-Raman equipped with a JASCO FT/IR-620 spectrometer. The results are reported in Fig. 3, black line. Although the response of acetone is dominant, the non negligible fluorescence background

confirms the contribution from Nafta6 molecules to the spectrum. Moreover, although weak, the two bands at 1602 and 1404 cm^{-1} corresponding to the stretching modes of naphthalene are visible. In particular, the one at 1602 cm^{-1} falls in a region where the Raman response of acetone is flat and it can be very well resolved.

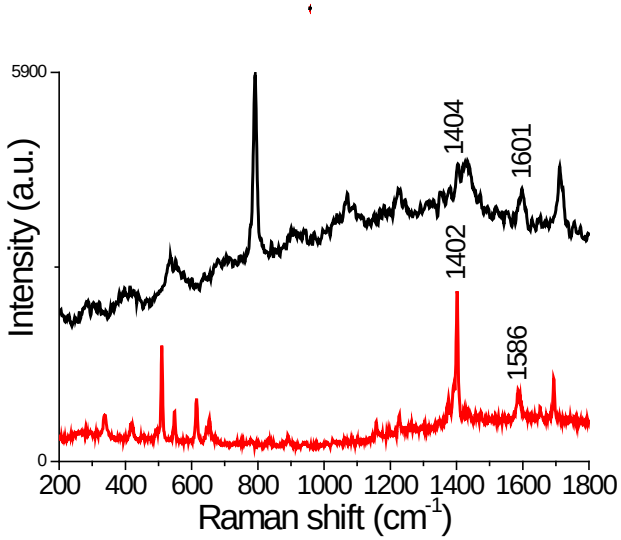

Figure 3. Red line: Raman spectrum of Nafta6 powders with 785nm excitation wavelength; black line: FT Raman spectrum of acetone suspensions of Nafta6-functionalized gold nanostars with 1064 nm excitation wavelength.

Their visibility suggests that, not only surface functionalization was achieved, but also that the metallic structure provided SERS enhancement to the Raman response of NAFTA6. Indeed, under 1064 nm excitation, the two bands at 1602 and 1404 cm^{-1} correspond to scattered wavelengths above 1200 nm, i.e. double enhancement of the impinging and scattered radiation is obtained. Indeed, calculation show that Raman enhancement factors provided by this batch of AuNSs are of the order of 10^7 for both 1064 and 1200 nm radiation.

CONCLUSIONS

We have proposed AuNSs as suitable systems to move SERS response towards IR wavelengths, up to 1200 nm. Such nanoparticles, which can be obtained by chemical reduction and whose morphological and spectral properties can be tuned by properly adjusting the synthesis parameters, can be functionalized with small thiol terminated compounds. Theoretical modelling and preliminary FT-Raman experiments have provided very encouraging results, in view of their application to enhanced IR spectroscopy.

ACKNOWLEDGEMENTS

This research was funded by the projects NABLA (Decree n.4508-September 1,2010 by Regione Toscana-Italy, PAR FAS 2007-2013 funds, Action 1.1.a.3) and PRIN2009 “Novel plasmon-based processes and materials for sensor applications” of the Italian Ministry of Research and supported by COST Action MP0702 “Towards Functional Sub-Wavelength Photonic Structures”.

REFERENCES

[1] S.J. Lee, Z. Guan, H. Xu, M. Moskovits: Surface-Enhanced Raman Spectroscopy and Nanogeometry: The Plasmonic Origin of SERS, *J. Phys. Chem. C* vol. 111, pp. 17985-17988, 2007.

[2] S. Trigari, A. Rindi, G. Margheri, S. Sottini, G. Dellepiane, and E. Giorgetti: Synthesis and Modelling of Gold Nanostars with Tunable Morphology and Extinction Spectrum, *J. Mat. Chem.*, vol. 21, pp. 6531-6540, 2011.

[3] E. Giorgetti, G. Dobrikov, D. Ivanova, I. Timtcheva, M. Ferrari, A. Chiappini: Noble metal nanoparticles functionalized with novel organic luminophores, *in Proc. ICTON 2009*, San Miguel de Azores, Portugal, June 2009, paper We.C1.5.

[4] E. Giorgetti, S. Trigari, A. Rindi, G. Margheri, S. Sottini, G. Dellepiane, G. Brusatin, L. Brigo, M. Muniz-Miranda, and I. Timtcheva: Synthesis and modelling of tunable gold nanostars for Surface Enhanced Raman Spectroscopy, *Physica Status Solidi* (in press).

NOTES

Using Effective Medium Approximation Methods in Study of Optical Coefficient of Palladium-carbonaceous Nanocomposites

Radosław Belka[1], Krzysztof Szęszoł[1],
[1] *Division of Photonics and Electronic Nanomaterials, Kielce University of Technology*
Al. Tysiąclecia P.P.7, 25-314 Kielce, Poland
Tel: +4841 3424767; e-mail: r.belka@tu.kielce.pl

ABSTRACT
In this paper theoretical analysis of the optical properties of palladium-carbonaceous (Pd-C) nanocomposites has been presented. A complex effective refraction coefficients were calculated using Effective Medium Approximation (EMA) theory. The complex refractive indices of Pd and a-C (amorphous carbon) in spectral region of 200 – 2000nm were used as the input data, as Raman spectra for experimental Pd-C samples show existence of amorphous graphite-like carbon structure with very small size of graphite clusters. It was shown that for wavelengths above 430nm the real part of refractive index (n) increases with metal content in relation to the value characteristic of pure carbon, while for λ<430nm, the value of n decreases.

Keywords: C-Pd nanocomposites, complex refractive index, Effective Medium Approximation, Raman spectroscopy

1. INTRODUCTION

The dynamic progress in the field of optoelectronic sensors requires the exploration of new materials with specific and desired properties. The carbon nanostructures (fullerenes, carbon nanotubes, carbon nanofoams) and also metallic-carbonaceous nanocomposites are interesting examples of these materials. For this reason, especially interesting are palladium-carbonaceous (Pd-C) nanostructures, due to their potential use as hydrogen sensors [1-3]. Palladium has uncommon ability to absorb hydrogen. This is because the size of gaps in the crystal lattice is well suited for particle size of hydrogen H_2. There appears a number of applications in reference to this property. This analysis is focused on hydrogen sensors based on composites containing Pd nanocrystals. In that case metal is obtained from palladium compound, which significant reduces costs. The layers based on carbonaceous materials look especially promising.

Based on Effective Medium Approximation (EMA) theory, optical properties of Pd-C nanocomposite should depend on the content of palladium and type of carbon allotropic form. Since the complex refractive index of Pd is clearly different from the refractive index of carbon, even a small admixture of metal can lead to significant changes in value of effective index and consequently to change the reflection coefficient of the layer. Moreover, the adsorbed hydrogen by Pd nanoparticles may also lead to changes in the final optical properties. This effect can be easily used in hydrogen sensing.

Using EMA methods allows to predict the optical properties of nanocomposites of Pd-C, produced as thin layers. Real nanolayers are characterized by a high degree of surface roughness, therefore experimental measurements (ellipsometry) are difficult. In this paper theoretical analysis of optical properties of Pd-C nanocomposites based on the EMA theory has been presented. The values of effective refractive indices and the reflection coefficients resulting from the Fresnel formula reflection were calculated.

2. THEORETICAL MODEL

The real palladium-carbonaceous (Pd-C) nanostructures were prepared in Tele- and Radioresearch Institute (Warsaw, Poland) using two-step PVD/CVD method, described in [4]. The thickness of the layers is approximately 300 – 400 nm. Based on the SEM images [3-5] palladium-carbon CVD nanostructures can be treated as nanocomposite consisting of Pd nanograins of the size of tens nanometers embedded in a carbonaceous matrix. In the figure 1 the model of the Pd-C CVD layer is presented. The positions of metallic nanograins of complex dielectric constant ε_M are marked by the darker places. Most of the film is filled with carbonaceous structure with a complex dielectric constant ε_C.

The optical properties of the nanocomposites can be calculated using the optical coefficients of individual components. Well-known optical properties of palladium were used to examine the terms of the behavior of optical performance, as the structure of Pd nanograins is similar with Pd bulk. In order to determine the allotropic form of the carbonaceous matrix, Raman spectra had to be performed first. This was necessary to properly establish the value of its refractive indices.

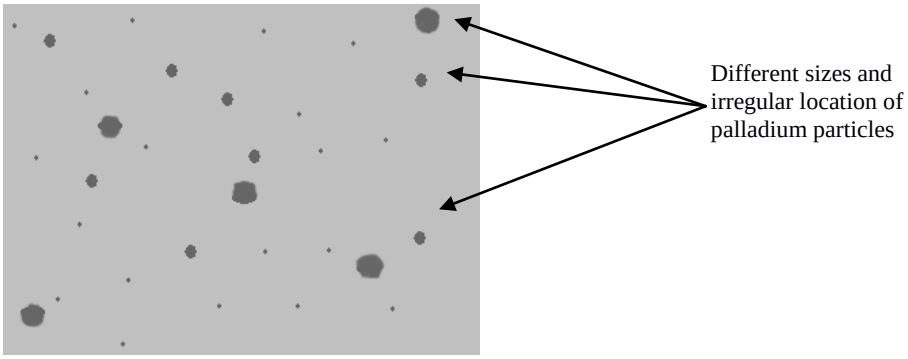

Figure 1. Model of Pd-C nanocomposite

For the calculation well-known Effective Medium Approximation (EMA) models, such as MGT (Maxwell Garnett Theory) and VAT (Volume Average Theory) can be used [6-9]. On the basis of that structure it seems reasonable to apply the MGT model for approximation of the complex refractive index layer, which includes diversity of molecules contained palladium.

Basing upon on MGT the effective complex dielectric constant of the considered Pd-C nanocomposite can be calculated as:

$$\varepsilon_{eff} = \varepsilon_M \frac{\varepsilon_M(1+2\delta)-\varepsilon_C(2\delta-2)}{\varepsilon_M(2+\delta)+\varepsilon_C(1-\delta)} \quad (1)$$

where: $\varepsilon_M = (n_M - i \cdot k_M)^2$ - complex dielectric constant of Pd

$\varepsilon_C = (n_C - i \cdot k_C)^2$ - complex dielectric constant of carbonaceous matrix

δ - volume fraction of Pd

While the effective refractive index is equal:

$$N = n - i \cdot k = \sqrt{\varepsilon_{eff}} \quad (2)$$

3. RESULTS AND DISCUSSION

3.1. Raman study

Figure 2 shows the Raman spectrum (Nicolet Almega XR Raman spectrometer, 532nm excitation) of Pd-C nanostructures prepared by use PVD/CVD method. In the range from 800 to 2000 cm^{-1} the characteristic G and D bands of amorphous graphite-like carbon (a-C) were observed [10]. In overtones range (2500-3500cm^{-1}) the second order of G and D bands, and also C-H fraction band are also appeared.

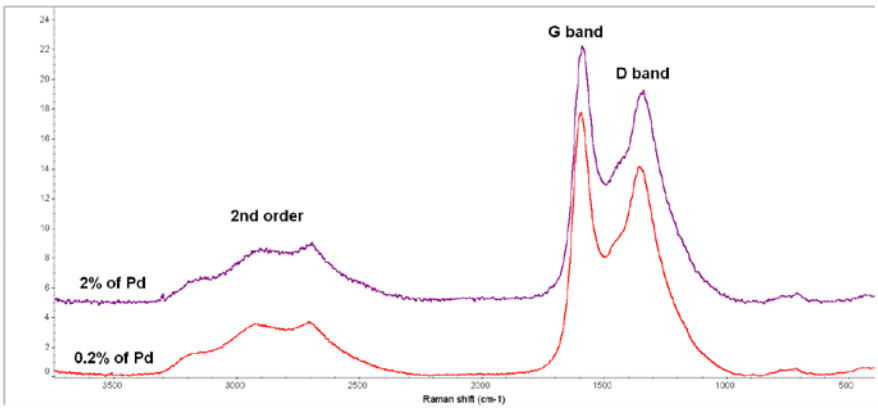

Figure 2. Raman spectra of Pd-C nanocomposites

The shape of the spectrum is characteristic for both amorphous carbon and defective graphite structures (sp^2 bond). The G peak observed approximately in 1590cm^{-1} was active primarily in monocrystal graphite and it is

caused by the spatial chain configuration of carbon bonds with sp^2 hybridisation. The D peak with the maximum observed in 1345cm^{-1} appears due to disordering of graphite structure. The I_D/I_G intensity ratio allows to determine the average graphite nanoclusters dimensions as 1-3nm. Based on the Raman studies it can be assumed that the carbon matrix of CVD samples possesses the optical properties similar to amorphous carbon.

Different volume content of Pd does not affect the shape and position of characteristic bands. This allows assuming the identical values of the optical parameters for the carbonaceous matrix, independently on Pd volume.

3.2. Theoretical calculation of optical coefficient

The values of the refractive indices of palladium and amorphous carbon in wide spectral range from 200nm to 2000nm are based on [11]. Based on presented above data it can be assumed the content of Pd from 0 to 10% of volume. To determine the effective complex refractive indices formulas (1) and (2) were used. The values of the complex effective indices of refraction were calculated. Figure 3 shows the absolute difference $\Delta n = n_{Pd\text{-}C} - n_C$ and $\Delta k = k_{Pd\text{-}C} - k_C$ of the Pd-C nanocomposite for different fraction volume of Pd (δ =1%, 2%, 3%, 4% and 5%).

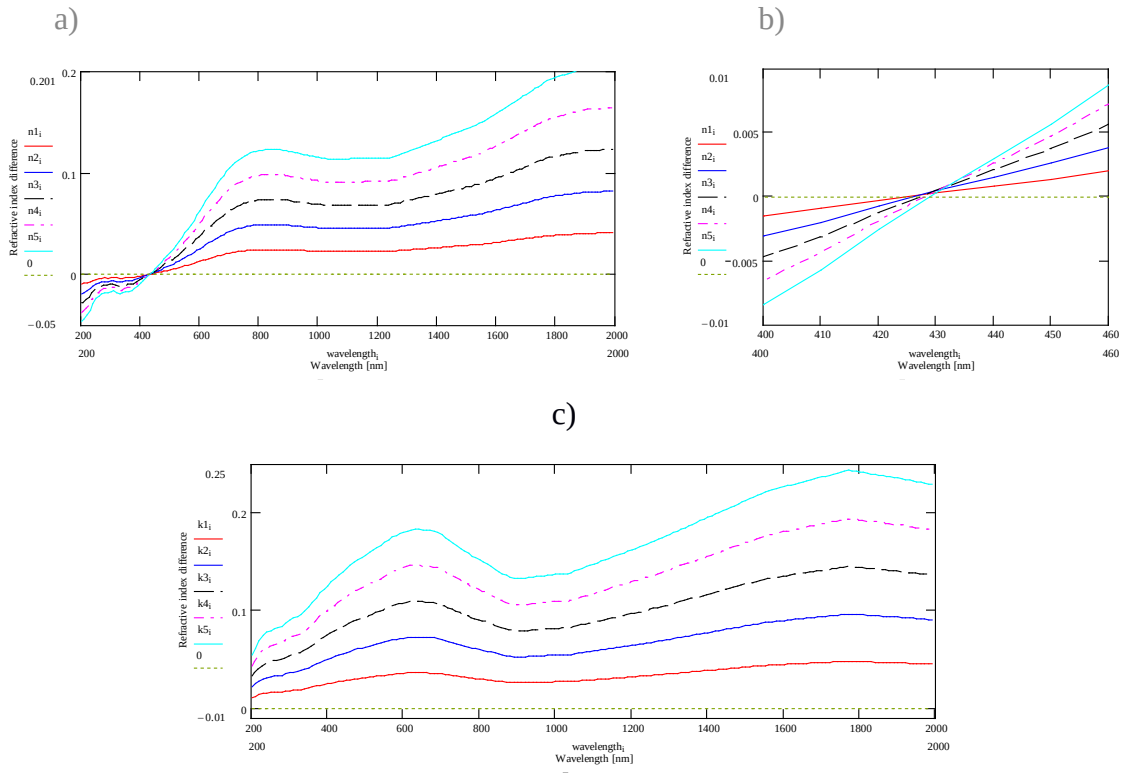

Figure 3. (a) Change of refractive index(n) of Pd-C nanocomposites at 1%, 2%, 3%, 4% and 5% volume content of Pd calculated by Maxwell-Garnett Theory in region 200-2000nm; (b) the same plot in a narrow wavelength range, showing the critical value to the wavelength of 430nm, (c) change of extinction coefficient (k)

An anomalous behaviour of refractive coefficient was clearly observed for photon energy of 2.88eV ($\lambda \approx$ 430nm). It was noted that for wavelengths above 430nm increasing of Pd content leads to an increase the refractive index n, while below 430nm, increasing of Pd leads to decrease of n. Change of the n value with the metal content is an almost linear for all considered range of wavelength and is equal ~ -0.01 per 1% of Pd for λ = 200nm and ~ +0.042 per 1% of Pd for λ = 2000nm. The increase of δ leads to an increase of the extinction coefficient in the analysed wavelength range.

The reflection coefficient (R) for normal incidence based on the Fresnel formula (3) was also calculated.

$$R = \frac{\left(n_{eff} - 1\right)^2 + {k_{eff}}^2}{\left(n_{eff} + 1\right)^2 + {k_{eff}}^2} \tag{3}$$

Figure 4 shows the calculated reflectance coefficient R for layers containing 0%, 1%, 3% and 5% Pd and changes of R value in relation to the pure a-C layer. The R values increase significantly with increasing of δ. In IR region the changes of R value almost do not depend on wavelength.

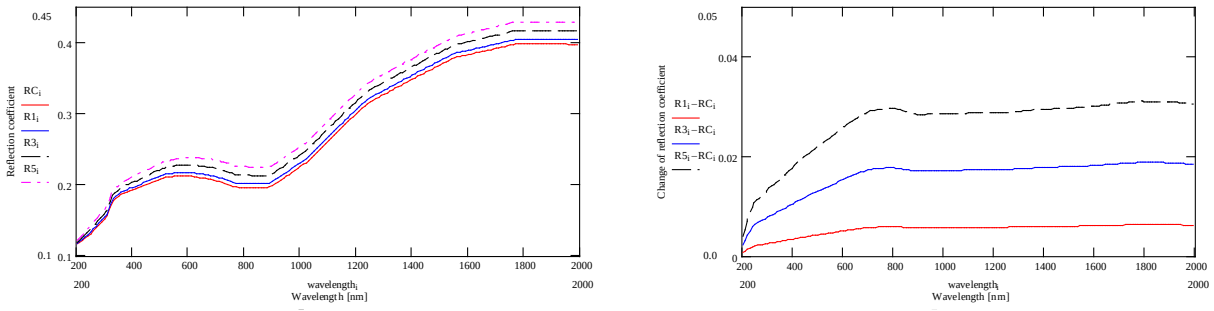

Fig. 4. Calculated reflection coefficient (R) of Pd-C nanocomposite (a) and changes of R value in relation to the pure a-C layer

CONCLUSIONS

Due to difficulties of experimental determination of the refractive indices in Pd-C nanocomposites, caused by large surface roughness and high dissipation of light, the values of n and k were calculated theoretically. The influence of Pd content on the value of the effective refractive index of Pd-C nanostructure was analyzed. The amount of the metal can lead to both growth and decline in the value of n, depending on the wavelength. Unfortunately, the results can also depend on the adopted model and the type of the carbon matrix. For this reason, the problem requires further experimental research and theoretical analysis.

ACKNOWLEDGMENTS

This research was performed in the framework of the EU COST Action MP0702 and financed by Polish Ministry of Science and Higher Education (577/N-COST/2009/0 research project).

REFERENCES

[1] E. A. Evard, *et al:* , Kinetics of sorption and release of hydrogen by nanoporous carbon, *Materials Science* 36, pp. 499-505, 2000.
[2] W. Grochala, P. P. Edwards: Thermal Decomposition of the Non-Interstitial Hydrides for the Storage and Production of Hydrogen, *Chem. Rev.* 104 (3), pp.1283–1316, 2004.
[3] E. Czerwosz, *et al:* Nanostructural Carbonaceous Films with Metal (Pd, Ni) Nanoparticles, *Nanostructured Materials for Advanced Technological Applications*, Springer Science + Business Media B.V., pp.227-230, 2009.
[4] M.Kozłowski, *et al*: Nanostructural C-Pd films obtained in 2-steps PVD/CVD technological process, *JAMME* , vol 37 (2), pp. 304, 2009.
[5] E.Czerwosz, *et al:* Properties of Pd-C films for hydrogen storage applications, Phys. Status Solidi C 8 No 7-8, pp.2527-31, 2011.
[6] M. Y. Koledintseva, R. E. DuBroff, R. W. Schwarz: A Maxwell Garnett Model For Dielectric Mixtures Containing Conducting Particles at Optical Frequencies, *Progress In Electromagnetics Research*, PIER 63, 223–242, 2006
[7] D. Stroud, The effective medium approximations: Some recent developments, *Superlattices and Microstructures*, Vol. 23, No. 3/4, 1998,
[8] A. Garahan, L. Pilon, J. Yin, I. Saxena: Effective Optical Properties of Absorbing Nanoporous and Nanocomposite Thin-Films, *J. of Appl. Phys.* , Vol. 101 (11), 2007
[9] A. Navid, L. Pilon, Effect of Polarization and Morphology on the Optical Properties of Absorbing Nanoporous Thin Films, *Thin Solid Films*, Vol. 516, pp.4159-4167, 2008
[10] A.C. Ferrari, J. Robertson: Interpretation of Raman spectra of disordered and amorphous carbon, *Phys. Rev. B*, vol. 61 (20), pp. 14095 – 14107, 2000
[11] http://refractiveindex.info.

Surface Plasmon Resonance as a monitor tool for the lateral mobility of solid supported bilayer lipid membranes

Giancarlo Margheri [1], Emilia Giorgetti [1],Bruno Tiribilli[1], Riccardo D'Agostino[2], Mario Del Rosso[2], Rolando Guidelli[3], Lucia Becucci[3]

[1] *ISC-CNR, Via Madonna del Piano 10, 50019 Sesto Fiorentino (Firenze), Italy.Tel: +390555226691; e-mail:* giancarlo.margheri@fi.isc.cnr.it

[2] *Department of Pathology and Experimental Oncology, Viale G.B.Morgagni 50,50134,Firenze,Italy*

[3]*Department of Chemistry, Via della Lastruccia, 3 , 50019 Sesto Fiorentino,Firenze ,Italy*

ABSTRACT

In this work we propose the Surface Plasmon Resonance (SPR) as method to obtain relative extimations of the lateral mobility of solid-supported bilayer lipid membranes (ssBLMs), that is a decisive factor for the formation of lipid rafts (LRs). As their formation is accompanied by an efficient recruitment of the ganglioside GM1, its presence on a ssBLM is an effective indicator of the lipids lateral mobility. We have measured the amount of GM1 recruited when ssBLMs are formed with and without raft forming mixtures on two molecular gold-linked spacers. The differences in the detected GM1 are consistent with the nominally different lipids mobility on these supports.

1.INTRODUCTION

Systems mimicking physiological cell membranes on solid supports (solid-supported biomimetic lipids membranes, ssBLMs) are excellent models for studying *in vitro* their interactions with several biological molecules (ionic pumps, signaling agents, etc…)[1,2]. In particular, the performances of solid-supported biomimetic membranes are expected to be much better if they present a lateral mobility analogous to the physiological environment. Lipid lateral mobility is required for the formation of important microdomains enriched in cholesterol, sphingolipids and proteins, called lipid rafts (LRs). Lipid rafts, that have been related to the immiscibility of liquid-ordered (Lo) and disordered (Ld) phases[3], serve as a platform for several membrane processes (e.g. signal transduction, neurotransmission, receptor trafficking) , with important pharmacological implications [4,5].

The formation of ssBLMs on a substrate is easily monitored with optical surface probe fields, mainly related to Surface Plasmon Resonance (SPR) phenomenon. As well known, this is a label-free surface sensitive tool, and the related techniques, easily implementable with a standard lab equipment, allow the detection of the upset of adlayers near an interface with high resolution. Nevertheless, no information about ssBLMs mobility can be directly inferred. For this purpose, alternative methods (Atomic Force Microscopy, fluorescence microscopy, optical waveguides) have been used, but each exhibits specific limitations in cost, hardware complexity or maximum measurement time. Even though SPR alone is not sufficient for the measurement of ssBLMs mobility, we show that it allows the detection of LRs formation in ssBLMs and therefore to obtain a relative evaluation of this important parameter.

We used the monosialoganglioside GM1 as a LRs marker, since GM1 has been reported to partition preferentially in the Lo phase[6]. (Fig.1a). The amount of GM1 in ssBLMs when the ganglioside is added to a raft-forming lipid mixture is thus an indicator of the capability of the ssBLM to self-assembly in lo-ld immiscible phases and, in the end, of the ssBLMs mobility.

GM1 recruitment can be easily detected via SPR by exploiting its well known high affinity for the homopentameric cholera toxin B subunit (ChTB) (Fig1b), a protein that strongly binds to the GM1 to form well ordered two-dimensional crystalline arrays extending ~2.5 nm in height above GM1-containing domains[7]**.** We report here results obtained forming lo-ld GM1:ssBLMs onto self-assembled monolayers (SAM) of two different molecular spacers, on which lipids have an *a priori* different mobility. The SPR tests confirm a higher presence of GM1 in the mobile ssBLM, thus validating at the same time the proposed approach for the mobility estimation.

2.TESTS AND RESULTS

In order to set evidence of the proposed procedure, we have compared two cases which differ for the gold-linked molecular spacer on which the ssBLMs are assembled. The ssBLM are formed using a lipid mixture of dioleoylphosphatidylcholine (**D**OPC), sphingomyelin (or the similar palmitoylsphingomyelin, **P**SM) and cholesterol (**C**hol) (briefly **DPC** mixture), added with 20%mol of ganglioside GM1.

The two molecular spacers were the tetraoxyethylene glycol-D,L-α-lipoic acid ester (TEGL,Fig.2a), on which lipids are expected to assemble in highly mobile ssBLMs, and the thiolipid 2,3-Di-O-phytanyl-sn-

glycerol-1-tetraoxyethylene glycol-D,L-α-lipoic ester,(DPTL,Fig.2b), on which only a scarcely mobile lipid monolayer can assemble, and form a tethered BLM (tBLM) .

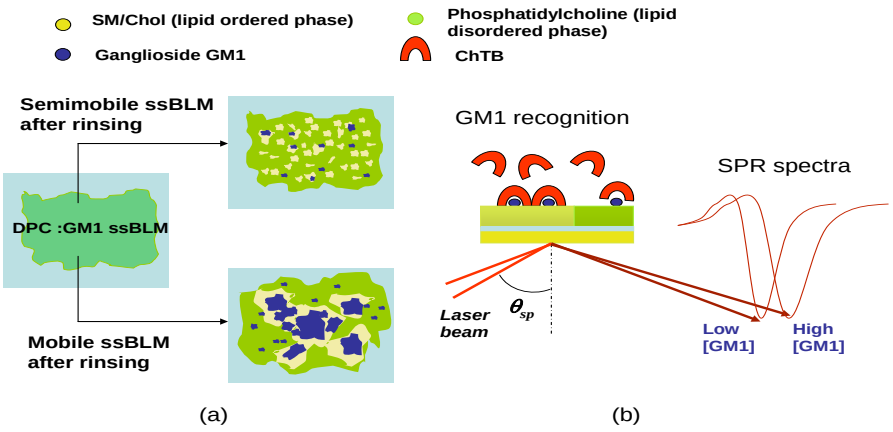

*Fig.1 (a) A solid-supported biomimetic lipids membrane (ssBLM), obtained starting from a lipid mixture made of dioleoylphosphatidylcholine (**D**OPC), sphingomyelin, cholesterol (**C**hol) and ganglioside GM1 , shows immiscibility of ordered (Lo) and disordered (Ld) liquid phases. If it can move laterally on a substrate it is more able to recruit GM1 in the lo areas. (b) The GM1 presence is detected with the binding to its specific ligand, ChTB. The different amount of bound ChTB produces different shifts in the resonance angle θ_{sp}*

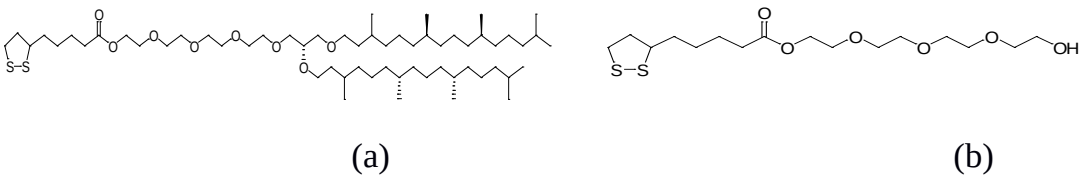

Fig.2 . Structures of: (a) 2,3-di-O-phytanyl-sn-glycerol-1-tetraethylene glycol-D,L-α-lipoic acid ester, (DPTL) and (b) [1,2]-Dithiloan-3-yl-pentanoic Acid 2-[2-[2-(2-hydroxy-ethoxy)-ethoxy]-ethoxy]-ethyl Ester (TEGL). ssBLMs. The S-S terminal groups favors the functionalization of gold transducers, while the other terminal groups are likely to favor the formation of partially mobile and mobile ssBLMs, respectively.

Both DPTL and TEGL have gold-affine S-S groups that allows the self-assembly of these molecules on a transducing gold layer (50 nm nominal thickness) deposited by electron gun evaporation in high vacuum ($2x10^{-6}$ torr residual pressure) on a SF4 glass slide.

The SPR measurements were performed with a RT 2005 setup (RES-TEC Resonant Sensor Technology) based on the angular interrogation by a collimated He-Ne laser beam (wavelength: 633nm) of a Kretschmann stage (a SF4 prism oil- matched to the metal-coated SF4 slide) coupled to a PTFE cell that hosts all the solutions necessary for the gold functionalization, for the ssBLMs formation and the GM1-ChTB binding reactions.

First, we functionalized a gold layer deposited on a SF4 slide with TEGL. Then, a hexane solution of raft-forming mixture plus GM1 20%mol is put in contact with the Au/TEGL support. Once the solvent has completely evaporated the dried lipid film (**DPC**:GM1) is exposed to water. The subsequent self-organization of the lipids is monitored recording the time course evolution of the SPR spectrum. After about 15 hours the spectrum reaches a steady state, which corresponds to the formation of a ssBLM with uniformity of the same order of that of TEGL/water interface, and an average membrane thickness of (6.2 +/- 0.3) nm, calculated by best fitting of the spectrum supposing a refractive index for lipids equal to 1.47 .

After the verification of SPR spectrum stabilization with two further rinsing cycles, a ChTB water solution ($0.86x10^{-7}$ M) was injected into the cell. ChTB binding to the ssBLM was monitored in time, recording the variations of the angular positions $\Delta\theta_{sp}$ *(DPC/TEGL)* of the SPR minima with respect to that obtained before the ChTB addition. In order to evaluate the uncertainty due to accidental inclusion of GM1, for example due to membrane defects, more tests have been performed to check the reliability of the method. Four samples were realized and tested, and the average regime value of the $\Delta\theta_{sp}$ *(DPC/TEGL)=2.1°* is found after 20 hours (Fig.3).

Then, we performed SPR reference tests to monitor the recruitment of GM1 onto ssBLMs obtained starting from lipid mixture mimicking only the ld-phase, therefore made of DOPC and GM1.

GM1 recognition is evidenced by the angular shifts $\Delta\theta_{sp}$ *(DOPC/TEGL)* of the spectra recorded after the DOPC:GM1-ssBLM rinsing and stabilization and by the successive recognition of ChTB .A regime average value of $\Delta\theta_{sp}$ *(DOPC/TEGL)=1.1°* is found after 20 hours (Fig.3)

The difference $\Delta\theta_{sp}$ *(DPC/TEGL)* - $\Delta\theta_{sp}$ *(DOPC/TEGL) =1.0°* increases with the quantity of GM1 recruited in the raft-like domains.

Subsequently, analogous test were performed with DPC:GM1-ssBLMs and with the control DOPC:GM1-ssBLMs assembled on Au/DPTL transducers. Also in this case the tests were repeated four times for each of the two lipids composition.

Average saturation values of the angular shifts were found to be $\Delta\theta_{sp}$(DPC/DPTL) = 0.48° and $\Delta\theta_{sp}$(DOPC/DPTL) = 0.38°. In this case, the difference $\Delta\theta_{sp}$ *(DPC/DPTL)* - $\Delta\theta_{sp}$ *(DOPC/DPTL) =0.1°* is ten times lower than that calculated for ssBLMs formed on TEGL. These results indicate that ssBLMs formed on TEGL have a more pronounced tendency to reorganize in GM1-rich domains, and proves at the same time a higher lateral mobility of lipids on TEGL

The reproducibility of the tests, evidenced by the error bars in the kinetics of Fig.4, proves that the GM1 enrichment on both TEGL and DPTL is not due to an accidental localization of the ganglioside, but it is imposed by lipids reorganization on DPTL and TEGL spacers.

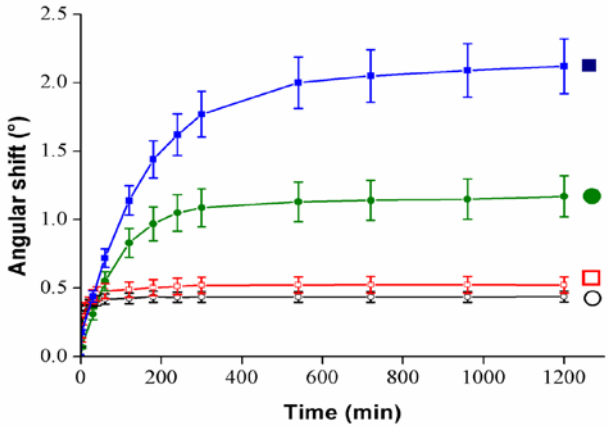

*Fig.3 SPR association kinetics of GM1-ChTB binding after the ssBLMs stabilization of : (■) **DPC**:GM1 and (●) DOPC:GM1 on Au/TEGL; (□) **DPC**:GM1 and (○) DOPC:GM1 on Au/DPTL.*

3.CONCLUSIONS

In conclusion, our results prove that SPR is an effective method to monitor lipids lateral mobility on a solid support via the formation of raft-like domains and the consequent enrichment with ganglioside GM1. With respect to other techniques, our SPR tests are able to detect lipids reorganization with no need of labeling molecules and have no problem of time duration (as would be the case of fluorescence related techniques), so getting evidence also of very slow lipids lateral movements. Moreover, the tests are not limited neither by the extension of the raft-like domains nor by the thickness of the spacers. Finally, they do not need expensive equipments or substrates with extremely low roughness requirements, as is typically requested by AFM diagnostics.

ACKNOWLEDGEMENTS

The authors wish to acknowledge the Italian project “Coinvolgimento di lipid rafts in medicina molecolare” funded by Ente Cassa di Risparmio di Firenze.We also wish to acknowledge Dr.Fabrizio Pieralli and Dr.Stefano Sottini for their valuable contribution

REFERENCES

[1] R. Naumann, A. Jonczyk, C. Hampel, H. Ringsdorf, W. Knoll, N. Bunjes , P. Gräber: Coupling of proton translocation through ATPase incorporated into supported lipid bilayers to an electrochemical process, *Bioelectrochem. Bioenerg.*, vol. 42, pp. 241-247 (1997).

[2] R. Naumann, E. K. Schmidt, A. Jonczyk, K. Fendler, B. Kadenbach, T. Liebermann, A. Offenhäusser , W. Knoll: Proton transport through a peptide-tethered bilayer lipid membrane by the H^+-ATP synthase from chloroplasts measured by impedance spectroscopy, *Biosens. Bioelectr*., vol. 14, pp. 651-662 (1999).

[3] Rietveld A, Simons K : The differential miscibility of lipids as the basis for the formation of functional membrane rafts . *Biochim. Biophys. Acta* vol. 1376, pp. 467–79 (1998).

[4] B. Chini , M. Parenti: G-protein coupled receptors in lipid rafts and caveolae: how, when and why do they go there?, *J. Mol. Endocrin*. vol 32, pp. 325-338 (2004).

[5] R.S.Ostrom, P.A. Insel: The evolving role of lipid rafts and caveolae in G protein-coupled receptor signaling: Implications for molecular pharmacology, *Br. Jour. Pharmacol*, vol. 145, pp. 235-245(2004).

[6] C.Yuan, J.Furlong, P.Burgos, L.J.Johnston: The Size of Lipid Rafts: An Atomic Force Microscopy Study of Ganglioside GM1 Domains in Sphingomyelin/DOPC/CholesterolMembranes, *Biophysical Journal*, vol.82, pp. 2526-2535 (2002).

[7] A.R. Burns: Domain Structure in Model Membrane Bilayers Investigated by Simultaneous Atomic Force Microscopy and Fluorescence Imaging , *Langmuir*, vol. 19, pp. 8358 (2003).

Optical characteristics of nanocomposite C-Pd thin films – experiment and modelling

Małgorzata Suchańska[1], Hovik Baghdasaryan[2], Justyna Kęczkowska[1]
[1] Kielce University of Technology, al. 1000 –lecia P.P. 7, 25-314 Kielce, Poland.
Tel: +48 41 34 24 167; e-mail: m.suchanska@tu.kielce.pl
[2] State Engineering University of Armenia, 105 Terian str, Yerevan 0009, Armenia.

ABSTRACT
In this paper the results of experimental study of optical properties of carbon-palladium (C-Pd) thin film nanocomposites are presented. These films were prepared by using the PVD method. The optical transmittance measurement shows a strong change of transmission properties in comparison to substrate – fused silicon. In the region 200 -400 nm the samples are not transparent, but in the region 400 - 850 nm transmittance is increased and remained constant for $\lambda > 850$ nm. For theoretical analysis the nanolayers approach is proposed to explain the unusual optical transmittance properties.

Keywords: Carbon-palladium nanocomposites, nanolayers, PVD, UV-VIS-NIR spectroscopy.

1. INTRODUCTION

Investigation of optical characteristics of disordered media is important from both fundamental and technological points of view [1]. Nanocomposite C-Pd thin films are becoming an interesting object of studies thanks to their physical features, especially electrical [2, 3] and optical properties [2, 4].

In recent years new nanocomposites containing palladium and carbon nanostructures have been prepared in Tele- and Radio Research Institute [3, 5]. In this paper the study of some structural and optical properties based on optical transmission spectroscopy (OS) and Raman Spectroscopy (RS) techniques are presented.

There are different simulation methods for theoretical analysis of specific optical properties of nanocomposite materials [1]. In the present work the nanolayers approach is suggested and tested.

2. EXPERIMENTAL SETUP

Thin carbon-palladium layers were obtained on fused silica substrate using PVD method, described in detail in [3,4]. The layers obtained are a carbon-palladium nanocomposite where palladium nanograins are embedded in the carbonaceous matrix.

The molecular structure of films was studied by using Raman spectroscopy (Nicolet Almega XR spectrometer, excited with 532nm line). The spectra were recorded in the range from 100 to 4000 cm^{-1}. The beam of a relatively small power, equal to 0.25mW, was focused in the area of 1μm x 1μm by using the microscopic lens x50. The transmission spectra measurement was carried out by means of Cary 5000 dispersion spectrophotometer in the range from 200 – 3200nm, with the resolution of 1nm.

3. RESULTS AND DISCUSSION

3.1. Raman study

In Fig. 1 the Raman spectra of PVD samples, described by different technological processes 1, 2 and 3, are presented. Different allotropic forms of carbon are observed in carbonaceous matrix. The location of characteristic bands in the spectra confirms the dominance of the fullerite structure in such type of samples. The spectra for particular samples are highly similar, differing slightly with respect to band width. Sample no. 2 is characterised with the spectrum most differing from the fullerene spectrum which may be related to the greater structure deformation degree. However, for each spectrum it is possible to isolate all 10 modes observed in C_{60} fullerene in every spectrum [6]. It should be stressed that the fully-symmetrical modes (breathing mode at 495cm^{-1} and pentagonal pinch mode at 1465cm^{-1} [6]) are clearly attenuated when compared to the pure fullerene. This confirms a certain long-range order in PVD samples. In the work [4, 7] it was shown that the fullerene spectra strongly depend on the crystallographic structure.

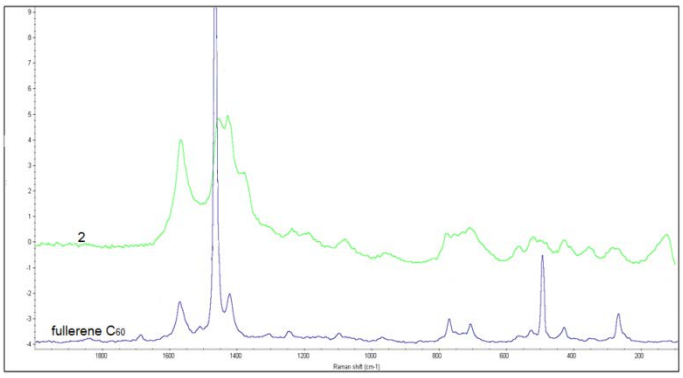

Fig. 1. Raman spectra of PVD sample 2 and fullerene [4]

3.2. Optical spectroscopy study

In Fig. 2 the optical transmittance spectra for PVD samples are presented. These samples are characterised with a very low attenuation coefficient in IR range and a high value of this coefficient in the UV range. This property is characteristic for fullerene, the presence of which was detected by using Raman spectroscopy. Results were published earlier in [4].

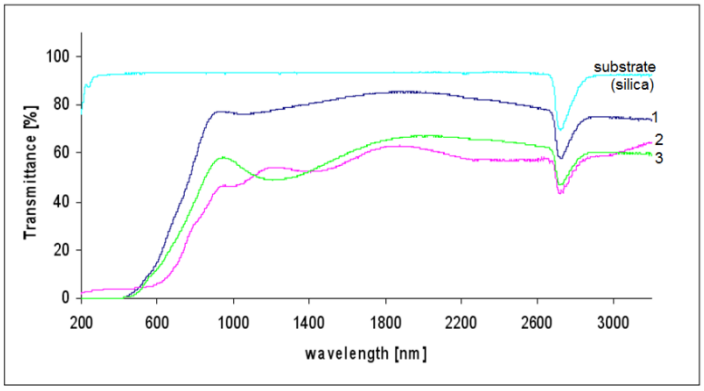

Fig. 2. Transmittance spectra of PVD samples [4]

UV-VIS spectroscopy of fullerenes indicates the presence of strong absorption bands in the range from 200-400nm, related to the electron transition in C_{60} molecule structure [6]. In PVD sample spectra below 800nm a gradual decrease in the optical transmittance coefficient value is observed, until it reaches zero in the UV range.

Near 2700nm (0.45eV), a strong absorption band originating from the silica substrate is observed. In NIR region the transmittance coefficients are subject to the quasi-periodic modulation resulting from the interference on the boundaries of the carbon-palladium layer. The location of the local minimums and maximums varies for particular samples which may confirm the diversified sample thickness and/or various values of the layer refractive effective coefficient n_{eff} . The minimum optical transmittance coefficient value falls for the wavelength values where the wave reflected from the layer-air boundary is phase-coincident with the wave reflected on the layer-substrate boundary.

3.3. Theoretical model

Thin films of PVD C-Pd nanocomposites (of overall thickness ~300 nm) deposited on SiO_2 substrate (of 1 mm thickness) can be treated as a multilayer structure consisted of different nanolayers of carbon, Pd and air. The consideration of disordered medium as the stack of nanolayers forming the material, is an alternative to the traditional theoretical approach known as an effective index approximation. The nanolayers approach needs the correct solution of relevant boundary problem for layers of composite by making the calculation for different alternations of layers. For the boundary problem solution the method of single expression (MSE) is proposed what permit to treat dielectric and metallic nanolayers with the same ease. The MSE is an advanced approach for boundary problems solution and oriented on correct wavelength scale tasks' solution [8]. In the MSE solution of Helmholtz's equation is presented as a single expression regarding the resulting amplitude and phase of electric or magnetic field component of electromagnetic wave. This type of solution presentation permits to escape severe restrictions of superposition principle, what is inherent feature of traditional counter-propagating waves

approach for Helmholtz's equation solution presentation.
By correct solution of relevant boundary problem for thin layers of composite and substrate it is possible to have suitable results in agreement with experimental ones.
Theoretical analysis of the results and further research in experimental direction will be useful for better understanding this unusual optical properties of nanoporous carbon–metal composite thin films.

ACKNOWLEDGEMENTS

This research was performed in the framework of the EU COST Action MP0702 and financed by Polish Ministry of Science and Higher Education (577/N-COST/2009/0 research project).

REFERENCES

[1] Flory, F., Escoubas, L. and Berginc, G., "Optical properties of nanostructured materials: a review", Journal of Nanophotonics, vol. 5, pp. 052502-1 - 052502-20, 2011.
[2] Czerwosz, E., Dłużewski, P., Kęczkowska, J., Kozłowski, M., Suchańska, M. and Wronka,H., "Palladium nanocrystals and their properties", Materials Science-Poland, vol. 26 (1), pp. 119-125, 2008.
[3] Czerwosz, *"Badania zmian własności przewodnictwa elektrycznego warstw palladowo-węglowych pod wpływem gazów zawierających związki wodoru"*, Przegląd Elektrotechniczny, vol. 10, pp.61-64, 2010.
[4] Belka, R., M. Suchańska, E. Czerwosz, A. Chiasera and M. Ferrari, *„The optical study of nanoporous C=Pd thin films"*, Proceeding of SPIE, vol. 7502, 750223, 2011.
[5] Kowalska, E., E. Czerwosz and J. Radomska, *„Metoda syntezy nanoporowatych materiałów węglowo-palladowych"*, Elektronika vol. 1, pp.32-35, 2009.
[6] Dresselhaus, M. S., Dresselhaus, G. and Eklund, P.C., "Raman scattering in fullerenes", J. of Raman Spect., vol. 27, pp.351-371, 1996.
[7] Blank, V.D., Buga, S.G., Dubitsky, G.A., Serebryanaya, N.R., Popow, M.Yu. and Sundovist D., "High pressure polymerized phase of C_{60}", Carbon, vol. 36 (4), pp. 319 – 343, 1998.
[8] Baghdasaryan, H.V. and T.M. Knyazyan, "Problem of Plane EM Wave Self-action in Multilayer Structure: an Exact Solution", Optical and Quantum Electronics, vol. 31, no.9/10, pp.1059-1072, 1999.

NOTES

Fibre to Chip Grating Coupler Designed on SOI Platform with Sub-Wavelength Grating

Anton Kuzma[1,2], Jozef Chovan[1,2], František Uherek[1,2]
[1] *ILC – International Laser Centre, Ilkovicova 3, 812 19 Bratislava, Slovakia.*
Tel: +421 265421385; e-mail: chovan@ilc.sk
[2] *STU FEI – Slovak University of Technology, Faculty of Electrical Engineering and Information Technology, Institute of Electronics and Photonics, Ilkovičova 3, 812 19 Bratislava, Slovakia.*

ABSTRACT
Fibre-to-chip grating couplers are efficient components for coupling radiation from optical fibre to waveguide, as they require no facet preparation and enable wafer scale testing. In this work this type of coupler was designed in SOI platform with sub-wavelength grating for refractive index transformation and matching, which is suitable for photonics integration circuits. The optimization of the coupler was performed by beam propagation method and 3D FDTD for maximization of coupling efficiency between telecom SM fibre and SOI wire waveguides. The input wavelength, pitch size and angle of launch field were optimized.

Keywords: fibre to chip grating coupler, sub-wavelength, silicon on isolator, pitch size

1. INTRODUCTION

Fibre-to-chip couplers are key components in Silicon photonics, because direct coupling optical radiation from optical fibre to facet of waveguide designed in silicon-on-isolator (SOI) is difficult. The cross section of waveguide is 250nm x 450nm. There is some designs as 3D tapers [1], inverse tapers [2], microlenses [3] and sub-wavelength waveguide grating couplers [4,5].
Grating couplers operates with extracted radiation from optical fibre and towards it in to waveguide. Dimensions of fibre-to-chip grating coupler were designed for conventional single mode optical fibre. Output of coupler is planar waveguide with dimensions for spreading of light in fundamental mode.
For the design and simulation we have used RsoftCAD that is the core program in the Rsoft Photonics Suite, and acts as a control program for passive device simulation module BeamPROP. The other suitable simulation method is finite-difference-time-domain (FDTD) method.

2. FIBRE-TO-CHIP COUPLER GRATING DESIGN

Geometry of the fibre-to-chip coupler is illustrated schematically in Fig. 1. The diffractive grating is along the z direction. The coupler consists of first segment with sub-wavelength grating along the x axes, following the next tapered segment which adjusts cross-section of segment with grating to cross-section of output waveguide (spot size converter). Along z axis the duty cycle of the structure is changed by size of holes in grating. It depends on effective refractive index. If the duty-cycle is large (small air holes) then effective refractive index is similar to Silicon and reduces back-reflections. If the duty-cycle is smaller, then effective refractive index is decreased.

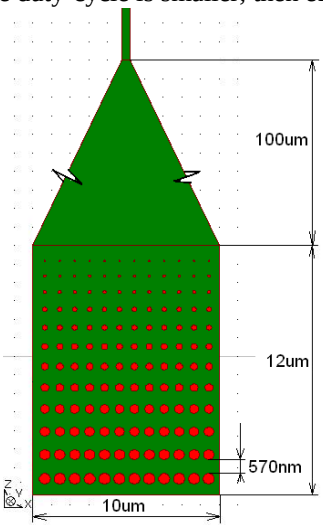

Figure 1. Schematic view of the fibre-to-chip grating coupler

Fibre-to-chip coupler is designed in SOI platform. It means using a 260nm thick silicon layer on a 2μm thick bottom oxide. Contour map of the refractive index such structure is shown in Fig. 2. Grating operates with TM (y

axis) polarized light. Sub-wavelength grating along the x axis seems like homogenous medium. The pitch size is 0.57 μm.

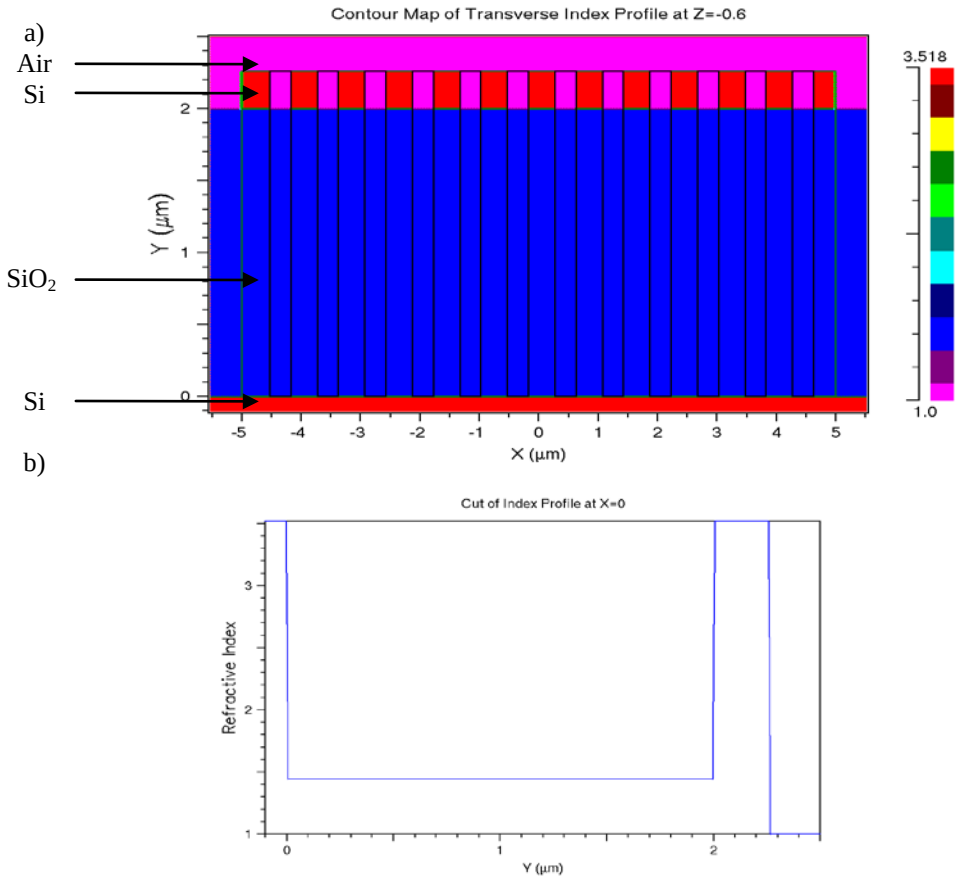

Figure 2. (a) Contour map of the refractive index of fibre-to-chip grating coupler. (b) Cut of index profile at x = 0

3. SIMULATION RESULTS

Simulations are performed by RSoft BeamPROP simulation tools.The computation core of the program is based on a finite difference beam propagation method. This technique uses finite difference methods to solve the well-known parabolic or paraxial approximation of the Helmholtz equation. In addition, the program uses "transparent" boundary condition following. We used simple implementation of the transparent boundary condition. It effectively lets radiation pass through the boundary and leave the computation domain. Fibre-to-chip coupler in simulation domain is illustrated in Fig. 3.

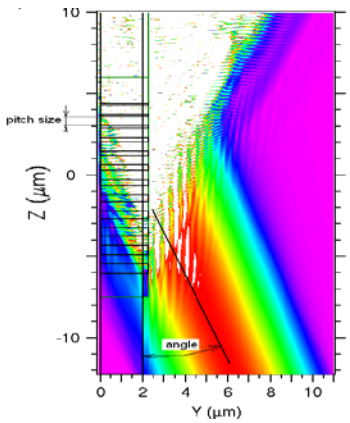

Figure 3. Fibre-to-chip coupler in simulation domain

Next approach used for the simulations is finite-difference-time-domain (FDTD) method. It calculates the

electromagnetic field as a function of time and space in a given refractive index structure in response to a given electromagnetic excitation. The FDTD method is a rigorous solution to Maxwell`s equations and does not have any approximations or theoretical restrictions.

3.1. Output power dependence on wavelength of launch field

Fibre-to-chip coupler is designed for telecom spectral C-band. In this relatively wide spectral range (cca 200 nm) the designed coupler can be effectively used for coupling of optical radiation from telecommunication optical fibre to planar waveguide. The spectral dependence of optical power level in output planar waveguide is shown in Fig. 4. Insertion losses are less than 1.22 dB at 1580 nm for pitch size 0.57 μm and angle of launch field 20° as the simulation parameters.

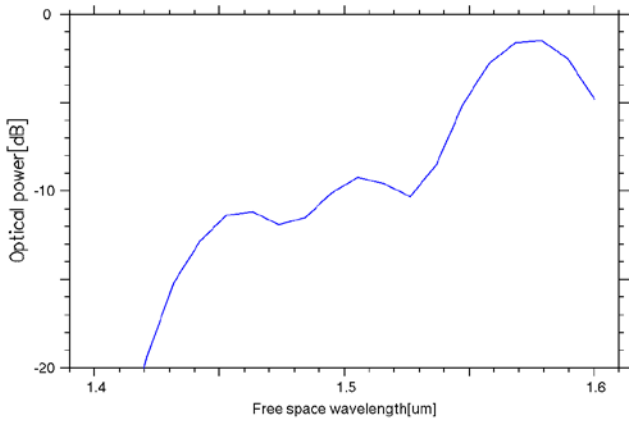

Figure 4. Spectral dependence of optical power level in output waveguide (for pitch size 0.57 μm and angle of launch field 20°)

3.2. Output power dependence on pitch size

In Fig. 5 is illustrated the optical power level dependence on pitch size of grating. Input wavelength 1.55 μm and angle of launch field 20° were taken as simulation parameters. The pitch size is critical parameter to achieve small insertion losses. As it is clear from this design there are two possible wavelengths to obtain small insertion losses (Fig. 5), 510 nm and 580 nm respectively.

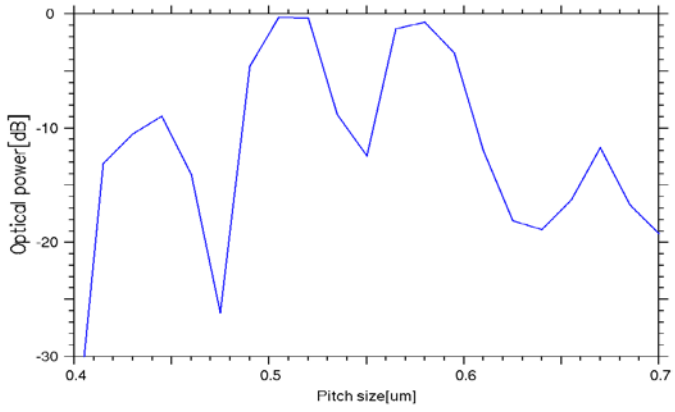

Figure 5. Dependence of optical power level in output waveguide on pitch size (for wavelength 1.55 μm and angle of launch field 20°)

3.3. Output power dependence on angle of launch field

Fibre-to-chip coupler is used for wide range of launch field angle. The simulated dependence of optical power level in output waveguide on angle of launch field is illustrated in Fig. 6. (The simulation parameters are wavelength 1.55 μm and pitch size 0.57 μm.)

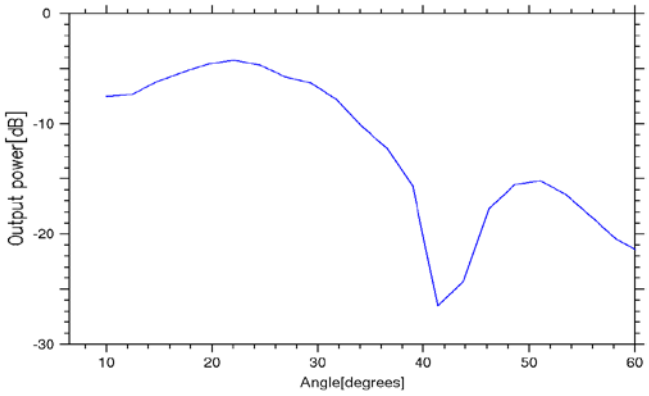

Fig. 6. Dependence of optical power level in output waveguide on angle of launch field for wavelength 1.55 μm and pitch size 0.57 μm.

4. CONCLUSIONS

In this paper the fibre-to-chip optical coupler design with sub-wavelength grating is optimized for maximization of coupling efficiency between telecom SM optical fibre and SOI wire waveguides. The simulation results showed appropriate parameters, which predisposed this photonic device for applications where the coupling of optical radiation from conventional telecommunication SM optical fibre to the SOI wire waveguides is needed. The optimized coupler design has less than 1.22 dB overall coupling losses at 1580 nm.

ACKNOWLEDGEMENTS

This work was supported by projects No. 1/0787/09 of VEGA grant agency of Slovak Ministry of education and APVV-0424-10, APVV VVCE-0049-07, SK-AT-0010-10 from Slovak research and development agency of Slovak Ministry of education and SK 13/2011 from Austrian Agency for International Cooperation in Education and Research (OeAD-GmbH).

REFERENCES

[1] A. Sure, T. Dillon, J. Murakowski, C. Lin, D. Pustai, and D. Prather, “Fabrication and characterization of three-dimensional silicon tapers,” Opt. Express 11(26), 3555–3561 2002.

[2] Almeida, V.; Panepucci, R. and Lipson, M. “Nanotaper for compactmode conversion,” Opt. Lett., vol. 28, pp. 1302-1304, 2003.

[3] A. Delage, S. Janz, D. Xu, D. Dalacu, B. Lamontagne, and A. Bogdanov, “Graded-index coupler for micropho-atonic SOI waveguides” in Proc. of SPIE Photonics North 2004: Optical Components and Devices, vol. 5577, pp.204–212, 2004.

[4] P. Cheben, D. Xu, S. Janz, and A. Densmore, “Subwavelength waveguide grating for mode conversion and light coupling in integrated optics,” Opt. Express 14(11), 4695–4702 2006.

[5] Roelkens, G.; Vermeulen, D.; Selvaraja, S.; Halir, R.; Bogaerts, W. &Van Thourhout, D. “Grating-Based Optical fibre Interfaces for Silicon-on-Insulator Photonic Integrated Circuits,” IEEE J. Sel. Top. Quantum Electron., to be published, 2010.

Eu^{3+} and Tb^{3+} codoped Y_2O_3 Nanocrystals Prepared by Pechini-Type Sol-Gel Process

F. Enrichi[1], R. Riccò[1], M. Back[1,2], P. Riello[2], D. Cristofori[2]
[1]CIVEN and Nanofab, via delle Industrie 5, 30175 Marghera (Venezia) – ITALY
Tel: +390415094281; e-mail: enrichi@civen.org
[2]Dip. Chimica Fisica, Univ. Ca' Foscari Venezia and INSTM, via Torino 155, 30170 Mestre (Venezia) – ITALY

ABSTRACT
RE-doped Y_2O_3 system are some of the most important optical materials: having high luminescence efficiency, chemical and thermal stability, they are used in the production of optoelectronic devices such as laser materials, energy conversion devices, display panels, bio imaging probes and anti-counterfeiting tags.

In this work we report an optical study of Eu^{3+} and Tb^{3+} codoped Y_2O_3 nanocrystals synthesized by Pechini-type sol-gel method. The particles have been investigated in terms of size and morphology by means of X-ray diffraction and transmission electron microscopy, showing how the simple Pechini method allows the growth of monocrystalline nanoparticles. Moreover the optical properties of Eu^{3+} and Tb^{3+} in the host lattice are studied in terms of PL, PLE and lifetimes as a function of their concentration and interaction. In particular an efficient energy transfer between the two ions occurs in co-doped samples, increasing the optical emission in the red spectral region.

Detailed analysis of the morphological and optical properties of the system is reported, demonstrating the feasibility of the method to easily obtain efficient red nanophosphors.

Keywords: nanophosphors, yttria, rare earths, energy transfer, europium, terbium.

1. INTRODUCTION

Nanophosphors are solid, inorganic, crystalline materials in the nanoscale dimensions that show luminescence upon excitation. These materials are increasingly attracting the interest of researchers for their possible use in many fields since they have characteristics absorption and emission properties, different from their bulk counterparts, with increased efficiency and lifetimes. Our group has already worked on rare-earth doped luminescent silica and zirconia nanoparticles [1, 2] for different applications. In this paper we explore the synthesis of luminescent Eu^{3+} and Tb^{3+} codoped Y_2O_3 nanocrystals. This oxide is chosen as host because it is characterized by a low phonon frequency, which makes the non-radiative relaxation of excited states inefficient, excellent refractory properties with a melting point of 2450°C and high thermal conductivity [3]. Indeed, rare earth doped Y_2O_3 systems are some of the most important optical materials: having high luminescence efficiency, chemical and thermal stability, they are used in the production of optoelectronic devices such as laser materials [4], energy conversion devices, display panels, bio imaging probes [5] and anti-counterfeiting tags [6].

Rare earths are considered the most promising elements as activator of nanophosphors since they have particular optical properties due to their special electronic configuration. The characteristic luminescence of rare-earth ions is attributed to the 4*f* shell, which is not entirely filled [7].

One of the goals in nanoparticle synthesis is to produce controlled, monodisperse nanoparticles. The Pechini method [8, 9] is a simple and inexpensive approach with the advantage to provide reproducible and monodispersed nanocrystals, therefore it is very interesting for our purposes. This technique consists in using a complexing agent, in our case citric acid, as chelating ligand of metals salts like nitrates. The formation of stable complexes and their polyesterification with a polyhydroxy alcohol (ethylene glycol) forms a polymeric resin, which immobilizes the metal complexes in a rigid organic polymer network, reducing segregation and ensuring compositional homogeneity. Calcination of the polymeric resin at a moderate temperature (500-1000°C) then produces pure phase multi-component metal oxides.

The aim of this work is the synthesis of Eu^{3+} and Tb^{3+} codoped Y_2O_3 nanocrystals via Pechini method and their morphological and optical characterization as a function of the synthesis procedure, reagents amounts and RE content. It will be shown the possibility to obtain monocrystalline highly luminescent nanoparticles which can have applications in many optical fields.

2. EXPERIMENTAL

$Y(NO_3)_3$ (Sigma Aldrich), $Eu(NO_3)_3$. $5H_2O$ (Sigma Aldrich), $Tb(NO_3)_3$. $6H_2O$ (Sigma Aldrich), citric acid (Carlo Erba), ethylenglycole (Acros Organics), and HNO_3 60% (Sigma Aldrich) were used for the preparation of Y_2O_3:Eu,Tb nanoparticles without further purification.

The Eu^{3+} and Tb^{3+} doped Y_2O_3 nanoparticles were synthesized using the Pechini sol-gel method. Every sample was prepared by addiction of yttrium, europium and terbium nitrate, citric acid and ethylenglycole in a solution

of HNO_3 60%: H_2O (1:1). The molar proportion between the salts, the citric acid and the ethylenglycole was chosen at 1:3:4.5. The solutions obtained were heated at 100 °C under magnetic agitation until gelation and let react about 12 h in order to eject completely NO_x gases. After this treatment the products were transferred in a crucible and burned in a muffle at 800 °C in air for about 2 hours. Different Eu and Tb concentrations were studied, from 0.5 mol% to 4 mol%.

The morphology of the synthesized particles was investigated by means of X-ray diffraction (XRD) and trasmission electron microscopy (TEM). The XRD patterns were collected at room temperature with a step size of 0.05° in the preset-time mode (10 s). To improve the signal-to-noise ratio at least 3 runs were measured. Philips diffractometers, equipped with a focusing graphite monochromator on the diffracted beam and with a proportional counter with electronic pulse height discrimination, were used. TEM images were taken at 300 kV with a JEOL 3010 instrument, having an ultrahigh resolution (UHR) polepiece (0.17 nm point resolution) equipped with a Gatan slow-scan CCD camera (model 794) and an Oxford Instrument EDS microanalysis detector (model 6636). The powdered samples were dispersed in isopropyl alcohol solution by sonication and then deposited onto a holey carbon film.

Photoluminescence properties in the UV and visible regions (260-750 nm) were measured with a FluoroLog-3 system Horiba JobinYvon. The system is equipped with a 450-W Xe excitation lamp for PL excitation and emission measurements. Time resolved PL measurements were carried out at R.T. under excitation at 310 nm using a pulsed laser Nd:YAG NT 342/3/UVE/AW Ekspla.

3. RESULTS AND DISCUSSION

3.1. Morphological analysis

An example of X-ray diffraction pattern for the sample containing 1 mol% Tb and 0.25 mol% Eu is shown in Fig. 1, evidencing a single crystalline phase which corresponds to the cubic phase of Y_2O_3 (ICSD #160890). The same result was found for all the samples, both containing Tb and Eu. The presence of the only cubic crystalline phase for yttrium oxide is in agreement with the thermal treatment made at 800 °C. Moreover the absence of other peaks in the X-ray diffraction spectrums is an evidence of the success of the synthesis. The determination of the crystallite sizes, the size distribution and the lattice microstrain was conducted by a line-broadening analysis. The reflection broadening in the XRD patterns is attributed mainly to three kinds of contributions: crystallite size, microstrain, and the instrument itself. The Warren-Averbach Fourier transfer method [10] was used for the line profile analysis in order to separate the effect of crystallite size and microstrain on reflection broadening and to calculate the distribution of crystallite size and microstrain of the samples. The results of the analysis show crystallites with a volume-weighted average size $< L >_{vol}$ of about 30 nm.

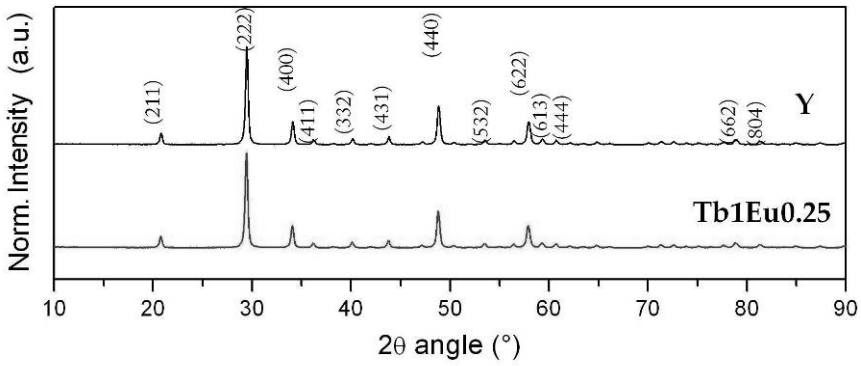

Fig. 1. X-ray diffraction patterns of Y_2O_3 and Tb 1% Eu 0.25% doped Y_2O_3 powders annealed for 2 h at 800 °C.

An example of HRTEM image of the synthesized nanoparticles is reported in Fig. 2. No changes in structure and sizes were noted in samples with different concentrations of europium and terbium. Aggregates composed of many nanoparticles were found in the samples. These nanoparticles are monocrystalline, as show in Fig. 2, with an average size of about 33 nm, in perfect agreement with the average crystallite size $< L >_{vol}$ calculated from the XRD line profile analysis. Furthermore the distance between the crystal planes of the nanoparticle is 3.01 Å, corresponding to the (222) crystal plane of cubic Y_2O_3. The presence of Tb or Eu in the Y_2O_3 structure as substitute of Y is also confirmed by the microanalysis. The results of the XRD and TEM analysis show that the Pechini method is able to produce monocrystalline nanoparticles of Eu^{3+} and Tb^{3+} codoped Y_2O_3.

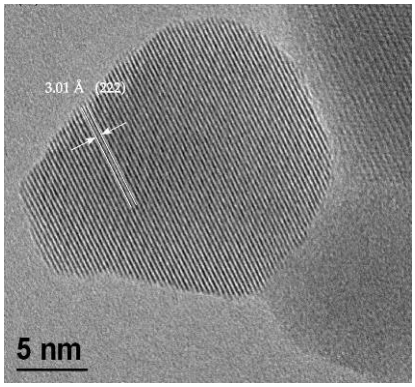

Fig. 2. High-resolution TEM image showing the crystal planes of a single monocrystalline nanoparticle.

3.2. Optical properties

The left side graph in Fig. 3 reports the PL emission spectra of single doped and codoped samples. The Eu doped samples show the characteristic peaks of Eu^{3+} ions, with a maximum emission related to the $^5D_0 \rightarrow {}^7F_2$ transition at 611 nm. The Tb doped samples show the characteristic peaks of Tb^{3+} ions, with a maximum emission related to the $^5D_4 \rightarrow {}^7F_5$ transition at 543 nm. All these spectra have been obtained by 310 nm excitation which is efficiently absorbed by Tb^{3+} ions. Both the emissions can be seen on samples containing 1 mol% Tb and increasing Eu contents. Moreover the 1 mol% Eu doped sample is also reported, showing very low emission intensity due to the low absorption of that wavelength by Eu^{3+} ions.

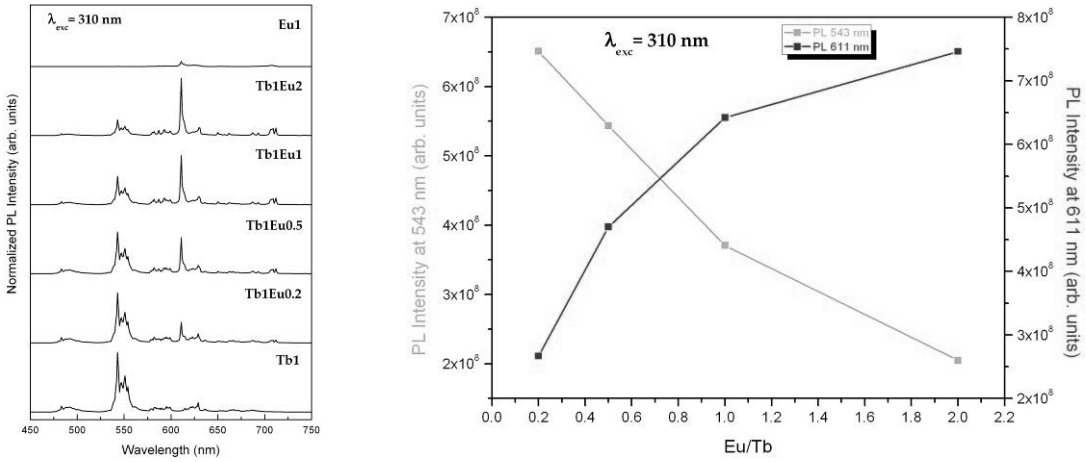

Fig. 3. PL emission spectra of the samples containing different Eu^{3+} and Tb^{3+} concentrations (left) and integrated PL intensities at 343 nm Tb^{3+} ions and 611 nm Eu^{3+} ions at increasing Eu contents.

By increasing the europium concentration in the codoped samples we can observe the lowering of the Tb^{3+} emission and the increasing of the Eu^{3+} one, pointing out an energy transfer mechanism between the two ions. This behaviour is even clearer in the right side graph of Fig. 3, showing the integrated intensities from the two ions. Photoluminescence excitation and lifetime measurements (not reported here) are fully in agreement with this hypothesis. Indeed the PLE spectra in samples containing only Eu^{3+} ions are characterized by specific absorption peaks, while in codoped samples they recall the excitation of Tb^{3+} ions, which consists of two overlapping bands centred at about 271 nm and 304 nm, in agreement with previous reports. The origin of these bands is associated with the charge transfer (CT) from the orbitals 2*p* of O^{2-} to the 4*f* of Tb^{3+} [11], or with the intra-band transitions 4*f*-5*d* of Tb^{3+} in the particles [12]. This means that Eu^{3+} emission can be excited via Tb^{3+} absorption.

Lifetime analysis further confirms the previous conclusions. In particular we measured the lifetime of Tb^{3+} emission related to the $^5D_4 \rightarrow {}^7F_5$ transition at 543 nm for different europium concentrations up to 2 mol%, obtaining a decrease from 4.5 ms to 3.7 ms.

4. CONCLUSIONS

The morphological and optical properties of Eu^{3+} and Tb^{3+} doped Y_2O_3 nanocrystals synthesized by Pechini-type sol-gel method is reported. X-ray diffraction and TEM analysis have shown the presence of monocrystalline Y_2O_3 nanoparticles in the cubic phase. Moreover, the average crystallites size calculated by line profile analysis of XRD spectra are in agreement with the average nanoparticles size evaluated by HRTEM of about 30 nm.

The study on PL, PLE and luminescence decay has indicated that an efficient energy transfer occurs between Tb^{3+} ions and Eu^{3+} ions in Y_2O_3, increasing the red emission at 611 nm and allowing exciting the europium ions in a larger wavelength range. The easy synthesis method and the efficient emission make these nanophosphors very interesting for a wide range of applications.

REFERENCES

[1] F. Enrichi, et al.: Comparison of $Eu(NO_3)_3$ and $Eu(acac)_3$ precursors for doping luminescent silica nanoparticles, *J. Nanopart. Res.* DOI 10.1007/s11051-009-9756-1.

[2] S. Silvestrini, et al.: Structural and luminescence properties of europium(III)-doped zirconium carbonates and silica-supported Eu^{3+}-doped zirconium carbonate nanoparticles. *J. Nanopart. Res.* DOI 10.1007/s11051-009-9655-5

[3] T.K. Anh, *et al.*: Luminescence, energy transfer and upconversion mechanisms of Y2O3 nanomaterials doped with Eu^{3+}, Tb^{3+}, Tm^{3+}, Er^{3+} and Yb^{3+} ions, *J. Nanomater*. DOI 10.1155/2007/48247.

[4] A.A. Kaminskii: Modern developments in the physics of crystalline laser materials. *Phys. Stat. Sol.* DOI:10.1002/pssa.200306705

[5] G.K. Das, T.T.Y. Tan: Rare-earth-doped and codoped Y_2O_3 nanomaterials as potential bioimaging probes, *J. Phys. Chem. C.* DOI 10.1021/jp802076n.

[6] D. Jiang, C.N. Chong: Anti-counterfeiting using phosphor PUF, *2nd International Conference on Anti-counterfeiting, Security and Identication*, 2008. ASID 2008, pp 59-62.

[7] G. Blasse, B.C. Grabmaier: Luminescent Materials. Springer, Berlin, 1994.

[8] M.P. Pechini: Method of preparing lead and alkaline earth titanates and niobates and coating method using the same to form a capacitor. US Patent, US3330697, 1967.

[9] J. Lin, *et al.*: Multiform oxide optical materials via the versatile pechini-type sol-gel process: Synthesis and characteristics, *J. Phys. Chem. C.* DOI 10.1021/jp070062c.

[10] B.E. Warren: X-Ray Diffraction. Addison Wesley, Reading, Massachuetts, 1969.

[11] R.E. Muenchausen, *et al.*: Effects of Tb doping on the photoluminescence of Y_2O_3:Tb nanophosphors. *J. Lumin.* DOI10.1016/j.jlumin.2006.12.004.

[12] Q. Meng, *et al.*: Size-dependent excitation spectra and energy transfer in Tb^{3+}-doped Y_2O_3 nanocrystalline. *J. Appl. Phys.* DOI 10.1063/1.2803502.

Pump-probe experiment for waveguiding semiconductor optical amplifier

E. Jelmakas[1], R.Tomašiūnas[1], M.Vengris[2], E.Rafailov[3], I.Krestnikov[4]
[1] *Institute of Applied Research, Vilnius University, Saulėtekio 10, 10223 Vilnius, Lithuania.*
Tel: +370 52366069; e-mail: rolandas.tomasiunas@ff.vu.lt
[2] *Dpt of Quantum Electronics, Vilnius University, Saulėtekio 10, 10223 Vilnius, Lithuania.*
[3] *School of Engineering, Physics and Mathematics, University of Dundee, Dundee, UK.*
[4] *Innolume GMBH, Konrad-Adenauer-Allee 11, 44263 Dortmund, Germany.*

ABSTRACT
Waveguiding configuration used in a femtosecond pump-probe experiment, when pumping/probing from the edge of waveguide, is presented. Photoinduced transmission and absorption recovery dynamic investigation was performed in a wide range of wavelength 1225-1380 nm covering resonant ground state levels of chirped quantum dot devices. Absorption saturation results compared with electroluminescence gave qualitative insight to density of states distribution. From the absorption recovery kinetics subnanosecond lifetimes for the ground state were considered.

Keywords: InGaAs quantum dots, waveguide, femtosecond.

1. INTRODUCTION

Pump-probe experiment is a traditional method for measuring transient processes in materials. Basically, the method is configured when exciting optically thin media. Waveguiding configuration of that experiment is a quite rare option specified by pump/probe from the edge of waveguide. Advantage of this technique is long distance light-media interaction. Signal detection using sophisticated heterodyne technique was used in the waveguide configuration to investigate dephasing and population dynamics in InGaAs quantum dot (QD) devices [1]. InGaAs QD serve as reliable active material in semiconductor optoelectronic devices (SESAM's [2], ridge waveguide modulators [3], photonic devices [4]). For developing new ultrafast optoelectronic devices charge carrier dynamics on femtosecond time scale are still challenging issues. Based on our experience to investigate InGaAs QD by femtosecond pump-probe technique we have applied the waveguiding configuration to measure photoinduced light transmission in InAs/InGaAs quantum dot waveguide.

2. RESULTS AND DISCUSSION

520 nm thick GaAs waveguide comprising InAs/InGaAs QD's surrounded by $Al_{35}Ga_{65}As$ claddings grown on a Si-doped GaAs substrate were fabricated. 10 layers of QD's in each structure split into 3 groups (4+3+3) of monolayer of 0.8 nm InAs, 1.3÷4.5 nm $In_{0.15}Ga_{0.85}As$, followed by 35 nm of GaAs buffer material formed the active region. Each group revealed a luminescence peak positioned at 1285, 1243 and 1211 nm, respectively. The chirped QD's structure was designed to gain broader spectra. Three semiconductor optical amplifiers (SOA) samples (Nr.1, 3 and 4) were selected. Devices had AR coating deposited on both front and back facet. The waveguide fabricated was 5.16 mm long with a 6μm ridge width.

To investigate propagation of ultra-short pulses through SOA a set-up for pump-and-probe measurements in a waveguiding configuration was constructed. Schematic of the configuration is depicted in Fig.1. From the optical source – Ti:Sapphire oscillator (1 kHz, 180 fs, 800 nm) with two „Superspitfire" amplifiers (Spectra Physics) with OPG (TOPAS, Lithuania) – pulses within wavelength range of interest 1210–1380 nm were selected. Two independently tuned channels for pump and probe beams were used. In order to investigate temporal changes in transmission due to absorption saturation affected by the pump pulse, the probe pulse was delayed in time by an optical delay line. Both beams orthogonally polarized collinearly overlapped, while coupling into the waveguide. Using a Glan prism behind the waveguide probe beam polarization was separated from the pump. Up to ~80 pJ per pulse was used for pump. Chopper served as to probe the sample in both excited and unexcited situation. The registration was performed using InGaAs photodiode. The track of measurement was as follows: at fixed points of the delay the probe beam with or without pump (fixed value) was measured, then, difference in signals was evaluated and presented as kinetic of photoinduced transmission change. Following that absorption saturation and absorption recovery kinetic was measured depending on the pump energy. The pump and probe pulse wavelength was tuned to 1260 nm (bandwidth 16 meV) to fit the ground state transition of the mid groupof the chirped QD's. All measurements were performed at room temperature.

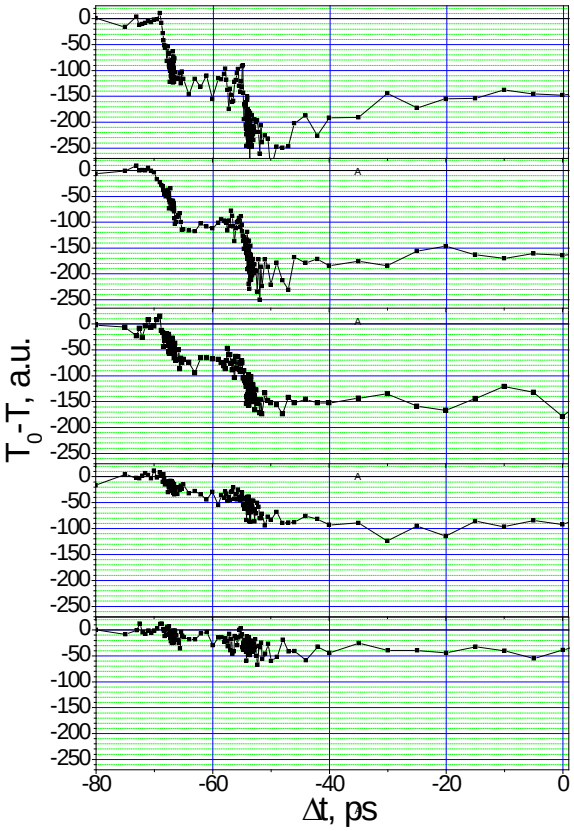

Figure 2. Kinetics of photoinduced optical transmission change of InAs/InGaAs SOA's (sample Nr.3) measured for various pump energies at wavelength 1260 nm (degenerate). Pump energy – 0.005(lowest curve), 0.01, 0.02, 0.04, 0.08 nJ.

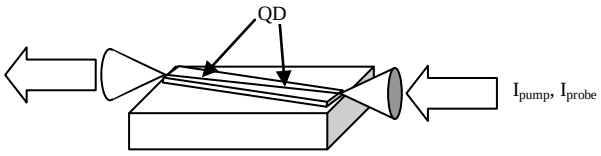

Figure 1. Schematic of the pump-probe measurement in waveguide configuration.

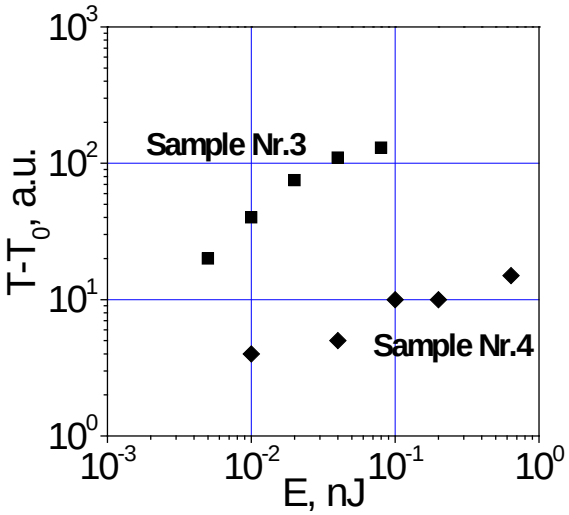

Figure 3. Photoinduced optical transmission of InAs/InGaAs SOA sample Nr.3 and Nr.4 depending on pump energy measured at 1260 nm and 1250 nm wavelength, respectively.

Spectroscopy of resonant levels by means of degenerate pump-probe technique was performed. The waveguiding configuration of the pulse propagation, when light traverses the active area for several millimetres, serves for relative prolonged interaction between light and QD, therefore high photoinduced transmission could be expected. Wavelength 1243 nm expressed as a relative peak in the electroluminescence spectra confirmed the characteristic ground state for the particular mid group of the chirped quantum dots. Taking into account femtosecond pulse spectral bandwidth wavelength 1260 nm was well selected for measuring photoinduced absorption saturation to cover the spectral interval of QD's. From three selected SOA samples (Nr.1, 3 and 4) sample Nr.3 featured best the phenomena manifesting relative high concentration of ground states involved (Fig.3). It corresponds quite well to the electroluminescence spectra range of 1220-1260 nm for the sample. The photoinduced transmission intensity dependence, however, indicates less density of ground states for sample Nr.4, what is expressed by saturation of absorption bleaching reached already at lowest pump energy of 0.01 nJ (Fig.3). Careful reading of the kinetic revealed that no fast component in the decay process appear for both samples Nr.3 and Nr.4. As seen from the kinetics measured absorption saturation lasts for tens of picoseconds without fast decaying (Fig. 2). Only after hundreds of picoseconds the probe got substantially absorbed indicating relative long lifetime for the ground state. However, we observe some inhomogeneity in the kinetics measured – an increase of the signal nearly doubled appears after ~15 ps delay, what speaks for some additional input to the photoinduced transmission signal. In non-degenerate experiment, when pumping the sample Nr.3 close to spectral maxima at wavelength 1260 nm, an increase of photoinduced transmission with decreasing quantum energy of the probe was observed. This tendency indicates rather broad distribution of states involved. Effective pumping of the wetting layer followed by carrier fast transition into QD's of different size may serve as an explanation. Spectroscopy of the resonant levels by means of degenerate pump-probe technique was also performed and is discussed.

3. CONCLUSIONS

Waveguiding configuration has been proved as an efficient tool to gain photoinduced effects via prolonged light–media interaction. Spectral investigation of photoinduced transmission demonstrated correlation with electroluminescence indicating ground state density variation for InAs/InGaAs quantum dot samples. Absorption recovery kinetics revealed lifetimes for the ground state lasting hundreds of picosecond, however, no ultrafast decay was observed.

ACKNOWLEDGEMENTS

This work was supported by the FP7 FAST-DOT project and the Agency of International Science and Technology Development Programs in Lithuania.

REFERENCES

[1] P. Borri, S. Schneider, W. Langbein, D. Bimberg: Ultrafast carrier dynamics in InGaAs quantum dot materials and devices, *J. Opt. A: Pure Appl. Opt.*, vol. 8. pp. S33-S46, 2006.

[2] A.A. Lagatsky, C.G. Leburn, W. Sibbett, S.A. Zolotovskaya, E.U. Rafailov: Ultrashort-pulse lasers passively mode locked by quantum-dot-based saturable absorbers, *Progr. Quantum Electron.*, vol. 34(1). pp. 1-45, 2010.

[3] M.A. Cataluna, D.B. Malins, A. Gomez-Iglesias, W. Sibbett, A. Miller, E.U. Rafailov: Temperature dependence of electroabsorption dynamics in an InAs quantum-dot saturable absorber at 1.3μm and its impact on mode-locked quantum-dot lasers, *Appl. Phys. Lett.*, vol. 97(12). pp. 121110, 2010.

[4] M. Laemmlin, G. Fiol, M. Kuntz, F. Hopfer, A. Mutig, N.N. Ledentsov, A.R. Kovsh, C. Schubert, A. Jacob, A. Umbach, D. Bimberg: Quantum dot based photonic devices at 1.3 μm: Direct modulation, mode-locking, SOAs and VCSELs, *Phys. Status Solidi C*, vol. 3(3). pp. 391-394, 2006.

NOTES

Fabrication of 65 nm wide Split Ring Resonators by Nanoimprint Lithography

Graham J. Sharp[1], Ali Z. Khokhar[1], Scott G. McMeekin[2], Nigel P. Johnson[1]
[1] *Optoelectronics Research Group, School of Engineering, University of Glasgow, Glasgow, G12 8LT, UK;*
e-mail: g.sharp.1@research.gla.ac.uk
[2]*School of Engineering and Built Environment, Glasgow Caledonian University, Glasgow, G4 0BA, UK.*

ABSTRACT
We report on the fabrication of 65 nm wide, high resolution rectangular U-shaped split ring resonators (SRRs) using nanoimprint lithography (NIL). Using both aluminium and gold metal lift-off to construct the structures, we measure an LC resonance peak under transverse electric (TE) conditions at the near ultraviolet range of the visible spectrum. Fabricating the SRRs by NIL rather than conventional electron beam lithography allows them to be scaled to smaller dimensions without any significant loss in resolution, partly because backscattered electrons and the proximity effect are not present with NIL. This in turn helps to shift the magnetic response to lower wavelengths while still retaining a distinct LC peak.

Keywords: metamaterials, optical resonators, nanoimprint lithography (NIL), visible spectrum.

1. INTRODUCTION

Since their inception, split ring resonators (SRRs) have been a fundamental element in the fabrication and characterisation of metamaterial structures. Their simple yet effective U-like shape sees them behave in a similar fashion to an LC oscillatory circuit with the gap between the two arms of the structure offering an intrinsic capacitance while the adjoining body gives rise to an inductance. When subjected to TE polarised light, the electric field component is coupled across the capacitive gap and a resulting current flows around the metal structure, inducing a magnetic resonance in the surrounding field, commonly referred to as the LC resonance [1]. The wavelength at which this resonance is present is largely, but not exclusively, dependant on the physical dimensions of the SRR unit cell. Scaling SRRs to ever smaller dimensions has shown to shift the LC resonance peak towards the blue region of the visible spectrum[2]. However, research into the scaling of SRRs suggests that the magnetic response at which there is a negative effective permeability, $\mu_{eff} < 0$, saturates when the SRR unit cell width is reduced to values below approximately 60nm[3]. Fabricating high resolution SRRs of this scale using e-beam lithography can be difficult due to the proximity effect, which can regularly result in enlarged feature sizes. However in this paper we demonstrate the use of nanoimprint lithography (NIL) to successfully fabricate well defined rectangular U-shaped split rings with a minimum feature size of around 20nm and a total width and length of approximately 70nm. Our SRR design and its dimensions are shown in figure 1.

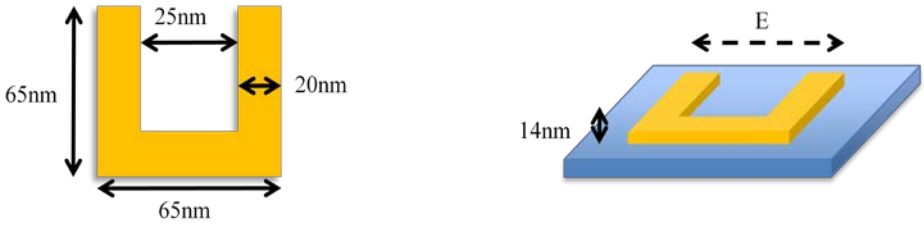

Figure 1: a) Schematic of a single SRR unit cell design detailing the dimensions of the features present on the imprinting stamp. The arms of the structure are 20nm wide, leaving a capacitive gap of 25nm and a total length and width of 65nm. b) The metals used to form the SRRs are deposited at a thickness of 14nm. The direction of the electric field in TE mode is shown to bridge the arms of the SRR.

Fabricating split-rings that are not only 70nm in width but also posses a high resolution should improve the magnetic response measured and help shift the LC resonance peak deeper into the visible spectrum.

2. FABRICATION AND MEASUREMENT

In order to pattern SRRs using NIL, a stamp with the appropriate features must first be fabricated. This is done using conventional e-beam lithography. When completed, the stamp is then impressed into a resist coated target

sample for patterning and metal deposition and lift-off is performed. Reflectance measurements of the SRRs can then be taken using a spectrometer operating in the visible range.

2.1. Fabrication of nanoimprint stamp and metal SRRs

To create the stamp used for imprinting, a 65nm thick layer of HSQ (diluted with MIBK at a ratio of 1:3) was spun onto a 500 micron thick polished silicon substrate and baked. A Vistec VB6 UHR EWF was then used to write the SRR patterns before the samples were developed using TMAH in a temperature controlled environment. As an alternative to dry etching into the silicon substrate and removing the HSQ mask with hydrofluoric acid (HF), we instead used the SRRs formed in HSQ to directly pattern the target sample. Because the stamp is subjected to both increased temperature and pressure during the imprinting process it is important, in the interests of pattern quality and fabrication repeatability, to ensure the HSQ structures will comfortably withstand the conditions. For this reason the stamp was annealed in a furnace for 3 hours at a temperature of 600°C. Scanning electron micrographs of the stamp can be seen in figure 2.

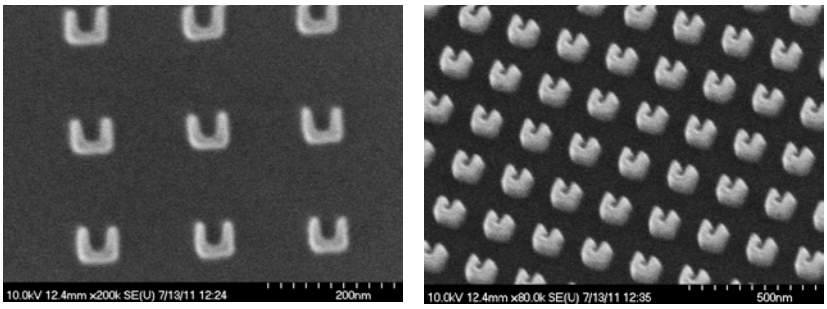

Figure 2: Electron micrographs of the SRR shaped structures formed in 65nm thick HSQ. The patterned area is 1.5mm square and is encased by a 100μm border so that it can be located by the naked eye.

The target sample used for imprinting into was a silicon substrate coated with a 60nm thin layer of PMMA – approximately equal to the height of the features on the stamp. It was found that treating the stamp in a F13 OTCS and heptane solution to create a hydrophobic, non-stick layer was necessary in preventing the PMMA adhering to the stamp during imprinting. The nanoimprinting itself was performed by heating both substrates to 180°C before impressing the stamp into the PMMA layer at a pressure of 15 bar for 5 minutes. The samples were then cooled to 70°C before separating the stamp from the target. The PMMA on the newly patterned sample was then etched by 20nm using reactive ion etching (RIE) to remove the residual PMMA compressed in the trenches of the profiled resist. The desired metal, 14nm aluminium or 12nm gold with a 2nm adhesion layer of titanium, was then deposited before lift-off of excess metal in warm acetone.

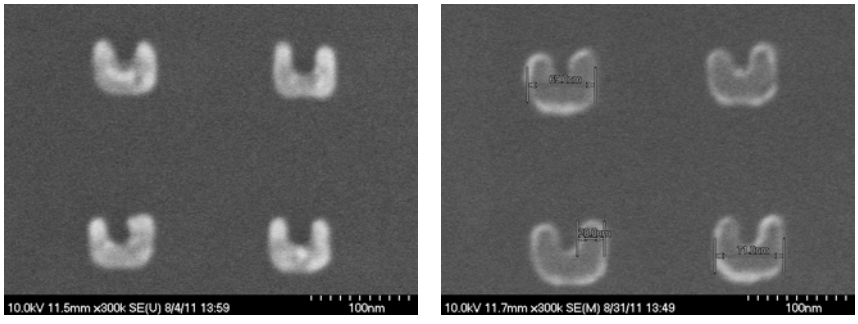

Figure 3: a) SRRs fabricated in gold, with a minimum feature size of 20nm and a width of 65nm, accurately resemble the HSQ structures used to pattern them. b) SRRs made using aluminium deposition show a slight growth in dimension from the features present on the stamp. In this case the minimum feature size is 25nm and the total width is 70nm.

2.2. Reflectance measurements

Optical measurements were taken using a component built visible range spectrometer with a white light source, 400nm to 1000nm monochromator grating size and a SiGe detector with lock-in amplifier attached. All measurements were obtained with a polarised beam at normal incidence to the sample and were referenced

against a highly reflective gold mirror. Polarisation control was achieved by rotating the substrate 90° to achieve both TE and TM mode measurements.

RESULTS

As can be seen in figure 4, there is a distinct LC resonance peak under TE mode at 450nm, deep into the visible range. It should of course be noted that as well as the physical dimensions of the SRRs, the refractive index of the substrate they are fabricated on has a significant impact on the LC resonant frequency[4]. As these structures have been developed on a silicon substrate, it is reasonable to expect an LC resonance shift to higher frequencies using a silica substrate whilst maintaining the dimensions detailed.

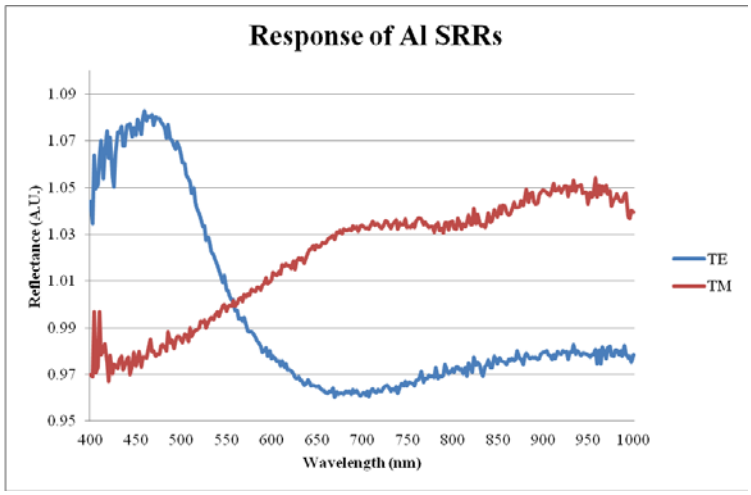

Figure 4: Reflectance spectra from 70nm wide Aluminium SRRs. A distinct LC resonance peak can be seen under TE mode at 450nm.

Previous research has detailed the fabrication of aluminium SRRs with an approximate width of 120nm using conventional e-beam lithography[2]. In this instance an LC resonance peak was measured at a wavelength of 530nm. However by using the nanoimprinting methods described, we have managed to scale the SRR further and achieve a high structure quality and shape, aiding the LC resonance peak shift to 450nm.

3. CONCLUSIONS

By employing nanoimprint lithography we have demonstrated a useful and reliable method in the fabrication of sub-100nm, high resolution split ring resonators. By successfully scaling SRR patterns to such small dimensions whilst not degrading the definition of the structures, we have measured an LC resonance peak at the near ultraviolet range, specifically 450nm. This has been achieved using aluminium to form the SRRs and polished silicon as a substrate.

ACKNOWLEDGEMENTS

The authors wish to acknowledge support from the European Commission through COST action MP0702 and thank the staff at the James Watt Nanofabrication Centre at the University of Glasgow.

REFERENCES

[1] S. Linden, C. Enkrich, M. Wegener, J. Zhou, T. Koschny, C.M. Soukoulis, “Magnetic Response of Metamaterials at 100THz”, Science, 306(5700), 1351-1361, 2004.

[2] B. Lahiri, S. McMeekin, A. Khokhar, R. De La Rue, N.P. Johnson, “Magnetic response of split ring resonators (SRRs) at visible frequencies”, Optics Express, 18, 3, 2010.

[3] J. Zhou, T. Koschny, M. Kafesaki, E.N. Economou, J.B. Pendry, C.M. Soukoulis, “Saturation of the Magnetic Response of Split-Ring Resonators at Optical Frequencies”, Physical Review Letters, 95, 223902(1-4), 2005.

[4] Z. Sheng, V.V. Varadan, “Tuning the effective properties of metamaterials by changing the substrate properties”, Journal of Applied Physics, 101(1), 4-7, 2007.

NOTES

Preparation and Characterization of Functional Materials for Energetic Applications

Chandrashekhar M. Malba[1], Luca Bellotto[1], I. Freris[1], F. Enrichi[2], P. Riello[1], A. Benedetti[1]

[1] *Dipartimento di Scienze Molecolari e Nanosistemi, Università Ca' Foscari Venezia, Via Torino 1455/b, 30172 Venezia-Mestre*

Tel: +39-041-234-6718; e-mail: chandrashekhar.malba@unive.it

[2] *CIVEN, Coordinamento Interuniversitario Veneto per le Nanotecnologie, Via delle Industrie 5, 30175 Marghera (Venezia), Italy*

ABSTRACT

Two different strategies for the encapsulation of organolanthanide complexes inside the pore channels of silica nanoparticles have been successfully demonstrated. The resulting highly luminescent nanoparticles were fully characterized by photoluminescence spectroscopy, XRD, TEM, FTIR, N_2 adsorption desorption measurements. In the first strategy, two different in-situ chemical precipitation techniques have been explored for the microencapsulation of Eu^{+3} complex $[Eu(Tp)_3]$ inside the pore channels of mesoporous silica nanoparticles by varying the sequence for precursor impregnation. The importance of addition sequence was demonstrated by the successful formation of the europium (III) tris-pyrazolyl borate complex. In the second strategy, $Eu(DBM)_3phen$ was incorporated into the pores of differently functionalized silica nanoparticles using wet impregnation technique and the effect of different functional groups on photoluminescence of $Eu(DBM)_3phen$ was studied. Among the studied samples, Amino ($–NH_2$) functionalized silica nanoparticles showed higher emission intensity and longer lifetime for the $Eu(DBM)_3phen$ complex. These highly luminescent silica nanoparticles can find applications in the field including biology, molecular photonics, optics, and electronics.

Keywords: europium, photoluminescence, silica nanoparticles.

NOTES

Structure of C-Pd thin films

Elżbieta Czerwosz[2], Małgorzata Suchańska[1], Anna Kamińska[2], Justyna Kęczkowska[1], Mirosław Kozłowski[2]

[1] Kielce University of Technology, al. 1000 –lecia P.P. 7, 25-314 Kielce, Poland.
Tel: +48 41 34 24 167; e-mail: m.suchanska@tu.kielce.pl
[2] Tele & Radio Research Institute, 03-450 Warsaw, Ratuszowa str.,11, Poland

ABSTRACT
In this paper, the results of structural investigations of nanocomposite C-Pd thin films structure are presented. These C-Pd films were obtained by a two-step PVD/CVD method. An influence of substrate's type and different parameters of PVD and CVD processes on morphology and structure of the nanocomposite C-Pd thin films were studied by Raman Spectroscopy, FTIR spectroscopy and Scanning Electron Microscopy.

K**eywords**: Carbon-palladium films, PVD, CVD, Raman Spectroscopy, Scanning Electron Microscopy, UV-VIS, FTIR

INTRODUCTION

Nanocomposite C-Pd films are promising materials for optoelectronics due to their unique electrical and optical properties [1,2]. The knowledge about the structure, topography and morphology of such films is necessary for further applications [3]. The structure and composition of these films is connected to the structure of nanoobjects forming them. Generally, it could be noticed that films are based on carbonaceous matrix (nanoporous, nanograins of fullerenes or graphite/graphene like nanostructures) in which palladium nanograins are included. Both, size and structure of carbon matrix as well as size and structure of palladium nanograins strongly depend on technological processes parameters. The form of nanoobjects affects on final properties of the film.
In this paper, we present some results of characterization of film composed of nanoporous carbonaceous matrix containing palladium nanograins. These results help us to understand phenomena connected to observed optical properties of films.

1. EXPERIMENTAL

C-Pd films were obtained by the two steps' PVD/CVD method elaborated in Tele- and Radio Research Institute [4]. In the first step, nanocomposite films formed of carbonaceous matrix with 2-5nm in size palladium nanograins were obtained by PVD (Physical Vapour Deposition) process under a dynamic vacuum of 10^{-5} mbar. As precursors of these films fullerene C_{60} and palladium acetate $Pd(C_2H_3O_2)_2$ were used. These precursors were evaporated from two separated sources [5]. The temperature of substrates in PVD process was 50-70 °C, growing time was 8 minutes and the distance between substrates and sources was 69 mm. For all processes (with applied different substrates) these parameters were the same.

During the second step, nanocomposite films from PVD were modified in CVD process. The pyrolysis of xylene (C_8H_{10}) proceeded in this process. CVD process was performed in a quartz reactor under an argon atmosphere and in the temperature of 650 °C. The total modification time was 30 minutes. The argon flow rate was maintained at 40 l/h while xylene flow rate was 0,1 ml/min. In order to eliminate the xylene residue after stopping of its supply into the quartz reactor, films were annealed in Ar for one hour. In CVD processes all parameters were the same for all used substrates.

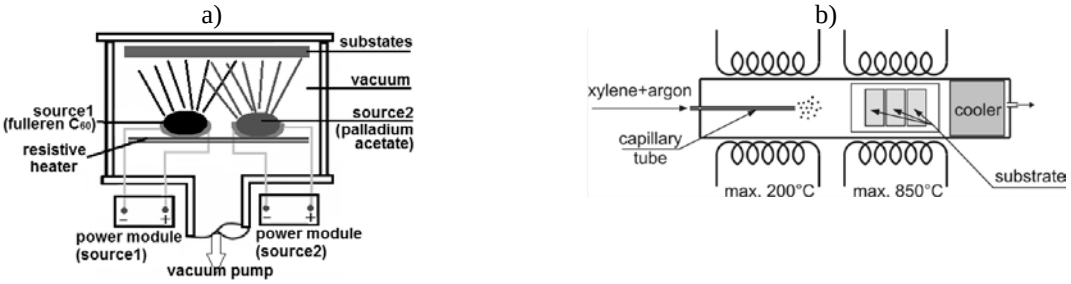

Fig. 1. Schema of experimental setup: a) PVD process, b) CVD process

Films were deposited on different substrates: Si wafers, Mo foil, ceramic plates Al_2O_3 and fused silica. The morphology and structure of C-Pd films were studied by Scanning Electron Microscopy (SEM) with JEOL-

JSM 7600F microscope with SE (Secondary Electron) detector and with LABE (Low Angle Backscattered Electron) detector showing a contrast composition (carbon and palladium). The microscope was operated at 1keV and 5 keV incident energy.

Raman spectra measurements were carried out using Jobin Yvon-Spex T64000 Raman spectrometer with triple-grid monochromator, equipped with confocal microscope and CCD detector (with the resolution of 1024 x 256 pixels) cooled with liquid nitrogen. For the measurements the single monochromatisation was applied, with Rayleigh dispersion used effectively by Notch-type filters. The measurements were carried out in ambient temperature for the excitation wavelength of 514.5 nm.

2. RESULTS AND DISCUSSION

2.1. SEM study

Typical SEM image of C-Pd film prepared on Si in PVD process is presented in Fig2.a. Morphology and structure of PVD film depends on substrate. Films obtained on fused silica have similar grains and its roughness is similar.

a) b)

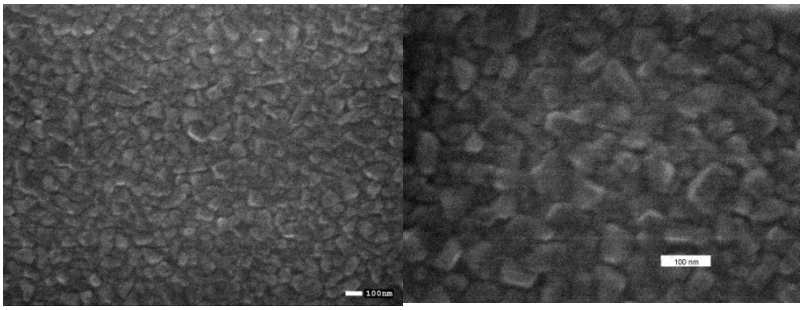

Fig. 2. SEM image (magnified 50 000x) of films from PVD process obtained on a) Si plate, b) fused silica

SEM images of film prepared in CVD process are presented in Fig. 3. In Fig.3a film prepared on fused silica is presented and in Fig.3b,c film prepared in Si . Fig.3b, c present film imaging in secondary electrons (SE) technique and back scattered electrons (BSE) technique. Big, isolated, bright nano-objects are identified as palladium nanograins. In case of fused silica substrate, these palladium objects are placed in carbonaceous (probably amorphous) matrix and in case of Si substrate in nanoporous carbonaceous matrix.

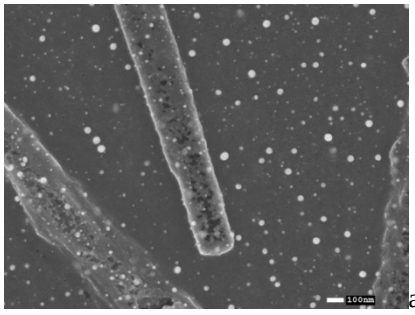

a)

b) c)

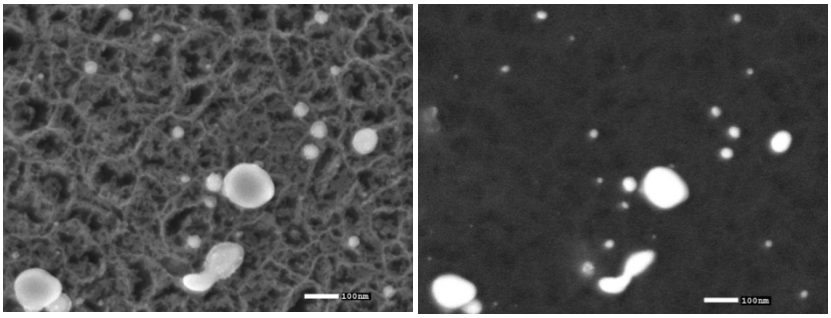

Fig. 3. SEM image (magnified 100 000x) for CVD film on a) fused silica substrate; on Si substrate in SE b) and BSE c) mode

2.2. Raman study

In Fig.4 the Raman spectra of films deposited on Si are presented. Fig.4a presents PVD film and Fig.4b presents CVD film. These spectra show that carbonaceous matrix is different for PVD and CVD film. In Raman spectrum of PVD film except of D and G bands attributed to graphite – like structures vibration a bands that could be connected to C_{60} molecule vibration is found. Raman spectrum of CVD film has only two bands – D and G. It could mean that nanoporous matrix has graphite ordering.

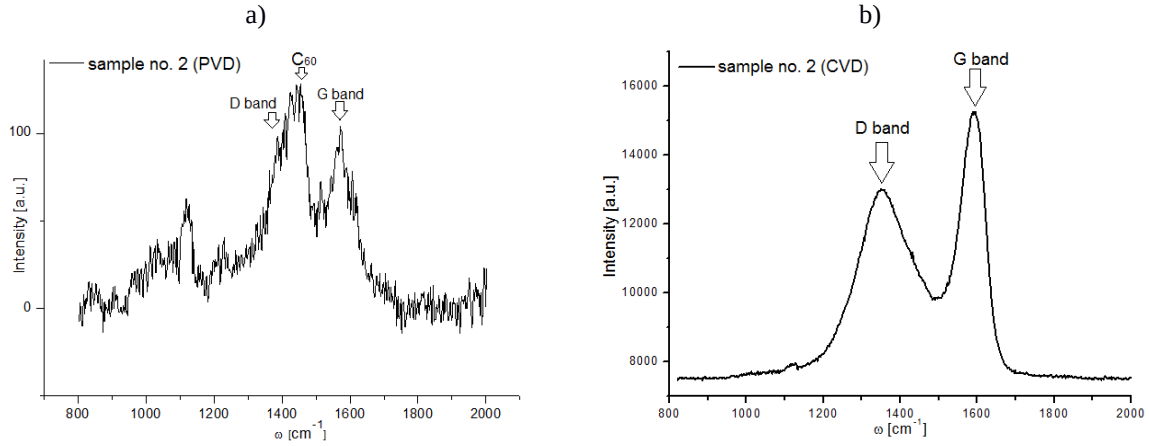

Fig. 4. .Raman spectra for sample 2 (Si substrate) obtained in a) PVD, b) CVD processes

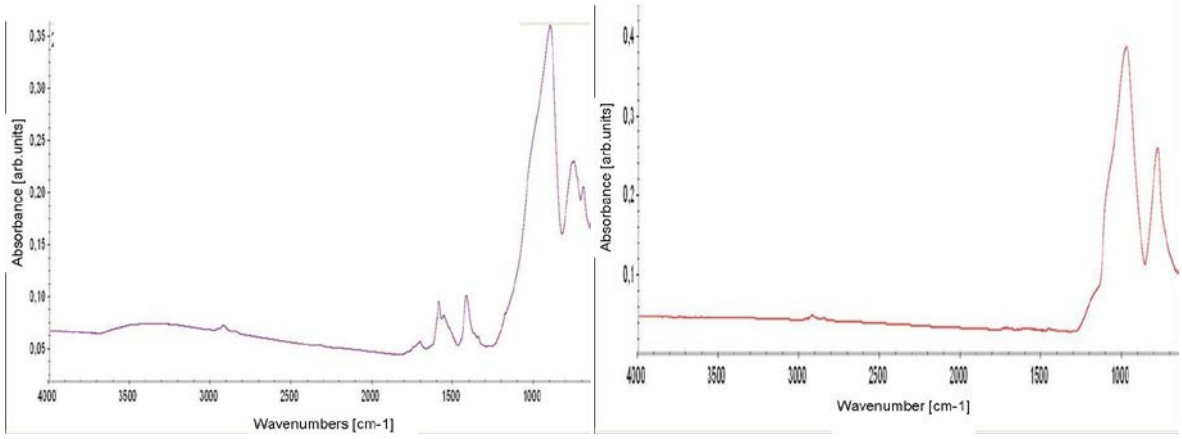

Fig.5 FTIR spectra of a) PVD film and b) CVD film deposited on fused silica substrate

In FTIR absorbance spectra of films obtained in PVD process we found band connected to substrate (fused silica) and characteristic bands connected to palladium acetate and fullerene C_{60} molecules vibrations. Such spectrum registered for PVD film modified in CVD process shows only bands that could be attributed to fused silica. We cannot explain these phenomena now, but authors of paper [6] while investigating graphite nanosheets observed similar effect.

3. CONCLUSIONS

The influence of parameters of technological processes and substrate's type on structures and properties of C-Pd films obtained in PVD/CVD method was studied. We also found that topography, structure and chemical composition of these films affect on their optical properties. Some observed phenomena cannot be explain on base of collected data and their interpretation and it needs additional studies.

ACKNOWLEDGEMENTS

This research was performed in the framework of the EU COST Action MP0702 and financed by Polish Ministry of Science and Higher Education (577/N-COST/2009/0 research project).

REFERENCES

[1] Czerwosz, E., Dłużewski, P., Kęczkowska, J., Kozłowski, M., Suchańska, M. and Wronka,H., "*Palladium nanocrystals and their properties*", Materials Science-Poland 26 (1), 119-125 (2008)

[2] Czerwosz E.] Czerwosz, *"Badania zmian własności przewodnictwa elektrycznego warstw palladowo-*

węglowych pod wpływem gazów zawierających związki wodoru", Przegląd Elektrotechniczny vol. 10, 61-64, 2010.

[3] Kozłowski, M., Diduszko, R., Olszewska, K., Wronka, H. and Czerwosz, E., "Nanostructural palladium films for sensor applications", Vacuum vol. 82, pp.956-961 (2008).

[4] Czerwosz E, Kowalska E, Wronka H, Radomska J, Patent Notification 2008 nr P384 591

[5] E.Czerwosz, R.Diduszko, P.Dłużewski, J.Kęczkowska, M.Kozłowski, J.Rymarczyk, M.Suchańska – *Properties of Pd nanocrystals prepared by PVD method* – Vacuum, vol.82, pp.372-376 (2008),

[6] Guohua Chen , Wengui Weng, Dajun Wu, Cuiling Wu, Jinrong Lu, Pingping Wang, Xiangfeng Chen, *Preparation and characterization of graphite nanosheets from ultrasonic powdering technique*, Carbon vol.42, pp.753–759 (2004)

Comparison of experimental and calculated spectral characteristics of Photonic-Crystal Vertical-Cavity Surface-Emitting Lasers

Tomasz Czyszanowski[1], Kent D. Choquette[2], Krassimir Panajotov[3]
[1] *Photonics Laboratory, IF, Technical University of Lodz, ul. Wólczańska 219, 90-924 Łódź.*
Tel: +48 42 631 36 65; e-mail: tomasz.czyszanowski@p.lodz.pl
[2] *Electrical & Computer Engineering Department, University of Illinois at Urbana Champaign (UIUC), Urbana 61801, IL, USA.*
[3] *Department of Applied Physics and Photonics, Vrije Universiteit Brussel, Pleinlaan 2, Brussels, Belgium*

ABSTRACT
In this paper, we present the comparison of the experimentally determined spectral characteristics of 980 nm Photonic-Crystal Vertical-Cavity Surface-Emitting Laser structures with full three dimensional, fully vectorial computational model based on Plane Wave Admittance Method. We have found the satisfactory agreement between experiment and calculations which is a reliable basis for further numerical optimisation of Photonic-Crystal Vertical-Cavity Surface-Emitting Laser.

Keywords:Vertical-Cavity Surface-Emitting Lasers, Photonic Crystals, numerical models.

1. INTRODUCTION

Vertical Cavity Surface Emitting Lasers (VCSEL) are very attractive light sources for short range telecommunication networks and portable gas detectors. Their main advantages which are: narrow emission spectral width and high rate modulation can be achieved by the single mode operation of the lasers. The competitive Distributed Feedback Lasers (DFB), which provide similar characteristics are far more expensive hence cannot be applied in cheap network systems and detection devices.
The single mode operation is assured by short cavity of VCSEL which induces single longitudinal mode emission. However true single mode emission with respect to the later modes can be realized by small optical apertures. The most often used technique, which laterally confines the light is selective wet oxidation mostly used in the arsenide technology. Such process must be tightly controlled to achieve ultimate performance of the device. The optical window formed by the oxidation is sensitive for temperature influence which is generated by the working device. The oxidation can propagate, especially if optical window is narrow (less than 4 μm), which contributes to the narrowing and - in severe cases – closing the optical window. That motivates the study on more reliable solutions, which can increase the lifetime of the devices. One of the approach is selective etching of the top Distributed Bragg Reflector (DBR) [1]. Deep enough etching of the mirror introduces the regions with very low refraction index (air) contributing to the strong confinement of the modes. On the other hand too shallow etching deteriorates the reflectivity of the mirror and causes the leakage losses of the laser modes [2]. Hence the selective etching with respect to the selective oxidation is not only more reliable but also provides one additional feature, which is the control of the losses. The proper designing of the etching depth can assure strong confinement of transversal fundamental mode and discrimination of all others [3]. Generally, the form of the etching can be arbitrary, it should only constitute the window for emitted light. However Photonic Crystal (PhC) which is a periodic structures takes advantage of Bragg reflections and can additionally magnify the lateral confinement. In such structures the photonic band gap is possible. However in the arsenide technology full 3 dimensional (3D) band-gap is difficult to realize because of too low contrast of the refractive index [4]. The most effective lateral reflection would be achieved by the means of coaxial rings etched in the DBR. But such a structure has number of drawbacks as mechanical instability and blocking of current flow, to mention only two of them. Hence the hexagonal net of air holes is the optimal design of confinement which provides Bragg reflections and does not block the current flow.

2. RESULTS

The main goal of the paper is the comparison of full 3D vectorial Plane Wave Admittance Method computational model of PhC VCSEL with experimental measurements based on the 980 nm PhC VCSEL structures The structures were processed on one wafer and were defined by different parameters of Photonic Crystals with respect to the diameter of holes, distance between them and etching depth. The current flow was funneled by the 12 μm oxide aperture. The PhC structures are defined by wide range of the geometrical parameters: 3.5μm < L < 7 μm, 0.4 < a/L < 0.7, 8 pairs < d_e < 25 pairs, where L – the distance between PhC holes, a – diameter of the

holes and de the etching depth given in the number of the etched DBR pairs. The difference of the cavity thickness for the analyzed structures was determined to be equal to 10 nm. Moreover the etching depth was determined with the accuracy of 2 DBR layers. The inaccuracy of the cavity length caused that measured PhC VCSEL's emission spectra were randomly shifted, but the spectral distance between the lateral modes was unaffected since this is a parameter which is solely depended on the lateral confinement scheme (Fig. 1). One could expect that deeper PhC etching contributes to the blue shift of the emitted wavelength [5] in the identical epitaxial structures.

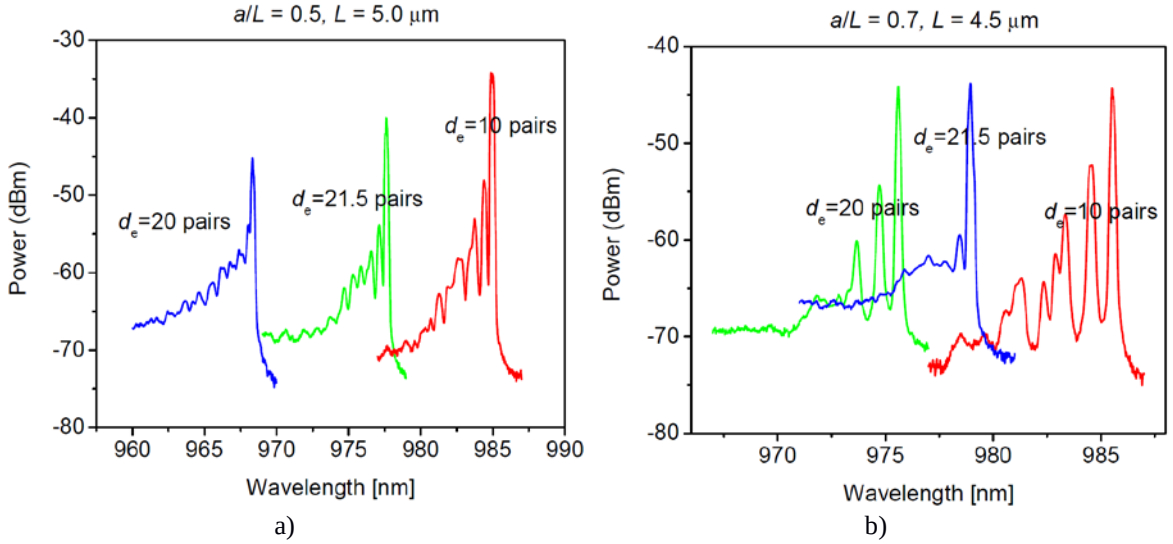

a) b)

Fig. 1 Emission spectra of PhC VCSELs for different geometry of PhC. The etching depth is given in the number of etched DBR pairs. The lateral geometry of the PhC is determined by a – the diameter of PhC hole and L – distance between the holes

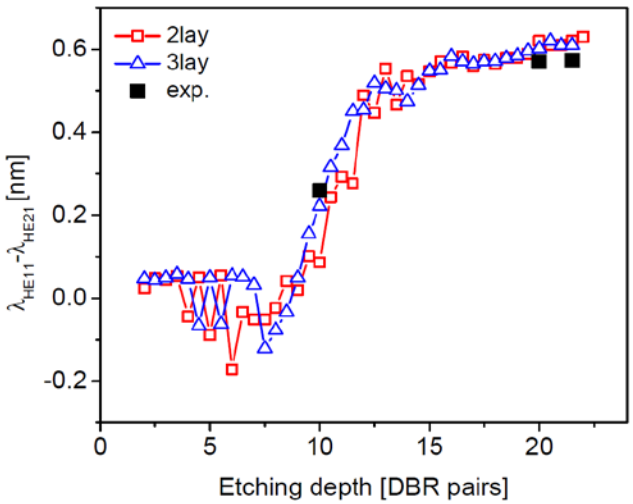

Fig. 2 Calculated (blue and red curves) and experimentally measured (black points) wavelength difference between HE_{11} and HE_{21} modes for a/L = 0.5 and L = 5 μm. Red curve corresponds to the bottom of the hole rounding through 2 layers (2lay) and blue one to the 3 layers rounding (3lay).

The inaccuracy of the etching depth experimentally exists, that is caused by the shape of the bottom of the holes, which are rounded instead of flat. Such shape is a consequence of the chemical etching and can be minimized in the case of broad holes. However typical holes of diameter in the range 1 – 3 μm are defined by rounded bottoms. Such hole geometry can contribute to increasing of the scattering losses. The consequences of above inaccuracy for the computational model was that denser discretization had to be applied to reconstruct the rounded bottoms of the holes. In our model we assumed two cases: the roundings of the bottoms of the holes are 2 layers and 3 layers deep.

The performed calculations are focused on the analysis of emitted wavelength of the modes confined by the photonic crystal as well as confined by broad oxide aperture. The exemplary calculated spectral distance between

the modes is confronted with experimental data in Fig. 2. The calculated results reveal significant variations between neighbouring points. It is related to not dense enough probing of the function of wavelength versus etching depth. Denser probing have been performed for quantum-dot VCSEL emitting 1.3 μm wavelength (Fig. 3). It showed that oscillatory behavior of emitted wavelength as a function of the etching depth is driven by the change of effective reflection of the light from the bottoms of the PhC. The behaviour is caused by the interaction of PhC and light and can be observed in all the VCSEL designs.

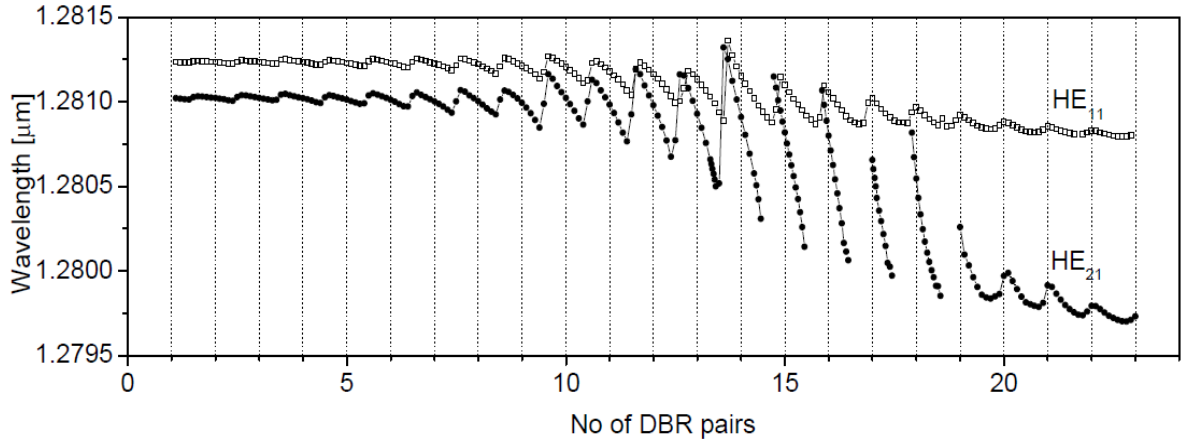

Fig. 3 Emitted wavelength as a function of the etching depth for the fundamental (HE_{11}) and first order (HE_{21}) modes.

3. CONCLUSIONS

We performed exhaustive comparison of the experimental spectral characteristics of 980 nm photonic-crystal VCSELs with simulation results of three dimensional, full vectorial optical model. We have found the satisfactory agreement between the results. The presented results are reliable basis for further optimisation of photonic-crystal VCSEL.

ACKNOWLEDGEMENTS

This work is the result of Short Term Scientific Mission supported by the COST Action MP0702: "Towards Functional Sub-Wavelength Photonic Structures"

REFERENCES

[1] D. F. Siriani, M. P. Tan, A. M. Kasten, A. C. Lehman Harren, P. O. Leisher, J. D. Sulkin, J. J. Raftery, Jr., A. J. Danner, A. V. Giannopoulos, K. D. Choquette "Mode Control in Photonic Crystal Vertical-Cavity Surface-Emitting Lasers and Coherent Arrays" *IEEE J. Sel. Top. Quantum Electron.* vol. 15 pp 909-917, 2009

[2] T. Czyszanowski, R. P. Sarza³a, M. Dems, W. Nakwaski, K. Panajotov "Optimal photonic-crystal parameters assuring single-mode operation of 1300 nm AlInGaAs vertical-cavity surface-emitting laser" *J. Appl. Phys.* vol. 105, p 093102, 2009

[3] T. Czyszanowski, R. P. Sarza³a, M. Dems, H. Thienpont, W. Nakwaski, K. Panajotov "Strong modes discrimination and low threshold in cw regime of 1300 nm AlInGaAs/InP VCSEL induced by photonic crystal" *Phys. Status Solidi A* vol. 206, pp 1396-1403, 2009

[4] K. Panajotov, M. Dems "Photonic crystal vertical-cavity surface-emitting lasers with true photonic bandgap" *Opt. Lett*. Vol. 35, pp 829-831, 2010

[5] T Czyszanowski, M Dems, H Thienpont, K Panajotov "Impact of the hole depth on the modal behavior of long wavelength photonic crystal VCSELs" *J. Phys. D: Appl. Phys*. vol. 41, p 085102, 2008

NOTES

UV-imprinted active waveguides in silica-germania RF-sputtered thin films

I. Scarpelli[1*], S. Berneschi[1], R. Calzolai[1], A. Chiasera[2], M. Ferrari[2], G. Nunzi Conti[1], S. Pelli[1], G. C. Righini[1], C. Trono[1]**

[1] IFAC – CNR, Via Madonna del Piano 10, 50019 Sesto Fiorentino, Italy
[2]IFN – CNR, Via alla Cascata 56/C, Povo, 38123 Trento, Italy
** Università di Firenze, Facoltà SMFN, Viale Morgagni, 40/44, 50134 Firenze*
***Centro Studi e Ricerche Enrico Fermi, Piazza del Viminale 2, 00184 Roma (Italy)*

ABSTRACT

UV photo-imprinting of channel waveguides and other structures, like gratings, in photorefractive glasses constitutes a simple and effective fabrication technique. Here we report on excimer laser irradiation of radio frequency (RF) sputtered silica-germania thin films, with germania concentrations inthe range 0.18 to 0.31 mol%, doped with erbium or co-doped with erbium and ytterbium.We found that the sputtering process may be critical, as testified by the fact that some samples do not exhibit the characteristic absorption band at around 248 nm (5 eV), generally assigned to germanium oxygen deficient centers (GeODC) or similar defects. Despite of it, similar variations of the refractive index in UV-irradiated areas are measured in both types of samples (namely with or without GeODCs). Channel waveguides,single mode at 1550 nm, were fabricated in samples with GeODCsand characterized. Propagation losses are less that 1 dB/cm at 1300 nm.

Keywords: silica-germania, photorefractivity, photoimprinting, optical waveguides

1. INTRODUCTION

The search for simple, reliable and cost-effective fabrication methods of optical waveguides, which are strongly required for the development of integrated optical circuits competitive with conventional micro-optical devices and/or microelectronic circuits, led to the investigation of a number of different experimental approaches. The method based on photo-induced refractive index changes, generated by an ultraviolet laser source, is simpler and potentially cheaper than conventional photolithographic methods, since it avoids time consuming and expensive fabrication steps such as lithography and chemical or physical etching. Two routes can be followed, namely direct writing (which is achieved by focusing and then translating a laser writing beam) anddirect imprinting: the latter one, that we have used, may imprint any refractive index structure, well defined at the microscopic scale, by a single step replica of an intensity mask. In practice, the main limitations are related to the entity and the stability of the light-induced refractive index changes.

Since the first demonstrations of UV photo-induced channel waveguides[1,2], germanosilicate glasses have played an important role in integrated optics, also thanks to the proof of stability of photoimprinted structures[3]. Single mode (at 1.5 μm) channel waveguides have been demonstrated in plasma enhanced chemical vapour deposited (PCVD)[4], flame hydrolysis deposited (FHD)[5], and radio-frequency (RF)-sputtered[6] thin films. Previous workshad shown that RF-sputtered SiO_2-GeO_2 thin films are highly photo-refractive and that the refractive index changes are positive when the GeO_2 content is around 25%[7,8].

Here we report on the results we have obtained by UV irradiating RF-sputtered silica-germania thin films having germania concentrations inthe range 0.18 to 0.31 mol%. Channel waveguides have also been UV-imprinted and characterized.

2. EXPERIMENTAL RESULTS

2.1. Film fabrication

Silica-germania films were deposited on silica or soda-lime glass substrates in an RF-magnetronsputtering system. A small concentration of rare-earth elements (Er alone or Er and Yb) was added in order to provide us the possibility of using photoluminescence as a further characterization tool. For this purpose, pieces of GeO_2, metallic erbiumand ytterbium were placed on a 4" silica target. The residual pressure in the sputtering chamber, before deposition, was about 2×10^{-5} Pa. The sputtering was carried out using Ar gas at a pressure of 0.7 Pa; the applied RF power was 150 W, with a reflected power of 18 W. The films were deposited on silica substrates of size about 75 mm × 25 mm, which were not heated. Films were subsequently annealed in air; a typicalprocesswas carried out at 600 °C for 6 hours. Typical filmthickness, obtained for a deposition time of 4 h 15 min,was 3.35±0.2 μm; correspondingly, the refractive index of the film was in the range 1.495 to 1.512 at 633 nm, depending on the germanium content and the presence of rare earths. A summary of the characteristics of the

deposited films is reported in Table 1.

Table 1. Composition and annealing parameters of the investigated samples

Sample	SiO_2 mol.%	GeO_2 mol.%	Er_2O_3 mol.%	Yb_2O_3 mol.%	Annealing temperature	Annealing time
PW5	**70.69**	**29.30**	**0.24**	**0**	**400 °C**	**6 h**
PW6	**69.00**	**31.00**	**0.24**	**0**	**400 °C**	**6 h + 12 h**
Q19	**84.00**	**15.60**	**0.20**	**0.20**	**600 °C**	**6 h**
Q22	**82.00**	**18.00**	**0.20**	**0.20**	**600 °C**	**6 h**
Q23	**82.00**	**18.00**	**0.20**	**0.20**	**600 °C**	**6 h**
Q24	**82.00**	**18.00**	**0.20**	**0.20**	**600 °C**	**6 h**

2.2. Film characterization

The sputtered films acted as planar optical waveguides; their optical and modal characteristics were measured by using the Metricon model 2010 and the *COMPASSO* instruments, both based on m-line spectroscopy; the latter one was built in-house at IFAC.

The deposited and annealed films generally supported 3 propagation modes at 632 nm and a single mode at 1550 nm. From the measurements of the effective indices of the modes it was possible to derive the refractive index of the films (assumed to be constant along the depth) and its thickness.The propagation losses of the planar waveguides were then measured, either by scanning a fiber optic probe and photodetector down the length of a propagating streak to measure the light intensity scattered from the surface of the guide (Metricon instrument) or taking an image of the streak by a Hamamatsu camera and then analysing the behaviour of the image intensity as a function of the propagation length; the results obtained by the two methods were in good agreement, and resulted to be less than 1 dB/cm at 1300nm for all the samples.

An example of measurements, referring to the Q22 sample, is shown in Table 2. The film thickness is calculated at 632 nm, where three modes are present, and then its value is taken as fixed at the other wavelengths too.

Table 2. Measured characteristics of the Q22 sample. The film index n_{film}@ 632 nm and thickness are numerically calculated from the effective indices n_0, n_1, n_2 of TE and TM modes. At longer wavelengths the thickness is assumed to be fixed and film index is calculated using the effective index of the single mode (TE and TM).

Wavelength (nm)		Refractive Index				Thickness(μm) ±0.1	Attenuation coefficient (dB/cm) ±0.2
		n_o ±0.0001	n_1 ±0.0001	n_2 ±0.0001	n_{film} ±0.002		
632	TE	1.4794	1.4714	1.4592	1.482	3.1	0.7
	TM	1.4794	1.4713	1.4589	1.482	3.1	0.8
1319	TE	1.4616	-	-	1.470		0.4
	TM	1.4613	-	-	1.470		0.5
1542	TE	1.4568	-	-	1.468		0.3
	TM	1.4563	-	-	1.468		0.4

The absorption spectra were measured by using a Perkin Elmer lambda19 spectro photometer and photoluminescence measurements of the $^4I_{13/2} \rightarrow {}^4I_{15/2}$ transition of the Er^{3+} ions were performed using the 514.5 nm line of an Ar^+ ion laser and dispersing the luminescence light region with a 320 mm single-grating monochromator with are solution of 2 nm. The waveguiding mode of the samples was excited by prism coupling and the light was detected using an NIR photomultiplier tube and standard lock-in technique..

A surprising result was obtained when measuring the absorption spectra of PW5 and PW6 samples: both of them did not present the absorption band at 5 eV, generally assigned to germanium oxygen deficient centers (GeODC) or similar defects. Further analysis, including XPS, are under way in order to understand the reason of absence of these defects.

2.3. UV-exposure of the films and discussion

The films were exposed to a KrF excimer laser source (Lambda Physics Compex 110) operating at 248nm, with different cumulative doses in order to test their photorefractivity. For all samples the exposure parameters were as follows: pulse frequency 10 Hz, pulse fluence 36 mJ/cm^2. By choosing the number of pulses, each sample was irradiated with cumulative doses up to 12 kJ/cm^2; after each exposure, both the absorption curve and the refractive index were measured again. As an example, Figures 1 and 2 show the changes in absorption coefficient and refractive index, respectively, for the sample Q22, for cumulative doses up to 10 kJ/cm^2. Figure 1 confirms what was expected, namely that irradiation bleaches the absorption band at 248 nm (partially for dose of 1 kJ/cm^2 and completely for dose 10 kJ/cm^2).

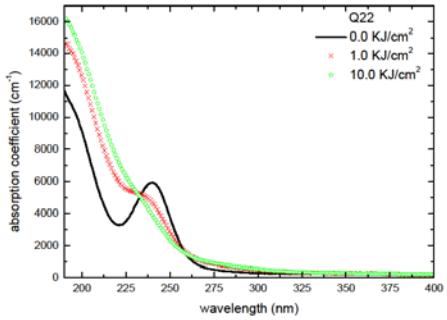

Figure 1. Absorption coefficient of the Q22 sample as a function of the cumulative dose.

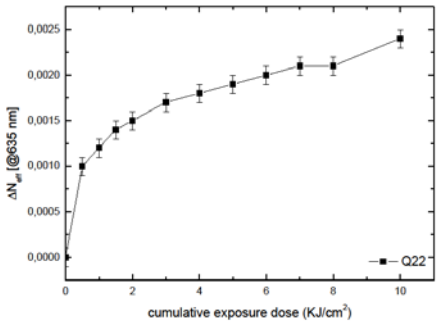

Figure 2. Variation of the film refractive index as a function of the dose in Q22 .

It can be underlined that a change of the refractive index of the same order (~2×10^{-3}) was achieved in the samples PW5 and PW6, too, despite the absence of the GODC absorption band to be bleached by the UV irradiation. Figure 3, for instance, shows the variation of the absorption coefficient, in samples Q 22 and PW6 (two zones of the film, labelled A and B), after irradiation with 8 kW/cm^2, with respect to the non-irradiated film. It is evident that UV exposure of PW6 has a quite different effect than in Q22; it turns out, moreover, that the PW6 sample presents compositional inhomogeneities, as testified by the different response in different areas (zone A and B) of the film. This difference is much more evident in Fig.4, where one can see that the index change in the zone A after irradiation is similar to the one produced in Q22, while the photoinduced Δn in the zone B is completely different, having negative sign.

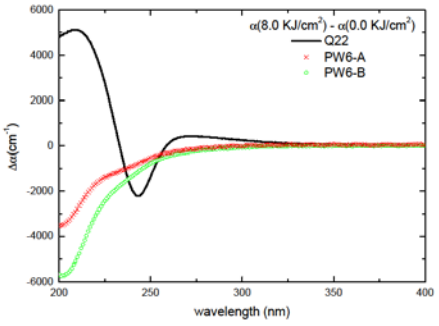

Figure 3. Variation of the absorption coefficient after irradiation at 8 kJ/cm^2 in Q22 and PW6 (zone A and zone B) samples.

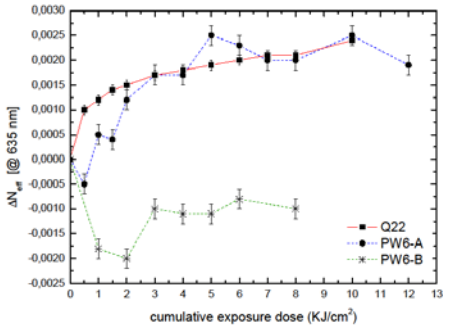

Figure 4. Variation of the film refractive index as a function of the dose in the Q22 and PW6 (two zones) samples..

Due to this incertitude, channel waveguides were produced in samples Qxx only. For that purpose, an intensity mask, constituted by a patterned Ti film, 200 nm thick, over a pure silica substrate was placed in contact with the silica-germania film, so that the film was irradiated through the mask using the same pulse parameters indicated above and a cumulative dose equal to 10 kJ/cm^2.We checked that the mask was not damaged by the UV irradiation and that the experiment was fully repeatable. The substrates were then properly cut (the channels being produced in direction parallel to the short side of the substrate), and their edges optically polished.

Channel waveguides, having width between 3 and 9 μm and length around 20 mm, appear to be well defined and of fine quality under a phase contrast microscope. Their propagation losses were measured at 1300nm, in order to avoid the absorption produced by the $^4I_{15/2} \rightarrow {}^4I_{13/2}$ transition of the Erbium ions, which are present in all the samples.It came out that these losses were almost the same as those we had previously measured on unexposed planar waveguides, even for relatively narrow (4 μm) channels, so confirming that the UV-imprintingdoes not appreciably increase the scattering losses of the material.

3. CONCLUSIONS

We have investigated the photorefractive properties of some RF-sputtered binary silica-germania films, having different concentrations of GeO_2 and very slightly doped with Er_2O_3 or with Er_2O_3 - Yb_2O_3. It has been found that in some samples the absorption band at 248 nm, usually associated to GeODC defects, is not present; despite of it, due to the absorption change anyway induced by the UV-irradiation, a change of the refractive index of the order of 2×10^{-3} was obtained in all the samples. This index change has been sufficient to photo-imprint channel waveguides having width in the range 4 to 9 μm, and integrated optical structures like 1×4 splitters.

We are still investigating the reason why some samples did not exhibit the 248 nm absorption band, which is probably related to some problem occurred during the sputtering process; this is confirmed by the compositional inhomogenities of those samples, indicated by the opposite behaviour ($\Delta n > 0$ or $\Delta n < 0$) measured in different zones of a same film.

ACKNOWLEDGEMENTS

This work has been carried out also in the frame of the COST-MP0702 Action.

REFERENCES

[1] V. Mizrahi, P. J. Lemaire, T. Erdogan, W. A. Reed, D. J. DiGiovanni, R. M. Atkins, “Ultraviolet laser fabrication of ultrastrong optical fiber gratings and of germania-doped channel waveguides,” Appl. Phys. Lett. **63**,1727-1729 (1993).

[2] M. Svalgaard, C.V. Poulsen, A. Bjarklev, O. Poulsen, “Direct UV writing of buried singlemode channel waveguides in Ge-doped silica films,” Electr. Lett. **30**, 1401-1403 (1994).

[3] R. Kashyap, “Strength, annealing, and lifetime of gratings” in *Fibre Bragg Gratings*, (Academic Press, San Diego, USA,1999), pp. 435.

[4] H. Nishiyama, I. Miyamoto, S. Matsumoto, M. Saito, K. Kintaka, J. Nishii, “Direct laser writing of thermally stabilized channel waveguides with Bragg gratings”, Opt. Express **12**, 4589-4595 (2004).

[5] G.D. Emmerson, S.P. Watts, C.B.E Gawith, V. Albanis, M. Ibsen, R.B. Williams, P.G.R. Smith, “Fabrication of directly UV-written channel waveguides with simultaneously defined integral Bragg gratings”, Electr. Lett. **38**(24), 1531-1532(2002).

[6] G. Nunzi Conti, S. Berneschi, M. Brenci, S. Pelli, S. Sebastiani, G. C. Righini, C. Tosello,A. Chiasera and M. Ferrari, “UV photoimprinting of channel waveguides on active SiO_2–GeO_2 sputtered thin films”, Appl. Phys. Lett.89, 121102 (2006).

[7] H. Hosono, J. Nishii, “High photosensitivity and nanometer-scale phase separation in GeO_2SiO_2 glass thin films,” Opt. Lett. **24**, 1352-1354 (1999).

[8] S. Sebastiani, G. Nunzi Conti, S. Pelli, G. C. Righini, A. Chiasera, M. Ferrari, C. Tosello, “Characterization of a highly photorefractive RF-sputtered SiO_2-GeO_2 waveguide”, Opt. Express **13**, 1696-1701 (2005).

Experimental Investigation of Transmission Losses in Special Dual-Core Microstructured Optical Fiber

Pavol Stajanca[1], Ignac Bugar[1,2], Jozef Chovan[2], Ryszard Buczynski[3], Frantisek Uherek[2]
[1]*Department of Experimental Physics, FMPH, Comenius University, 842 48 Bratislava, Slovakia.*
Tel: +421 2 65421385; e-mail: stajanca@fmph.uniba.sk
[2]*International Laser Centre, Ilkovicova 3, 841 04 Bratislava, Slovakia.*
[3]*Institute of Electronic Materials Technology, Wolczynska 133, 01-919 Warsaw, Poland.*

ABSTRACT
The following article presents the results of an experimental study of transmission losses in a new type of dual-core microstructured fiber made of multi-component glass PBS-57A. The investigated fiber was custom designed to exhibit an increased nonlinearity and a sub-centimeter coupling length in a near infrared region. The spectral character of losses was examined for separate excitation of each fiber core in the spectral region of 1460-1580 nm using the cutback method. Attenuation coefficient values obtained for separate core excitation correspond with each other implying a good quality and symmetry of the fiber microstructure. The presented results are in agreement with other publications concerning transmission losses in microstructured optical fibers made of multi-component glasses and provides valuable information for future theoretical and experimental studies of the investigated fiber.

Keywords: microstructured optical fibers, dual-core optical fibers, multi-component glasses, transmission losses, cutback method

1. INTRODUCTION

Invention and development of the concept of microstructured optical fibers (MOFs) is one of the significant impulses stimulating innovation in the area of fiber optics the last decades. Light guiding mechanism implied by periodical character of fiber microstructure [1] and a possibility of tailoring fiber's transmission parameters enabled development of several new types of fibers such as endlessly single-mode MOF, fibers with ultra-flattened dispersion curve [2] or large-mode-area fibers. In order to employ fiber technologies in middle infrared region, where silica glass losses are too high, development of alternative fiber materials such as polymers or multi-component glasses has been introduced [3]. Some of new materials may also simplify fiber manufacturing process and possess a great potential in nonlinear applications due to their high nonlinear coefficients
Stack-and-pull method utilized for MOF manufacturing offers an easy way of fabrication of dual-core fibers which are widely used as couplers in fiber optics technologies. Dual-core MOF have a high potential in development of components enabling all-optical switching [4, 5], but supercontinuum generation in dual-core MOFs also attracted considerable attention [6, 7]. Exploration of fundamental transmission characteristics of this type of fiber is inevitable for understanding and employing their special coupling properties. Transmission losses, or attenuation, are one of the most important characteristics of optical fibers. While transmission losses measurement of standard index-guiding fibers is nowadays routine straightforward task, determination of dual-core MOF attenuation coefficient is still rather complex and challenging problem. The reason is mostly the small dimension of microstructure features and coupling processes in the fiber. This article presents our method of solving this problem and resulting outputs of experimental determination of transmission losses in dual-core MOF made of soft glass in near infrared (NIR) region.

2. METHODS

A sample of special new type of dual-core microstructured optical fiber was examined. The fiber was designed to exhibit increased nonlinearity and sub-centimeter coupling length in near infrared region and was custom fabricated by Institute of electronic materials technology (ITME) fiber group in Warsaw. The fiber has hexagonal microstructure (Fig. 1) with elliptical cores and is made of soft glass PBS-57A with composition SiO_2-PbO- Al_2O_3- Na_2O- K_2O- As_2O_3. The cutback method was used to determine spectrally resolved transmission losses of the examined fiber. About a half meter long sample was cut from the fiber. Since preserving of excitation conditions during the experiment is essential, the input end of the sample was carefully fixed to an optomechanical stage. An objective with 60 X magnification was used to couple NIR radiation into the sample. The input objective together with auxiliary standard single-mode fiber, used for guiding the radiation from a source to the objective, was fastened to the piezoelectric 6-axis flexure platform Thorlabs MansMax ensuring nanopositioning of the input optics in front of the fiber sample.

This research was supported by ERDF OP R&D, Project 'meta-QUTE – Centrum excelentnosti kvantovych technologii'

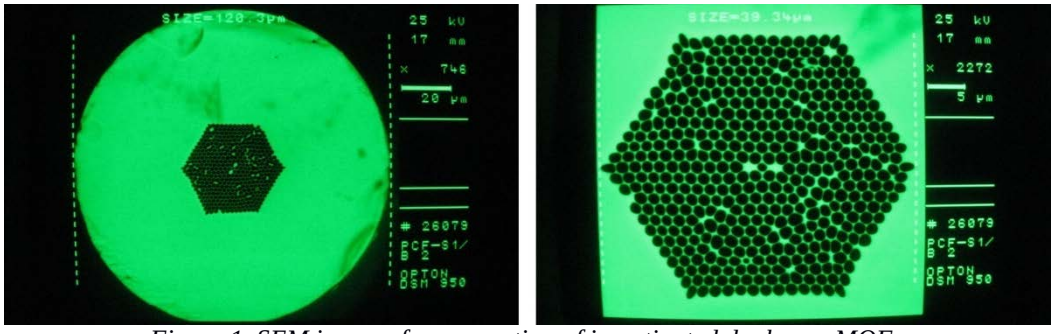

Figure 1. SEM image of cross-section of investigated dual-core MOF.

Initial adjustment of fiber excitation state was performed upon fiber output near-field monitoring utilizing objective with 20 X magnification and CMOS camera (Fig. 2a). Since the spectral responsivity of the camera does not allow us to register radiation with wavelengths longer than 1100 nm, we used praseodymium spontaneous emission amplifier IPG PAD-10 pump diodes operating at 1028 nm as radiation source. To optimize excitation position the input face of the sample was scanned by 3D nanopositioning of input objective at simultaneous monitoring of the near-field image. After determination of the optimal excitation position for both fiber cores, the output end of the sample was placed into the optical head HP 81521B of power meter Agilent 8163A with interface module HP 81533B (Fig. 2b). HP 8164A tunable semiconductor laser with HP 81680A module generating radiation in range of 1460-1580 nm, with precision of 0.01 nm was used as a radiation source for output power measurements. Additional optimization of the 3D excitation position for both cores was performed for 1520 nm central wavelength by tracking and maximizing output power.

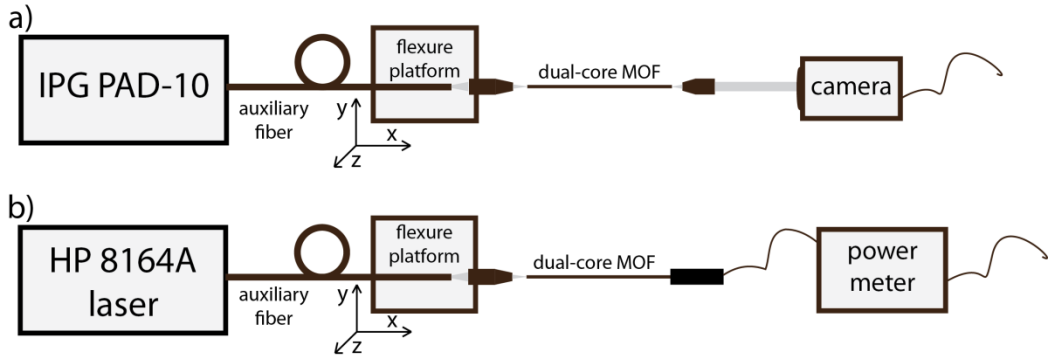

Figure 2. Scheme of experimental setup utilized for a) fiber output near-field monitoring; b) output power measurement.

Output power measurement for every, gradually decreasing, length of the sample was an automated process yielding a set of output power values for selected spectral interval of 1460-1520 nm scanned by 0,25 nm steps. Output power spectral dependencies were measured separately for anticipated optimal excitation position of each fiber core. Despite our efforts, stability of input system remained insufficient causing detuning of the input system during the experiment, hence supplementary adjustment of excitation positions before every measurement was required.

The obtained set of data was processed and analyzed in Microcal Origin 8.0 software. In order to determine spectral character of fiber transmission losses, measured output power spectral dependencies were divided into 12 intervals with uniform spectral width of 10 nm and attenuation coefficient was evaluated separately for all of the intervals.

3. EXPERIMNTAL RESULTS

A 432 mm long sample of the dual-core MOF was gradually shortened by six individual cuts to the length of 165 mm which was the minimum length required to perform measurement utilizing our experimental setup. In Fig. 3 we provide comparison of the images of fiber output near-field intensity distribution for identified optimal excitation position of each core. The optimal excitation positions of the input system determined at the wavelength of 1028 nm by near-field intensity distribution optimization served also as an initial excitation positions for the output power measurements. Despite the validation of the optimal excitation positions by CMOS camera was no longer possible during output power measurements, precision of the nanopositioning system and careful tracking of output power extremes enabled separate identification and measurement for each fiber core.

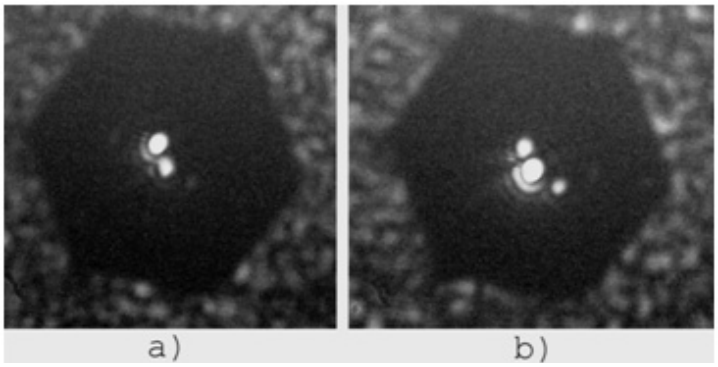

Figure 3. Comparison of the output near-field distribution images for optimal excitation of the a) upper; b) lower core of examined dual-core MOF sample.

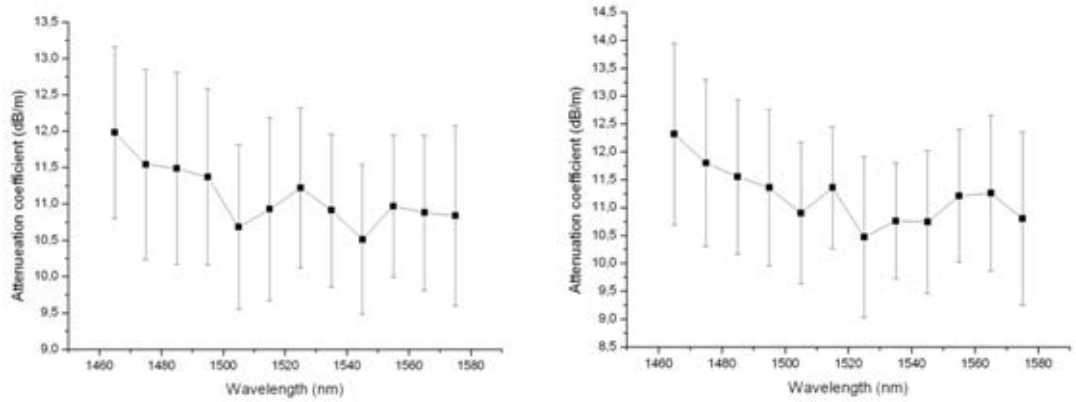

Figure 4. Spectral dependence of attenuation coefficient for separate excitation of a) upper; b) lower core of examined dual-core MOF sample.

Spectral dependencies of attenuation coefficient determined for separate excitation of each fiber core are depicted in Fig. 4. An average uncertainty of attenuation coefficient values for all partial spectral intervals is about 11 % for upper core and about 12 % for lower core. Due to the considerable uncertainty of the partial attenuation coefficients it was not possible to conclusively determine the overall spectral character of the fiber transmission losses in the examined spectral region. Hence we characterize the fiber by integral attenuation coefficient for spectral region of 1460-1580 nm which takes value of 11,1 ± 1,2 dB/m in case of upper core excitation and 11,2 ± 1,4 dB/m in case of lower core excitation. Dependence of integral spectral power on fiber length is shown in Fig. 5. Based on the presented results we can conclude the attenuation coefficients obtained for both fiber cores correspond with each other indicating symmetrical character of investigated dual-core MOF. Obtained results were verified by experiment reproduction on another sample of studied MOF providing average integral attenuation coefficient value of 11,8 ± 1,1 dB/m, which, considering the uncertainty, is in agreement with the first experiment.

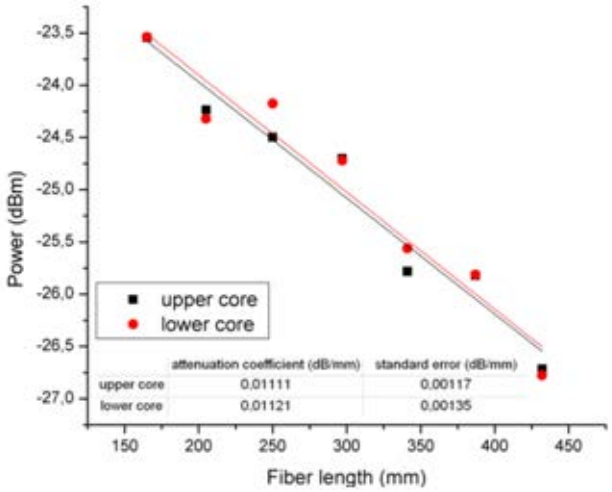

Figure 5. Comparison of integral spectral power and overall integral attenuation coefficient dependencies on fiber length for both cores of studied dual-core MOF.

4. DISCUSSION

Even though, the obtained attenuation coefficient values may seem fairly high compared to those of standard index-guiding fibers, they are in agreement with other publications regarding losses in soft glass MOFs. Transmission loss in soft glass MOFs can be as high as several tens of dB/m [3, 8, 9] depending on the fiber material, core dimension and air-filling coefficient. Major causes of additional losses are fiber microstructure deficiencies and light scattering on crystallization centers of the soft glass material. Taking into account that new experimental type of dual-core MOF with relatively small core dimensions was examined, the obtained results meet our expectations and are in a good agreement with published information on the topic. Comparing values of attenuation coefficient of both fiber cores, we can conclude the investigated fiber is symmetric which is very important for coupling processes in the fiber. Only fiber with ideally symmetric cores exhibit 100% energy coupling. Otherwise, only the portion of the total energy oscillates between both fiber cores, which is undesirable for all-optical switching applications. Fiber asymmetry also complicates analytical description of coupling mechanism. Presented findings are therefore valuable for further analysis of the fiber.

On the other hand considerable uncertainty of determined attenuation coefficient values disabled determination of fiber transmission losses spectral character. We assume that the insufficient stability of the input system causing misalignment of optimized excitation positions is the major source of this uncertainty. We tried to eliminate the effect of detuning by additional adjustment of optimal position before every measurement, but readjusting the exactly same position is impossible. Micro-movements of sample input end during manipulation or cutting of the output end can also have negative impact on the measurement accuracy. Improving stability of experimental setup would be beneficial for increasing overall accuracy of attenuation coefficient determination.

Additionally, for power measurement we used Ge-based large-area photodetector which measures integral power from whole output face of the fiber. Since a radiation that escapes cores during its propagation along a fiber but is still confined within the fiber outward cladding can no longer be considered as a transmitted signal, its registration by a power meter introduces systematic error. Even though the ratio of radiation power transmitted in the outward fiber cladding should be small enough, so the introduced error is not crucial, output beam spatial filtering could help to eliminate this error and to obtain more relevant results. Finally, utilization of tunable laser source that will enable measurements in wider spectral region might lead to possibility of assessing the attenuation coefficient spectral character, as the contrast between determined attenuation coefficients for different wavelengths may at some point exceed measurement uncertainty.

5. CONCLUSIONS

Transmission losses of a new special type of dual-core MOF made of multi-component glass were experimentally determined by cutback method. Fiber transmission losses were measured in 1460-1580 nm spectral region in which the fiber is intended for nonlinear transformations of ultrafast laser pulses. Despite inability to determine transmission losses spectral character, attenuation coefficient was evaluated for separate excitation of each fiber core and results were verified by two independent measurements. Obtained results imply good fiber symmetry which is important for future fiber coupling applications. Presented results are in good agreement with other publications concerning transmission losses in soft glass MOFs and are valuable for future theoretical and experimental studies of the investigated fiber.

REFERENCES

[1] J. D. Joannopoulos, *et al.*: Photonic crystals, Molding the flow of light, 2nd edition, Princeton: Princeton University Press, 2008.

[2] K. Saitoh, et al.: Chromatic dispersion control in photonic crystal fibers: application to ultra-flattened dispersion, *in Optics Express*, vol. 11, no. 8, p. 843–852, 2003.

[3] J. M. Dudley, J. R. Taylor: Supercontinuum generation in optical fibers, Cambridge : Cambridge University Press, 2010.

[4] L. Zhang, C. Yang: Polarization splitter based on photonic crystal fibers, *in Optics Express*, vol. 11, no. 9, p. 1015-1020, 2003.

[5] I. Bugar, et al.: Polarization-controlled dispersive wave redirection in dual-core photonic crystal fiber, *in Laser Physics*, vol. 18, no. 12, p. 1420-1428, 2008.

[6] I. Cristiani, et al.: Dispersive wave generation by solitons in microstructured optical fibers, in *Optics Express*, vol. 12, no. 1, p. 124-135, 2003.

[7] A. B. Fedotov: Frequency-tunable supercontinuum generation in photonic-crystal fibers by femtosecond pulses of an optical parametric amplifier, *in Optical Society America*, vol. 19, no. 9, p. 2156-2164, 2002

[8] D. Pysz, et al.: Single mode PCF made of soft glass, *in Proc. SPIE 2010*, vol. 7746, no. 774618, 2010

[9] J. Y. Y. Leong, et al: High-nonlinearity dispersion-shifted lead-silicate holey fibers for efficient 1-um pumped supercontinuum generation, *in Journal of lightwave technology*, vol. 24, no. 1, p. 183-190, 2006

Silver-dielectric layered nano-devices preserving planar phase-fronts

Anna Pastuszczak[1], Rafał Kotyński
Department of Informational Optics, Faculty of Physics, University of Warsaw
Pasteura 7, 02-093 Warsaw, Poland
[1]e-mail: anna.pastuszczak@igf.fuw.edu.pl

ABSTRACT
We demonstrate a low-loss silver-dielectric layered nano-device, which does not refract the phase-fronts of an incident plane wave, and at the same time focuses its energy. The phase of an electromagnetic wave propagating within the structure remains homogeneous and planar both inside and after leaving the device. Moreover, owing to the strong effective anisotropy of the multilayers, the phase fronts of a visible electromagnetic wave propagate always in the direction of incidence, however the energy transport is perpendicular to the layers. Therefore, an incident Gaussian beam may be focused reaching the FWHM of a quarter of wavelength while its phase characteristics remains not aberrated.

Keywords: metal-dielectric multilayers, diffraction-free light propagation

1. INTRODUCTION

The perfect lens introduced in [1] consists of a thin slab of silver and is capable of overcoming the diffraction limit by enhancing the evanescent components of the spatial spectrum. This phenomenon was later experimentally verified using only 50-nm thick silver slab to resolve subwavelength gratings in the near UV [2]. Since then, subwavelength imaging in the optical wavelength range has been demonstrated in metal-dielectric periodic structures [3-14]. In our recent paper [9] the Ag-TiO_2, Ag-Gap and Ag-$SrTiO_3$ layered structures were optimised in terms of simultaneously large transmission coefficient and subwavelength resolution. The comparison of several simple theoretical models applied to these structures, such as the effective medium model, coupled cavities model, impedance matching, or Fabry-Perot resonator, led to the conclusion that optimised multilayers outstand the simpler designs in terms of both resolution and transmission as well as they exhibit different internal field pattern. Low-loss diffraction-free layered structures with slanted layers were proposed in [10]. In [12] the influence of the fabrication inaccuracies on the performance of silver-dielectric layered imaging devices is studied. Light focusing using metal-dielectric-metal layered waveguides was demonstrated in [14].

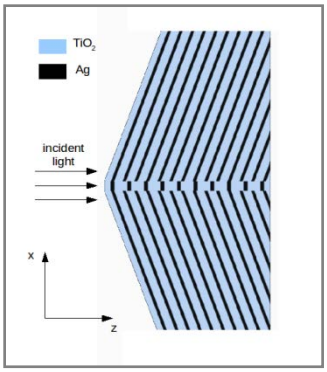

Figure 1. Schematic view of the examined structure.

2. RESULTS

We analyse a nano-device composed of silver and titanium dioxide thin films organised in three multilayers with different orientations. The schematic view of this device is illustrated in Fig. 1. The layers of the inner stack are positioned perpendicularly to the incidence direction, while the outer symmetrical multilayers are inclined at a small angle. Both multilayers were optimised in terms of high transmission coefficient and diffraction-free light propagation [9]. Moreover, the spatial periods of the multilayers and the angle of inclination were chosen in such a way that the effective wavelength of an electromagnetic wave propagating along the Z axis is exactly the same in both multilayers. As a result, for the device submerged in an impedance matched medium, the wave-fronts remain parallel to the incidence plane, and are continuous within the entire cross-profile of the structure. In consequence, the outgoing electromagnetic wave propagates as a plane wave with a modulated intensity profile.
The phase pattern of the magnetic field component H_y within the device obtained with the FDTD method is

presented in the left plot of Fig. 2. The device was illuminated with a monochromatic Gaussian beam with the vacuum wavelength $\lambda_0 = 390$ nm and the standard deviation $\sigma = \lambda_0$. The refractive index of the surrounding impedance matched medium is n = 2.18. Despite significant thickness of the layers: $d_{Ag} = 14$ nm, $d_{TiO2} = 46$ nm for the inner stack and $d_{Ag} = 11$ nm, $d_{TiO2} = 29$ nm for the outer multilayers, the shape of the phase-fronts remains consistent with the predictions based on the effective medium model.

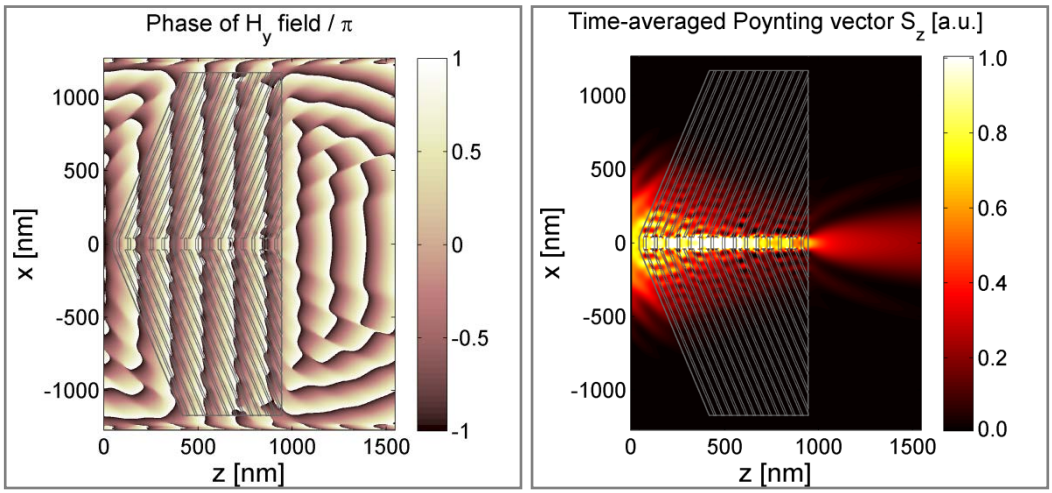

Figure 2. Phase of the magnetic field (left) and time-averaged z-component of the Poynting vector (right) in the structure illuminated with Gaussian monochromatic beam with $\lambda_0 = 390$ nm.

In the right plot of Fig. 2, the time-averaged component of the Poynting vector along the Z axis is presented. At the output of the device we obtain a narrower Gaussian beam than the incident one. Moreover, due to the planar phase characteristics, the outgoing wave diverges slowly allowing to obtain a subwavelength beam profile even at a distance of 100 nm behind the structure. At the same time, the energy transmission of the device is about 20%, which is relatively high for a structure with total thickness of 900 nm and containing over 25% of silver.
The detailed cross-sections along the X axis of the Poynting vector component S_z in the area of the output beam are presented in Fig. 3. Particular plots refer to different positions in the Z direction. Additionally, the corresponding profile of the incident Gaussian beam is shown for comparison (black line). It is observed that the peak just behind the output interface of the device (z = 950 nm) has a similar maximal value as the incident beam, however it is approximately 7 times narrower. Due to the diffraction, the full width at half maximum (FWHM) of the beam profile reaches the value of the diffraction limit of resolution at the distance of z = 1100 nm, which is about 100 nm from the output interface, and the peak maximum drops by a factor of 2 at the same time.

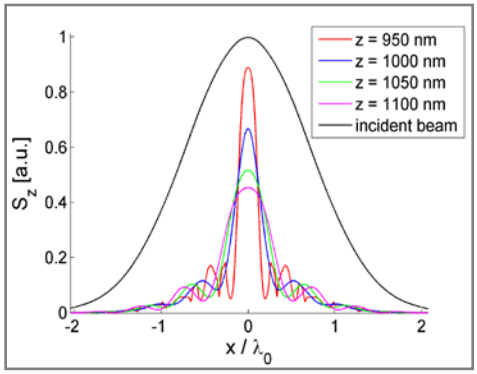

Figure 3. Time-averaged component of the Poynting vector S_z in several cross-sections at the output of the device: z = 950 – 1100 nm. For comparison – the profile of the incident Gaussian beam (black line).

3. CONCLUSIONS

We have demonstrated that a low-loss nano-device composed of two differently oriented silver-dielectric multilayers is capable of concentrating the energy of the incident electromagnetic wave within the volume of the inner multilayer and transforms an incident Gaussian beam into a beam with subwavelength FWHM of only $0.24\,\lambda_0$ right behind the structure. At the same time the specific parameters of the multilayers provide planar propagation of the wave-fronts within the whole structure and allow to preserve the wave-front shape even in the area of the output beam. The phase-fronts remain flat and homogeneous despite the significant thickness of the component layers. In consequence, the outgoing beam propagates as a plane wave with a narrow and slowly diverging intensity profile, and it remains subwavelength up to approximately 100 nm behind the structure.

ACKNOWLEDGEMENTS

We acknowledge support from the (Polish) National Centre for Research and Development project N R15 0018 06, and National Science Centre project DEC-2011/01/B/ST3/02281, and the framework of European Cooperation in Science and Technology - COST action MP0702.

REFERENCES

[1] J. B. Pendry: Negative refraction makes a perfect lens, *Phys. Rev. Lett.* vol. 85, pp. 3966-3969, 2000.
[2] D. O. Melville and R. J. Blaikie: Super-resolution imaging through a planar silver layer, *Opt. Express*, vol. 13, pp. 2127–2134, 2005.
[3] B. Wood, J. B. Pendry, and D. P. Tsai: Directed subwavelength imaging using a layered metal-dielectric system, *Phys. Rev. B*, vol. 74, 115116, 2006.
[4] P. A. Belov, Y. Hao: Subwavelength imaging at optical frequencies using a transmission device formed by a periodic layered metal-dielectric structure operating in the canalization regime, *Phys. Rev. B* vol. 73, pp. 113110, 2006.
[5] D. de Ceglia, M. A. Vincenti, M. G. Cappeddu, M. Centini, N. Akozbek, A. D'Orazio, J. W. Haus, M. J. Bloemer, and M. Scalora: Tailoring metallodielectric structures for superresolution and superguiding applications in the visible and near-ir ranges, *Phys. Rev. A*, vol. 77, 033848, 2008.
[6] M. Conforti, M. Guasoni, and C. De Angelis: Subwavelength diffraction management, *Opt. Lett*., vol. 33, pp. 2662-2664, 2008.
[7] R. Kotyński, T. Stefaniuk: Multiscale analysis of subwavelength imaging with metal-dielectric multilayers, *Opt. Lett.* vol. 35, pp. 1133-1135, 2010.
[8] N. Mattiucci, D. Aguanno, M. Scalora, M. J. Bloemer, and C. Sibilia: Transmission function properties for multi-layered structures: Application to superresolution, *Opt. Express*, vol. 17, pp. 17517-17529, 2009.
[9] A. Pastuszczak, R. Kotyński: Optimised low-loss multilayers for imaging with sub-wavelength resolution in the visible wavelength range, *J. Appl. Phys.*, vol. 109, 084302, 2011.
[10] R. Kotyński, T. Stefaniuk, and A. Pastuszczak: Sub-wavelength diffraction-free imaging with low-loss metal-dielectric multilayers, *Applied Physics A*, vol. 103, pp. 905-909, 2011.
[11] R. Kotyński, T. J. Antosiewicz, K. Król, and K. Panajotov: Two-dimensional point spread matrix of layered metal–dielectric imaging elements, *J. Opt. Soc. Am. A*, vol 28, pp. 111-117, 2011.
[12] R. Kotyński, H. Baghdasaryan, T. Stefaniuk, A. Pastuszczak, M. Marciniak, A. Lavrinenko, K. Panajotov, T. Szoplik: Sensitivity of imaging properties of metal-dielectric layered flat lens to fabrication inaccuracies, *Opto-Electron. Rev.*, vol. 18, pp. 446-457, 2010.
[13] R. Kotyński: Fourier optics approach to imaging with sub-wavelength resolution through metal-dielectric multilayers, *Opto-Electron. Rev.*, vol. 18, pp. 366-375, 2010.
[14] W. M. Saj: Light focusing on a stack of metal-insulator-metal waveguides sharp edge, *Optics Express*, vol. 17, pp. 13615-13623, 2009.

NOTES

Bottom-up Method of Manufacturing Three-dimensional Bulk Plasmonic Nanocomposites with Silver Nanoparticles

M.Gajc, B.Surma, A.Klos, D.A.Pawlak.
Institute of Electronic Materials Technology (ITME), ul. Wolczynska 133, 01-919 Warsaw, Poland.
e.mail: Andrzej.Klos@itme.edu.pl

ABSTRACT
Three dimensional metallodielectric material made of sodium borophosphate $Na_5B_2P_3O_{13}$ (NBP) dielectric matrix doped with silver nanoparticles was obtained by micro-pulling down method. Optical measurements performed in visible and near infrared regions of the spectrum, showed localized surface plasmon resonance in two regions at 405 nm and broad peak at 1 – 2 μm . In case of NBP matrix doped with Ag nanoparticles and simultaneously with Er^{3+} ions an enhancement of photoluminescence of erbium at 1,5 μm of wavelength was observed. This is due to local field enhancement mechanism.

Keywords: nanoplasmonics, surface plasmonic resonance, silver nanoparticles.

1. INTRODUCTION

Metallodielectric materials with resonances at optical and IR wavelengths have been the subject of increasing interest due to their prospective exploitation for photonic/plasmonic applications. In small plasmonic objects, surface plasmons can interact with photons at characteristic frequency and cause occurrence of localized surface plasmon resonance (LSPR) manifested by increased absorption and scattering. Additionally, the local field enhancement (LFE) around the nanoplasmonic elements enables enhancement of subsequent optical processes as photoluminescence, and optical nonlinearity.

2. EXPERIMENT

In this work we demonstrate a fast and low-cost bottom-up method for manufacturing of nanoplasmonic composites. This method is based on a direct doping of dielectric matrices with plasmonic nanoparticles and it enables obtaining volumetric three-dimensional materials through a non-chemical process. The main idea is based on utilizing the matrices with lower melting temperature than that of the applied nanoparticles. The dielectric matrices is made of sodium borophosphate dielectric glass $Na_5B_2P_3O_{13}$ (NBP), and reported in the literature melting point is $m_p=780^0C$ [1], [2]. For the plasmonic nanoparticles with resonances at visible region we have chosen silver nanoparticles, nominally spherical with 20 nm in diameter. Differential scanning calorimetry (DSC) measurements confirms that Ag nanopowder melts with the melting temperature of bulk silver m_p (Ag) $=961,8^0C$, while NBP glass melts at lower temperature than the one given in literature, $m_p=750^0C$.

Metallodielectric materials have been obtained by micro-pulling down method [3]. This method is based on directional solidification of the melt, which flows through a capillary placed in a die at the crucible bottom. The pulling rate was equal to 3mm/min and the diameter of obtaining rods was in the range from 3 to 5 mm. The extinction and transmission measurements in Vis and NIR region of the spectrum were performed. It was demonstrated, that NBP:nanoAg rods exhibit the resonance at visible wavelengths – Fig. 1. The NBP glass rod was doped nominally with 0, 15 wt. % of silver nanoparticles.

In order to achieve PL plasmonic enhancement, NBP glass was doped simultaneously with silver nanoparticles and erbium Er^{3+} ions. Preliminary PL measurements confirmed 1-fold enhancement of PL of erbium ions (at 1, 5 μm of wavelength).

The demonstrated here method of manufacturing bulk nanoplasmonic composites differs significantly from other methods of manufacturing nanoparticles-based composites. It enables obtaining bulk three-dimensional materials through a non-chemical process. This provides the possibility to introduce nanoparticles of various chemical compositions with different electromagnetic properties – metals (silver, gold, nickel) highly doped semiconductors (for example ITO, ATO Nan particles). It also enables addition of other doping agents as rare earth ions and quantum dots.

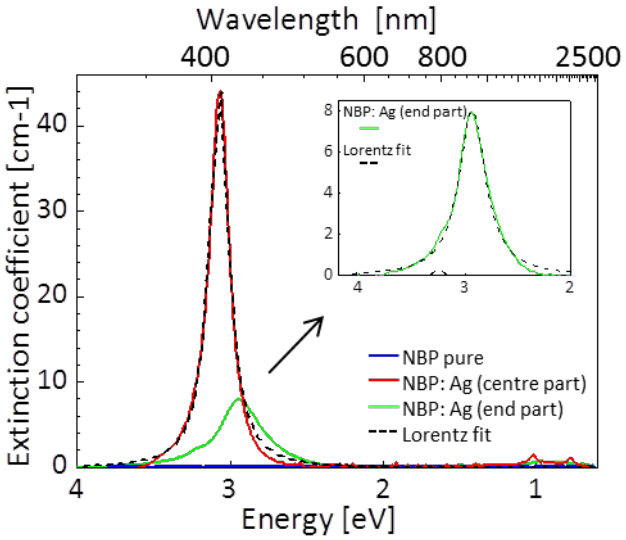

Fig. 1. Extinction spectra of pure NBP, and NBP:nanoAg at different places along the plasmonic rod, demonstrating LSPR effect at Vis range; red curve– sample from centre part of the rod, sample thickness 368 µm; green curve – sample cut from the end of the NBP:nanoAg rod.

ACKNOWLEDGEMENTS

The authors thank the COST Action MP0702 for support. The authors thank the FP7 NMP ENSEMBLE Project (GA NMP4-SL-2008-213669) for partially supporting this work. AK, MG and DAP thank the Project operated within the Foundation for Polish Science Team Programme co-financed by the EU European Regional Development Fund for partial support of this work.

REFERENCES

[1] M. Berkowski, *et al*.: Conditions of maintenance of a flat crystal/melt interface during Czochralski growth of bismuth germanium oxide single crystals, *J. Cryst. Growth*, vol. 103, pp. 225-232, 1991.

[2] A. Klos, M. Gajc, R. Diduszko, D. A. Pawlak : Bottom-up approach to hybrid metallodielectric materials" *Proc. ICTON 2009,* San Miguel de Azores June 2009. VOLS 1 and 2, pp. 421-424 art. no. 5185322

[3] Yoon, D. H., Yonenaga, I., Ohnishi, N., & Fukuda: T. Crystal growth of dislocation-free LiNbO3 single crystals by micro pulling down method. *J. Cryst. Growth* vol. 142, pp.339-343 (1994).

Third order nonlinear optical properties with Oligophenylenedyads

I. Guezguez[1, 2], K. Iliopoulos[2], M. Hjiri[1], N. Jaba[1], A. Haj Said[3], H. Belmabrouk[1], B. Sahraoui[2]
[1] *Laboratory Electronic and Microelectronic, University of Monastir, Tunisia*
[2] *Laboratory MOLTECH - Anjou, University of Angers, France*
[3] *Laboratory Polymers, Biopolymers,Organic materials, University of Monastir, Tunisia*
e-mail : imen.guezguez@etud.univ-angers.fr

Introduction:

This study concerns the nonlinear optical characterization of different materials presenting a side chain on the oligophenylene. Strong nonlinearity has been found, which is in general dependent upon the side chain.

Discussion:

The chemical structure can be described as an oligophenylene backbone with different molecular moieties as side chains. These moieties are the (Z)-3-(4-methoxyphenyl)acrylonitrile and the (Z)-3-(dimethylamino)acrylonitrile, mentioned as DMPA and Faa, respectively.

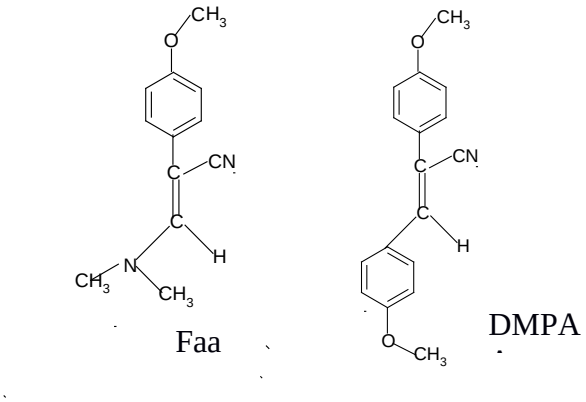

Fig 1. Structures of the molecular moieties Faa and DMPA

Concerning the nonlinear optical characterization a Two Photon Absorption (TPA) setup has been used in order to determine the two photon absorption efficiency. In particular, by these measurements, the corresponding nonlinear optical parameters (two photon absorption coefficient, imaginary part of the third order nonlinear susceptibility and second hyperpolarizability) have been found. For this investigation the 532 nm, frequency doubled exit, of a 30 ps diode pumped passively mode-locked Nd: YVO4 laser with a repetition rate of 10 Hzhas been used. In all cases the concentration and energy dependence of the nonlinearity has been determined in order to verify that no saturation of the response was taking place during the measurements.

The results have shown that these systems possess strong optical nonlinearity which has been strongly dependent upon the concentration, the incident laser energy, the intermolecular π-π stacking interactions, as well as the conformational structure changes.

Conclusion:

In this work novel nonlinear optical systems have been synthesized. The fact that these systems are also accompanied by high nonlinear optical response renders possible the utilization of such systems for nonlinear optics. Also new prospects are opening, which include the incorporation of a metal atom in the molecular structure in order to further enhance the nonlinearity and/or modify the nonlinear optical parameters in order to match specific photonic applications.

Reference:

[1] I. Ben Khalifa, Journal of Molecular Structure, 997, 37-45, 2011
[2] R. W Boyd Nonlinear Optics, Rochester, New York, 2007

Photoluminescence studies of selected styrylquinolinium thin films made using thermal evaporation deposition technique.

H. El Ouazzani[1], B. Derkowska[2], Z. Łukasiak[2], K. Iliopoulos[1], B. Sahraoui [1], M. Todorova[3], R. Bakalska[3], Ts. Kolev[3], M.Bakasse[4] and A.Arbaoui[4].
E-mail: hasnaa.elouazzani@etud.univ-angers.fr
[1]*Laboratory of MOLTECH-Anjou, CNRS UMR 6200, University of Angers,2 Bd Lavoisier, 49045 Angers cedex, France*
[2]*Institute of Physics, N. Copernicus University, Grudziądzka 5 87-100 Toruń, Poland*
[3]*Plovdiv University "P. Hilendarski", Faculty of Chemistry, 24, Tzar Assen Str., 4000 Plovdiv, Bulgaria3 Plovdiv*
[4]*Faculty of Science, University Chouaib Doukkali, 24000, El Jadida, Morocco*

Abstract

In this paper we present a photoluminescence (PL) study of new styrylquinolinium dyes. We made a comparative study of the luminescent properties of thin films grown on quartz substrates using thermal evaporation deposition method. Investigated films show PL emission from the violet to near-IR region at room temperature.
Keywords: photoluminescence, styrylquinolinium organic dye, thin films.

1. Introduction

Modern science and technology of new materials require with special properties to make innovations. This helps focus the development on improving the technological devices and procedures operation. This means, make them faster, more economically viable, and better quality. At the same time, new materials are introduced to improve our quality of life. In general opens possibility for its applications in optoelectronic devices [1,2].

Our work is mainly focused on the production of high quality optical films for novel laser devices. The thin-film format of styrylquinolinium dyes compounds are ideal for the study of the electronic transfer process and for displaying photo-induced energy and electron transfer process, in particular for applications in the field of photonic devices. In the second part, the photoluminescence of these compounds is investigated. We have studied the photoluminescence emission spectra of thin under pulsed excitation using nitrogen laser (emission at 337.1 nm). Luminescence spectroscopy can provide a valuable and needed tool for the study of details of intramolecular energy transfer processes.

2. styrylquinolinium dyes

In the present investigation, three new organic compounds, *i.e*. 4-[(*E*)-2-(2-hydroxynaphthalen-1-yl)ethenyl]-1-methylquinolinium tosylate (D**13**), 4-[(*E*)-2-(2-hydroxynaphthalen-1-yl)ethenyl]-1-methylquinolinium iodide (**D7**), and 4-{(*E*)-2-[4-(dimethylamino)naphthalen-1-yl]ethenyl}-1-methylquinolinium iodide (**D9**) (see Figure 1) have been synthesized by Knoevenagel condensation of 2-hydroxy- or 4-N,Ndimethylaminonaphtaldehyde and the respective quaternary lepidinium salts in good yields.

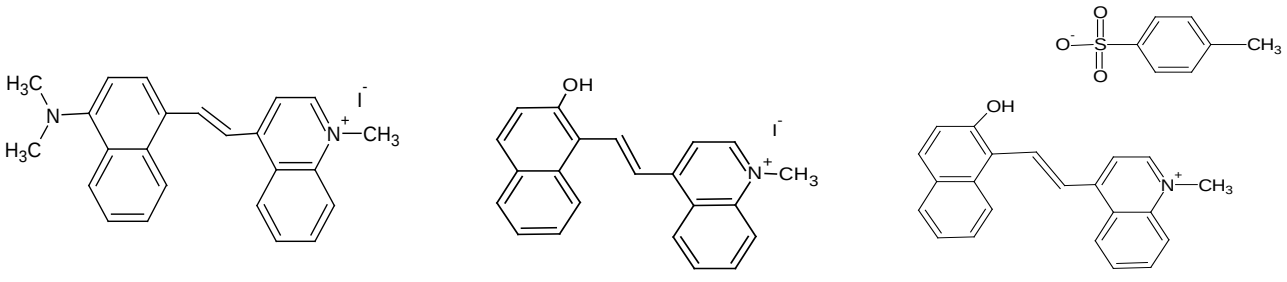

Dye 9 **Dye 7** **Dye 13**

Figure 1: Chemical structures of styrylquinolinium dyes D9, D7 and D13.

The basic idea of the design of the new styrylquinolinium dyes system is to enlarge the conjugation by using quinolinium and naphthalene moieties. All three dyes are salts, two of them D9 and D7 are N-methylquinolinium iodides, and D13 is N-methylquinolinium tosylate (p-toluene sulfonate) as anion, such a popular compound DAST. As an electrondrawing group in naphthalene nucleus D9 has N-dimethylamino group N(CH3)2, and D7 and D13 have a phenolic hydroxyl group OH at position 2.
The absorption spectra of solution were measured in the spectral region 200-700 nm at room temperature. In the case of Dye 7and Dye 9 dissolved in THF the absorption peak is shown at around 480 nm for both of them. However, in the case of Dye 13 dissolved in methanol the absorption peak is presented at around 500 nm and a small one at around 650 nm.

3. Thermal evaporation deposition method

Evaporation is a common method of thin film deposition. The source material is evaporated in a vacuum. The vacuum allows vapor particles to travel directly to the target object (substrate), where they condense back to a solid state. The vacuum thermal evaporation deposition technique consists in heating until evaporation of the material to be deposited. The material vapor finally condenses in form of thin film on the cold substrate surface and on the vacuum chamber walls. Usually low pressures are used, about 10^{-6} or 10^{-5} Torr, to avoid reaction between the vapor and atmosphere. At these low pressures, the mean free path of vapor atoms is the same order as the vacuum chamber dimensions, so these particles travel in straight lines from the evaporation source towards the substrate. In thermal evaporation techniques, different methods can be applied to heat the material.
Thin films of styrylquinolinium dyes were prepared by thermal evaporation deposition method on quartz substrate. The process of preparing has been carried out under pressure about $2 \cdot 10^{-5}$ Tr and at temperature of the source about 200°C.

4. Photoluminescence studies

Photoluminescence spectroscopy is a contactless, nondestructive method of probing the electronic structure of materials. Light is directed onto a sample, where it is absorbed and imparts excess energy into the material in a process called photo-excitation. One way this excess energy can be dissipated by the sample is through the emission of light, or luminescence. In the case of photo-excitation, this luminescence is called photoluminescence. The intensity and spectral content of this photoluminescence is a direct measure of various important material properties.

Photoluminescence spectra were registered using pulse nitrogen laser (home made) as a source of excitation (l = 337.1 nm, FWHM=5 ns, power in pulse 20 kW, 10 Hz repetition rate). Intensity of laser illumination was strongly decreased by slit and glass filter. The proper band of emission was selected by a monochromator (SPM-2 ZEISS) and registered by a combination of photomultiplier (R-928 HAMAMATSU) and analog boxcar (162/164 PAR) [5,6].
For photoluminescence spectra measurements the time constant of the sampling head 1 SH t = m s and pulse-simultaneous delay were selected. PL experiments were carried out at room temperature and samples were enclosed in helium cryostat in vacuum environment. The signals were processed and analysed by personal computer.

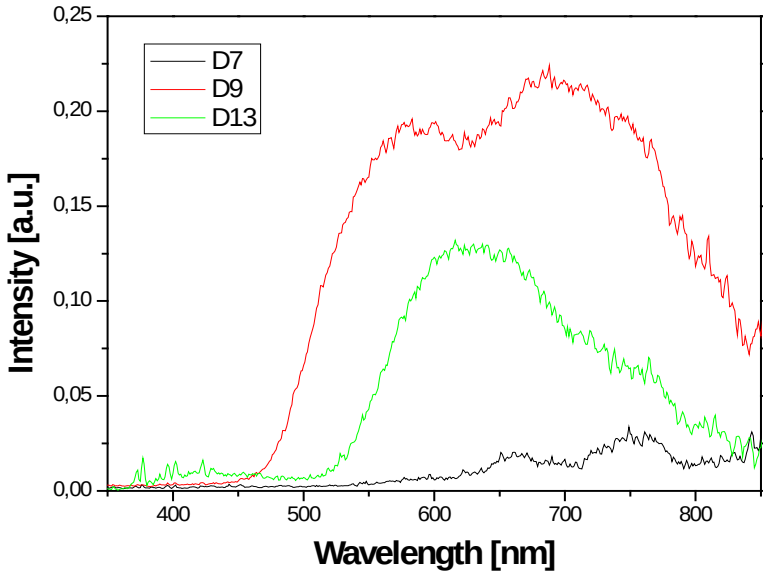

Figure 2: PL spectra at room temperature for investigated compounds on quartz substrate.

Figure 2 shows the photoluminescence spectra of organic materials thin films obtained by thermal evaporation deposition method on quartz substrate. These experiments were carried out at room temperature.

We obtained high signal for both D9 and D13 compared to weak signal of D7. We observe two main peaks on PL spectra (first near 570 nm and second near 680 nm) for the compound D9 (red curve). Similar results we got for D7 but the low signal was observed. In the case of D13 we can see only one peak near 600 nm and a small shoulder at around 750 nm (green curve). We supposed that it is caused the similar chemical structures of these dyes. We can also see shift the peak to the longer wavelength.

Conclusions

We have prepared thin films stryrylquinolinium dyes using thermal evaporation deposition method. We have obtained a good quality and homogenous films. Then we investigated the photoluminescence at the room temperature. Good results have been obtained for D9 and D13, while D7 show a weak signal.

Acknowledgements

The author would like to thank the COST action MP0702 (Towards Functional Sub-Wavelength Photonic Structures) for the financial support.

References

[1] H.S. Nalwa, M. Hanack, G. Pawlowski, M.K. Engel, Chem. Phys. 245 (1999) 17.
[2] C.J. Yang, S.A. Jenekhe, Chem. Mater. 6 (1994) 196.
[3] Karim Bouchouit, El-Eulmi Bendeif, Hasnaa El Ouazzani, Slimane Dahaoui, Claude Lecomte, Nourredine Benali-Cherif and B. Sahraoui,"Correlation between structural studies and third order NLO properties of selected new quinolinium semi-organic compound", Chemical Physics, (2010)
[4] D. Josse, R. Heirle, I. Ledoux, J. Zyss, Appl. Phys. Lett. 53 (1988) 2251.
[5] K. Bartkiewicz, Z. Łukasiak, A. Zawadzka, P. Płóciennik, A. Korcala,"Photoluminescence of ZnO Thin Films on Si Substrate", 10.1109/ICTON.2010.5548975, 2010 IEEE
[6] A. Zawadzka, P. Płóciennik, K. Brodzińska, Z. Łukasiak, K. Bartkiewicz and A. Korcala, "Investigations of Temperature Dependent Photoluminescence Process in MgO Thin Films", 10.1109/ICTON.2010.5549017 2010 IEEE.

NOTES

Calculations of nonlinear optical properties and surface relief gratings studies of some selected azo-azulenes derivatives

A. Migalska- Zalas[1], Sylvie Dabos-Seignon[2] , Z. Essaidi[2] and B. Sahraoui[2],
[1]Institute of Physics, J. Dlugosz Academy of Czestochowa PL-42217, Aleja Armii Krajowej 13/15, Częstochowa, Poland; e-mail:aniazal@op.pl.
[2]Institute of sciences and molecular technologies of Angers MOLTECH Anjou - UMR CNRS 6200 Molecular interaction nonlinear optics and structuring MINOS 2 bd Lavoisier 49045 ANGERS cedex2, France.

ABSTRACT
The nonlinear optical properties and the photo-induced structuration of the azo-azulenes derivatives using standard methods like: degenerate four wave mixing experiment, transmission holographic technique and the atomic force microscopy (AFM) were studied. The experimental results were completed by quantum chemical semi empirical calculations for molecules in vacuum. Theoretical calculation of second order molecular hyperpolarisabillity for the studied was done.

Keywords: nonlinear optics, hyperpolarisabillity, susceptibility, relief gratings,

1. INTRODUCTION

Functionalized azo-azulene derivatives compounds with azobenzene molecules are materials interesting for study of the linear, nonlinear optical properties and electronic transfer processes. The studied molecules (Figure 1.) based on azulene moiety (acting as the donor) linked through the azo (-N=N-) group to an acceptor. The last one was either substituted by phenyl, thiazole or benzothiazole rings. The azulene molecule possess both electron donating and electron accepting character through respectively five-membered ring and seven-membered unsaturated ring. Conecting donor and acceptor moieties with a conjugated bridge is a well established strategy to obtain molecules with high values of nonlinear hyperpolarizability.

In this work a study in picosecond regime the influence of light polarization of imprinting beams on the formation dynamics of these gratings were performed. For these measurements, the two imprinting beams have been polarized in s-s and p-p states. In order to deduced the values of third–order nonlinear optical susceptibility $\chi^{(3)}$ degenerate four wave mixing efficiency (at λ = 532 nm) as a function of the intensity of the wave pumps for all compounds were done. This work reported theoretical calculations of second order frequency-dependent molecular hyperpolarizability in order to propose a NLO study of these complexes on a molecular scale.

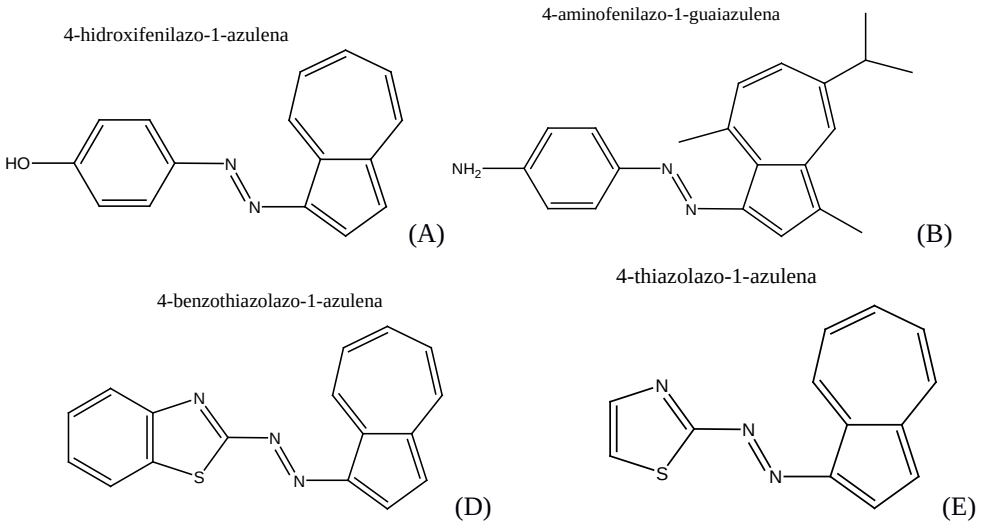

Figure 1. Chemical structures of studied azo-azulene derivative molecules.

Comparison of theoretical results with experimental data received from the degenerate four wave mixing experiment may give important information concerning the origin of the observed nonlinear optical properties. Especial attention will be devoted to the delocalisation of π electrons along the molecular backbone influence of different ions on the output of third order optical properties.

2. THEORETICAL CALCULATIONS

The MM^+ molecular force field method was used for total energy minimization and for building of the molecular optimized geometry [i,ii]. Quantum chemical calculations were performed by semi-empirical PM3 [iii,iv] method within a framework of the restricted Hartree-Fock approach and convergence limit up to 10^{-6} eV after 500 iterations was achieved. The calculations mixes all single determinant wavefunctions that can be obtained from the ground state by exciting electrons from a subset of the occupied orbitals to a subset of the unoccupied orbitals. The electronic spectra were calculated by the configuration interaction (CI) method with the maximum excitation energy up to 9 eV. Local perturbation were considered only within a framework of the isolated molecule in vacuum. The values of second order hyperpolarizabillity may be expressed in terms of different energy levels from g to n of the molecule and is described by equation (1)[v].

$$\gamma_{ijkl} = K\sum_{g=1}^{n}\frac{\left|\mu_i^{(g)}\right\|\mu_j^{g}\left\|M_k^{(g)}-M_k^{(0)}\right\|M_l^{(g)}-M_l^{(0)}\right|}{(E_g^2-(2\hbar\omega)^2+H)} \qquad (1)$$

where $\mu^{(g)}_I$, $\mu^{(g)}_j$, are the transition dipole moment between the high occupied molecular orbital (HOMO) and the exited state, $|M^{(g)}_k - M^{(0)}_k|$-difference between the excited (configuration interaction (CI) level) state dipole moment and ground state one, E_g- transition energy from the ground to exited state, $\hbar\omega$ is the energy of a incident laser photon, H determines the line shape broadening, n is a number of exited state. Indices i,j,k,l = x, y, z are defined as laboratory Coordinate Cartesian system. In a present work we calculated only γ_{yyyy}, where the y direction corresponds to the maximal permanent dipole moment.

Table 1. present the measured third-order susceptibilities and the calculated second order hyperpolarizabilities γ for the investigated molecules. The obtained values of calculated second order nonlinear hyperparizabilties are comparable with the nonlinear coefficients obtained for similar molecules in Ref. [vi]. The second –order hyperpolarizabilities γ are measured and deduced from degenerate four wave mixing (DFWM) technique at fundamental wavelength of 532 nm described in Ref. [vii].

The difference between the experimental and theoretical data it results with taken into account different origin of the third order nonlinearity. The experimental results are interpreted by relating the nonlinearities to an additional contribution arising from the intramolecular charge transfer. We can expect that for these molecules also intermolecular electron vibration electronic interactions and a reorientation under applying of electric field plays key role in the observed nonlinearities what are not taken into account in suggested theoretical calculations. As you know the greatest problem associated with non-linear optical compounds is connected not only with ideal molecules but also the incorporation of these molecules to form ideal macroscopic samples for non-linear optics. So the preparation of the samples play a key role in the obtained big non-linear optical properties of the samples.

Table 1. Values of calculated and measured nonlinear optical properties.

Molecule	$\chi^{(3}$ [m²/V²]	γ_{xxxx} (ESU) Calculated at λ = 532nm	Dipole moment (D)	Homo (eV)	LUMO (ev)	Optical gap (ev)
Molecule A	$0{,}16\times10^{-20}$	$1{,}8\times 10^{-35}$	3,42	-7,75	-1,55	6,20
Molecule B	$1{,}42\times10^{-20}$	$2{,}31\times 10^{-34}$	1,85	-7,19	-1,25	5,94
Molecule D	$6{,}54\times10^{-20}$	$3{,}05\times 10^{-35}$	5,67	-8,09	-1,99	6,10
Molecule E	$5{,}07\times10^{-20}$	$1{,}60\times 10^{-35}$	5,46	-8,08	-1,95	6,13
CS_2	-	$3{,}95\times 10^{-35}$	-	-	-	-

Taking under attention the different mechanism of formation of nonlinearity in experiment and introduced in calculations we can compare the only trend of changes of non-linear coefficient collected in Table 1. We have rather good coincidence between the theoretical calculations and experimental data of second-order hyperpolarizabity for all compounds. We can see that the adjunction of a functional methyl grup to the seven-membered unsaturated ring in molecule B (4-aminofenilazo-1-guaiazulena) lead to the substantial increase of the cubic hyperpolarisability γ . It can be explained by longer extent of molecule B favouring electron delocalization. From the other sid the remainig molecules are more stabilised owing to pronounced steric hindrance and resulting larger dipole moments presented in the Table 1. The azo-azulene molecules are radicals of different natures, one donor and one acceptor and have a large third order nonlinearity since the radicals add their effects, thus intensify the asymmetric distortion of the conjugated system. Further the electronic properties of this type of molecules exibit a unsual property, the intramolecular [viii] charge transfer between the two radicals.

3. PHOTO-INDUCED SURFACE RELIEF GRATINGS

The surface relief gratings continue to provide numerous research works due to their applicative potential in diffractive gratings for laser cavities [ix], couplers in waveguides [x, xi], alignment control in liquid crystal molecules [xii], chemical and biological probes [xiii], or in optical data storage as well [xiv]. There are several hypotheses on the mechanisms of surface relief gratings formation. Nevertheless, the principal existing models (in continuous regime) have demonstrated that the origin of the effects observed is mainly due to a macroscopic transport of matter induced at microscopic level by photoisomerization of azo compounds. The experimental set-up used in this study is simple technique of Degenerate Two Waves Mixing (DTWM) set up in transmission mode (first time presented by Shank *et al.*) [xv, xvi].

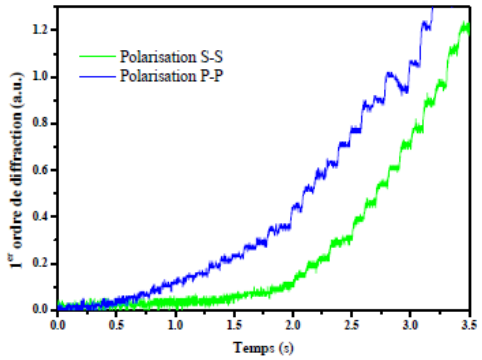

Figure 2. First order diffraction efficiency (for complex D) as function of irradiation time for different polarization states of writing beams (at 7 GW cm^{-2}).

Photoinduced surface relief gratings have been written on 300 nm thin layers of A, B, D, E complexes. The incidence angle of the two writing beams (from picosecond laser Nd:YAG at 532 nm) has been settled at $\theta \approx 60°$ in order to obtain a grating space equivalent to the wavelength of the writing beams ($\Lambda = \lambda / 2\sin(\theta/2) \approx 532$ nm). The photoinduced gratings are characterized either by their diffraction efficiency or by their average modulation amplitude, (determined mostly using an atomic force microscope (AFM)) [xvii].
For the determination of diffraction efficiency of a surface relief grating, the efficiency of the first order of diffraction is registered (the ratio between the diffracted intensity of +1 order and the intensity of the incident beam).

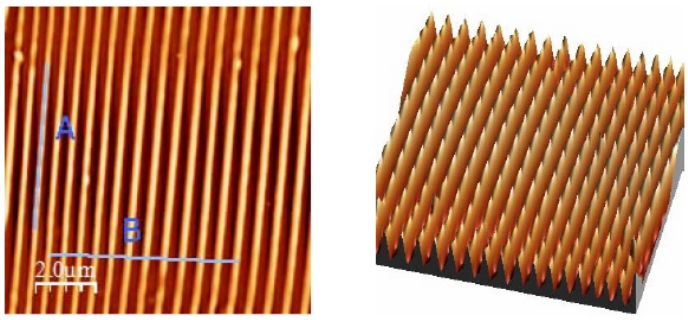

Figure 3. Two (left) and three (right) dimensional AFM scans of a photoinduced surface relief grating (complex D) at 7GW cm^{-2} (in polarization s-s*).*

The diffracted light came from a continuous reading laser with the wavelength outside the absorption band of the studied compounds (cw laser He-Ne 30 mW at 632.8 nm polarized vertically). Lagugné-Labarthet *et al.* [xviii] have demonstrated that the local molecular orientation in surface relief gratings depends on the polarization of incident beams. Our study allowed to confirm these results by evidencing the influence of the polarization of writing beams (at 7 GW cm^{-2}) on the surface relief gratings diffraction efficiency. The highest diffraction efficiency and modulation amplitude (100 nm) have been observed for the complex D in *p-p* polarization state. Figure 2. shows that the complex D (benzothiazolazo-1-azulena) exhibits faster response in *p-p* polarization state. The different results obtained for the polarizations *s-s* and *p-p* are related to preferential orientation of the chromophores along direction perpendicular to the substrate. In such a way that molecular movement which

determines the grating formation is delayed. Surface relief gratings are easy to scan by atomic force microscope (AFM) due to open (to air) surface. The 2D and 3D SRGs images (see Figure 3) are visualized by *Nanotec WSxM4.0 Develop 8.6* (program to determine the principal orientation directions of the gratings). It can be deduced that the surface relief gratings are written perpendicularly to the polarization direction of writing beams. The investigations show that from among the investigated molecules, the molecule D represent the best results, with regard on the band absorption including the wavelength excitation what favours the absorption of light and the transfer of the excitation energy to the chromophores.

4. CONCLUSIONS

We have investigated contribution of the different radicals of different natures one donor and one acceptor in azo-azulene molecules to the output of the nonlinear coefficient. The difference between experimental and theoretical data show that the second–order hyperpolarizabilities γ depends from the intermolecular interactions and the molecular reorientation. Different moieties causes the substantial changes of non-linear optical coefficients.

We have presented the properties of photo-induced structuration composed of the most powerful: the benzothiazolazoazulene. We have shown that it is possible to create different structures on the same sample by varying intensity. Results show a periodic structure in a first time corresponding to figures interference, followed by self-organization. It thus passes from a structuring dimensional to a two-dimensional structuration. The highest first order diffraction efficiency have been obtained for the complex **D** with regard on the band absorption including the wavelength excitation what favours the absorption of light and the transfer of the excitation energy to the chromophores.

The study of nonlinear effects and efficiency of diffraction gratings is interesting for its applicative potential allows a thorough characterization of new materials with strong NLO properties and materials for data storage.

ACKNOWLEDGEMENTS

Acknowledgements to the Institute of Sciences and Molecular Technologies of Angers MOLTECH Anjou and Service Commun d'Imageries et Analyses Microscopiques (CIAM, University of Angers) for performing AFM measurements. The author would like to thank the COST action MP0702 (Towards Functional Sub-Wavelength Photonic Structures) for the financial support.

REFERENCES

[1] 1. S.J. Weiner *et al*.: *J. Am. Chem. Soc*., 106, 765, (1984).
[2] 2. S.J. Weiner, *et al*.: *J. Comput. Chem*., 7, 230, (1986).
[3] M. J. S. Dewar, *et al*.: *J. Am. Chem. Soc*., 107, 3902 (1985).
[4] M. J. S. Dewar and K. M. Dieter: *J. Am. Chem. Soc*., 108, 8075, (1986).
[5] A. Migalska-Zalas, *et al*.: *Spectrochimica Acta Part A: Molecular and Biomolecular Spectroscopy*, 69, 1, pp. 178-182, (2008).
[6] J.L.Oudar ,D.S.Chemla: *J.of Chem.Phys*. 66 ,6, 2664, (1977).
[7] B. Sahraoui, G. Rivoire: *Opt. Commun*. 138, 109, (1997).
[8] G. Kelly, *et al*.:*Inorganic Chem*. Com. 8, 10, 874, (2005).
[9] R. D. Boyd, *et al*.: *Appl. Opt.* 34 1697 (1995).
[10] B. D. Clymer, *Appl. Opt.* 28 5374, (1989).
[11] A. Natansohn, *et al*.: *Academic Press, San Diego* (2002).
[12] X. T. Li, A. Natansohn and P. Rochon: *Appl. Phys. Lett*. 74 3791 (1999).
[13] N. Kinrot and M. Nathan, J. Lightwave: *Technol.* 24 2139 (2006).
[14] R. Hagen and T. Bieringer: *Adv. Mat*. 13 1805 (2001).
[15] J. H. Hong and R. Saxena: *Opt. Lett*. 16 180, (1991).
[16] C. V. Shank, J. E. Bjorkholm and H. Kogelnik: *Appl. Phys. Lett.* 18 395 (1971).
[17] J. Luc, *et al*.: *Opt. Express*, 16 15633, (2008)
[18] F. Lagugné-Labarthet, T. Buffeteau, and C. Sourisseau: *J. Phys. Chem*. B 102 5754 (1998)

The main objective of the **COST Action MP0702: Towards Functional Sub-Wavelength Photonic Structures [http://cost-mp0702.nit.eu/]** has been to establish active links between European laboratories working in the field of artificial materials for photonics applications, where the structural dimensions are at or below the wavelength of light.

MINAP2012 (Micro- and nano-photonic materials and devices) is the Final Conference of the COST Action MP0702 and is focused on the properties of photonic materials and devices at micro- and nano-scale, as well as on their novel or advanced applications, especially in telecommunications, computing, sensing, and energy.

ISBN: 978-83-7798-020-0